BEILSTEIN JOURNAL OF NANOTECHNOLOGY

# Towards multifunctional inorganic materials: biopolymeric templates

Edited by Claudia Steinem and Joachim Bill

# Imprint

Beilstein Journal of Nanotechnology
www.bjnano.org
ISSN 2190-4286
Email: journals-support@beilstein-institut.de

The *Beilstein Journal of Nanotechnology* is published by the Beilstein-Institut zur Förderung der Chemischen Wissenschaften.

Beilstein-Institut zur Förderung der Chemischen Wissenschaften
Trakehner Straße 7–9
60487 Frankfurt am Main
Germany
www.beilstein-institut.de

BEILSTEIN JOURNAL OF NANOTECHNOLOGY

# Towards multifunctional inorganic materials: biopolymeric templates

Claudia Steinem*[1] and Joachim Bill*[2]

Editorial

Open Access

Address:
[1]Institute of Organic and Biomolecular Chemistry, Georg-August University Göttingen, Tammannstr. 2, 37077 Göttingen, Germany and [2]University of Stuttgart, Institute of Materials Science, Heisenbergstr. 3, 70569 Stuttgart, Germany

Email:
Claudia Steinem* - claudia.steinem@chemie.uni-goettingen.de;
Joachim Bill* - bill@imw.uni-stuttgart.de

* Corresponding author

*Beilstein J. Nanotechnol.* **2015,** *6,* 1698–1699.
doi:10.3762/bjnano.6.172

Received: 19 June 2015
Accepted: 17 July 2015
Published: 05 August 2015

This article is part of the Thematic Series "Towards multifunctional inorganic materials: biopolymeric templates".

Editor-in-Chief: T. Schimmel



Inorganic functional materials are widely applied due to their electrical, optical, magnetic and mechanical properties. Accordingly, these materials exhibit an enormous impact on key technologies relevant for future fields such as energy generation and storage, information and medical technology as well as automotive engineering. The manufacturing of such materials is usually performed at elevated temperature and/or pressure combined with enormous experimental effort and extensive equipment. Consequently, problems arise due to shrinkage or grain growth. In addition, the production of composite materials with multifunctional properties may be severely limited because of the mismatch between the thermal expansion coefficients of the different components. This is also an issue in the combination of inorganic components with temperature sensitive materials, which is limited or even impossible.

In contrast to the aforementioned manufacturing methods, biomineralization leads to fascinating, complex-structured, inorganic materials under ambient conditions. The corresponding processes have been evolutionarily optimized over millions of years and involve biopolymeric templates, which control the mineralization and the structure formation of inorganic components in an aqueous environment. Accordingly, composites made of inorganic solids (i.e., calcium phosphate or carbonate) and biopolymers are formed. Furthermore, the resulting combination of inorganic and bioorganic components yields biominerals with unique multifunctional features and an expanded spectrum of properties as compared to those of the pure inorganic components.

Although the composition of biominerals comprises only a limited number of chemical elements, the principles of biomineralization and the obtained structures can be considered archetypes for the generation of inorganic functional materials not found in living nature. This highly topical research field is currently drawing worldwide attention and is a main subject of the Priority Program 1569, “Generation of multifunctional inorganic materials by molecular bionics”, of the Deutsche Forschungsgemeinschaft in Germany. Correspondingly, this Thematic Series addresses multifunctional, inorganic materials generated by templating with biomolecules. The reader of this series will gain a comprehensive overview about the general

ideas and principles of biopolymeric templating by means of selected examples presented in the contributions.

We would like to acknowledge all contributors for their invaluable participation in this Thematic Series and thank the referees for their great support to ensure that this Thematic Series fulfills high quality standards. Many thanks also go to the Beilstein Journal of Nanotechnology for providing us with the opportunity to present this novel, exciting research field to a broad audience and in particular Dr. Uli Fechner from the Editorial Team for his guidance and support.

Claudia Steinem and Joachim Bill

Göttingen and Stuttgart, June 2015

Beilstein Journal of Nanotechnology

# Magnesiothermic conversion of the silica-mineralizing golden algae *Mallomonas caudata* and *Synura petersenii* to elemental silicon with high geometric precision

Janina Petrack[1], Steffen Jost[2], Jens Boenigk[2] and Matthias Epple[*1]

Full Research Paper

Open Access

Address:
[1]Inorganic Chemistry and Center for Nanointegration Duisburg-Essen (CeNIDE), University of Duisburg-Essen, Universitaetsstr. 5–7, 45141 Essen, Germany and [2]Department of Biodiversity, University of Duisburg-Essen, Universitaetsstr. 5–7, 45141 Essen, Germany

Email:
Matthias Epple[*] - matthias.epple@uni-due.de

* Corresponding author

Keywords:
biomineralization; golden algae; magnesiothermic conversion; silica; silicon

*Beilstein J. Nanotechnol.* **2014,** *5,* 554–560.
doi:10.3762/bjnano.5.65

Received: 16 January 2014
Accepted: 24 March 2014
Published: 30 April 2014

Guest Editor: J. Bill



## Abstract

Chrysophyceae, also known as golden algae, contain characteristic, three-dimensional biomineralized silica structures. Their chemical composition and microscopic structure was studied. By high-temperature conversion of the skeleton of *Mallomonas caudata* and *Synura petersenii* into elementary silicon by magnesium vapour, nanostructured defined replicates were produced which were clearly seen after removal of the formed magnesium oxide with acid.

## Introduction

In nature, there are many biominerals which form silica-mineralized structures [1-3]. This process is also referred to as biosilification. The structural characteristics of these biominerals are species-specific [4-7]. For example, diatom frustules consist of silica which is assembled into complex 3-D structures and hierarchical forms [8-12]. These porous biominerals can serve as template for chemical conversion reactions, such as the calcium carbonate skeleton of sea urchins or the silica cases of diatoms [8,13]. In 2002, such a conversion reaction was first described in which biominerals were chemically transformed by a high-temperature conversion process [14].

Because it leads to delicate three-dimensional micro- or nanoscaled objects, the conversion of silica from biominerals into silicon is of potential interest for catalytic, biochemical, electronic and thermal applications. Furthermore, the use as electrodes in lithium batteries has been proposed [9,15,16]. Another advantage of such biofabrication approaches is the

conversion of a large number of almost identical biological objects into defined materials.

Different approaches which start from porous silica-mineralizing organisms as template are possible. The deposition of gold or silver coatings on diatom frustules by thermal evaporation has been described [8]. Sandhage et al. have shown that diatom structures can be chemically converted at higher temperature, e.g., with magnesium to magnesium oxide or with calcium to calcium oxide. The principal reaction that occurs has been formulated as follows (s = solid; g = gaseous) [9,14]:

$$SiO_2(s) + 2\,Mg(g) \rightarrow 2\,MgO(s) + Si(s)$$

Sandhage et al. have found that silicon is formed first in a binary phase mixture of magnesium and silicon (magnesium silicide) and does not deposit on the cell walls, so that the deposition of magnesium oxide occurs onto the diatoms [9]. Shen et al. have demonstrated the chemical transformation of diatoms into silicon by magnesium [17].

The chrysophytes *sensu lato*, also commonly referred to as golden algae because of the yellowish colour of their chloroplast, belong to the Stramenopiles [18]. Chrysophytes, and stramenopiles in general are heterokont, i.e., they have a long flagellum bearing tripartite hairs and a short flagellum without such hairs. The flagella are used for locomotion [19]. The chrysophytes are usually photoautotrophic even though some lineages of the Chrysophyceae have secondarily reduced their plastid. The photoautotrophic chrysophytes form chlorophyll a and c and the accessory pigments α- and β-carotene. The characteristic golden-brown colour of the chrysophytes is based on the formation of the carotenoid zeaxanthin, a xanthophyll which masks the green colour of chlorophyll. They are mainly found in fresh water [20]. The chrysophytes *sensu lato* comprise the two classes Chrysophyceae and Synurophyceae. Some taxa, specifically the synurophycean genera *Mallomonas* and *Synura,* form silica scales.

Here we report on the analysis of the structure of the chrysophyte biomineral and their subsequent replication into elemental silicon with high geometric precision.

## Results and Discussion

Before the conversion experiments, the skeletal structure of the golden algae was investigated. Figure 1 shows scanning electron micrographs of the skeletal elements of *Mallomonas caudata*. These elements consist of a kind of "head" (the so-called shield) and a serrated spike. This spike is about 50 µm long, has a diameter of about 400 nm and a wall thickness of about 45 nm (Figure 1C). The spikes have an edge where they tend to break even by small mechanical stress (Figure 1B). The spherical shield consists of an outer ring and an apical pore field. The shield is about 8 µm in diameter.

In Figure 2, scanning electron micrographs of *Synura petersenii* are shown. *Synura petersenii* consists of a mineralized skeleton with an average width of 1.5 µm and a length of 3 µm. They are composed of the base plate, the rims, the keel, the keel tips and the base plate hole. Similar to *Mallomonas caudata*, a pore field can also be seen in *Synura petersenii*. The golden algae were further characterized by X-ray diffraction, thermogravimetry and infrared spectroscopy (Figure 3).

*Synura petersenii* and *Mallomonas caudata* both contain only X-ray amorphous mineral, as expected for biogenic silica. IR spectra showed for both species the characteristic bands of water, silica and organic material. Thermogravimetry showed the decomposition in two steps. The first between 80 and 200 °C is associated with the loss of water (4.8 wt %). The second is attributed to the combustion of organic matter and also to dehydration of biogenic silica (43.0 wt % in total). The

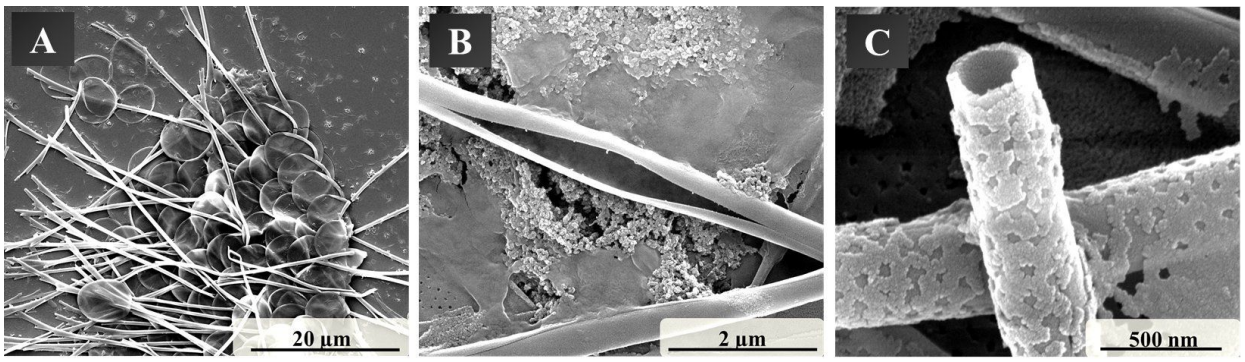


**Figure 1:** Scanning electron micrographs of the skeletal elements of *Mallomonas caudata* with an overview of spikes and shields (A), a broken spike (B), and a view into a broken spike (C).

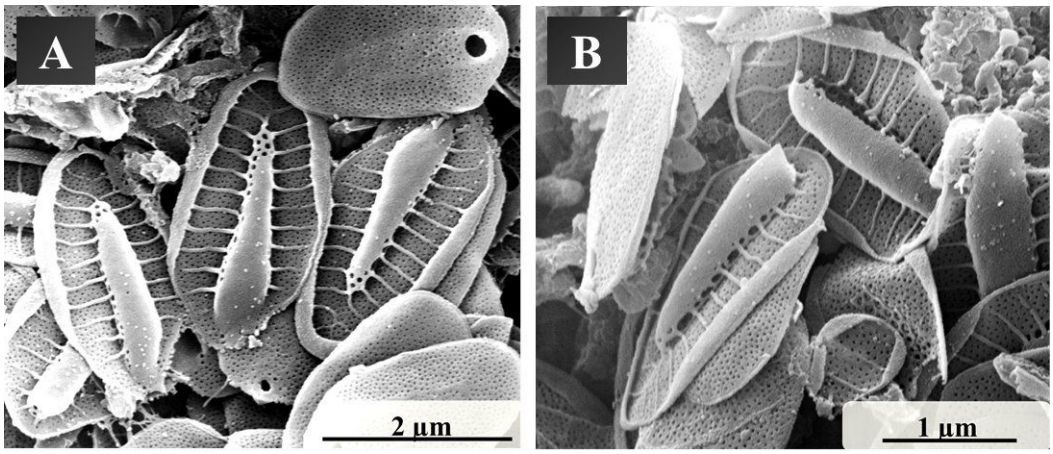


**Figure 2:** Scanning electron micrographs of the skeletal elements of *Synura petersenii*, showing the skeleton from various angles (A, B).

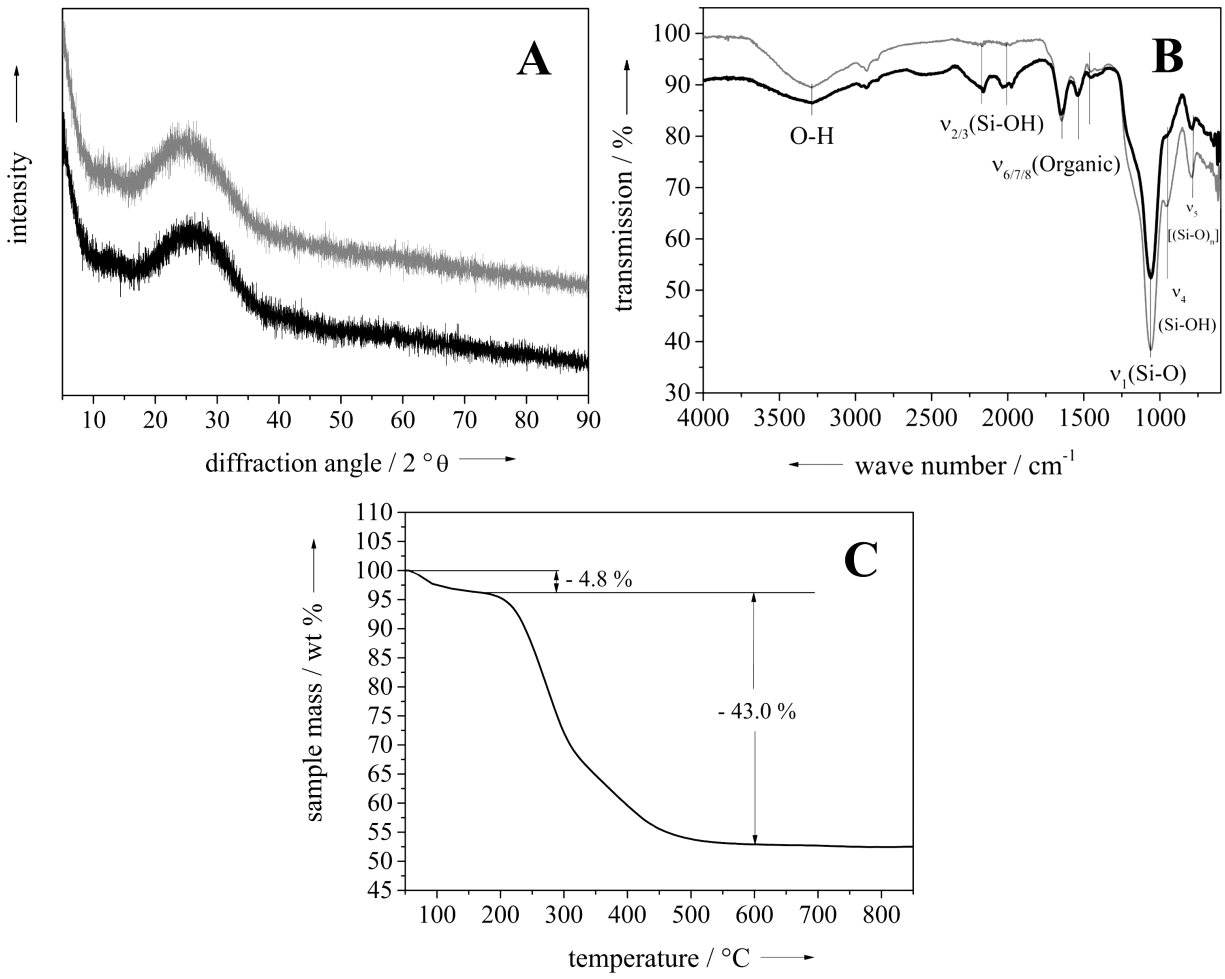


**Figure 3:** Characterization of the golden algae before the conversion. (A) shows powder diffractograms of *Synura petersenii* (black) and *Mallomonas caudata* (grey), (B) shows IR spectra of *Synura petersenii* (black) and *Mallomonas caudata* (grey), and (C) shows a thermogravimetric analysis of *Synura petersenii* in dynamic air atmosphere.

remaining 52.2 wt % of the sample can be assigned to inorganic silica, i.e., the dehydrated mineral ("$SiO_2$").

The results of energy-dispersive X-ray spectroscopy (EDX) of the golden algae before the conversion are shown in Figure 4. Besides silicon, a couple of other elements were detected. The carbon and gold signals are due to the carbon sample holder and the gold sputtering, but the elements oxygen, sodium, magnesium, sulfur, calcium, and iron were present in the golden algae. However, it cannot be decided whether the metals were present in the organic matrix or as traces of salts from the culture medium.

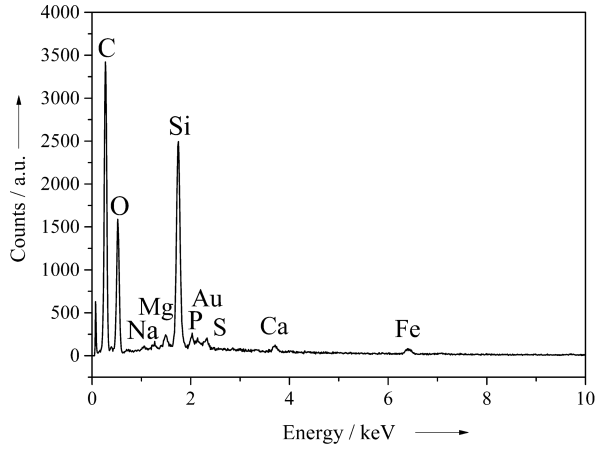


**Figure 4:** EDX analysis of golden algae (*Synura petersenii*) before the conversion.

The conversion of the skeletal elements of the golden algae *Synura petersenii* and *Mallomonas caudata* was carried out in a custom-made reactor consisting of heat-resistant steel (Figure 5). The reactor had an inner length of 18 cm and an outer length of 22 cm. The outer diameter was 7 cm; the inner diameter was 5 cm. Inside the tube was a rack with a large reservoir on both sides which each contained 3 g of magnesium powder ($4 \times 2 \times 0.3$ $cm^3$). Golden algae were placed into 12 small wells, which were 0.2 cm in diameter and 0.3 cm in depth.

The dried golden algae were put into the wells (each filled about half) to carry out the conversion experiments. Then the reactor was tightly closed and transferred into a furnace, heated from room temperature to 900 °C within 4 h and kept at this temperature for 5 h. Finally, the furnace was freely cooled to room temperature and opened. The golden algae were removed gently from the wells. The formed magnesium oxide on the surface was carefully dissolved in 17% aqueous hydrochloric acid. The samples were dried at 37 °C in air. After the conversion to elemental silicon and removal of magnesium oxide, the

**Figure 5:** The tube reactor used for the chemical conversion of the golden algae.

structures of the golden algae were analysed by scanning electron microscopy (Figure 6).

The conversion led to a good replication of the initial biomineral structure of *Synura petersenii* (Figure 6A,B). All characteristic structural elements seen before conversion, such as the pore field or the wedge, were obtained. The "skeleton", as well as the keel and the base plate, interspersed with pores, were clearly visible. The fragility of the structures has been previously described [21]. The structures of *Mallomonas caudata* were more damaged by the chemical conversion and handling (Figure 6C,D). The spikes were mostly broken. The shield of the golden algae was preserved and shows a defined pore structure like before the conversion reaction. The size of the mineral structures was well preserved without noticeable shrinkage. Structures of 50 nm or less were well replicated.

EDX-analysis showed the complete conversion of silica into silicon (Figure 7).

Besides silicon, only carbon (due to the sample holder), oxygen, and traces of magnesium and chlorine were detected. Similar results were reported by Bao et al. They reported that the conversion of diatoms with magnesium leads to silicon and magnesium oxide on the frustules. The latter was then washed out using hydrochloric acid and hydrofluoric acid (to remove traces of remaining $SiO_2$) [22]. Sandhage et al. found that the conversion of diatoms with magnesium under flowing argon atmosphere does not lead to the formation of silicon because of the formation of a two-phase mixture of silicon and magnesium, which is not deposited on the surface of the diatoms. EDX spectra showed the absence of silicon and only the formation of magnesium oxide [9,14,23]. The formation of the mixed binary

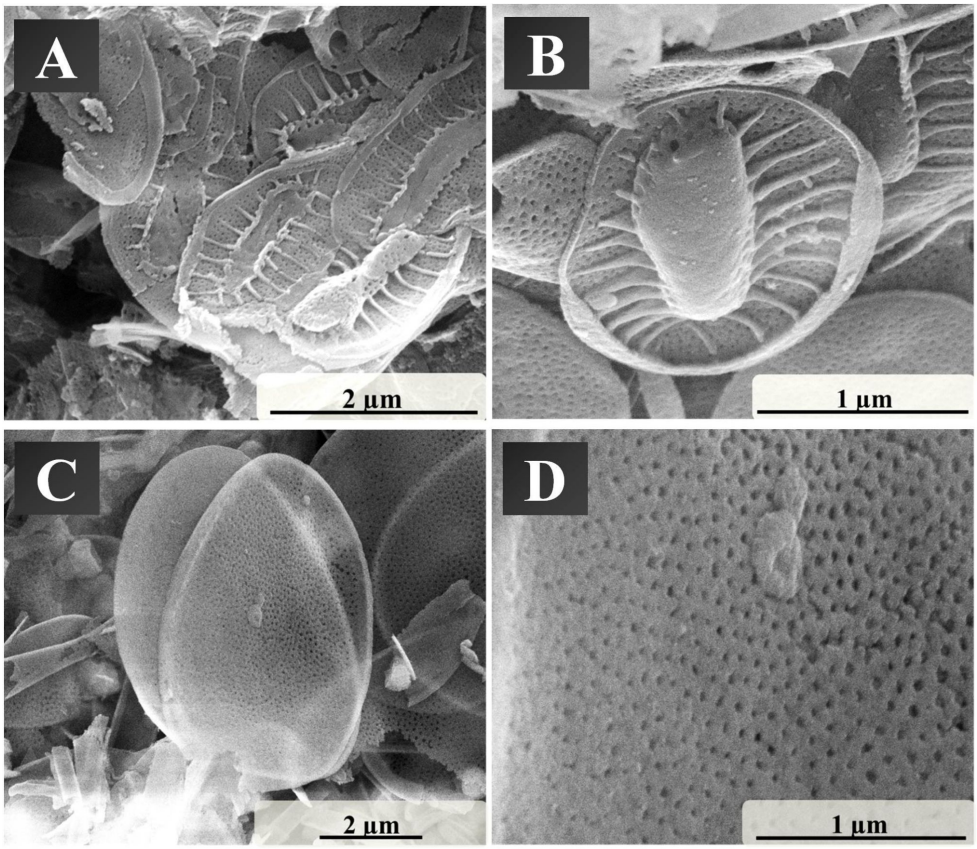


**Figure 6:** Scanning electron micrographs of the skeletons of *Synura petersenii* (A, B) and the shields of *Mallomonas caudata* (C, D) after conversion to silicon.

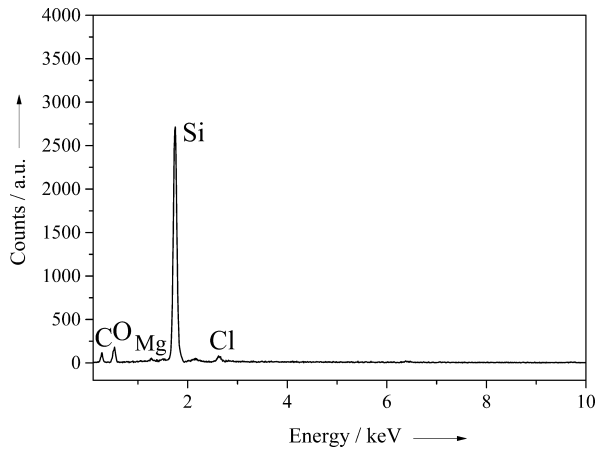


**Figure 7:** EDX spectra of *Synura petersenii* after conversion into silicon. The EDX spectra of *Mallomonas caudata* shows almost identical signals.

phase $Mg_2Si$ was also described in the literature, but the formation of the alloy phase occurs only as an intermediate that reacts in a subsequent step with silica to the products silicon and magnesium oxide [16].

$$SiO_2(s) + 3\,Mg(g) \rightarrow Mg_2Si(s) + MgO(s)$$
$$2\,SiO_2(s) + Mg_2Si(s) \rightarrow 3\,Si(s) + 2\,MgO(s)$$

These equations correspond to our results because the formation of silicon was clearly detected by energy dispersive X-ray spectroscopy. Yamada et al. also showed that it is possible to convert magnesium silicide powder with magnesium into silicon [24]. In addition, magnesium silicide reacts with oxygen to magnesium oxide and silicon above 450 °C [25]. As our conversion is performed under an oxygen atmosphere, the presence of the binary mixed phase after the reaction can be excluded.

## Conclusion

The skeletal structures of the golden algae *Synura petersenii* and *Mallomonas caudata* were extensively characterized. They form typical delicate structures, such as the apical pore field, spikes and keels. The chemical conversion of the silica-mineralizing structure was conducted by magnesium powder in a tubular reactor at 900 °C. It was found that the delicate skeletal structures of the golden algae structures were well replicated. This shows that the magnesiothermic conversion route is well

suited also for golden algae with their special skeletal features like rods and porous shells.

# Experimental

## Cultivation of *Mallomonas caudata* and *Synura petersenii*

We used the synurophytes *Synura petersenii*, strain WA18K-A, and *Mallomonas sp*., strain WA40K-F. Both strains were taken from the culture collection at the University of Duisburg-Essen (Department of Biodiversity). All strains were grown on modified WC medium at 15 °C and 90 µE [26]. In order to obtain a sufficiently high biomass for further analysis, the strains were serially transferred to higher culture volumes. Briefly, the cultures were first transferred to 100 mL Erlenmeyer flasks. After the strains reached the stationary phase (after approximately two weeks), the cultures were transferred to 500 mL Erlenmeyer flasks. The culture volume was then increased to 150 mL by adding fresh medium. After approximately ten more days, the culture volume was again doubled and after another ten days further increased to a final volume of 400 mL by adding fresh medium. After another ten days the biomass of 5 to 10 flasks was pooled prior to further analyses in order to obtain a sufficiently high yield of biomass. The golden algae were collected by filtration. The yield was dependent on the density of the biomass and varied strongly. Thus, the yield for *Synura petersenii* was between 2 and 5 mg per L culture medium. The yield for *Mallomonas caudata* was significantly lower with a maximum of 1 mg per L culture medium.

## Characterization

*Mallomonas caudata* and *Synura petersenii* were characterized by thermogravimetric analysis (STA 409 EP thermobalance from Netzsch; heating from 30 to 1200 °C with 2 K $min^{-1}$ in dynamic air atmosphere), scanning electron microscopy (SEM, ESEM Quanta 400 FEG instrument with gold-palladium-sputtered samples), X-ray diffraction (XRD, Bruker D8 Advance powder diffractometer with Cu Kα-radiation), energy dispersive X-ray spectroscopy (EDX, ESEM Quanta 400 FEG instrument) and infrared spectroscopy (IR, Bruker Alpha-Platinum FTIR-Spectrometer).

# References


1. Lowenstam, H.; Weiner, S. *On Biomineralization;* Oxford University Press: New York, 1989.
2. Mann, S. *Biomineralization;* Oxford University Press: Oxford, 2001.
3. Baeuerlein, E.; Behrens, P.; Epple, M. *Handbook of Biomineralization;* Wiley-VCH: Weinheim, 2007.
4. Belton, D. J.; Deschaume, O.; Patwardhan, S. V.; Perry, C. C. *J. Phys. Chem. B* **2010,** *114,* 9947–9955. doi:10.1021/jp101347q
5. Fang, Y.; Wu, Q.; Dickerson, M. B.; Cai, Y.; Shian, S.; Berrigan, J. D.; Poulsen, N.; Kröger, N.; Sandhage, K. H. *Chem. Mater.* **2009,** *21,* 5704–5710. doi:10.1021/cm9011525
6. Sheppard, V.; Poulsen, N.; Kröger, N. *J. Biol. Chem.* **2010,** *285,* 1166–1176. doi:10.1074/jbc.M109.039529
7. Wolf, S. E.; Schlossmacher, U.; Pietuch, A.; Mathiasch, B.; Schröder, H.-C.; Müller, W. E. G.; Tremel, W. *Dalton Trans.* **2010,** *39,* 9245–9249. doi:10.1039/b921640e
8. Bao, Z.; Ernst, E. M.; Yoo, S.; Sandhage, K. H. *Adv. Mater.* **2009,** *21,* 474–478. doi:10.1002/adma.200801499
9. Sandhage, K. H.; Dickerson, M. B.; Huseman, P. M.; Caranna, M. A.; Clifton, J. D.; Bull, T. A.; Heibel, T. J.; Overton, W. R.; Schoenwaelder, M. E. A. *Adv. Mater.* **2002,** *14,* 429–433. doi:10.1002/1521-4095(20020318)14:6<429::AID-ADMA429>3.3.CO;2-3
10. Kröger, N.; Sandhage, K. H. *MRS Bull.* **2010,** *35,* 122–126. doi:10.1557/mrs2010.631
11. Belton, D. J.; Patwardhan, S. V.; Annenkov, V. V.; Danilovtseva, E. N.; Perry, C. C. *Proc. Natl. Acad. Sci. U. S. A.* **2008,** *105,* 5963–5968. doi:10.1073/pnas.0710809105
12. Dickerson, M. B.; Sandhage, K. H.; Naik, R. R. *Chem. Rev.* **2008,** *108,* 4935–4978. doi:10.1021/cr8002328
13. Wang, Y.; Cai, J.; Jiang, Y.; Jiang, X.; Zhang, D. *Appl. Microbiol. Biotechnol.* **2013,** *97,* 453–460. doi:10.1007/s00253-012-4568-0
14. Sandhage, K. H. *JOM* **2010,** *62,* 32–43. doi:10.1007/s11837-010-0085-8
15. Oumellal, Y.; Delpuech, N.; Mazouzi, D.; Dupré, N.; Gaubicher, J.; Moreau, P.; Soudan, P.; Lestriez, B.; Guyomard, D. *J. Mater. Chem.* **2011,** *21,* 6201–6208. doi:10.1039/c1jm10213c
16. Xing, A.; Zhang, J.; Bao, Z.; Mei, Y.; Gordin, A. S.; Sandhage, K. H. *Chem. Commun.* **2013,** *49,* 6743–6745. doi:10.1039/c3cc43134g
17. Shen, L.; Guo, X.; Fang, X.; Wang, Z.; Chen, L. *J. Power Sources* **2012,** *213,* 229–232. doi:10.1016/j.jpowsour.2012.03.097
18. Šlapeta, J.; Moreira, D.; López-García, P. *Proc. R. Soc. London, Ser. B* **2005,** *272,* 2073–2081. doi:10.1098/rspb.2005.3195
19. Adl, S. M.; Simpson, A. G. B.; Farmer, M. A.; Andersen, R. A.; Anderson, O. R.; Barta, J. R.; Bowser, S. S.; Brugerolle, G.; Fensome, R. A.; Fredericq, S.; James, T. Y.; Karpov, S.; Kugrens, P.; Krug, J.; Lane, C. E.; Lewis, L. A.; Lodge, J.; Lynn, D. H.; Mann, D. G.; McCourt, R. M.; Mendoza, L.; Moestrup, Ø.; Mozley-Standridge, S. E.; Nerad, T. A.; Shearer, C. A.; Smirnov, A. V.; Spiegel, F. W.; Taylor, M. F. J. R. *J. Eukaryotic Microbiol.* **2005,** *52,* 399–451. doi:10.1111/j.1550-7408.2005.00053.x
20. Remias, D.; Jost, S.; Boenigk, J.; Wastian, J.; Lütz, C. *Phycol. Res.* **2013,** *61,* 277–285. doi:10.1111/pre.12025
21. Allen, M. B. *Annu. Rev. Microbiol.* **1969,** *23,* 29–46. doi:10.1146/annurev.mi.23.100169.000333
22. Bao, Z.; Weatherspoon, M. R.; Shian, S.; Cai, Y.; Graham, P. D.; Allan, S. M.; Ahmad, G.; Dickerson, M. B.; Church, B. C.; Kang, Z.; Abernathy, H. W., III; Summers, C. J.; Liu, M.; Sandhage, K. H. *Nature* **2007,** *446,* 172–175. doi:10.1038/nature05570
23. Cai, Y.; Allan, S. M.; Sandhage, K. H.; Zalar, F. M. *J. Am. Ceram. Soc.* **2005,** *88,* 2005–2010. doi:10.1111/j.1551-2916.2005.00388.x
24. Yamada, T.; Itahara, H.; Yamane, H. *Mater. Lett.* **2013,** *98,* 157–160. doi:10.1016/j.matlet.2013.02.022
25. Tani, J.; Takahashi, M.; Kido, H. *IOP Conf. Ser.: Mater. Sci. Eng.* **2011,** *18,* 142013. doi:10.1088/1757-899X/18/14/142013
26. Guillard, R. R. L.; Lorenzen, C. J. *J. Phycol.* **1972,** *8,* 10–14. doi:10.1111/j.1529-8817.1972.tb03995.x

Beilstein Journal of Nanotechnology

# Biocalcite, a multifunctional inorganic polymer: Building block for calcareous sponge spicules and bioseed for the synthesis of calcium phosphate-based bone

Xiaohong Wang*, Heinz C. Schröder and Werner E. G. Müller

Review

Open Access

Address:
ERC Advanced Investigator Grant Research Group at Institute for Physiological Chemistry, University Medical Center of the Johannes Gutenberg University Mainz, Duesbergweg 6, D-55128 Mainz, Germany

Email:
Xiaohong Wang* - wang013@uni-mainz.de

* Corresponding author

Keywords:
biocalcite; bioprinting; bone; bone formation; calcareous spicules; sponge

*Beilstein J. Nanotechnol.* **2014,** *5,* 610–621.
doi:10.3762/bjnano.5.72

Received: 10 January 2014
Accepted: 16 April 2014
Published: 12 May 2014

Associate Editor: C. Steinem



## Abstract

Calcium carbonate is the material that builds up the spicules of the calcareous sponges. Recent results revealed that the calcium carbonate/biocalcite-based spicular skeleton of these animals is formed through an enzymatic mechanism, such as the skeleton of the siliceous sponges, evolutionarily the oldest animals that consist of biosilica. The enzyme that mediates the calcium carbonate deposition has been identified as a carbonic anhydrase (CA) and has been cloned from the calcareous sponge species *Sycon raphanus*. Calcium carbonate deposits are also found in vertebrate bones besides the main constituent, calcium phosphate/hydroxy-apatite (HA). Evidence has been presented that during the initial phase of HA synthesis poorly crystalline carbonated apatite is deposited. Recent data summarized here indicate that during early bone formation calcium carbonate deposits enzymatically formed by CA, act as potential bioseeds for the precipitation of calcium phosphate mineral onto bone-forming osteoblasts. Two different calcium carbonate phases have been found during CA-driven enzymatic calcium carbonate deposition in in vitro assays: calcite crystals and round-shaped vaterite deposits. The CA provides a new target of potential anabolic agents for treatment of bone diseases; a first CA activator stimulating the CA-driven calcium carbonate deposition has been identified. In addition, the CA-driven calcium carbonate crystal formation can be frozen at the vaterite state in the presence of silintaphin-2, an aspartic acid/glutamic acid-rich sponge-specific protein. The discovery that calcium carbonate crystals act as bioseeds in human bone formation may allow the development of novel biomimetic scaffolds for bone tissue engineering. Na-alginate hydrogels, enriched with biosilica, have recently been demonstrated as a suitable matrix to embed bone forming cells for rapid prototyping bioprinting/3D cell printing applications.

## Introduction

The size and complexity of a metazoan taxon is correlated with the dimensioning of its respective complex composite skeleton. This statement can be exemplarily illustrated by comparing different sponge [phylum: Porifera] species. These animals are grouped to the classes of the siliceous sponges, the Hexactinellida and the Demospongia, and the calcareous sponges, the Calcarea [1,2]. Sponges of the ''crusty'' asconoid type Calcarea, e.g., the encrusting *Clathrina coriacea*, measure about 2 mm in thickness, the syconoid type calcareous sponges, e.g., *Sycon raphanus* have an axis length of 1–5 cm, while species with a leuconoid type Bauplan can be up to 3 m in size, e.g., the demosponge *Spheciospongia vesparium*, or the hexactinellid *Monorhaphis chuni* [1,2]. The evolutionary oldest animals on earth to comprise a skeleton formed of biosilica and are found among the siliceous sponges, the Hexactinellida and later in the Demospongiae [3,4], while the mineralized skeletons of the calcareous sponges are built of calcite [5]. The selection of the mineral appears to parallel the levels of silicate and carbonate in the marine environment [6].

The distinguished feature of biosilica-based skeletons is the fact that this polymer is formed enzymatically, a finding that resulted in the introduction of a new paradigm in biochemistry that also *inorganic polymers* and not only *organic polymers* can be formed enzymatically from their respective precursors [7]. This first clue, together with the finding that all animals, including the sponges, are of monophyletic origin gave the basis for the view that the bodyplan of the metazoans follows more universal genetic blueprints and, in turn, more general biochemical relationships [8].

Following this intellectual approach we asked the question, does the evolutionary oldest inorganic polymer, biosilica, share a functional relationship with the skeletal elements of the crown mammals, the calcium phosphate/hydroxyapatite (HA)-based skeletal systems. The understanding of the genetic blueprint of any morphogenetic event must begin with the identification and functional characterization of the individual expressed genes (proteins), followed by the elucidation of the interaction of the proteins, e.g., acting during mineralization, in other words, should start with the disclosure of the regulatory network of the proteins involved. It should be the aim to unravel the regulatory genetically-controlled architecture of proteins, based on the expression of a few molecules, and to pinpoint a single master gene that, after switching on, initiates the direction of development of a structural skeletal element.

Only recently it was possible to describe the molecular level of the formation of a hard skeleton (reviewed in [4]). Initial investigations were successfully performed with the siliceous sponge spicules. The key discovery was the identification of silicatein, the enzyme that initiates the biocatalytic biosilica-condensation reaction [9-11]. It initiated the resolution of the biochemical processes leading to biosilica formation (Figure 1A). The silicateins are members of the cathepsin L and papain family of proteases. They have been discovered in the demosponge *Tethya aurantium* by the group of Morse [9,10] and soon thereafter were also identified in the demosponge *Suberites domuncula* [11]. Based on biochemical studies, three isoforms of silicatein have been described in *T. aurantium*, silicatein-α to -γ. They have similar molecular weights (approximately 34 kDa). Among them the silicatein-α is the dominant isoform, forming the axial filament, residing in the axial canal. In *T. aurantium* the molar ratio between silicatein-α and silicatein-β was determined to be 2:1, while in *S. domuncula* the molar ratio amounts to 4:1. Soon after the expression of the silicateins and after the first formation of silica nanoparticles, the silicatein-interacting proteins, the silintaphins, are read out (Figure 1A). Until now two silintaphins, silintaphin-1 [12] and silintaphin-2 [4], have been described extensively. Silintaphin-1 significantly enhances the biosilica-forming activity of silicatein in vitro. A 5.3-fold increase of the biosilica-forming activity is measured at a molar ratio of 4:1 [silicatein-α/silintaphin-1] [13]. Likewise, in *S. domuncula* the 15-kDa protein silintaphin-2 had been identified as a second silicatein-interactor. Like silintaphin-1, this protein is located in the axial filament, but particularly in the organic cylinder around the growing spicules. Silintaphin-2 is a $Ca^{2+}$-binding protein that complexes four $Ca^{2+}$ ions [14].

The formation of HA and HA resorption by osteoclasts and osteoblasts in bone tissue are controlled by a network of cytokines and growth factors. The receptor activator of NF-KB (RANK) and its ligand, receptor activator of NF-KB ligand (RANKL) and osteoprotegerin (OPG) play a key function in regulation of bone formation and bone degradation (reviewed in [16]). The molecular triad OPG/RANKL/RANK not only regulates the differentiation of osteoclasts, but also differentiation processes in the vascular system and in the immune system. Addition of biosilica leads to an increased expression of OPG. The consequence is an inhibition of the differentiation of osteoclasts from their respective precursor cells (Figure 1B). In addition, after exposure of SaOS-2 cells to biosilica these cells increase the synthesis of the bone morphogenetic protein 2 (BMP2), a cytokine that induces osteoblast differentiation and mineralization (Figure 1C) (see [17,18] and reviewed in [16]).

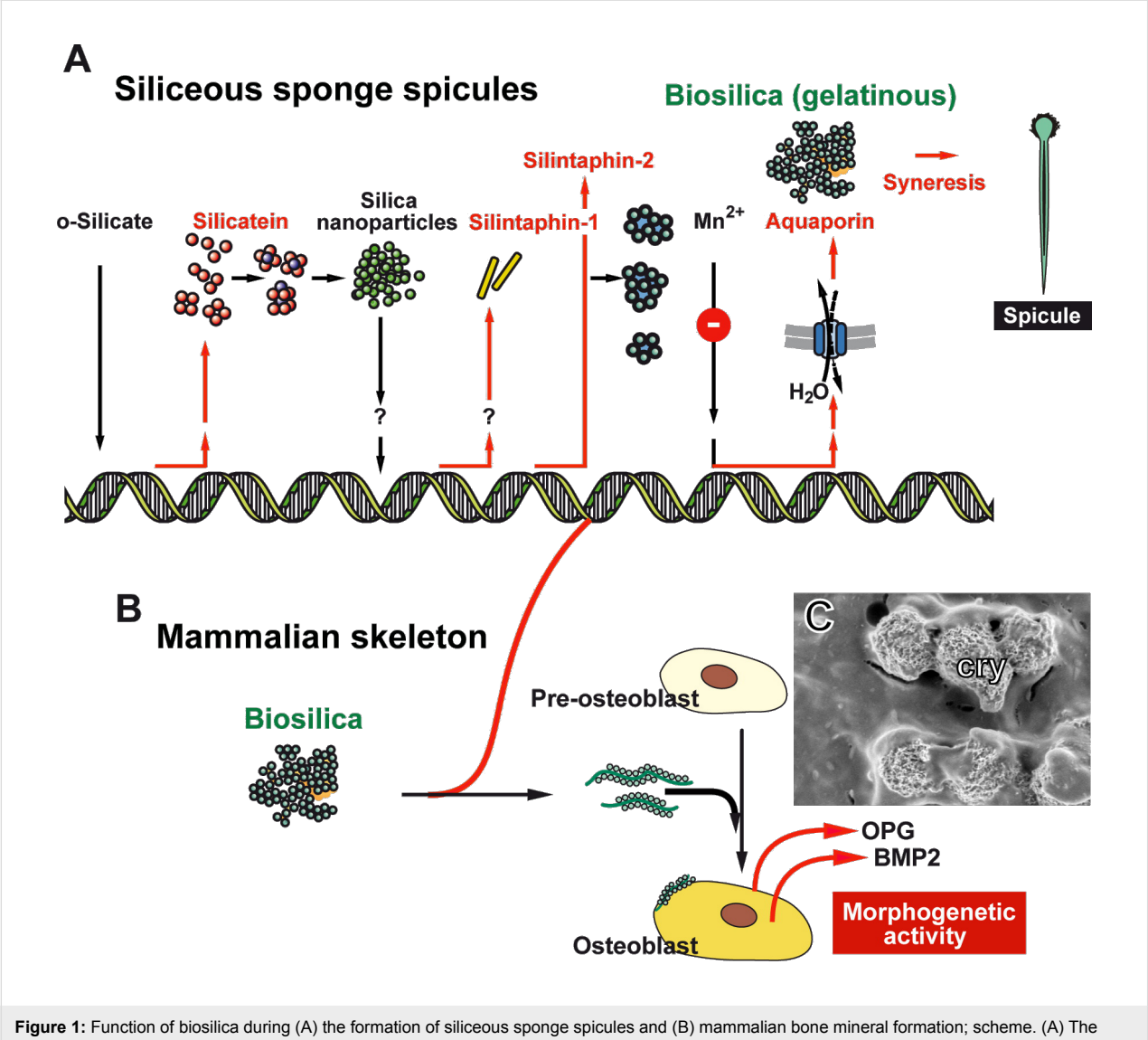


**Figure 1:** Function of biosilica during (A) the formation of siliceous sponge spicules and (B) mammalian bone mineral formation; scheme. (A) The different key molecules involved in spicule formation are sequentially expressed [11]. o-Silicate induces the expression of silicatein, followed by the expression of silintaphin-1 and silintaphin-2, a process that is most likely induced by biosilica nanoparticles. These two classes of molecules (silicateins and silintaphins) form mesoscopic gelatinous flocs that harden through syneresis to spicules [15]. The latter process is driven by water extrusion via aquaporin channels. (B) Effect of biosilica on mammalian bone-forming cells (SaOS-2 cells) in vitro. After incubation with biosilica those cells differentiate and express osteoprotegerin (OPG) and the bone morphogenetic protein 2 (BMP2), two components of their newly acquired morphogenetic activities. (C) SaOS-2 cells that have formed calcium-based carbonate and phosphate crystallites (cry).

## Review

### Calcium carbonate/bicarbonate a potential bioseed for Ca phosphate mineral formation by osteoblasts

It is well established that the calcium salt of carbonate is an effective diet supplement for amelioration of bone-loss during postmenopausal osteoporosis [19]. Recently, we could show in in vitro studies, by using SaOS-2 cells growing in calcium bicarbonate-deprived medium that these cells respond with a significant increase in calcium deposit formation after exposure to bicarbonate [20]. The cells start to form larger crystallite nodules on their surfaces, compared to the controls. Of course, the prerequisite has to be fulfilled that simultaneously with bicarbonate the cells have to be treated with the mineralization activation cocktail (MAC), composed of β-glycerophosphate, ascorbic acid and dexamethasone. One plausible explanation that emerged from this observation was that those crystalloids, which have been formed metabolically, are composed of calcium carbonate. This assumption was corroborated by the well established finding that mammalian skeletons contain, besides of HA-composed bones, biomineralized otoliths in the vestibular labyrinth of the vertebrate ear. There the inorganic matrix consists to 90 to 95% of calcium carbonate in the arago-

nite form [21,22]. Not only in those skeletal elements but also in the vertebrate bones calcium carbonate co-exists to a considerable amount with Ca phosphate [23].

Under physiological conditions the major processes of biomineralization of bone, teeth and otoconia proceeding in vertebrates mainly occur extracellularly, while intracellular mineral deposits are predominantly assembled during pathological calcifications of soft tissues [24]. Bone formation is based on a tightly controlled process between osteoblasts and fibrillar organic structures that starts from collagen fibrils around which poorly crystalline carbonated apatite aggregates are deposited [25,26]. Carbonated apatite are deposits in which carbonate ions ($CO_3^{2-}$) reversibly substitute either phosphate ($PO_4^{3-}$) or hydroxyl ($OH^-$). Analyses by X-ray and electron diffraction and Fourier transform infrared spectroscopy, as well as determination of the chemical composition revealed that at least under in vitro conditions in osteoblasts low concentrations of carbonate ions exist in their $Ca^{2+}$/phosphate mineral phase. Parallel spectroscopic studies suggested that Ca-deposition in osteoblasts starts intracellularly in calcium-rich vesicles that substantially contribute to the formation of bone apatite [27].

Both calcium phosphate formation [28] and calcium carbonate deposition [29] are exergonic processes that, in turn, are thermodynamically possible, but are strictly controlled in a biochemical system through the activation energy barriers that prevent a chemical reaction from occurring at physiological temperatures/conditions [30]. A modulation of the activation energy barriers enables an organism to control under which physiological conditions a thermodynamically possible reaction can be initiated or prevented [30]. Almost exclusively, alterations of the heights of the activation energy barriers are adjusted by enzymes or by the surface architecture of membranes separating two phases. The recent findings that in animals the inorganic polymer biosilica (see: [4,7]) is synthesized enzymatically through silicatein prompted us to study if also during calcium carbonate deposition there is an enzyme-driven step involved [31].

## Carbonic anhydrase, the basis for the accelerated calcium carbonate synthesis in calcareous sponges

The prevalent enzymes that allow bicarbonate to be formed in an organism are the carbonic anhydrases [CAs] [32]. These enzymes, which are characterized by an extremely high turnover number, catalyze the reversible hydration of carbon dioxide ($CO_2$) to bicarbonate. This reaction occurs also in the presence of Ca ions [33]. Four of the seven metazoan CA isoenzymes are cytosolic, CA-I, -II, -III, and -VII. Among them the CA-II is a widely studied one [34]. Recently, experimental evidences have been presented revealing that the CAs might be involved in bone formation [35]. The mammalian CA-II, a cytosolic enzyme, is targeted in intact cell systems under certain physiological conditions to the cell membrane [36,37].

Among the phylogenetically oldest animals that have a skeleton based on calcium carbonate are the calcareous sponges with *Sycon raphanus* as an example (Figure 2A), the CA enzyme was cloned, expressed and functionally tested [38]. From this organism the complete cDNA encoding for the CA was obtained (accession number CCE46072). The complete 1,476 nts cDNA encodes, within its ORF [open reading frame] (from $nt_{68–70}$ to $nt_{1001–1003}$), the 312 aa putative CA, having a $M_r$ of 33,251 and an pI of 5.81. The closest human related CA to the *Sycon* enzyme (Figure 2C), the human CA-X (CAHA_HUMAN; Q9NS85), and -XI (CAHB_HUMAN; O75493), are grouped to the "acatalytic" CA isoforms of unknown function, which have been proposed to be devoid of $CO_2$ hydration activity [39]. However, the branch with the two sponge CAs comprises a common origin with the stony coral *Stylophora pistillata* enzyme [40] for which an enzymatic activity has been proven. Those human CAes, comprising $CO_2$ hydration activity (the catalytic CA), are in the CA group I to IV.

The Zn-binding sites that are involved in the catalytic reaction (hydration of $CO_2$) are present in the CA-alpha (vertebrate-like) group stretch of the *S. raphanus* protein. The Zn ions are bound to the enzyme through the three His residues in the catalytic center of the enzyme [41]. The presence of a signal peptide cleavage site in the sponge CA indicates that this enzyme is secreted by the sponge cells or bound to the cell membrane. The spicules from the calcareous sponges (Figure 2B), e.g., *Sycon* used in our studies [38,42], consists of almost pure calcium carbonate (calcite). In a first approach to investigate the formation of the calcareous spicules on the molecular level, the function of the CA in this process has been studied by using *S. raphanus* as a model. The cDNA of the *Sycon* CA was prepared in a recombinant way and used to raise antibodies. Immunostructural studies revealed that the *Sycon* CA is localized on the surface of mature, developed spicules, the ca. 300 µm long diactines and the ca. 300 µm large triactines and tetractines (Figure 3A and B). It is assumed that the membranous, organic sheaths described to cover the spicules [43,44] are composed predominantly of this enzyme. Subsequently the recombinant enzyme was used to determine the in vitro calcium carbonate formation by applying the in vitro diffusion assay [45].

Even though the present-day oceans are supersaturated with respect to calcium carbonate, only very rarely spontaneous abiotic precipitation is seen [46]. Like in other metazoan

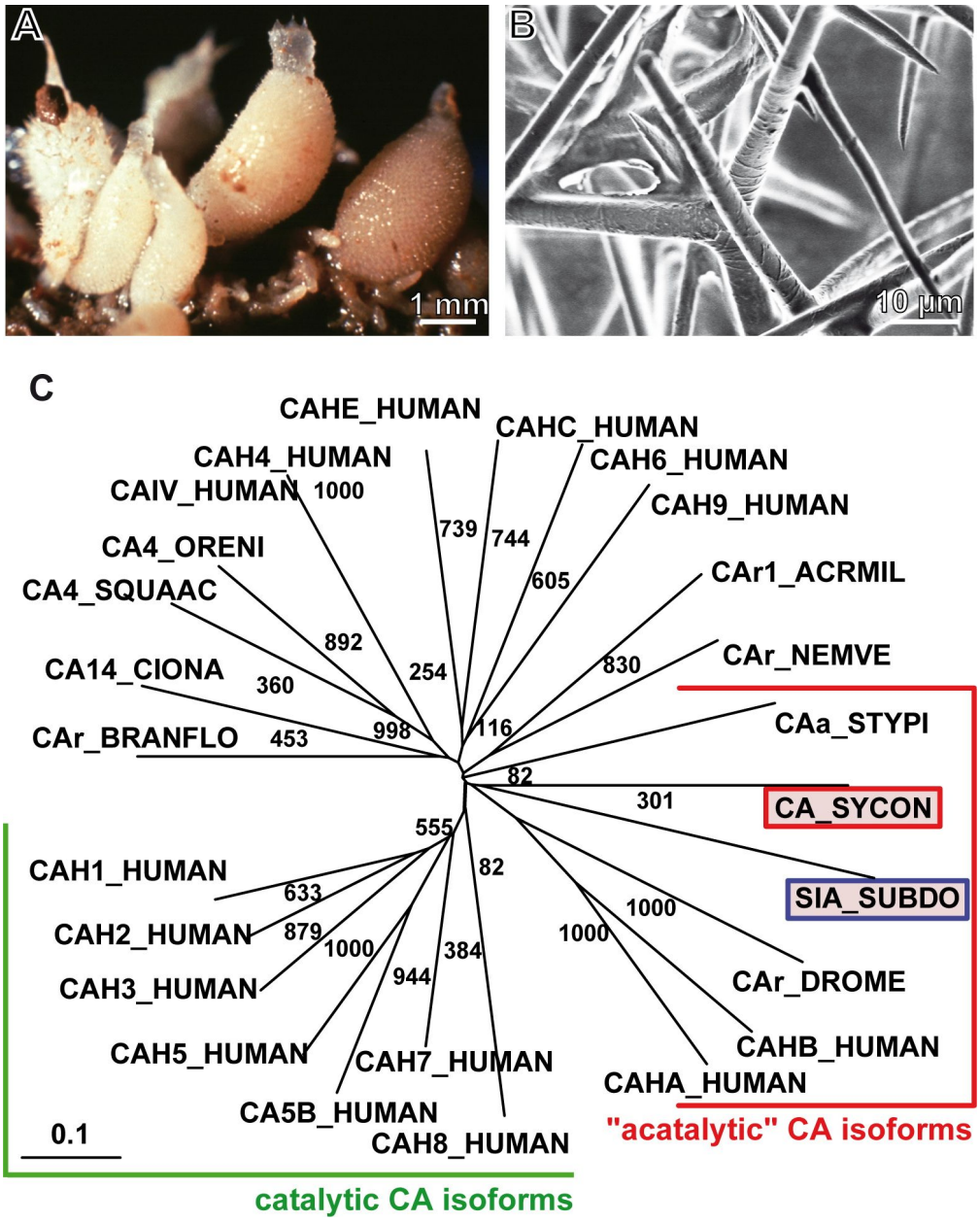


**Figure 2:** *Sycon raphanus*, its spicules and its CA. (A) Specimens of *S. raphanus*; (B) the calcareous spicules. (C) Phylogenetic, radial tree computed with the putative calcareous sponge *S. raphanus* carbonic anhydrase (CA_SYCON; accession number CCE46072) and the demosponge *S. domuncula* silicase (SIA_SUBDO; DD298191), as well as the carbonic anhydrase isoforms from human: I (CA-I) (CAH1_HUMAN; P00915); II (CA-II) (CAH2_HUMAN; P00918); II-2 (CA II) (CAHB_HUMAN; O75493), III (CA-III) (CAH3_HUMAN; P07451); IV (CAIV_HUMAN; AAA35625.1); IV (CA-IV) (CAH4_HUMAN; P22748); VA (CAH5_HUMAN; P35218); VB (CA5B_HUMAN; O75493); VI (CA-VI) (CAH6_HUMAN; P23280); VII (CA-VII) (CAH7_HUMAN; P43166); VIII (CA-VIII) (CAH8_HUMAN; P35219); IX (CA-IX) (CAH9_HUMAN; Q16790); X (CA-RP X) (CAHA_HUMAN; Q9NS85); XII (CA-XII) (CAHC_HUMAN; O43570); XIV (CA-XIV) (CAHE_HUMAN; Q9ULX7). In addition, the related sequences from the scleractinian *Acropora millepora*-1 (CAr1_ACRMIL; ACJ64662.1), the stony coral *Stylophora pistillata* (CAa_STYPI; ACA53457.1, EU159467.1), the anthozoan *Nematostella vectensis* (CAr_NEMVE; XP_001627923.1), the tunicate *Ciona intestinalis* (CA14_CIONA; XP_002123314.1), the lancelet *Branchiostoma floridae* (CAr_BRANFLO; XP_002601262.1), the shark *Squalus acanthias* (CA4_SQUAAC; AAZ03744.1), the fish *Oreochromis niloticus* (CA4_ORENI; XP_003456174.1), and the insect enzyme from *Drosophila melanogaster* (CAr_DROME; NP_572407.3) are included. The CAs, belonging to the "acatalytic" CA isoforms and of the catalytic CA isoforms, are surrounded. Partially taken from [38] with permission.

systems, e.g., mollusks or echinoderms, in sponges carbonate is taken up from the aqueous environment as bicarbonate via specific membrane transporters, characterized by a Michaelis–Menten constant of around 50 mM [47], or is produced metabolically. At this concentration, calcium carbonate precipitates at an extent of about 50% during an incu-

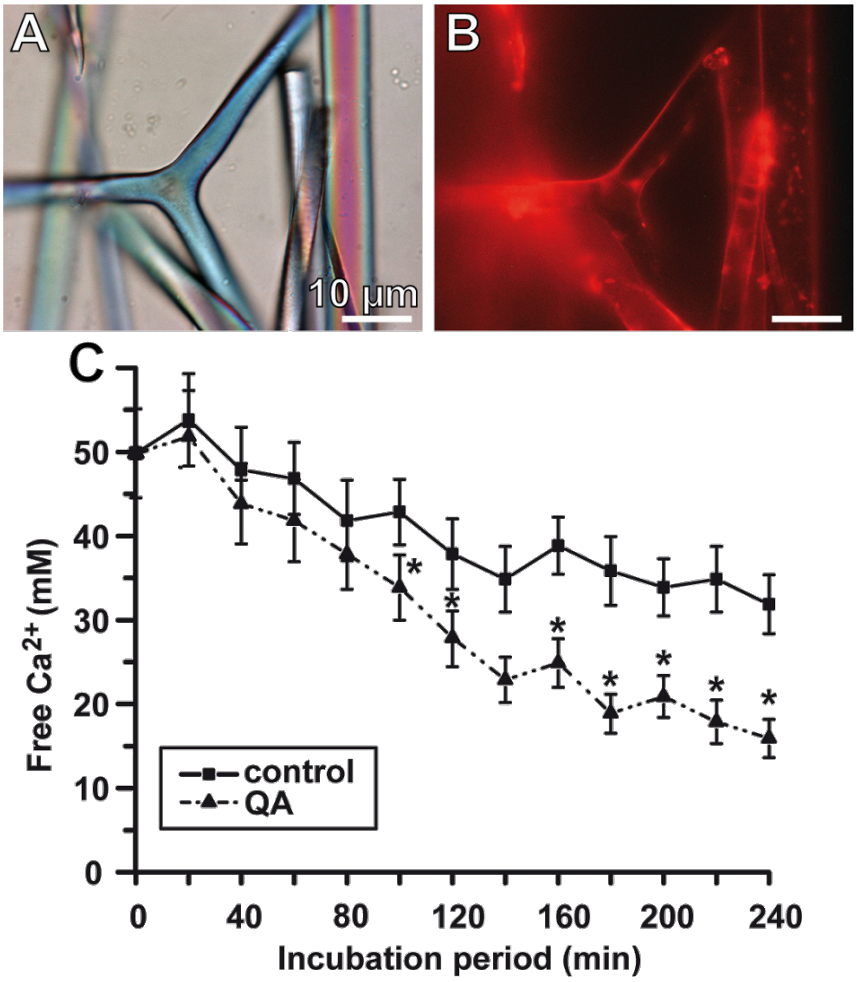


**Figure 3:** *Sycon* CA, its localization and in vitro function. Reacting of *Sycon* spicule with antibodies, raised against the homologous CA. (A) Light microscopic image of the spicules (in the center is a large triactine). (B) The spicules have been reacted with polyclonal antibodies, raised against the *Sycon* CA. The immunocomplexes were stained with Cy5-labelled anti-rabbit IgG. (C) Formation of $CaCO_3$ in the ammonium carbonate diffusion assay in the presence of CA. For this series of experiments the recombinant human CA2 enzyme, expressed in *Escherichia coli* (C6624, Sigma), with a specific activity of about 5,000 units/mg, was added at a concentration of 35 W-A units (10 µg)/500 µL of $CaCl_2$ to the assays. The formation of calcium carbonate was determined quantitatively on the basis of the consumption of free $Ca^{2+}$ ions using the EDTA titration procedure [31]. The assays either remained free of additional compound(s) (filled square) or were supplemented with 10 µM quinolinic acid (QA, filled triangle). Samples of six parallel determinations were quantitated; means ± SD are given. *$p < 0.05$.

bation period of only 20 h in an ammonium carbonate diffusion/"dessicator assay" at pH 7–8 [48]. However, this reaction velocity is too slow to account for the rate of calcium carbonate deposition measured in vivo, e.g., in the sponge spicule formation in *Sycon* sp. [49]. The *Sycon* spicules, with a diameter of about 4 µm and a length greater than 100 µm, show a very fast growth rate of 65 µm/h. Hence it has to be concluded that an acceleration of the velocity of the exergonic reaction at ambient environmental conditions has to occur by lowering the activation energy by an enzyme, or by allowing the calcium carbonate process to proceed on a functionalized organic surface. In our previous studies we tested the first possibility [7,31].

As the substrate for the enzymatic reactions in the "dessicator assay" we used a solution of 50 mM $CaCl_2$ over which $CO_2$ vapor, generated from $NH_4HCO_3$ solution, was passed. The pH of the reactions was adjusted to 7.5 [7,31]. The mineralization process (based on the decrease of free $Ca^{2+}$ concentration measured) started after an initial lag phase of 5 h. Addition of the recombinant CA (35 W-A units/500 µL) significantly increased the reaction velocity and accelerated the mineralization process; after 50 min already 25% of the $CaCl_2$ had been precipitated, in the presence of $CO_2$, to calcium carbonate (Figure 3C). An extent of 80% of precipitated calcium carbonate was reached after 10 h. To highlight again, the major role of the CA during the stages of enzymatic synthesis of

calcium carbonate is to accelerate the reaction velocity, an essential feature of any enzyme. Furthermore, the CA allows the process of calcium carbonate deposition to occur at ambient physiological conditions.

Two morphologically different deposits are formed in the in vitro assay in the presence of the CA (35 W-A CA units per assay): first prisms with an average size of 80–120 µm and second round-shaped deposits of similar dimensions (Figure 4). Predominantly prisms with a rhombohedral morphology are formed, which are composed of calcite, as analyzed by MIDAC Fourier transform infrared spectroscopy (the characteristic vibrational bands at 873 $cm^{-1}$ and 711 $cm^{-1}$; Figure 4, left crystal). Intermediately, during the formation of the calcite crystals, round-shaped vaterite deposits are formed (875 $cm^{-1}$ and 744 $cm^{-1}$; Figure 4, right crystal). It is remarkable and likewise indicative that the biogenic CA-driven calcium carbonate crystal formation can be frozen at the vaterite state (in spite of the overall thermodynamically possible "end-point" transition formation to calcite) if the CA-driven reaction proceeds in the presence of silintaphin-2, a sponge-specific protein that is rich in aspartic acid (Asp, D) and glutamic acid (Glu, E) [50]. The hardness, elastic modulus and creep of the two forms of the calcium carbonate deposits, the calcitic prisms and the round-shaped vaterite deposits were determined by nanoindentation. The load–displacement curves obtained for the two calcium carbonate forms revealed the following values: for the rhombohedral calcite 1.98 ± 0.31 GPa and for the round-shaped vaterite deposits only 1.38 ± 0.39 GPa. Concurrently, a distinct decrease of the elastic modulus was measured for the vaterite deposits (39.13 ± 8.04 GPa), in comparison to the rhombohedral calcite prisms (72.83 ± 11.68 GPa). This significant difference in the mechanical properties between the two morphologies can also be deduced from the creep behavior. While the creep characteristics for the rhombohedral calcitic prisms was found to be 5.44 ± 1.15 (per maximal depth [%]), the corresponding value for the round-shaped vaterite deposits is 9.95 ± 1.60.

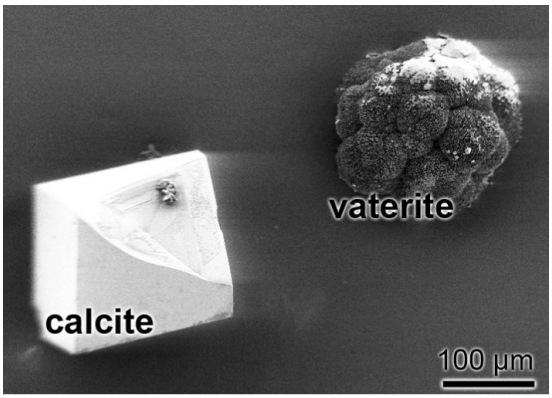


**Figure 4:** Calcium carbonate crystals formed in vitro (ammonium carbonate diffusion assay) by using *Sycon* CA. Left: a calcite crystal formed; at the right a vaterite crystal that has been formed.

The enzyme-mediated deposition of calcium carbonate is markedly temperature dependent [31]. While at 10 °C the reaction velocity of calcium carbonate deposition is almost identical in the enzyme-containing and enzyme-lacking assays, at higher, physiologically more relevant incubation temperatures (e.g., 22 °C [42]), the reaction velocity of the CA-driven calcium carbonate formation is significantly higher (about 2-fold) than that in the absence of CA. Varying the pH value in the precipitation assay shows that in the absence of CA the precipitation of calcium carbonate increases only slightly from pH 6.0 to pH 8.1. In contrast, the CA-driven reaction velocity increases markedly (by over 5-fold) from pH 6.0 to pH 8.0. Importantly, the increased rate in the reaction velocities seen in the CA-containing assays can be inhibited almost completely by the CA-specific inhibitor acetazolamide at 3 µM. In those assays the calcium concentration had been 50 mM with respect to $CaCl_2$ [31]. These findings are compatible with the view that the calcium carbonate deposition in the system described is enzymatically driven by the CA.

In order to underscore the dominant enzymatic contribution to the calcium carbonate deposition in vitro, one kinetic characteristic, the Michaelis–Menten constant, for CA, was determined [31]. At first it should be mentioned that the reaction follows substrate saturation kinetics. Under the assay conditions used (50 mM $CaCl_2$, pH 7.5, 25 °C), the linear increase of the reaction velocity is seen between 0 and 20 mM $CaCl_2$. Only at higher concentrations a saturation level is approached. It is well established that the CAs function both as hydratase, in the formation of bicarbonate, and also as esterase [51]. The Michaelis–Menten constants ($K_m$) for both reactions are almost identical at around 5 mM for the hydratase (using $CO_2$ as substrate) and for the esterase (with the substrate 4-nitrophenylacetate). The constant $K_m$ for the sponge CA/esterase was determined by applying the method of Lineweaver and Burk. The apparent $K_m$ constant for the sponge recombinant CA using 4-nitrophenylacetate as esterase substrate was found to be 6.2 ± 1.0 mM, at a maximal reaction velocity of 0.32 ± 0.05 $mmol \cdot mL^{-1} \cdot min^{-1}$. Using the same approach, the apparent $K_m$ constant in the hydratase/$CO_2$ diffusion assay was calculated to be 9.9 ± 2.1 mM (with respect to $CaCl_2$) at a corresponding $v_{max}$ of 24.9 ± 3.7 $mmol \cdot mL^{-1} \cdot min^{-1}$.

## Carbonic anhydrase: Evidence for forming bioseeds during mammalian hydroxyapatite formation

Our experimental data show that SaOS-2 cells, exposed to bicarbonate and the MAC, form a significantly increased

amount of Ca-deposits, as analyzed by a staining procedure with alizarin red S [7]. The MAC supplement (ascorbic acid, β-glycerophosphate and dexamethasone) stimulates cellular differentiation processes. Importantly, it had been measured that this process is paralleled by an enhanced expression of the CA-II gene, suggesting its participation in the Ca-deposit formation. Furthermore, the CA-II inhibitor acetazolamide significantly inhibited the Ca-mineral deposition process. These data favor the assumption that a CA-II-driven enzymatic process is involved in the formation of calcium carbonate bioseeds, required for the initial Ca phosphate deposit synthesis onto SaOS-2 cells. The CA-II is ubiquitously present in the cytoplasm of almost all metazoan cells and, focusing on mammalian bone cells, is probably involved in bone resorption [52]. There, CA-II causes proton production, resulting in a drastic acidification of the resorption lacuna/bone regions. However, recent studies implicate that this enzyme is also involved in bone formation [35]. These surprising Janus-faced catabolic/anabolic metabolic reactions, controlled by CAs might be explained on account of the reversibility of the CA-catalyzed reaction. The CA acts both as a calcium carbonate anabolic enzyme, facilitating and accelerating bicarbonate formation, a precursor molecule for calcium carbonate synthesis, and also as a catabolic enzyme that promotes calcium carbonate dissolution, as shown, e.g., in corals [53]. Experimental data revealed that during the initial phase of the controlled bone-synthesizing process poorly crystalline carbonated apatite is deposited, which contains several percents (4–6 wt %) of carbonate in the apatite crystals [54,55]. Recent studies suggest that the increased carbonate content in apatite crystals has an anabolic effect on bone formation [56]. Our EDX mapping studies [20] indicate that the crystallites initially formed onto SaOS-2 cells are not only rich in the elements calcium and phosphorous but also in carbon. We have taken this observation as a further indication that carbonate and phosphate deposits are co- or sequentially synthesized onto SaOS-2 cells, during the initial phase of mineral formation. Furthermore, the CA-II has been proven to be (under certain physiological conditions [pH regulation]) localized at the plasma membranes of human pancreatic cells [36], where the enzyme is involved both in pH regulation and in the secretion of bicarbonate through the $Cl^-/HCO^-$ exchanger [57] and/or an additional $HCO_3^-$ channel [36]. We concluded from the data gathered [20] that the calcium phosphate/HA deposition reactions in bone tissue are preceded by calcium carbonate precipitation, a process that is driven by an increased CA activity (Figure 5).

## Carbonic anhydrase: A new target for bone anabolic agents

A number of therapeutic targets have been described influencing signaling pathways, and/or transcription factors to stimulate bone growth (see [59]). Among those are the BMP/SMAD, Wnt/β-catenin, Hedgehog/Gli, IGF, and FGF pathways. Emerging evidence indicate that the CA enzyme could also be tackled as a promising target for activators to stimulate calcium carbonate/phosphate mineral deposition onto bone cells. Only very little experimental evidence has been presented that supports our supposition that CA activators exert a potential therapeutic effect on bone anabolism [60]. Until now only a few CA activators have been identified, but none of them have been tested for its potential in the treatment of bone disorders [61-63]. This view might be changed in view of the now available data indicating that calcium carbonate deposits might function as bioseeds for calcium phosphate precipitation onto bone-forming cells.

It is known that mineralization of osteoblasts, bone mineral-forming cells, is significantly induced by polyphosphate [polyP] in vitro even in the presence of orthophosphate [64]. PolyP is a linear polymer of phosphate linked by energy-rich phosphodiester bonds. Moreover, polyP turned out to be an inducer of osteoblast-specific alkaline phosphatase. This finding is interesting in view of published data indicating that intracellularly polyP might be formed in the vesicles of bone-forming cells as a Ca salt, which may act as a potential precursor of carbonated HA [65] (Figure 5).

In our recent study we could show that CA-driven $CaCO_3$ deposition can be stimulated by CA activators in vitro [66]. As activator(s) we have chosen extracts from the sponge *S. domuncula* and one component, isolated from those extracts, quinolinic acid (QA). In the in vitro CA-driven calcium carbonate deposition assay we could demonstrate that the *S. domuncula* extract and QA stimulate mineral formation (Figure 3C); as controls, the assays had been performed in the absence of sponge extract or of pure QA. Furthermore the results revealed that the stimulatory effect of bicarbonate ions on mineralization onto osteoblast-like SaOS-2 cells is strongly enhanced if the cells are exposed to polyP [64]. Finally, after hydrolysis of polyP through the alkaline phosphatase, the liberated orthophosphate inhibits in a negative feedback circle the CA (Figure 5).

## Future direction: 3D printing

In the repair of critical-size bone defects, autogenous bone grafts are considered to be the gold standard [67]. This technique has, however, several limitations which cannot be solved by using allogenous bone grafts, which have additional disadvantages, such as immunogenicity and risk of infection. Synthetic bone scaffolds can provide several advantages if they meet the following conditions: (i) similar physiochemical characteristics as the natural bone, and (ii) ability to attract the bone forming cells (the progenitor cells or the functionally active

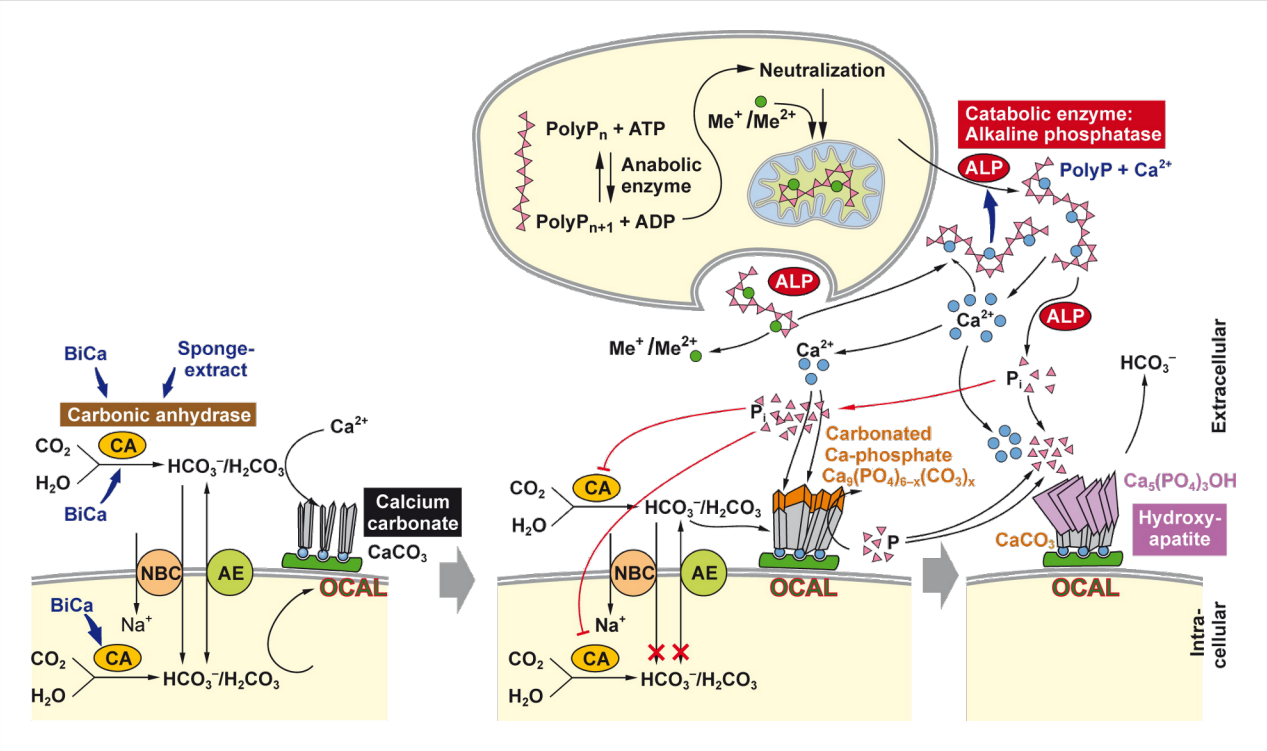


**Figure 5:** Sketch proposing the sequential deposition of calcium carbonate and Ca phosphate on the surface of bone-forming cells (SaOS-2 cells). The CA drives/accelerates the formation of bicarbonate, which reacts to carbonic acid and finally undergoes precipitation to calcium carbonate. Bicarbonate is provided to the CA via the chloride/bicarbonate anion exchanger (AE), or by the sodium bicarbonate co-transporter (NBC). It is proposed that the calcium carbonate crystallites are formed in the vicinity of the plasma membrane, perhaps under the participation of osteocalcin (OCAL). Sponge extracts (as well as their components, e.g., quinolinic acid) and bicarbonate (abbreviated as BiCa) stimulate the CA. In the second step calcium phosphate precipitates in the extracellular space onto the calcium carbonate bioseeds under formation of calcium carbonated apatite. Finally, orthophosphate, released from polyphosphate (polyP), downregulates the activity of the CA. In the third step it is outlined that the $Ca^{2+}$-salt of polyphosphate (polyP) undergoes hydrolysis through the alkaline phosphatase (ALP), resulting in the liberation of both orthophosphate (pink filled triangles) and $Ca^{2+}$, both components are required for the synthesis of HA [$(Ca_5(PO_4)_3(OH)$]. Partially taken from [58] with permission.

differentiated cells), two challenging tasks, limiting the routine application of synthetic materials in the treatment of bone defects. Bone repair materials like calcium phosphate, calcium carbonate, calcium sulfate and coralline carbonate grafts are characterized by good mechanical properties. They can be used as osteoconductive implant materials. They also may show osteointegrative properties. However, these implants lack any osteoinductivity and must be functionalized to become biologically active (for a review, see [68]).

The prerequisite for any scaffold applicable for bone tissue engineering is that it is accepted by the cells as a suitable 3D platform for their growth, differentiation and mineralization (HA deposition). These requirements can be met by scaffolds made of natural fibers, which correspond in their structure and composition to the extracellular matrix. A suitable scaffold must possess the inorganic/organic 3D structure of bone and an appropriate porosity [69] that allows the ingrowth of cells and an efficient transport of cytokines, growth factors, and nutrients. To avoid necrosis within larger implants, a suitable scaffold must also allow an efficient vascularization and tissue supply with oxygen. Much progress has been achieved in rapid prototyping/3D printing techiques in the last years. 3D printing is a computer-controlled layer-by-layer technology. Thereby a binder (binding solution) is printed into each layer of powder, a step-wise process that finally results, after blowing-away the unbound powder, in a 3D printed copy of the sliced virtual model [70,71]. 3D printing has turned out to be of promising technique for the fabrication of implants used as bone substitution materials [72]. The advantage of this method is that the implants can be customized to the 3D geometry of the bone defect of an individual patient, based on medical imaging data. Such implants allow an optimal integration and can be provided with the required functional properties using suitable materials such as bioactive glasses and Ca phosphate.

Based on published data, indicating that alginate/chitin, also together with silica [73,74], provides a suitable matrix for the encapsulation of mammalian cells we have recently also embedded SaOS-2 cells into Na alginate that has been supplemented with silica [75-77]. Silica displays morphogenetic activity towards SaOS-2 cells (see above); this biological

activity of silica is retained by SaOS-2 cells that have been encapsulated into Na alginate. Based on the finding that Na alginate is a suitable matrix for embedding bone cells [78] we have successfully started to print 3D structures in order to apply this technology for bioprinting and construction of bioartificial tissues or organs. In a first step we have encapsulated separately bone-forming (SaOS-2) and bone-degrading (RAW 264.7) cells to develop a biomimetic synthetic scaffold suitable for tissue engineering [75]. In the alginate matrix applied the SaOS-2 cells retain their capacity to synthesize HA crystallites. Furthermore, the mechanical properties, including surface roughness and hardness, of the hydrogel were determined. If silica is included in the hydrogel matrix, the encapsulated SaOS-2 cells were found to increasingly express the gene encoding for osteoprotegerin in co-cultivation experiments with RAW 264.7 cell beads, suggesting that under the applied conditions the differentiation capacity of the RAW 264.7 cells is impaired. In continuation it was found that under these conditions (SaOS-2 cells cultured together with RAW 264.7 cells) the RAW 264.7 cells show a reduced capacity to express the gene for tartrate-resistant acid phosphatase. For rapid prototyping bioprinting we are using a computer-aided tissue engineering printer (3D-Bioplotter; Corporate EnvisionTEC GmbH, Gladbeck; Germany). With this technology we succeeded to embed SaOS-2 cells into the Na alginate, with the indicated supplements, and allowed the matrix to be passed through the capillary of the 3D printer (Figure 6). The arrays of strands were computed to 4 mm high blocks into which the cells remained viable and retained the capacity to form mineral crystallites. We are convinced that this strategy will contribute to a further improvement of the formulation of a suitable artificial scaffold for rapid prototyping 3D bioprinting of organ-like tissue units.

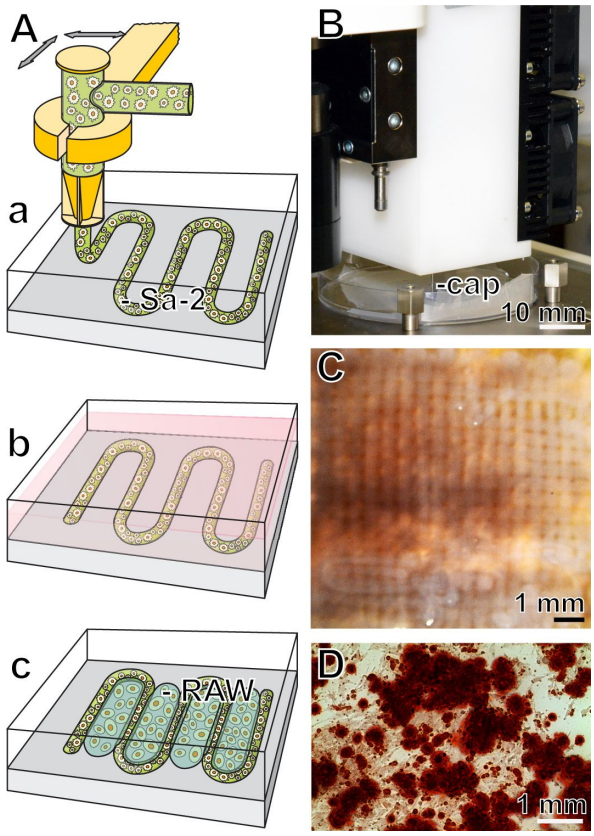


**Figure 6:** Computer-aided rapid prototyping bioprinting. (A-a) A sketch outlining the computer-guided extrusion of Na alginate hydrogel (supplemented with biosilica or bicarbonate) through a capillary in a meander-like pattern. This matrix contained SaOS-2 cells (Sa-2). (A-b and A-c) The blocks formed were incubated in medium into which RAW 264.7 cells (RAW) had been suspended. (B) Part of the bioplotter showing the capillary (cap) through which the alginate/cell matrix is extruded. (C) Completed 4 mm high blocks into which the cells have been embedded into the alginate. (D) The cells retain the capacity to form crystallites, which can be visualized after staining with Alizarin Red S.

## Acknowledgements

W. E. G. M. is a holder of an ERC Advanced Investigator Grant (No. 268476 “BIOSILICA”) and of an ERC Proof-of-Concept Grant (No. 324564 “Si-Bone-PoC”). This work was supported by grants from the Deutsche Forschungsgemeinschaft (Schr 277/10-3), the European Commission (Industry-Academia Partnerships and Pathways “CoreShell”: No. 286059; “MarBioTec*EU-CN*”: No. 268476; “Bio-Scaffolds”: No. 604036; and “BlueGenics”: No. 311848) and the International Human Frontier Science Program, as well as the BiomaTiCS research initiative of the University Medical Center, Mainz.

## References

1. Müller, W. E. G.; Wiens, M.; Adell, T.; Gamulin, V.; Schröder, H. C.; Müller, I. M. *Int. Rev. Cytol.* **2004,** *235,* 53–92. doi:10.1016/S0074-7696(04)35002-3
2. Wang, X.; Schröder, H. C.; Müller, W. E. G. *Int. Rev. Cell Mol. Biol.* **2009,** *273,* 69–115. doi:10.1016/S1937-6448(08)01803-0
3. Morse, D. E. *Trends Biotechnol.* **1999,** *17,* 230–232. doi:10.1016/S0167-7799(99)01309-8
4. Wang, X.; Schröder, H. C.; Wang, K.; Kaandorp, J. A.; Müller, W. E. G. *Soft Matter* **2012,** *8,* 9501–9518. doi:10.1039/c2sm25889g
5. Knoll, A. H. *Rev. Mineral. Geochem.* **2003,** *54,* 329–356. doi:10.2113/0540329
6. Müller, W. E. G.; Li, J.; Schröder, H. C.; Qiao, L.; Wang, X. *Biogeosciences* **2007,** *4,* 219–232. doi:10.5194/bg-4-219-2007
7. Müller, W. E. G.; Schröder, H. C.; Burghard, Z.; Pisignano, D.; Wang, X. *Chem.–Eur. J.* **2013,** *19,* 5790–5804. doi:10.1002/chem.201204412
8. Müller, W. E. G. Spatial and temporal expression patterns in animals. In *Encyclopedia of Molecular Cell Biology and Molecular Medicine;* Meyers, R. A., Ed.; Wiley-VCH: Weinheim, Germany, 2005; Vol. 13, pp 269–309.
9. Shimizu, K.; Cha, J.; Stucky, G. D.; Morse, D. E. *Proc. Natl. Acad. Sci. U. S. A.* **1998,** *95,* 6234–6238. doi:10.1073/pnas.95.11.6234

10. Cha, J. N.; Shimizu, K.; Zhou, Y.; Christianssen, S. C.; Chmelka, B. F.; Stucky, G. D.; Morse, D. E. *Proc. Natl. Acad. Sci. U. S. A.* **1999,** *96,* 361–365. doi:10.1073/pnas.96.2.361
11. Krasko, A.; Lorenz, B.; Batel, R.; Schröder, H. C.; Müller, I. M.; Müller, W. E. G. *Eur. J. Biochem.* **2000,** *267,* 4878–4887. doi:10.1046/j.1432-1327.2000.01547.x
12. Wiens, M.; Bausen, M.; Natalio, F.; Link, T.; Schlossmacher, U.; Müller, W. E. G. *Biomaterials* **2009,** *30,* 1648–1656. doi:10.1016/j.biomaterials.2008.12.021
13. Schloßmacher, U.; Wiens, M.; Schröder, H. C.; Wang, X.; Jochum, K. P.; Müller, W. E. G. *FEBS J.* **2011,** *278,* 1145–1155. doi:10.1111/j.1742-4658.2011.08040.x
14. Müller, W. E. G.; Binder, M.; von Lintig, J.; Guo, Y.-W.; Wang, X.; Kaandorp, J. A.; Wiens, M.; Schröder, H. C. *Biochim. Biophys. Acta, Gen. Subj.* **2011,** *1810,* 1178–1194. doi:10.1016/j.bbagen.2011.09.006
15. Wang, X.; Schloßmacher, U.; Schröder, H. C.; Müller, W. E. G. *Soft Matter* **2013,** *9,* 654–664. doi:10.1039/c2sm27109e
16. Wang, X.; Schröder, H. C.; Wiens, M.; Ushijima, H.; Müller, W. E. G. *Curr. Opin. Biotechnol.* **2012,** *23,* 570–578. doi:10.1016/j.copbio.2012.01.018
17. Katagiri, T.; Yamaguchi, A.; Komaki, M.; Abe, E.; Takahashi, N.; Ikeda, T.; Rosen, V.; Wozney, J. M.; Fujisawa-Sehara, A.; Suda, T. *J. Cell Biol.* **1994,** *127,* 1755–1766. doi:10.1083/jcb.127.6.1755
18. Mukherjee, A.; Rotwein, P. *J. Cell Sci.* **2009,** *122,* 716–726. doi:10.1242/jcs.042770
19. Heaney, R. P.; Recker, R. R.; Watson, P.; Lappe, J. M. *Am. J. Clin. Nutr.* **2010,** *92,* 101–105. doi:10.3945/ajcn.2009.29085
20. Müller, W. E. G.; Schröder, H. C.; Schlossmacher, U.; Grebenjuk, V. A.; Ushijima, H.; Wang, X. *Biomaterials* **2013,** *34,* 8671–8680. doi:10.1016/j.biomaterials.2013.07.096
21. Mann, S.; Parker, S. B.; Ross, M. D.; Skarnulis, A. J.; Williams, R. J. P. *Proc. R. Soc. London, Ser. B* **1983,** *218,* 415–424. doi:10.1098/rspb.1983.0048
22. Pisam, M.; Jammet, C.; Laurent, D. *Cell Tissue Res.* **2002,** *310,* 163–168. doi:10.1007/s00441-002-0622-z
23. Pellegrino, E. D.; Biltz, R. M. *Calcif. Tissue Res.* **1970,** *6,* 168–171. doi:10.1007/BF02196196
24. Azari, F.; Vali, H.; Guerquin-Kern, J.-L.; Wu, T.-D.; Croisy, A.; Sears, S. K.; Tabrizian, M.; McKee, M. D. *J. Struct. Biol.* **2008,** *162,* 468–479. doi:10.1016/j.jsb.2008.03.003
25. Rey, C.; Kim, H.-M.; Gerstenfeld, L.; Glimcher, M. J. *Connect. Tissue Res.* **1996,** *35,* 343–349. doi:10.3109/03008209609029210
26. Boonrungsiman, S.; Gentleman, E.; Carzaniga, R.; Evans, N. D.; McComb, D. W.; Porter, A. E.; Stevens, M. M. *Proc. Natl. Acad. Sci. U. S. A.* **2012,** *109,* 14170–14175. doi:10.1073/pnas.1208916109
27. Omelon, S.; Georgiou, J.; Henneman, Z. J.; Wise, L. M.; Sukhu, B.; Hunt, T.; Wynnyckyj, C.; Holmyard, D.; Bielecki, R.; Grynpas, M. D. *PLoS One* **2009,** *4,* e5634. doi:10.1371/journal.pone.0005634
28. Posner, A. S.; Betts, F.; Blumenthal, N. C. *Metab. Bone Dis. Relat. Res.* **1978,** *1,* 179–183. doi:10.1016/0221-8747(78)90057-7
29. Li, W.; Chen, W.-S.; Zhou, P.-P.; Cao, L.; Yu, L.-J. *Colloids Surf., B* **2013,** *102,* 281–287. doi:10.1016/j.colsurfb.2012.08.042
30. Meldrum, F. C.; Cölfen, H. *Chem. Rev.* **2008,** *108,* 4332–4432. doi:10.1021/cr8002856
31. Müller, W. E. G.; Schröder, H. C.; Schlossmacher, U.; Neufurth, M.; Geurtsen, W.; Korzhev, M.; Wang, X. *FEBS Open Bio* **2013,** *3,* 357–362. doi:10.1016/j.fob.2013.08.004
32. Lindskog, S. *Pharmacol. Ther.* **1997,** *74,* 1–20. doi:10.1016/S0163-7258(96)00198-2
33. Sanyal, G.; Maren, T. H. *J. Biol. Chem.* **1981,** *256,* 608–612.
34. Sly, W. S.; Hu, P. Y. *Annu. Rev. Biochem.* **1995,** *64,* 375–401. doi:10.1146/annurev.bi.64.070195.002111
35. Chang, X.; Zheng, Y.; Yang, Q.; Wang, L.; Pan, J.; Xia, Y.; Yan, X.; Han, J. *Arthritis Res. Ther.* **2012,** *14,* R176. doi:10.1186/ar3929
36. Alvarez, L.; Fanjul, M.; Carter, N.; Hollande, E. *J. Histochem. Cytochem.* **2001,** *49,* 1045–1053. doi:10.1177/002215540104900812
37. Mahieu, I.; Becq, F.; Wolfensberger, T.; Gola, M.; Carter, N.; Hollande, E. *Biol. Cell* **1994,** *81,* 131–141. doi:10.1016/S0248-4900(94)80004-9
38. Müller, W. E. G.; Wang, X.; Grebenjuk, V. A.; Korzhev, M.; Wiens, M.; Schloßmacher, U.; Schröder, H. C. *PLoS One* **2012,** *7,* e34617. doi:10.1371/journal.pone.0034617
39. Lovejoy, D. A.; Hewett-Emmett, D.; Porter, C. A.; Cepoi, D.; Sheffield, A.; Vale, W. W.; Tashian, R. E. *Genomics* **1998,** *54,* 484–493. doi:10.1006/geno.1998.5585
40. Furla, P.; Galgani, I.; Durand, I.; Allemand, D. *J. Exp. Biol.* **2000,** *203,* 3445–3457.
41. Tripp, B. C.; Smith, K.; Ferry, J. G. *J. Biol. Chem.* **2001,** *276,* 48615–48618. doi:10.1074/jbc.R100045200
42. Müller, W. E. G.; Schlossmacher, U.; Schröder, H. C.; Lieberwirth, I.; Glasser, G.; Korzhev, M.; Neufurth, M.; Wang, X. *Acta Biomater.* **2014,** *10,* 450–462. doi:10.1016/j.actbio.2013.08.025
43. Jones, W. C. *Nature* **1967,** *214,* 365–368. doi:10.1038/214365a0
44. Ledger, P. W.; Jones, W. C. *Cell Tissue Res.* **1977,** *181,* 553–567. doi:10.1007/BF00221776
45. Han, T. Y.-J.; Aizenberg, J. *Chem. Mater.* **2008,** *20,* 1064–1068. doi:10.1021/cm702032v
46. Tyrrell, T. *J. Plankton Res.* **2008,** *30,* 141–156. doi:10.1093/plankt/fbm105
47. Gasbjerg, P. K.; Brahm, J. *J. Gen. Physiol.* **1991,** *97,* 321–349. doi:10.1085/jgp.97.2.321
48. Li, W.; Chen, W.-S.; Zhou, P.-P.; Zhu, S.-L.; Yu, L.-J. *Chem. Eng. J.* **2013,** *218,* 65–72. doi:10.1016/j.cej.2012.12.034
49. Ilan, M.; Aizenberg, J.; Gilor, O. *Proc. R. Soc. London, Ser. B* **1996,** *263,* 133–139. doi:10.1098/rspb.1996.0021
50. Müller, W. E. G.; Neufurth, M.; Schlossmacher, U.; Schröder, H. C.; Pisignano, D.; Wang, X. *RSC Adv.* **2014,** *4,* 2577–2585. doi:10.1039/c3ra45193c
51. Kirley, J. W.; Day, R. A. *Biochem. Biophys. Res. Commun.* **1985,** *126,* 457–463. doi:10.1016/0006-291X(85)90627-8
52. Margolis, D. S.; Szivek, J. A.; Lai, L.-W.; Lien, Y.-H. H. *Calcif. Tissue Int.* **2008,** *82,* 66–76. doi:10.1007/s00223-007-9098-x
53. Müller, W. E. G.; Müller, I.; Zahn, R. K.; Maidhof, A. *J. Histochem. Cytochem.* **1984,** *32,* 285–288. doi:10.1177/32.3.6141203
54. Termine, J. D.; Eanes, E. D.; Greenfield, D. J.; Nylen, M. U.; Harper, R. A. *Calcif. Tissue Res.* **1973,** *12,* 73–90. doi:10.1007/BF02013723
55. Biltz, R. M.; Pellegrino, E. D. *Clin. Orthop. Relat. Res.* **1977,** *129,* 279–292.
56. Matsuura, A.; Kubo, T.; Doi, K.; Hayashi, K.; Morita, K.; Yokota, R.; Hayashi, H.; Hirata, I.; Okazaki, M.; Akagawa, Y. *Dent. Mater. J.* **2009,** *28,* 234–242. doi:10.4012/dmj.28.234

57. Novak, I.; Greger, R. *Pfluegers Arch.* **1988,** *411,* 546–553. doi:10.1007/BF00582376
58. Wang, X.; Schröder, H. C.; Feng, Q.; Draenert, F.; Müller, W. E. G. *Mar. Drugs* **2013,** *11,* 718–746. doi:10.3390/md11030718
59. Garrett, I. R. *Curr. Top. Dev. Biol.* **2007,** *78,* 127–171. doi:10.1016/S0070-2153(06)78004-8
60. Supuran, C. T.; Scozzafava, A. *Expert Opin. Ther. Pat.* **2000,** *10,* 575–600. doi:10.1517/13543776.10.5.575
61. Pastorekova, S.; Parkkila, S.; Pastorek, J.; Supuran, C. T. *J. Enzyme Inhib. Med. Chem.* **2004,** *19,* 199–229. doi:10.1080/14756360410001689540
62. Supuran, C. T. *Nat. Rev. Drug Discovery* **2008,** *7,* 168–181. doi:10.1038/nrd2467
63. Supuran, C. T. *Curr. Pharm. Des.* **2008,** *14,* 603–614. doi:10.2174/138161208783877884
64. Müller, W. E. G.; Wang, X.; Diehl-Seifert, B.; Kropf, K.; Schloßmacher, U.; Lieberwirth, I.; Glasser, G.; Wiens, M.; Schröder, H. C. *Acta Biomater.* **2011,** *7,* 2661–2671. doi:10.1016/j.actbio.2011.03.007
65. Mahamid, J.; Sharir, A.; Gur, D.; Zelzer, E.; Addadi, L.; Weiner, S. *J. Struct. Biol.* **2011,** *174,* 527–535. doi:10.1016/j.jsb.2011.03.014
66. Wang, X.; Schröder, H. C.; Schlossmacher, U.; Neufurth, M.; Feng, Q.; Diehl-Seifert, B.; Müller, W. E. G. *Calcif. Tissue Int.* **2014,** *94,* 495–509. doi:10.1007/s00223-013-9833-4
67. Epple, M. Biomimetic Bone Substitution Materials. In *Biomineralisation: Medical and Clinical Aspects;* Epple, M.; Baeuerlein, E., Eds.; Wiley-VCH: Weinheim, Germany, 2007; pp 81–95.
68. Brydone, A. S.; Meek, D.; Maclaine, S. *J. Eng. Med.* **2010,** *224,* 1329–1343. doi:10.1243/09544119JEIM770
69. Holzwarth, J. M.; Ma, P. X. *Biomaterials* **2011,** *32,* 9622–9629. doi:10.1016/j.biomaterials.2011.09.009
70. Seitz, H.; Rieder, W.; Irsen, S.; Leukers, B.; Tille, C. *J. Biomed. Mater. Res., Part B* **2005,** *74,* 782–788. doi:10.1002/jbm.b.30291
71. Fierz, F. C.; Beckmann, F.; Huser, M.; Irsen, S. H.; Leukers, B.; Witte, F.; Degistirici, Ö.; Andronache, A.; Thie, M.; Müller, B. *Biomaterials* **2008,** *29,* 3799–3806. doi:10.1016/j.biomaterials.2008.06.012
72. Detsch, R.; Schaefer, S.; Deisinger, U.; Ziegler, G.; Seitz, H.; Leukers, B. *J. Biomater. Appl.* **2011,** *26,* 359–380. doi:10.1177/0885328210373285
73. Gimeno-Fabra, M.; Peroglio, M.; Eglin, D.; Alini, M.; Perry, C. C. *J. Mater. Chem.* **2011,** *21,* 4086–4089. doi:10.1039/c0jm04463f
74. Madhumathi, K.; Sudheesh Kumar, P. T.; Kavya, K. C.; Furuike, T.; Tamura, H.; Nair, S. V.; Jayakumar, R. *Int. J. Biol. Macromol.* **2009,** *45,* 289–292. doi:10.1016/j.ijbiomac.2009.06.009
75. Schloßmacher, U.; Schröder, H. C.; Wang, X.; Feng, Q.; Diehl-Seifert, B.; Neumann, S.; Trautwein, A.; Müller, W. E. G. *RSC Adv.* **2013,** *3,* 11185–11194. doi:10.1039/c3ra23341c
76. Müller, W. E. G.; Wang, X.; Grebenjuk, V.; Diehl-Seifert, B.; Steffen, R.; Schloßmacher, U.; Trautwein, A.; Neumann, S.; Schröder, H. C. *Biomater. Sci.* **2013,** *1,* 669–678. doi:10.1039/c3bm00001j
77. Wang, X.; Schröder, H. C.; Diehl-Seifert, B.; Kropf, K.; Schlossmacher, U.; Wiens, M.; Müller, W. E. G. *J. Tissue Eng. Regener. Med.* **2013,** *7,* 767–776. doi:10.1002/term.1465
78. Song, S.-J.; Choi, J.; Park, Y.-D.; Hong, S.; Lee, J. J.; Ahn, C. B.; Choi, H.; Sun, K. *Artif. Organs* **2011,** *35,* 1132–1136. doi:10.1111/j.1525-1594.2011.01377.x


## License and Terms

BEILSTEIN JOURNAL OF NANOTECHNOLOGY

# Ionic liquid-assisted formation of cellulose/calcium phosphate hybrid materials

Ahmed Salama[1,2], Mike Neumann[1], Christina Günter[3] and Andreas Taubert[*1]

Full Research Paper

Open Access

Address:
[1]Institute of Chemistry, University of Potsdam, D-14476 Potsdam, Germany, [2]Cellulose and Paper Department, National Research Center, El-Tahrir Street, Dokki, Cairo, Egypt and [3]Institute of Earth and Environmental Sciences, University of Potsdam, D-14476 Potsdam, Germany

Email:
Andreas Taubert[*] - ataubert@uni-potsdam.de

* Corresponding author

Keywords:
biomineralization; calcium phosphate; carbohydrates; cellulose; hybrid materials; ionic liquid

*Beilstein J. Nanotechnol.* **2014,** *5,* 1553–1568.
doi:10.3762/bjnano.5.167

Received: 02 June 2014
Accepted: 12 August 2014
Published: 16 September 2014

This article is part of the Thematic Series "Towards multifunctional inorganic materials: biopolymeric templates".

Guest Editors: C. Steinem and J. Bill



## Abstract

Cellulose/calcium phosphate hybrid materials were synthesized via an ionic liquid-assisted route. Scanning electron microscopy, transmission electron microscopy, energy-dispersive X-ray spectroscopy, X-ray diffraction, infrared spectroscopy, and thermogravimetric analysis/differential thermal analysis show that, depending on the reaction conditions, cellulose/hydroxyapatite, cellulose/chlorapatite, or cellulose/monetite composites form. Preliminary studies with MC3T3-E1 pre-osteoblasts show that the cells proliferate on the hybrid materials suggesting that the ionic liquid-based process yields materials that are potentially useful as scaffolds for regenerative therapies.

## Introduction

One of the key advantages of carbohydrates, especially cellulose and chitin, is their abundance and favorable properties such as mechanical robustness and biocompatibility [1-4]. Moreover, the growth (mineralization) of calcium phosphate on polysaccharides may lead to composites with properties that are useful for the regeneration of hard tissue even though the chemical composition of these materials is different from the original biomaterial [5-11]. Unfortunately, the synthesis of carbohydrate-based hybrid materials is not straightforward. This is due to the fact that many carbohydrates exhibit low solubilities in aqueous media. Aqueous solutions, however, are the most commonly used media for calcium phosphate mineralization [12,13]. As a result, mineralization of carbohydrates often yields heterogeneous materials with properties that are not suited for an application. In spite of this, a number of authors have reported the successful mineralization of carbohydrates with various calcium phosphates.

Falini and coworkers used β-chitin from a squid pen for mineralization of octacalcium phosphate (OCP) and hydroxyapatite (HAP) [14,15]. They found a distinct change of the chitin fiber organization on OCP mineralization. Moreover, the OCP–HAP

transition is delayed with respect to OCP grown in the absence of the carbohydrate matrix. One of the issues of chitin, however, is again its limited solubility in most mineralization media. This limits the processing and mineralization efficiencies. Chitosan, which exhibits a higher water solubility than chitin, has therefore been used as an alternative scaffold for calcium phosphate mineralization [16,17]. Among others, chitosan/HAP scaffolds show good osteoconductivity and biodegradability, as has been shown for some synthetic composites in rats [18].

Chiono et al. developed a photochemical approach towards the triggered nucleation of calcium phosphate on chitosan cast films [19]. Mineralization is induced by photoexcitation of fluorescein molecules grafted to the chitosan films. The authors claim that the formation of local positive charges by electron transfer from the fluorophore to reactive species in the surrounding medium like $O_2$ or water leads to singlet oxygen radicals and superoxide radical anions. According to the authors, these may then act as nucleation sites. One unresolved question here is the fact that these results differ significantly from other work [16,18] where calcium phosphate deposition on chitosan was equally successful, but without the need to photoactivate the mineralization reaction.

Besides chitin and chitosan, carboxymethyl inulin (CMI) [20,21] and carboxymethyl cellulose (CMC) [22,23] have been studied as mineralization additives. Composites of CMC, calcium phosphate nanoparticles, and the antibiotic chlorhexidine efficiently remineralize dentin tubules [23]. In contrast, CMI inhibits or at least delays calcium phosphate mineralization [20-22].

There are also a few reports on the mineralization of unmodified cellulose [11,24-33], but like in the case of chitin, the poor solubility of cellulose in conventional solvents hampers the development of true calcium phosphate/carbohydrate hybrid materials because it prevents, or at least dramatically reduces, the penetration of the precursor ions into the carbohydrate templates and thus results in materials mostly exhibiting surface or near-surface mineral layers.

The most straightforward strategy towards real, nanostructured and hierarchical carbohydrate/calcium phosphate composites would therefore be a synthesis protocol using a solvent that is able to dissolve carbohydrates as single molecules or very small aggregates. At the same time the solvent should enable the growth of calcium phosphate.

Ionic liquids (ILs) could provide a viable access for the synthesis of such nanoscale carbohydrate/inorganic hybrids. Some ILs dissolve up to 25 wt % of cellulose [34-37]. This efficiency has mainly been attributed to the ability of the ILs to break hydrogen bonds, which is the key interaction stabilizing cellulose and chitin [34,38-40]. Moreover, ILs are efficient reaction media for the synthesis of new and interesting inorganic materials [35,41-45] although there are only a few reports on IL-based protocols for the synthesis of carbohydrate/inorganic hybrid materials.

Mumalo-Djokic et al. studied the formation of ZnO/carbohydrate hybrid materials using a hydrated IL, tetrabutylammonium hydroxide [TBA][OH], as the solvent and hydroxide source for ZnO formation [46]. This study revealed significant differences between the two carbohydrates studied, cellulose and starch. While starch was soluble in the water/IL mixture, cellulose was, due to the high water content in the reaction mixture, not. As a result, while the mineralization of starch led to a nanoscale hybrid material, the mineralization of cellulose led to cellulose fibers with a high degree of surface mineralization. In spite of this, the cellulose fibers appeared to "imprint" some features of their surface structure on the mineral layers.

Venkataramanan et al. synthesized cellulose/$TiO_2$ hybrids via a sol–gel reaction in 1-butyl-3-methylimidazolium chloride, [Bmim][Cl] [47]. $Ti(OBu)_4$ was used as $TiO_2$ precursor and a network of $TiO_2$ layered fibers was observed after the sol–gel reaction. Amarasekara and Owereh prepared cellulose carbamate/silica hybrid materials in [Bmim][Cl] [48]. Cellulose-based hybrid materials with calcium carbonate [49], copper oxide [50], or calcium silicate [51] have been grown in [Bmim][Cl]. Finally, there is a report on the synthesis of cellulose/calcium phosphate composites using ILs [52]. The authors of this study, however, did not grow inorganic matter in the IL, but dispersed prefabricated hydroxyapatite (HAP) nanoparticles into a solution of cellulose in [Bmim][Cl] to form composites with limited homogeneity.

Besides the approaches introduced above, [Bmim][Cl] has also been used for calcium carbonate precipitation [53]. [Bmim][Cl] is thus a prime candidate for the generation of new calcium phosphate/carbohydrate hybrid materials. The current study therefore evaluates the potential of [Bmim][Cl] for the synthesis of well-defined calcium phosphate/cellulose composites with a defined morphology, chemical composition, calcium phosphate crystal phase, crystal organization, and suitable compatibility for cells. The approach is based on the precipitation of calcium phosphate from IL/cellulose solutions rather than adding pre-fabricated calcium phosphate nanoparticles to the IL/cellulose solution and thus provides a rather simple, one-step approach towards cellulose/calcium phosphate hybrid materials.

## Experimental

**Materials.** [Bmim][Cl] (≥95%, Aldrich) was freeze-dried from water. The final water content was below 0.3%, as determined by volumetric Karl Fischer titration. After freeze-drying the IL was stored under argon until use. Microcrystalline cellulose (extra pure, average particle size 90 μm, Acros), calcium chloride dihydrate $CaCl_2{\cdot}2H_2O$ (extra pure, Merck), dibasic potassium phosphate $K_2HPO_4$ (≥98%, Sigma-Aldrich), sodium dihydrogen phosphate dihydrate $NaH_2PO_4{\cdot}2H_2O$ (≥98%, Roth), and glacial acetic acid (100%, p.a., water content below 0.1%, Roth), NaOH (puriss. p.a. ACS, pellets, ≥98%, Sigma-Aldrich), and ethanol (p.a., absolute, Merck) were used as received.

**Calcium phosphate synthesis.** 0.6 g of powdered calcium chloride (4.1 mmol) were dissolved in 6 g of [Bmim][Cl] at 80 °C under vigorous stirring. After complete dissolution, 2.46 mmol of the phosphate precursor (0.43 g of dibasic potassium phosphate or 0.38 g of sodium phosphate) were added at 80 °C, yielding a reaction mixture with a Ca/P ratio of 1.67. Then 0.4 mL of ethanolic NaOH or glacial acetic acid was added and the ethanol was removed by evaporation. The reaction mixture was subsequently stirred for 24 or 48 h at 80 °C. The reaction products were precipitated by adding an excess amount of water to the reaction mixture after cooling. The precipitates were filtered, washed with distilled water, and the IL was removed from the products via Soxleth extraction (methanol, 48 h). The purified products were dried at 40 °C for 24 h in a vacuum oven. Samples are labeled $CP^{Xy}$, where X = NaOH or GAA (glacial acetic acid) indicates the additive and y = 24 or 48 indicates the reaction time, 24 or 48 h. For example, $CP^{NaOH24}$ is a sample grown in the presence of NaOH for 24 h.

**Preparation of cellulose/calcium phosphate hybrid materials.** Cellulose was dissolved in [Bmim][Cl] at 80 °C overnight in different weight fractions (Table 1). 0.6 g of powdered calcium chloride (4.1 mmol) per 6 g of IL was added to the cellulose/IL solution at 80 °C under vigorous stirring. After complete dissolution/dispersion, 2.46 mmol of the phosphate precursor (0.43 g of dibasic potassium phosphate or 0.38 g of sodium phosphate) were added at 80 °C, yielding a reaction mixture with a Ca/P ratio of 1.67. Then 30 μL GAA or ethanolic NaOH were added and the ethanol and water from the inorganic precursor salts were removed under high vacuum ($10^{-3}$ mbar) for 30 min. The reaction mixture was subsequently stirred for 24 or 48 h at 80 °C during which time a white precipitate formed. The reaction products were precipitated by adding an excess amount of water to the reaction mixture after cooling. The precipitate was filtered, washed with distilled water, and the IL was extracted from the products by Soxleth extraction with methanol for two days. The products were subsequently dried at 40 °C for 24 h in a vacuum oven.

**Characterization.** Attenuated total reflection-Fourier transform infrared spectroscopy was done on a Thermo Nicolet FT-IR Nexus 470 with a diamond crystal. Spectra were recorded from 500 to 4000 $cm^{-1}$ with a resolution of 2 $cm^{-1}$. X-ray diffraction patterns were recorded with a Siemens D5005 (Cu Kα, 0.154 nm) between 3 and 70° 2θ with a step size of 0.02° per second. Samples were mounted on a silicon support. Scanning electron microscopy was done on a FEI Phenom operated at 5 kV. Transmission electron microscopy was done on a Zeiss 912 Omega operated at 120 kV. Cross sections were obtained with a Leica Ultra Cut Microtome. For sectioning, the powder samples were embedded in "LR white" resin (Plano GmbH). Samples were cut at 1 mm/s at room temperature. Energy dispersive X-ray spectroscopy was done on a JEOL JSM 6510 SEM with tungsten hairpin filament (15 kV) and an Oxford INCAx-act SN detector with a resolution of 135 eV at 5.9 keV. Elemental analysis was done on a Vario EL III analyzer. Thermogravimetric analysis/differential thermal analysis was done on a Linseis STA PT-1600 thermal balance in air from 20 to 600 °C with a heating rate of 10 K/min and air flow of 50 mL/min.

## Results

### Calcium phosphate precipitated without cellulose

Table 1 summarizes the samples obtained after reaction in [Bmim][Cl]. Figure 1 shows the XRD patterns and the FTIR spectra of the reaction products after purification. The IR spectra of the calcium phosphates obtained by reaction in the presence of glacial acetic acid (GAA) after 24 h ($CP^{GAA24}$, for details of labeling see Experimental part) show no band in the range of 3500 $cm^{-1}$, which suggests that these precipitates are relatively free from water or hydroxy groups. In contrast, all other samples ($CP^{GAA48}$, $CP^{NaOH24}$, $CP^{NaOH48}$) show strong bands at 3350 to 3360 $cm^{-1}$ indicating the presence of significant amounts of hydroxy- or water-containing calcium phosphate phases [54,55].

FTIR spectroscopy (Figure 1A) further corroborates the formation of calcium phosphate. Products prepared with GAA after 24 h ($CP^{GAA24}$) exhibit major bands for the phosphate group at 1022 and 1126 $cm^{-1}$ (P–O $\nu_3$), 565 $cm^{-1}$ (P–O $\nu_4$), and 990 $cm^{-1}$ (P–O $\nu_1$) which can be attributed to the presence of $PO_4^{3-}$ and/or $HPO_4^{2-}$ groups. The IR spectra of the calcium phosphates precipitated in the presence of glacial acetic acid (GAA) after 48 h ($CP^{GAA48}$) mainly shows bands associated with apatite at 1045 and 1169 $cm^{-1}$ (P–O $\nu_3$), 563 and 606 $cm^{-1}$ (P–O $\nu_4$ ), and 960 and 802 $cm^{-1}$ (P–O $\nu_1$).

Similar spectra were observed for the samples precipitated in the presence of NaOH after 24 and 48 h ($CP^{NaOH24}$ and

**Table 1:** Samples investigated in this study. CP is calcium phosphate, GAA is glacial acetic acid, 24 and 48 are reaction times in hours.

| Sample | Phosphate precursor[a] | GAA or NaOH | Reaction conditions |
|---|---|---|---|
| $CP^{GAA24}$ | $NaH_2PO_4{\cdot}2H_2O$ | GAA | 24 h, 80 °C |
| $CP^{GAA48}$ | $NaH_2PO_4{\cdot}2H_2O$ | GAA | 48 h, 80 °C |
| $CP^{NaOH24}$ | $K_2HPO_4$ | NaOH | 24 h, 80 °C |
| $CP^{NaOH48}$ | $K_2HPO_4$ | NaOH | 48 h, 80 °C |

[a]Calcium precursor was always $CaCl_2{\cdot}2H_2O$.

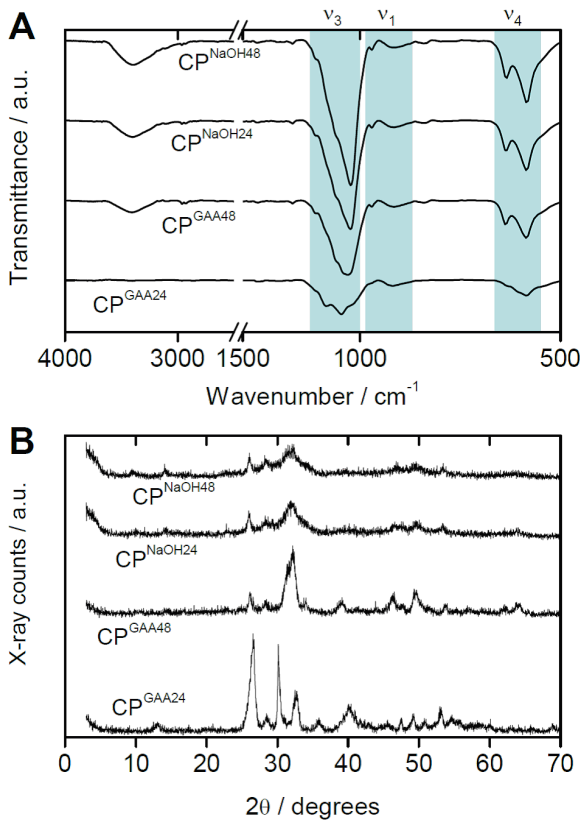


**Figure 1:** (A) ATR-FTIR spectra and (B) XRD patterns of calcium phosphates obtained from [Bmim][Cl]. The reflection at 14.2 degrees 2θ is from the sample holder (Si).

$CP^{NaOH48}$). Here the bands are at 1034 and 1168 (P–O $\nu_3$), 563 and 602 (P–O $\nu_4$), and 963 and 802 $cm^{-1}$ (P–O $\nu_1$). This suggests that the $CP^{GAA48}$, $CP^{NaOH24}$, and $CP^{NaOH48}$ materials are structurally similar.

X-ray diffraction (XRD, Figure 1B) shows that the addition of glacial acetic acid (GAA) or NaOH, respectively, to the reaction mixture leads to different calcium phosphates. XRD patterns of $CP^{GAA24}$ show reflections at 2θ (°) = 13.08, 26.66, 28.52, 30.14, 32.70, 35.86, 40.16, 45.54, 47.52, 49.24, 50.88, 53.08, and 54.64, which can be assigned to monetite ($CaHPO_4$, dicalcium phosphate anhydrate, DCPA, ICDD09-0080). In contrast, XRD patterns of $CP^{GAA48}$ show intense reflections at 2θ (°) = 26.18, 28.46, 32.20, 34.00, 39.10, 46.36, 49.48, 53.70, 62.16, and 63.86. They can be assigned to either hydroxyapatite ($Ca_5(OH)(PO_4)_3$, HAP, ICDD01-1008) or chlorapatite ($Ca_5(Cl)(PO_4)_3$, ClAP, ICDD33-0271, ICDD24-0214) but the experimental data match better with ClAP.

The addition of NaOH instead of GAA leads to the formation of HAP or ClAP already after 24 h ($CP^{NaOH24}$); an exact assignment of the reflections at 2θ (°) = 26.02, 28.42, 31.94, ca. 46.6, 49.64, 53.49, and 63.90 is difficult due to the fact that the reflections are very broad and the reflections of HAP and ClAP are very close.

Reflections in the XRD patterns of $CP^{NaOH48}$ at 2θ (°) = 26.14, 28.42, 31.78, ca. 46.88, ca. 49.40, and 53.48 can again be assigned to HAP or ClAP. As the reflections are broader than in the patterns obtained from samples grown with GAA and because the positions of the reflections in HAP and ClAP are very close, it is difficult to make an irrefutable assignment to either HAP or ClAP. No indication of brushite or monetite can however be observed here.

Figure 2 shows representative scanning electron microscopy (SEM) images of the precipitates. With addition of GAA, SEM shows a clear morphological transition between the samples isolated after 24 and 48 h of reaction time, consistent with IR and XRD data. At 24 h, large and thin platelets form. Their size distribution is broad (from ca. 2 to 80 µm) and the crystal shapes are well developed. In most cases the plates are not present as individual platy crystals, but they form dense aggregates and exhibit steps and overgrowth of other crystals. At 48 h, the samples are dense large blocks with thicknesses in the micrometer range. These large blocky features are accompanied by smaller, less densely aggregated nanoparticles with sizes in the 100 to 300 nm range. These particles form small irregular aggregates with diameters of a few micrometers. All features (the large blocks and the less dense aggregates) are composed of smaller nanoparticles in the 100 nm range. These particles appear to be the primary constituents of all larger features observed in the SEM.

In contrast to the samples grown with GAA, the samples grown with NaOH exhibit a relatively uniform morphology, where small particles with sizes of 100 to 200 nm aggregate into larger structures. The main difference between the samples isolated at 24 and 48 h is the increased aggregation of the smaller particles. That is, at longer reaction times, the aggregated features are

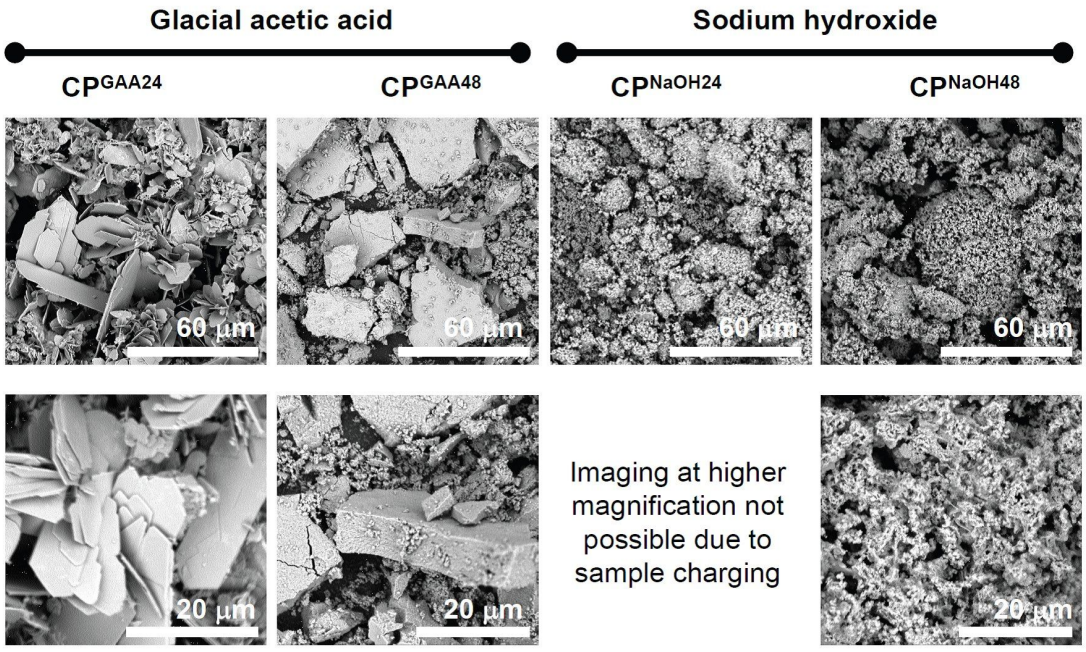


**Figure 2:** Low magnification (top row) and higher magnification (bottom row) SEM images of the precipitates. High magnification imaging of $CP^{NaOH24}$ led to rapid sample charging and very poor imaging conditions even after sputtering; no image is thus shown.

larger and reach tens of microns at 48 h. Moreover, the reaction in the presence of NaOH appears to favor an open structure with interstitial spaces with a few 100 nm to a few microns in diameter. Overall, the sample morphologies of the powders obtained in the presence of NaOH is more uniform than in the samples obtained in the presence of GAA.

Table 2 summarizes data obtained from energy dispersive X-ray spectroscopy (EDXS). The samples grown in the presence of GAA have a Ca/P ratio of 0.8 to 0.9. This is on the order of the Ca/P ratio of 1 in stoichiometric DCPD or DCPA [12,13,56]. Moreover, $CP^{GAA24}$ also contains roughly equivalent amounts of sodium and chlorine, while the amount of chlorine in $CP^{GAA48}$ is higher at around 2.3%. Consequently, the Ca/Cl ratios are slightly different at 8.6 and 6.7, respectively, at 24 and 48 hours of reaction.

Samples grown in the presence of NaOH have a Ca/P ratio of 1.3 to 1.4, which is typical (although at the low end [12,13,56]) for calcium-deficient HAP or ClAP. None of the samples grown with NaOH contains Na in measurable amounts, while the fraction of Cl is on the order of 1%. Consequently, the Ca/Cl ratio is much higher than in the samples grown with GAA.

## Cellulose/calcium phosphate hybrid materials

The neat cellulose used in this study is a white powder. During mineralization, the precipitation of the hybrid materials can be observed visually by the appearance of a solid in the IL. The cellulose/calcium phosphate hybrid (CCPH) materials obtained after mineralization are either white (when synthesized in the presence of NaOH, see experimental part) or light brown (when synthesized in the presence of glacial acetic acid, GAA). This color change may be due to the acid-induced degradation of the

**Table 2:** EDXS data of the precipitates; n.d. = not detected. EDXS does not observe any nitrogen indicative of the ionic liquid. Elemental analysis (EA) finds ca. 1% of carbon. Nitrogen is below the detection limit of the EA instrument (0.3%).

| Sample | Ca [atom %] | P [atom %] | Cl [atom %] | Na [atom %] | N[a] [atom %] | Ca/P | Ca/Cl |
|---|---|---|---|---|---|---|---|
| $CP^{GAA24}$ | 15.6 ± 1.5 | 18.4 ± 0.8 | 1.8 ± 0.8 | 1.7± 0.1 | n.d. | 0.8 ± 0.1 | 8.6 ± 1.8 |
| $CP^{GAA48}$ | 15.4 ± 0.8 | 18.3 ± 0.2 | 2.3 ± 0.1 | 1.3 ± 0.2 | n.d. | 0.9 ± 0.1 | 6.7 ± 2.1 |
| $CP^{NaOH24}$ | 21.6 ± 1.6 | 16.1 ± 0.9 | 1.1 ± 0.2 | n.d. | n.d. | 1.3 ± 0.2 | 19.7 ± 3.3 |
| $CP^{NaOH48}$ | 22.0 ± 0.7 | 15.8 ± 0.1 | 1.2 ± 0.6 | n.d. | n.d. | 1.4 ± 0.1 | 18.3 ± 3.4 |

[a]From elemental analysis.

cellulose by HCl [37,57,58] produced during the mineralization reaction: The reaction of the $CaCl_2$ and $NaH_2PO_4$ yields the desired calcium phosphate precipitate along with NaCl and HCl as side products. While NaOH is able to neutralize some of the HCl formed during the reaction (and thus effectively removes acidic protons from the reaction mixture), GAA will contribute additional protons. The higher amount of protons in the latter case will then lead to a somewhat stronger acid-induced degradation of the cellulose. Alternatively, other degradation reactions of cellulose in ILs have also been reported [59,60]; these could also play a role here. Table 3 summarizes the reaction conditions.

**Table 3:** Reaction conditions for preparation of cellulose calcium phosphate hybrids (CCPH).

| Sample | Additive | Reaction time [h] | Cellulose in IL [wt %] |
|---|---|---|---|
| Neat cellulose | — | — | — |
| CCPH1 | GAA | 24 | 3 |
| CCPH2 | GAA | 48 | 3 |
| CCPH3 | GAA | 24 | 6 |
| CCPH4 | GAA | 24 | 9 |
| CCPH5 | NaOH | 24 | 3 |
| CCPH6 | NaOH | 48 | 3 |
| CCPH7 | NaOH | 24 | 6 |
| CCPH8 | NaOH | 24 | 9 |

Figure 3 shows representative SEM images of the as-received microcrystalline cellulose and cellulose regenerated from the IL 1-butyl-3-methylimidazolium chloride, [Bmim][Cl]. Neat, untreated microcrystalline cellulose consists of heterogeneous and highly aggregated fibers with sizes in the micrometer to hundreds of micrometers range. Regenerated cellulose exhibits a more uniform, less aggregated morphology of intertwined fibers with diameters on the order of tens of microns. This is consistent with other observations on cellulose reconstituted from ILs [34,58,61].

Figure 4 shows SEM images of the CCPH materials obtained after mineralization in the presence of GAA. SEM shows particles with sizes on the order of several hundreds of micrometers that are broken into pieces of several tens of microns with irregular shapes. All samples appear rather dense and no obvious pores can be observed. Moreover, closer inspection shows that the particles and fragments appear to have a layer-like architecture. Finally, the precipitates appear composed of small subunits, possibly of particles with diameters in the nanometer range, but this is, due to significant charging of the samples in the SEM, difficult to evaluate.

Figure 5 shows that the addition of NaOH instead of GAA dramatically alters the product morphology. In contrast to GAA, the addition of NaOH leads to the formation of heterogeneous samples. At low cellulose concentrations (3%, CCPH5 and 6), the samples exhibit prominent round and holey features, presumably composed mostly of the inorganic, calcium phosphate. These features transform into smaller, poorly defined features after 48 h of reaction (CCPH6). The darker matrix material in these samples can be assigned to cellulose, because the brightness in the SEM images is roughly related to the atomic number of the respective region of the sample [62]. At higher cellulose concentrations, the round features are, although still

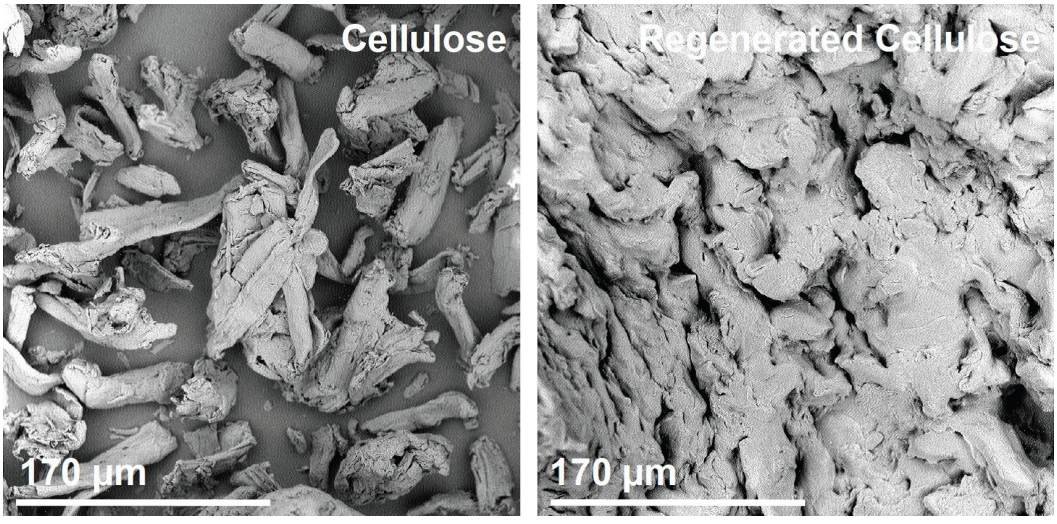


**Figure 3:** SEM images of as-received microcrystalline and regenerated cellulose.

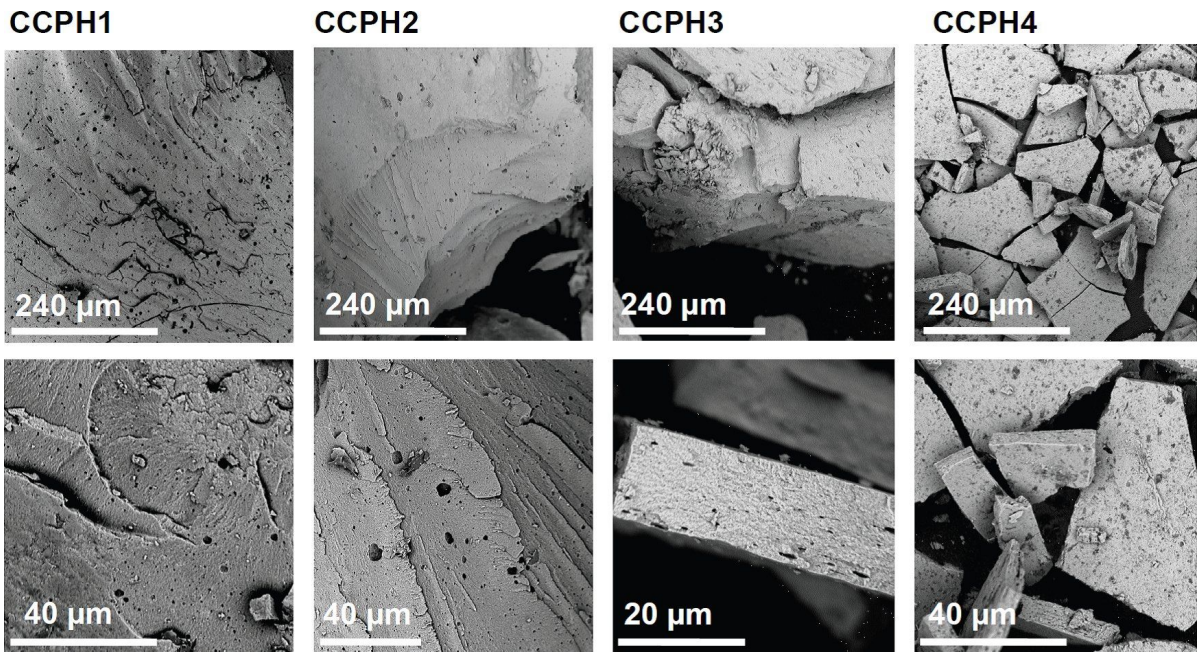


**Figure 4:** Low (top row) and high magnification (bottom row) SEM images of the hybrid materials prepared in the presence of GAA. Note the different scale bar in the lower row for CCPH3.

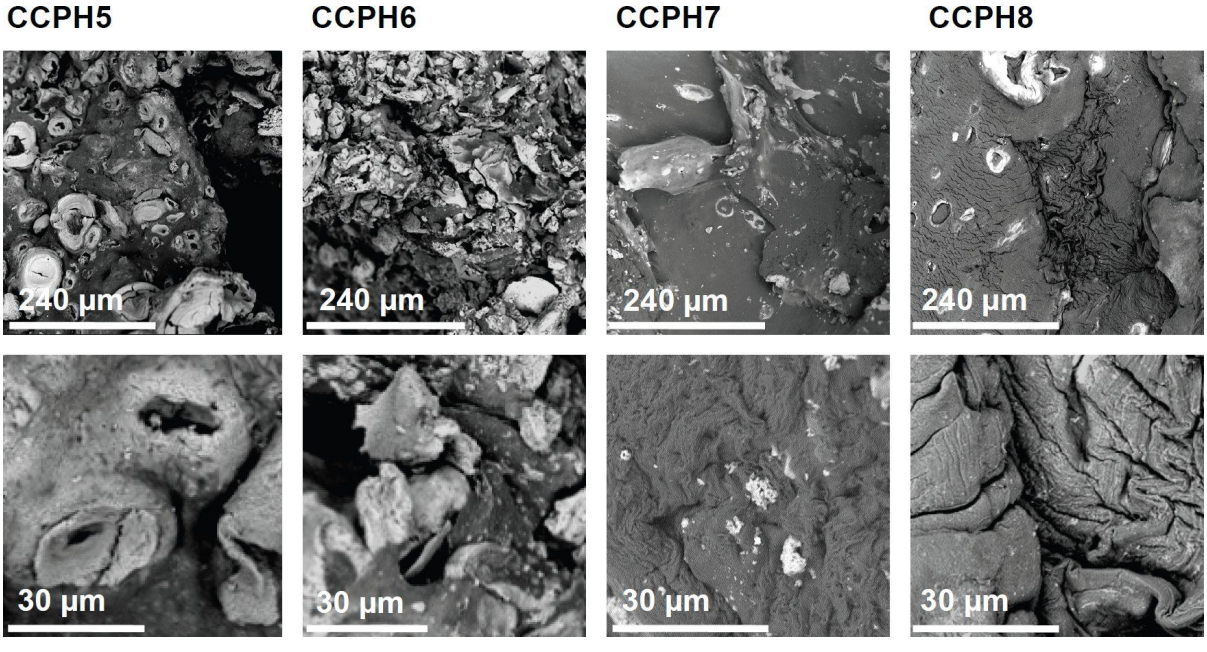


**Figure 5:** Low (top row) and high magnification (bottom row) SEM images of the hybrid materials prepared in the presence of NaOH.

present, much less prominent. In these samples, the morphology is largely defined by a darker background with morphologies similar to pure reconstituted cellulose, Figure 3.

Figure 6 shows representative TEM images of thin sections of GAA and NaOH. Overall, TEM cross-sections show a high conservation of structures between the two different approaches. Samples obtained in the presence of GAA (CCPH1-4) are highly homogeneous and consist of densely packed nanorods with a length on the order of 50–150 nm, that are densely packed, but, unlike a previous example [63], do not exhibit a common preferred orientation. In contrast, samples

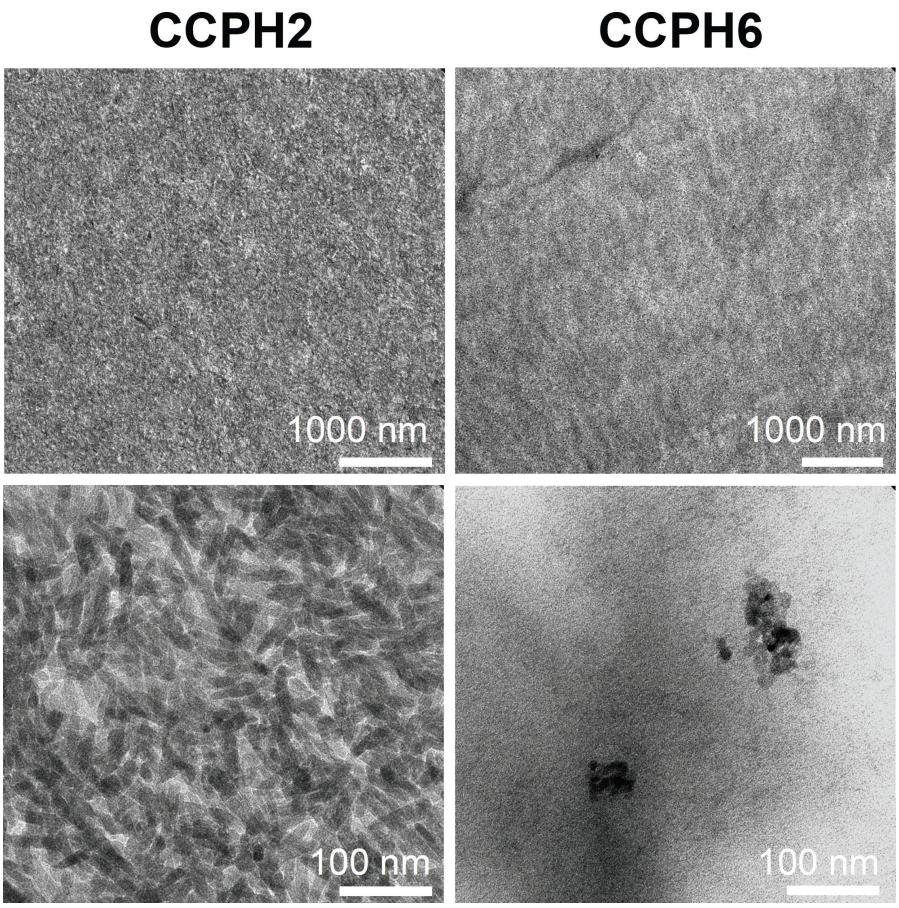


**Figure 6:** TEM images of thin sections of CCPH2 and CCPH6. Top row are low magnification and bottom row are high magnification images of the same samples.

obtained with NaOH (CCPH5-8) appear homogeneous at lower magnifications, but higher magnification imaging clearly reveals their heterogeneous structure. The samples exhibit regions with low degrees of mineralization inorganic particles, sparsely mineralized regions and densely mineralized regions. The individual particles are roughly spherical and have a diameter of around 10–30 nm. Most particles are highly aggregated and form clusters of 100–200 nm in diameter; often also larger aggregates are observed.

Table 4 shows energy-dispersive X-ray spectroscopy (EDXS) data of the samples. The samples prepared with NaOH have Ca/P ratios between 1.2 and 1.3. This ratio is lower than the Ca/P ratio of 1.67 in pure stoichiometric hydroxyapatite (HAP) but Ca/P ratios lower than 1.67 are known for HAP and usually assigned to calcium-deficient apatite. Alternatively, the Ca/P ratios from EDXS could also indicate the formation of amorphous calcium phosphate (Ca/P = 1.5), octacalcium phosphate (OCP, Ca/P = 1.33), or β- or γ-tricalcium phosphate (TCP, Ca/P = 1.5) [13,56,64], or a mixture of phases.

Samples grown in the presence of GAA have a Ca/P ratio of ca. 1 after 24 h of reaction time and ca. 1.2 after 48 h. The Ca/P ratio of ca. 1 is indicative of brushite or monetite, two calcium phosphate phases that precipitate (in aqueous media) at rather low pH. The ratio of 1.2 is rather unspecific and could indicate the formation of most of the above phases, although DCPD and DCPA are usually less prone to forming non-stoichiometric products than the other calcium phosphates.

EDXS also suggests that there are compositional differences between the samples. Generally, the chlorine content of the samples grown with higher cellulose content (CCPH3, 4, 7, 8) appears lower than the content of the samples grown at lower cellulose concentrations (CCPH1, 2, 5, 6). Moreover, EDXS seems to suggest that the chlorine content is slightly higher in the samples grown with NaOH (CCPH5, 6) instead of GAA (CCPH1, 2). These data must however be treated carefully because of their large errors: the standard deviations of most datasets are large and there is a significant overlap of the data;

**Table 4:** EDXS data of the CCPH materials.

| Sample | Ca [atom %] | P [atom %] | Cl [atom %] | Ca/P | Ca/Cl |
|---|---|---|---|---|---|
| stoichiometric HAP | 22.73 | 13.64 | n/a | 1.67 | n/a |
| stoichiometric ClAP (OH completely substituted by Cl) | 23.81 | 14.29 | 4.76 | 1.67 | 5.00 |
| CCPH1 | 18.2 ± 1.3 | 17.8 ± 0.2 | 1.8 ± 1.2 | 1.0 ± 0.06 | 10.1 ± 4.4 |
| CCPH2 | 18.2 ± 2.1 | 17.1 ± 1.1 | 2.5 ± 1.2 | 1.1 ± 0.2 | 7.3 ± 4.7 |
| CCPH3 | 17.1 ± 2.9 | 18.1 ± 1.1 | 1.1 ± 0.2 | 0.9 ± 0.2 | 15.5 ± 5.4 |
| CCPH4 | 16.6 ± 1.1 | 18.4 ± 0.2 | 1.3 ± 1.5 | 0.9 ± 0.1 | 12.7 ± 3.9 |
| CCPH5 | 19.2 ± 0.4 | 16.6 ± 0.5 | 3.2 ± 1.7 | 1.2 ± 0.1 | 6.0 ± 1.4 |
| CCPH6 | 19.4 ± 1.9 | 16.2 ± 0.4 | 3.5 ± 1.8 | 1.2 ± 0.2 | 5.6 ± 1.9 |
| CCPH7 | 19.7 ± 0.5 | 16.7 ± 0.8 | 1.8 ± 1.6 | 1.2 ± 0.1 | 10.9 ± 1.9 |
| CCPH8 | 20.4 ± 1.6 | 16.4 ± 0.8 | 1.5 ± 0.2 | 1.3 ± 0.2 | 13.6 ± 1.6 |

EDXS is thus not able to clearly distinguish between the different samples.

Figure 7 shows representative X-ray elemental maps of all elements detected in energy dispersive X-ray spectroscopy (EDXS), that is, carbon, oxygen, phosphorus, chlorine, and calcium. The maps indicate fairly homogeneous elemental distributions on a hundreds of micrometers length scale even in CCPH5 to CCPH8, which suggests that all materials are uniform over the mm length scale. While carbon (from the cellulose), oxygen (from cellulose and calcium phosphate), phosphorus, and calcium (both from calcium phosphate) can be expected in these samples, the presence of chlorine and its homogeneous distribution throughout the sample is somewhat unexpected but highly reproducible. The fact that the location of the chlorine signal overlaps with the calcium and phosphorus signals suggests that it is also part of the mineral phase, possibly as chloride in chlorapatite.

In spite of the limitations of the EDXS data just discussed, EDXS clearly shows, by way of the low Ca/P ratios, that the samples obtained by mineralization from the IL likely are crystallographically poorly defined. This is supported by powder X-ray diffraction (XRD), which in all cases yields patterns with broad reflections indicative of small crystallites, poor crystallinity, and poor crystallographic correlation, Figure 8.

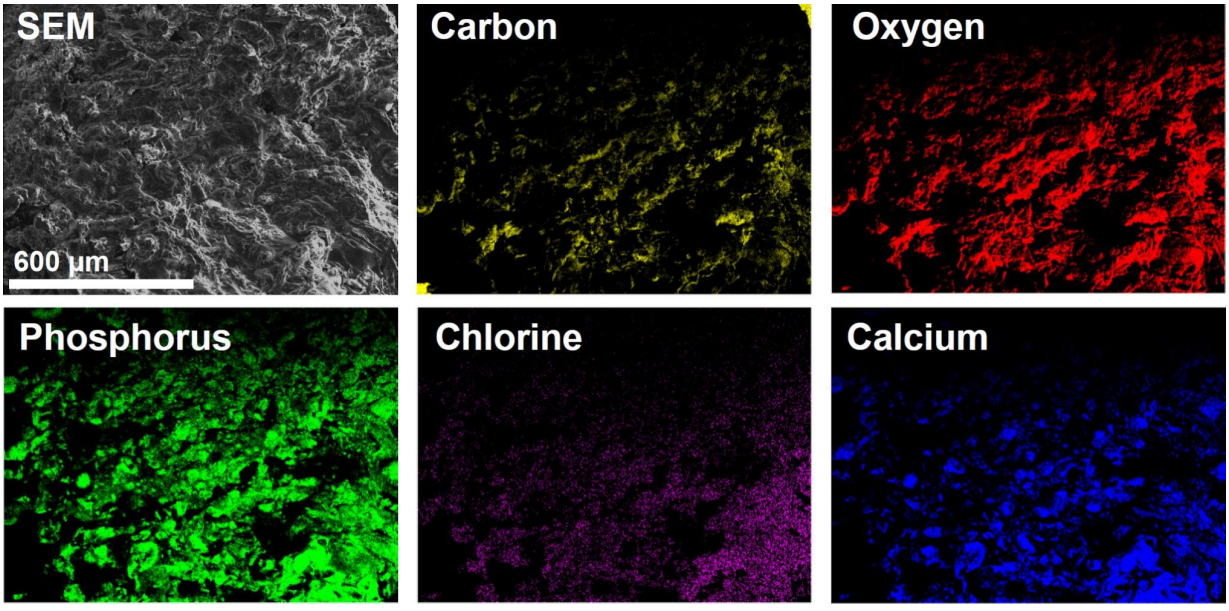


**Figure 7:** SEM image and elemental map of CCPH6.

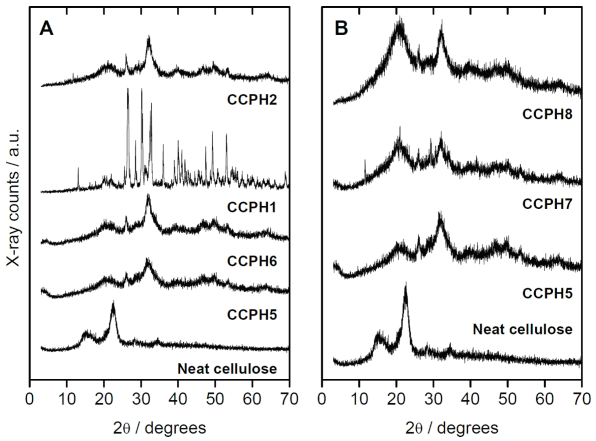


**Figure 8:** XRD patterns of cellulose and mineralized samples. Panel A shows effects of acid or base addition, panel B shows effects of cellulose concentration in the case of the samples grown with NaOH.

Patterns of neat microcrystalline cellulose show reflections at 15.1 and 22.8° 2θ; these can be attributed to the crystalline structure of the cellulose. XRD patterns of all samples show that the order of the cellulose decreases after reconstitution from IL because the cellulose reflections are significantly broader after regeneration.

XRD patterns of samples prepared in the presence of GAA after 24 h show reflections at 2θ (°) = 13.1, 27.0, 30.5, 33.0 and 49.2, which can be assigned to monetite and, possibly, brushite. Patterns of samples obtained after 48 h show reflections at 2θ (°) = 26.0, 28.6, 32.3, 39.0, and 49.4, which can be assigned to HAP or ClAP. Similarly, samples prepared in the presence of NaOH after 24 and 48 h show broad reflections; they can again be assigned to HAP or ClAP. Increasing cellulose concentrations yield in all cases samples consisting of HAP and cellulose.

Figure 9 shows representative attenuated total reflection-Fourier transform infrared (ATR-FTIR) spectra of the samples. Neat cellulose exhibits bands at 3335, 2890, 1427, and 1055 $cm^{-1}$, which can be assigned to the OH, $CH_2$, C–H symmetrical deformation, and C–O–C stretching vibration of cellulose, respectively.

The spectra of the hybrid materials prepared with GAA (CCPH1, 2, 3, and 4) show intense bands at 1031, 1090 $cm^{-1}$ (P–O $\nu_3$), 562, 605 $cm^{-1}$ (P–O $\nu_4$), and 956 $cm^{-1}$ (P–O $\nu_1$), which can be attributed to the presence of $PO_4^{3-}$ and/or $HPO_4^{2-}$ groups. The intensity of the cellulose bands increases with increasing cellulose concentration from 3 to 6 to 9% of cellulose. The weak and broad –OH vibration band at around 3400 $cm^{-1}$ in CCPH1 and CCPH2 is presumably due to the

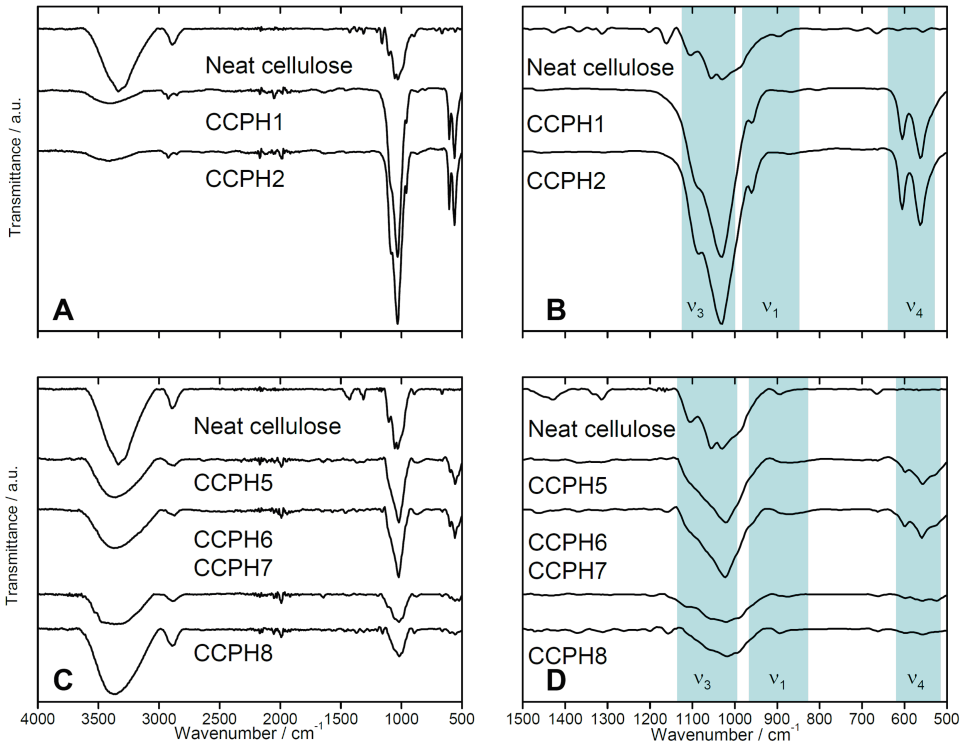


**Figure 9:** ATR-FTIR spectra of neat cellulose, for sample nomenclature see Table 3. Panels B and D are higher magnification views of the region showing the calcium phosphate vibration bands. Spectra are shifted vertically for better visibility.

hydroxyl groups of cellulose, water, and hydroxide ions in the calcium phosphate. The relatively low intensity of the band suggests that (i) the fraction of cellulose is relatively low or that the –OH groups are strongly coordinated to the calcium phosphate and (ii) that the calcium phosphate is low in water or hydroxide content.

In contrast, IR spectra of the samples grown in the presence of NaOH at 3% cellulose concentration (CCPH5, 6) show typical bands associated with apatitic calcium phosphates. Bands at 960 (P–O $\nu_1$), 563 and 601 (P–O $\nu_4$), 1029 and 1095 $cm^{-1}$ (P–O $\nu_3$) [54,55]. However, the calcium phosphate/cellulose hybrids prepared in the presence of NaOH at 6% and 9% of cellulose (CCPH7, 8) show slightly shifted and broadened phosphate bands at 901 (P–O $\nu_1$), 555 and 597 (P–O $\nu_4$), 1014 and 1160 $cm^{-1}$ (P–O $\nu_3$). The intensity of the band at 3360 $cm^{-1}$ suggests that (i) the fraction of cellulose is relatively high or (ii) that the calcium phosphate is relatively high in water or hydroxide content. Moreover, the spectra suggest, by way of the intense cellulose bands mentioned above, that, possibly, the degree of mineralization is lower than in the samples prepared in the presence of GAA. This is qualitatively supported by the fact that especially the intensity of the phosphate vibration bands is fairly low in the samples prepared at higher cellulose concentrations.

Figure 10 shows thermogravimetric analysis/differential thermal analysis (TGA/DTA) data. Table 5 summarizes the results from elemental analysis (CHN analysis) and TGA/DTA. TGA of the neat cellulose finds a weight loss of 96.1%, indicating that even the neat cellulose contains some fraction of non-volatile components. Overall the TGA curve is consistent with earlier data [65] on cellulose decomposition, where a first weight loss of ca. 4.5% is assigned to water desorption below ca. 120 °C. This initial weight loss is followed by the main decomposition step between ca. 280 and 340 °C (accounting for a loss of ca. 78.5%), followed by the final decomposition of the organic and carbonaceous residues up to 600 °C (13.1%). The corresponding DTA data confirms these assignments.

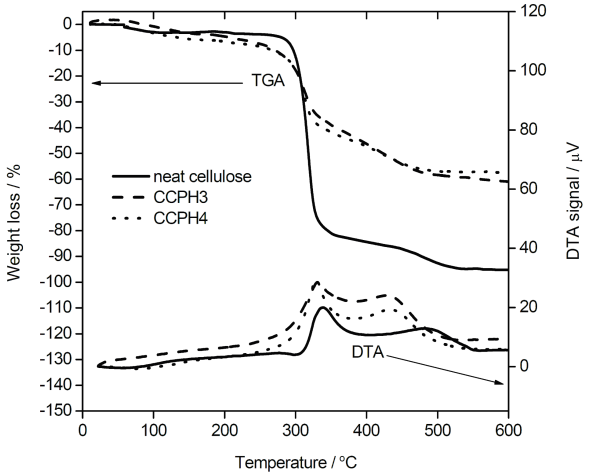


**Figure 10:** Representative TGA and DTA data of select samples. For full data see Table 3.

The same general observation can be made from the TGA/DTA data of all hybrid materials, Table 5. The samples exhibit a first weight loss of a few % assigned to water desorption and drying processes, followed by a two-step, thermally induced and exothermic, decomposition of the organic fraction. The fact that two steps are observed in TGA and two broad and overlapping, but distinct, signals in DTA clearly shows that the decomposition is in all cases a sequential but overlapping process.

**Table 5:** EA and TGA data obtained for CCPHs. No N was detected in EA; the detection limit of the instrument is 0.3%.

| Sample | C & H from EA [%] | | Weight loss at 600 °C [%] (residue) | *T* of step in TGA [°C] | | | Theoretical C & H from TGA[a] [%] | |
|---|---|---|---|---|---|---|---|---|
| | C | H | | Step 1 | Step 2 | Step 3 | C | H |
| Cellulose | 43.18 ± 0.07 | 6.31 ± 0.0 | 96.01 (3.99) | 246 | 350 | 530 | 42.70 | 5.92 |
| CCPH1 | 11.59 ± 0.09 | 1.98 ± 0.08 | 34.71 (65.29) | 218 | 338 | 597 | 13.04 | 2.06 |
| CCPH2 | 21.80 ± 0.30 | 4.10 ± 0.10 | 56.49 (43.51) | 218 | 343 | 596 | 21.90 | 3.35 |
| CCPH3 | 24.46 ± 0.02 | 3.98 ± 0.04 | 59.60 (40.40) | 182 | 333 | 462 | 21.00 | 3.50 |
| CCPH4 | 26.90 ± 0.10 | 5.00 ± 0.10 | 69.30 (30.70) | 183 | 342 | 458 | 25.10 | 4.20 |
| CCPH5 | 23.49 ± 0.10 | 3.99 ± 0.14 | 62.91 (37.09) | 167 | 340 | 597 | 24.53 | 3.73 |
| CCPH6 | 23.00 ± 0.04 | 3.92 ± 0.02 | 57.36 (42.64) | 215 | 368 | 590 | 21.26 | 3.39 |
| CCPH7 | 29.19 ± 0.04 | 4.66 ± 0.04 | 75.98 (24.02) | 249 | 348 | 596 | 27.89 | 4.50 |
| CCPH8 | 32.84 ± 0.23 | 4.79 ± 0.33 | 82.71 (17.29) | 252 | 342 | 593 | 31.94 | 4.89 |

[a]Theoretical amounts C and H were calculated from the fraction of organic material (= cellulose) as determined from TGA. The weight fraction of water (represented by the first weight loss at around 100 °C) was was subtracted and the molecular weight of anhydroglucose was used for calculation.

Table 5 summarizes the results from TGA/DTA and elemental analysis (EA). EA shows that the carbon (= organic) content in the materials obtained in the presence of GAA (CCPH1, 2, 3, and 4) is lower than in the samples obtained with NaOH under the same conditions. This is supported by TGA, which also finds a lower overall weight loss in samples prepared with GAA (ca. 34–57%) than in samples prepared with NaOH (ca. 57–83%). Both EA and TGA therefore indicate that the mineralization in the presence of GAA is more effective in the sense that the fraction of inorganic is higher with the GAA additive than with NaOH. Both TGA and EA also show that, not surprisingly, the organic content in the hybrid materials increases as the initial cellulose concentration in the reaction mixture increases.

As stated in the introduction, calcium phosphate cellulose hybrid materials could be interesting biomaterials. Preliminary attempts to study the biocompatibility with MC3T3-E1 pre-osteoblasts, however, only provided qualitative information because of sample disintegration in the cultivation medium (PBS buffer). Likely this is due to the fact that the materials are quite brittle and tend to rapidly form a powdery product, which is difficult to handle quantitatively in cell assays. In spite of this, qualitative analysis showed that the pre-osteoblasts did proliferate on the hybrid materials. More detailed experiments are underway.

## Discussion

As stated in the introduction, ILs are interesting reaction media for the synthesis of advanced inorganic materials. ILs have, however, not been explored for the synthesis of inorganic biomaterials such as calcium phosphate, possibly for toxicity concerns [66,67]. The only examples the authors are currently aware of is an interesting study by de Zea Bermudez and colleagues, who have reported strong effects on the morphology of calcium carbonate but, interestingly, not on the crystal phase [53].

The current study shows that in all cases investigated here, calcium phosphate can be obtained from [Bmim][Cl]. In analogy to water-based precipitation reactions [12,13,68,69], the addition of an acid, GAA, or a base, NaOH, leads to different crystal phases (likely, one parameter that is significant here, is the presence of water traces). In the presence of GAA, DCPA forms, as can be verified from XRD (Figure 1B). XRD is further supported by FTIR spectroscopy (Figure 1A) which finds no –OH band at 24 h, indicating the formation of DCPA rather than DCPD, consistent with XRD. EDXS (Table 2) further supports these findings as it detects a Ca/P ratio of just below 1. Moreover EDXS also suggests that some sodium and chlorine are present in the samples grown with GAA. Although XRD does not show any indication of NaCl, we have previously observed the formation of minor NaCl fraction in a different system [70]. The formation of NaCl could thus also be possible here, especially because alkali salts are generally poorly soluble in ILs [65]. The low fraction of sodium and chlorine observed in the EDXS data could be due to the fact that the precipitates were washed with water after synthesis and most NaCl would thus have been washed out.

Additionally, both $Na^+$ and $Cl^-$ can also substitute into calcium phosphate; the residual fraction observed in the EDXS could thus also be incorporated in the calcium phosphate crystal lattice, although this is most common in the apatites and not in DCPA formed with GAA [12,13,64,71,72].

Moreover, SEM (Figure 2) shows that the particle size of the crystals grown with GAA after 24 h is orders of magnitude larger than the size of the crystals obtained after 48 h. This is similar to work by Shkilnyy et al. [73] who have shown that calcium phosphate grown from aqueous solution in the presence of poly(ethylene imine) follows a precipitation-redissolution-reprecipitation pathway before forming the final product, HAP nanoparticles with a diameter on the order of 5–10 nm. The current study thus suggests that at least some of the findings from water-based calcium phosphate mineralization studies may have analogies in IL-based precipitation processes; this matter is however still under debate and more work is necessary to understand and quantify the intricacies of precipitation of inorganic matter from ILs.

SEM also shows that the samples grown from GAA-containing ILs are large blocks consisting of nanoparticles with diameters on the order of 100–300 nm. This suggests that the resulting materials could be mesocrystals [74,75]. At the moment this is, however, difficult to asses because the samples are highly unstable under the electron beam during electron diffraction.

In contrast to the samples grown with GAA, samples grown with NaOH are more uniform and SEM (Figure 2) shows the typical nanoparticle morphology that is also observed for calcium phosphate grown from aqueous solution at basic conditions [12,13]. Also consistent with conventional processes in aqueous solutions, XRD and FTIR spectroscopy (Figure 1) show that these precipitates are HAP and ClAP. Likely the reason for ClAP formation is the fact that the IL [Bmim][Cl] contains a high amount of chloride. The formation of Ca-deficient HAP or ClAP is further confirmed by EDXS (Table 2).

Importantly, EA and EDXS find no nitrogen in the precipitates. This suggests that the fraction of IL in the final materials is low. This is important for reasons of toxicity, as outlined above: if

the precipitates synthesized in the current study are to be used in implantation or toothpaste, toxic compounds such as ILs must of course be removed. Apparently the washing process used here is sufficient to remove most of the IL such that no nitrogen (that is, IL cation) can be detected.

As pointed out in the introduction, there is a need for viable, flexible, and robust protocols towards (nano- and mesostructured) carbohydrate/calcium phosphate hybrid materials with the potential for scale-up. While the organic modification of cellulose in ILs has yielded a large number of publications [35,37,40,57] the synthesis of carbohydrate/inorganic hybrid materials from ILs is still in its infancy. The current study therefore addresses the problem by exploiting the potential of [Bmim][Cl] to both dissolve cellulose in significant weight fractions and to yield nanoscale calcium phosphate precipitates. Besides, we have also explored the effects of additives, NaOH and GAA, in the reaction mixture on sample architecture, crystal phase, crystal organization, and sample homogeneity.

SEM (Figures 2, 4, 5) and TEM (Figure 6) show that the additive, GAA vs NaOH, has a dramatic influence on the sample morphology. In the presence of GAA very uniform and highly organized nanoscale hybrid materials are obtained. In contrast, the addition of NaOH leads to heterogeneous sample morphologies with a poorly defined architecture of the inorganic building blocks. EDXS (Table 4) shows that all samples have Ca/P ratios that are lower than expected for stoichiometric HAP, although the initial Ca/P ratio in the reaction mixture was 1.67. In some cases (CCPH1, 2) the ratios of around 1 are indicative of DCPD or DCPA. Moreover, X-ray maps of elemental distribution (Figure 7) confirm SEM by showing that samples precipitated with NaOH are not homogeneous on a micrometer to nanometer scale.

Overall, the homogeneity of the samples precipitated with GAA suggests that here (i) the reaction mixture is homogeneous and nucleation and growth occurs throughout the reaction mixture or (ii) that the GAA molecules act as growth modifiers, possibly by stabilizing intermediates or nuclei which would then again yield the uniform particles observed in the TEM. Indeed, citrate has been suggested as a strong growth modifier for calcium phosphate from aqueous solution [76]. In contrast, the heterogeneity of the samples obtained with NaOH could be due to solubility issues of NaOH in the IL; as ILs are known to only poorly solubilize alkali halides [65]. A similar argument may apply to the case here.

The presence of Cl in all samples is surprising at first, but can be assigned to the fact that the reaction is done in an environment rich in chloride, the IL [Bmim][Cl]. The incorporation of chloride into the precipitates is further confirmed by XRD (Figure 8) because the XRD patterns can – at least partly – be assigned to chlorapatite.

XRD and IR spectroscopy (Figure 9) further show that in the presence of GAA not HAP or ClAP forms initially, but dicalcium phosphate anhydrate (monetite $CaHPO_4$, DCPA). This is interesting because DCPA is a calcium phosphate phase that (in water) forms at relatively low pH values of around 5 [64,68,71,72]. This suggests that at least some of the growth of calcium phosphate in ILs, such as the effects of pH in water vs the presence of protons or hydroxide ions in IL, could be similar, but this claim will need further investigation.

The seeming discrepancy between the observation, that in the current work DCPA forms instead DCPD (which would be expected in aqueous media), can be resolved by the fact that the materials investigated in the current study were synthesized at 80 °C. At this temperature, DCPA also forms in aqueous media [68].

This observation, however, points to an issue with the current system. While most carbohydrates are fairly stable against temperature, it may for other reasons be desirable to operate at lower temperatures. To achieve this, [Bmim][Cl] is, due to its high melting point, not well suited. Other ILs such as acetates or formates would likely be more suitable candidates.

TGA/DTA (Figure 10, Table 5) and IR spectroscopy (Figure 9) show that the mineralization of calcium phosphate in the presence of NaOH yields materials with significantly lower degrees of mineralization than in the presence of GAA. This is different from aqueous systems, where the solubility product of HAP (formed at high pH) is significantly lower than that of DCPA (formed at low pH). Here the current study shows that concepts known from mineralization of calcium phosphate in aqueous media cannot in all cases directly be transferred to ILs. While both in water and ILs, higher temperatures seem to favor the formation of DCPA over DCPD, the higher degree of mineralization is somewhat counterintuitive when drawing inspiration from aqueous media: the reason for the higher mineralization level of the samples grown in the presence of GAA could well be related to issues of solubility products of the respective calcium phosphates in [Bmim][Cl] and these could be significantly different than in aqueous solution.

Finally it is important to address the aspect of biocompatibility and cytotoxicity. ILs are nowadays (after an initial phase, where this aspect was completely ignored) regarded as moderately toxic. This is mostly due to the fact that (i) many ILs either have long alkyl tails on the cation or that (ii) some of the anions such

as $PF_6^-$ can degrade and form, among others, hydrofluoric acid, which is toxic [65,66]. In spite of this, the current data show that the extraction process used for sample purification is suitable to produce materials free of IL: neither EA (Table 5) nor EDXS (which is less sensitive, Table 2 and Table 4) detected any nitrogen in the current samples. As nitrogen is only present in the IL cation, this indicates that no more imidazolium moieties are present in the final, purified materials. Indeed, preliminary tests with MC3T3-E1 cells show that they proliferate on our materials without significant damage. This thus shows that IL-based synthesis protocols are also viable for biomaterials development.

## Conclusion

The current study presents a new approach towards true carbohydrate/calcium phosphate hybrid materials with a highly ordered, uniform, and chemically well defined mesostructure. The study has three key findings: (i) the use of suitable ILs enables the synthesis of hybrid materials with carbohydrates that have so far not been accessible for the formation of true nanoscale architectures in hybrid materials research, (ii) the addition of an acid or a base dramatically affects the outcome of materials synthesis; these data also suggest that some, but by far not all, concepts of calcium phosphate growth known from aqueous media can be transferred to ILs. Much more work is however needed to understand the processes leading to the observed morphologies. (iii) Soxleth extraction with a suitable solvent is a viable method for producing essentially IL-free hybrid materials that could find use in hard tissue repair or other fields. Clearly, as stated throughout the discussion, there are numerous open questions both with respect to synthesis optimization and the fundamentals of materials formation from ILs. This article is but the start down this interesting and promising new avenue of materials research and development.

## Acknowledgements

We thank Ms. C. Pilz-Allen (funded by the Biomaterials Department, MPI of Colloids and Interfaces) for generously supporting us with the cell culture experiments. We thank the University of Potsdam for financial support. A.S. acknowledges a Channel Fellowship awarded by the Egyptian Government.

## References

1. Ravi Kumar, M. N. V. *React. Funct. Polym.* **2000,** *46,* 1. doi:10.1016/S1381-5148(00)00038-9
2. Mohanty, A. K.; Misra, M.; Hinrichsen, G. *Macromol. Mater. Eng.* **2000,** *276-277,* 1–24. doi:10.1002/(SICI)1439-2054(20000301)276:1<1::AID-MAME1>3.0.CO;2-W
3. Klemm, D.; Heublein, B.; Fink, H.; Bohn, A. *Angew. Chem., Int. Ed.* **2005,** *44,* 3358. doi:10.1002/anie.200460587
4. Eichhorn, S. J.; Dufresne, A.; Aranguren, M.; Marcovich, N. E.; Capadona, J. R.; Rowan, S. J.; Weder, C.; Thielemans, W.; Roman, M.; Renneckar, S.; Gindl, W.; Veigel, S.; Keckes, J.; Yano, H.; Abe, K.; Nogi, M.; Nakagaito, A. N.; Mangalam, A.; Simonsen, J.; Benight, A. S.; Bismarck, A.; Berglund, L. A.; Peijs, T. *J. Mater. Sci.* **2009,** *45,* 1. doi:10.1007/s10853-009-3874-0
5. Epple, M., Ed. *Biomaterialien und Biomineralisation;* Teubner: Suttgart-Leipzig-Wiesbaden, 2003; Vol. 1.
6. Bäuerlein, E. *Biomineralization - Progress in Biology, Molecular Biology and Application,* 1st ed.; Wiley-VCH: Weinheim, 2004.
7. Cölfen, H.; Antonietti, M. *Mesocrystals and Nonclassical Crystallization: New Self-assembled Structures;* John Wiley & Sons: Chichester, 2008. doi:10.1002/9780470994603
8. Cölfen, H.; Mann, S. *Angew. Chem., Int. Ed.* **2003,** *42,* 2350. doi:10.1002/anie.200200562
9. Lannutti, J.; Reneker, D.; Ma, T.; Tomasko, D. F. *Mater. Sci. Eng., C* **2007,** *27,* 504. doi:10.1016/j.msec.2006.05.019
10. *Handbook of Biomineralization.;* Wiley-VCH: Weinheim, 2007.
11. Rodríguez, K.; Renneckar, S.; Gatenholm, P. *ACS Appl. Mater. Interfaces* **2011,** *3,* 681. doi:10.1021/am100972r
12. Bleek, K.; Taubert, A. *Acta Biomater.* **2013,** *9,* 6283. doi:10.1016/j.actbio.2012.12.027
13. Schweizer, S.; Taubert, A. *Macromol. Biosci.* **2007,** *7,* 1085. doi:10.1002/mabi.200600283
14. Falini, G.; Fermani, S.; Ripamonti, A. *J. Inorg. Biochem.* **2001,** *84,* 255. doi:10.1016/S0162-0134(01)00169-6
15. Falini, G.; Fermani, S.; Ripamonti, A. *J. Inorg. Biochem.* **2002,** *91,* 475. doi:10.1016/S0162-0134(02)00471-3
16. Schweizer, S.; Schuster, T.; Junginger, M.; Siekmeyer, G.; Taubert, A. *Macromol. Mater. Eng.* **2010,** *295,* 535. doi:10.1002/mame.200900347
17. Rusu, V. M.; Ng, C.-H.; Wilke, M.; Tiersch, B.; Fratzl, P.; Peter, M. G. *Biomaterials* **2005,** *26,* 5414–5426. doi:10.1016/j.biomaterials.2005.01.051
18. Danilchenko, S. N.; Kalinkevich, O. V.; Pogorelov, M. V.; Kalinkevich, A. N.; Sklyar, A. M.; Kalinichenko, T. G.; Ilyashenko, V. Y.; Starikov, V. V.; Bumeyster, V. I.; Sikora, V. Z.; Sukhodub, L. F. *J. Biomed. Mater. Res., Part A* **2011,** *96,* 639. doi:10.1002/jbm.a.33017
19. Chiono, V.; Gentile, P.; Boccafoschi, F.; Carmagnola, I.; Ninov, M.; Georgieva, V.; Georgiev, G.; Ciardelli, G. *Biomacromolecules* **2010,** *11,* 309–315. doi:10.1021/bm901169v
20. Dogan, O.; Öner, M.; Cinel, O. *J. Ceram. Soc. Jpn.* **2010,** *1118,* 579–586. doi:10.2109/jcersj2.118.579
21. Thula, T. T.; Svedlund, F.; Rodriguez, D. E.; Podschun, J.; Pendi, L.; Gower, L. P. *Polymers (Basel, Switz.)* **2011,** *3,* 10–35. doi:10.3390/polym3010010
22. Liuyun, J.; Yubao, L.; Chengdong, X. *J. Biomed. Sci.* **2009,** *16,* 65. doi:10.1186/1423-0127-16-65
23. Kovtun, A.; Kozlova, D.; Ganesan, K.; Biewald, C.; Seipold, N.; Gaengler, P.; Arnold, W. H.; Epple, M. *RSC Adv.* **2012,** *2,* 870–875. doi:10.1039/c1ra00955a
24. Granja, P. L.; Barbosa, M. A.; Pouységu, L.; de Jéso, B.; Rouais, F.; Baquey, C. *J. Mater. Sci.* **2001,** *36,* 2163. doi:10.1023/A:1017587815583
25. Granja, P. L.; de Jéso, B.; Bareille, R.; Rouais, F.; Baquey, C.; Barbosa, M. A. *Eur. Cells Mater.* **2005,** *10,* 31.
26. Granja, P. L.; Ribeiro, C. C.; de Jéso, B.; Baquey, C.; Barbosa, M. A. *J. Mater. Sci.: Mater. Med.* **2001,** *12,* 785. doi:10.1023/A:1013960601330

27. Liebner, F.; Dunareanu, R.; Opietnik, M.; Haimer, E.; Wendland, M.; Werner, C.; Maitz, M.; Seib, P.; Neouze, M.-A.; Potthast, A.; Rosenau, T. *Holzforschung* **2012,** *66,* 317. doi:10.1515/hf.2011.163
28. Nge, T. T.; Sugiyama, J. *J. Biomed. Mater. Res., Part A* **2007,** *81,* 124. doi:10.1002/jbm.a.31020
29. Higashi, K.; Kondo, T. *Cellulose* **2012,** *19,* 81. doi:10.1007/s10570-011-9627-7
30. Hong, L.; Wang, Y. L.; Jia, S. R.; Huang, Y.; Gao, C.; Wan, Y. Z. *Mater. Lett.* **2006,** *60,* 1710. doi:10.1016/j.matlet.2005.12.004
31. Cromme, P.; Zollfrank, C.; Müller, L.; Müller, F. A.; Greil, P. *Mater. Sci. Eng., C* **2007,** *27,* 1. doi:10.1016/j.msec.2005.11.001
32. Wan, Y. Z.; Huang, Y.; Yuan, C. D.; Raman, S.; Zhu, Y.; Jiang, H. J.; He, F.; Gao, C. *Mater. Sci. Eng., C* **2007,** *27,* 855. doi:10.1016/j.msec.2006.10.002
33. Ma, M.-G.; Zhu, J.-F.; Jia, N.; Li, S.-M.; Sun, R.-C.; Cao, S.-W.; Chen, F. *Carbohydr. Res.* **2010,** *345,* 1046. doi:10.1016/j.carres.2010.03.004
34. Swatloski, R. P.; Spear, S. K.; Holbrey, J. D.; Rogers, R. D. *J. Am. Chem. Soc.* **2002,** *124,* 4974. doi:10.1021/ja025790m
35. Plechkova, N. V.; Seddon, K. R. *Chem. Soc. Rev.* **2008,** *37,* 123. doi:10.1039/b006677j
36. Heinze, T.; Liebert, T. *Prog. Polym. Sci.* **2001,** *26,* 1689. doi:10.1016/S0079-6700(01)00022-3
37. Zhu, S.; Wu, Y.; Chen, Q.; Yu, Z.; Wang, C.; Jin, S.; Ding, Y.; Wu, G. *Green Chem.* **2006,** *8,* 325. doi:10.1039/b601395c
38. Xie, H.; Zhang, S.; Li, S. *Green Chem.* **2006,** *8,* 630. doi:10.1039/b517297g
39. El Seoud, O. A.; Koschella, A.; Fidale, L. C.; Dorn, S.; Heinze, T. *Biomacromolecules* **2007,** *8,* 2629. doi:10.1021/bm070062i
40. Pinkert, A.; Marsh, K. N.; Pang, S. S.; Staiger, M. P. *Chem. Rev.* **2009,** *109,* 6712–6728. doi:10.1021/cr9001947
41. Taubert, A. *Acta Chim. Slov.* **2005,** *52,* 183.
42. Taubert, A. In *Nanomaterials: Inorganic and Bioinorganic Perspectives,* 2nd ed.; Lukehart, C. M.; Scott, R. A., Eds.; John Wiley & Sons: New York, 2008; pp 369–380.
43. Taubert, A.; Li, Z. *Dalton Trans.* **2007,** *7,* 723. doi:10.1039/b616593a
44. Morris, R. E. *Angew. Chem., Int. Ed.* **2008,** *47,* 442. doi:10.1002/anie.200704888
45. Parnham, E. R.; Morris, R. E. *Acc. Chem. Res.* **2007,** *40,* 1005. doi:10.1021/ar700025k
46. Mumalo-Djokic, D.; Stern, W. B.; Taubert, A. *Cryst. Growth Des.* **2008,** *8,* 330. doi:10.1021/cg0701372
47. Venkataramanan, N. S.; Matsui, K.; Kawanami, H.; Ikushima, Y. *Green Chem.* **2007,** *9,* 18. doi:10.1039/b609887h
48. Amarasekara, A. S.; Owereh, O. S. *Carbohydr. Polym.* **2009,** *78,* 635. doi:10.1016/j.carbpol.2009.05.032
49. Ma, M.-G.; Dong, Y.-Y.; Fu, L.-H.; Li, S.-M.; Sun, R.-C. *Carbohydr. Polym.* **2013,** *92,* 1669. doi:10.1016/j.carbpol.2012.11.034
50. Ma, M.-G.; Qing, S.-J.; Li, S.-M.; Zhu, J.-F.; Fu, L.-H.; Sun, R.-C. *Carbohydr. Polym.* **2013,** *91,* 162. doi:10.1016/j.carbpol.2012.08.025
51. Jia, N.; Li, S.-M.; Ma, M.-G.; Sun, R.-C.; Zhu, L. *Carbohydr. Res.* **2011,** *346,* 2970. doi:10.1016/j.carres.2011.10.006
52. Tsioptsias, C.; Panayiotou, C. *Carbohydr. Polym.* **2008,** *74,* 99. doi:10.1016/j.carbpol.2008.01.022
53. Fernandes, M.; Almeida Paz, F. A.; de Zea Bermudez, V. *Eur. J. Inorg. Chem.* **2012,** *2012,* 2183. doi:10.1002/ejic.201101228
54. Osaka, A.; Miura, Y.; Takeuchi, K.; Asada, M.; Takahashi, K. *J. Mater. Sci.: Mater. Med.* **1991,** *2,* 51. doi:10.1007/BF00701687
55. Cazalbou, S.; Combes, C.; Eichert, D.; Rey, C. *J. Mater. Chem.* **2004,** *14,* 2148. doi:10.1039/b401318b
56. Amjad, Z. *Calcium Phosphates in Biological and Industrial Systems,* 1st ed.; Springer: New York, 1998.
57. Olivier-Bourbigou, H.; Magna, L.; Morvan, D. *Appl. Catal., A* **2010,** *373,* 1–56. doi:10.1016/j.apcata.2009.10.008
58. Turner, M. B.; Spear, S. K.; Holbrey, J. D.; Rogers, R. D. *Biomacromolecules* **2004,** *5,* 1379. doi:10.1021/bm049748q
59. Heinze, T.; Schwikal, K.; Barthel, S. *Macromol. Biosci.* **2005,** *5,* 520. doi:10.1002/mabi.200500039
60. Vitz, J.; Erdmenger, T.; Haensch, C.; Schubert, U. S. *Green Chem.* **2009,** *11,* 417. doi:10.1039/b818061j
61. Yuan, T.-Q.; Wang, W.; Zhang, L.-M.; Xu, F.; Sun, R.-C. *Biotechnol. Bioeng.* **2013,** *110,* 729–736. doi:10.1002/bit.24743
62. Williams, D. B.; Carter, C. E. *Transmission Electron Microscopy-A Textbook for Materials Science;* Plenum Press: New York, London, 1996. doi:10.1007/978-1-4757-2519-3
63. Shkilnyy, A.; Brandt, J.; Mantion, A.; Paris, O.; Schlaad, H.; Taubert, A. *Chem. Mater.* **2009,** *21,* 1572. doi:10.1021/cm803244z
64. Dorozhkin, S. V. *Materials* **2009,** *2,* 399–498. doi:10.3390/ma2020399
65. Taubert, A. *Top. Curr. Chem.* **2009,** *290,* 127. doi:10.1007/128_2008_34
66. Zhao, D.; Liao, Y.; Zhang, Z. *Clean: Soil, Air, Water* **2007,** *35,* 42–48. doi:10.1002/clen.200600015
67. Pham, T. P. T.; Cho, C.-W.; Yun, Y.-S. *Water Res.* **2010,** *44,* 352–372. doi:10.1016/j.watres.2009.09.030
68. *Calcium Phosphates in Biological and Industrial Systems;* Kluwer Academic Publishers: Norwell-Dordrecht, 1998.
69. Amjad, Z. *Phosphorus Res. Bull.* **2005,** *18,* 1.
70. Junginger, M.; Kübel, C.; Schacher, F. H.; Müller, A. H. E.; Taubert, A. *RSC Adv.* **2013,** *3,* 11301. doi:10.1039/c3ra23348k
71. Dorozhkin, S. V. *J. Mater. Sci.* **2007,** *42,* 1061–1095. doi:10.1007/s10853-006-1467-8
72. Dorozhkin, S. V. *J. Mater. Sci.* **2008,** *43,* 3028–3057. doi:10.1007/s10853-008-2527-z
73. Shkilnyy, A.; Schöne, S.; Rumplasch, C.; Uhlmann, A.; Hedderich, A.; Günter, C.; Taubert, A. *Colloid Polym. Sci.* **2011,** *289,* 881. doi:10.1007/s00396-011-2403-2
74. Cölfen, H.; Antonietti, M. *Angew. Chem., Int. Ed.* **2005,** *44,* 5576. doi:10.1002/anie.200500496
75. Niederberger, M.; Cölfen, H. *Phys. Chem. Chem. Phys.* **2006,** *8,* 3271. doi:10.1039/b604589h
76. Hu, Y.-Y.; Rawal, A.; Schmidt-Rohr, K. *Proc. Natl. Acad. Sci. U. S. A.* **2010,** *107,* 22425–22429. doi:10.1073/pnas.1009219107

BEILSTEIN JOURNAL OF NANOTECHNOLOGY

# Nanocrystalline ceria coatings on solid oxide fuel cell anodes: the role of organic surfactant pretreatments on coating microstructures and sulfur tolerance

Chieh-Chun Wu, Ling Tang and Mark R. De Guire*

Full Research Paper

Open Access

Address:
Department of Materials Science and Engineering, Case Western Reserve University, 10900 Euclid Avenue, Cleveland, Ohio, 44106-7204, USA

Email:
Mark R. De Guire* - mrd2@case.edu

* Corresponding author

Keywords:
cerium(IV) oxide; microstructure; organic self-assembled monolayers; solid oxide fuel cells; sulfur tolerance

*Beilstein J. Nanotechnol.* **2014,** *5,* 1712–1724.
doi:10.3762/bjnano.5.181

Received: 31 May 2014
Accepted: 12 September 2014
Published: 06 October 2014

This article is part of the Thematic Series "Towards multifunctional inorganic materials: biopolymeric templates".

Guest Editors: C. Steinem and J. Bill



## Abstract

Treatments with organic surfactants, followed by the deposition of nanocrystalline ceria coatings from aqueous solution, were applied to anodes of solid oxide fuel cells. The cells were then operated in hydrogen/nitrogen fuel streams with $H_2S$ contents ranging from 0 to 500 ppm. Two surfactant treatments were studied: immersion in dodecanethiol, and a multi-step conversion of a siloxy-anchored alkyl bromide to a sulfonate functionality. The ceria coatings deposited after the thiol pretreatment, and on anodes with no pretreatment, were continuous and uniform, with thicknesses of 60–170 nm and 100–140 nm, respectively, and those cells exhibited better lifetime performance and sulfur tolerance compared to cells with untreated anodes and anodes with ceria coatings deposited after the sulfonate pretreatment. Possible explanations for the effects of the treatments on the structure of the coatings, and for the effects of the coatings on the performance of the cells, are discussed.

## Introduction

Fuel cells convert chemical energy directly to electrical energy. Compared to conventional power sources, fuel cells offer higher efficiencies, lower emissions, modular installation scalable from milliwatts to megawatts, and distributed power generation to reduce transmission losses [1]. Among fuel cell technologies, solid oxide fuel cells (SOFCs) offer unique benefits [1,2]. They run not only on hydrogen, but also on widely available hydrocarbon fuels. They need little or no precious-metal catalysts. They provide high-quality utility-grade heat, which in combination with electrical efficiencies of up to 60% leads to total system efficiencies of 80–85%, exceeding conventional power sources. SOFCs thus have tremendous potential to meet rising global demand for electrical energy more efficiently and with lower environmental impact than conventional power sources.

A fuel cell consists of a dense ionically conducting layer (electrolyte) with porous electronically conducting layers (the electrodes) on each side, separating the fuel (e.g., $H_2$) from its oxidant (typically $O_2$ in air). In typical solid oxide fuel cells (SOFCs), oxygen molecules are reduced to oxide ions at the air electrode (the cathode) by electrons from the external circuit. The oxide ions cross the electrolyte and combine with $H_2$ at the fuel electrode (the anode, the focus of the present study) to form $H_2O$, releasing electrons into an external circuit to do electrical work before they pass to the cathode for consumption in the oxygen reduction reaction.

It is well known that the performance of SOFC anodes, typically composites of nickel metal with a zirconia or ceria ionic conductor, is degraded by sulfur impurities in the fuel, severely reducing both the power generated by the cell and its operating lifetime. (For recent reviews, see [3,4].) The extent and permanence of this "sulfur poisoning" varies with operating temperature, current density, sulfur concentration (as low as a few ppm), and anode materials [5-12]. Current consensus holds that adsorption of sulfur onto the nickel surface [13] may impede the ability of nickel to catalyze the oxidation of hydrogen [9,14-16]. Understanding sulfur poisoning is crucial to developing SOFCs that could operate on commercial, sulfur-containing hydrocarbon fuels (such as diesel and aeronautical fuels) and fuels derived from sulfur-containing sources such as coal.

Studies [17-21] have shown that incorporating ceria into the anode, either to replace yttria-stabilized zirconia (YSZ) as the ionic conductor or infiltrated into a porous anode structure, can lead to the reduction or elimination of sulfur poisoning. The procedures used by other groups to infiltrate ceria into SOFC anodes usually involve immersing the anodes into a precursor solution, e.g., of cerium nitrate [16,18,22-24] or through a sol–gel route [25]. After drying and high-temperature treatment, a ceramic film results.

Recent developments in the aqueous-phase deposition of functional oxides [26] can lead to a greater degree of control over the properties and morphology of films on SOFC anodes. Specifically, the surfaces of a commercial SOFC anode were treated with surfactants prior to immersion in an aqueous precursor solution [27]. By this approach, a nanocrystalline ceria film was formed without further heat treatment. The thickness of the film and its morphology and distribution within the microstructure of the porous SOFC anode depended significantly on the type of pretreatment used.

The present research sought to distinguish sulfur tolerance due to replacing YSZ with ceria from that due to protecting Ni from sulfur exposure. Few studies of sulfur poisoning have characterized the microstructural changes associated with the loss of performance [6,19,20,28]. In the present work the microstructural changes and the degree of sulfur tolerance were related to the presence or absence of the ceria coating, its morphology (which depended on the prior surfactant treatment), and the extent of sulfur exposure.

## Results

First we illustrate general characteristics of the performance of the cells in sulfur-containing environments. Then SEM and EDXS analyses of the microstructures of the cells, before and after operation, with and without surfactant pretreatments are presented. The performance of the cells, grouped by type of anode treatment, is then discussed to show correlations between surfactant treatment, coating characteristics, and cell performance. The anode treatments were of four types:

- Treatment 1: no ceria coating or surfactant treatment
- Treatment 2: ceria coating with no surfactant treatment (direct-treated)
- Treatment 3: ceria coating after thiol surfactant treatment
- Treatment 4: ceria coating after sulfonate surfactant treatment

### Effects of sulfur exposure on cell performance

The initial value of current density for each cell was chosen to give an output voltage of 0.7 V. If voltage dropped by more than 10% in a 24 h period, the current density was reduced to raise the voltage back to 0.7 V. Common measures of SOFC performance are the change in output voltage over time at a fixed current density, and area specific resistance (ASR, units of $\Omega \cdot cm^2$).

Figure 1 shows the change in output voltage and ASR in a cell with no ceria coating (treatment 1) running on $H_2/N_2$ fuel at 107 $mA \cdot cm^{-2}$ (8.4% fuel utilization) throughout the 192 h test. This cell exhibited sulfur tolerance, i.e., only a gradual loss in power (no worse than that observed in sulfur-free fuel in the first 24 h of operation) throughout the test, though $H_2S$ levels progressively increased from 0 and 500 ppm in 24 h intervals. Such behavior was observed in many cells operated at current densities below 200 $mA \cdot cm^{-2}$, regardless of the presence or absence of a ceria coating.

Figure 2 shows the change in output voltage and ASR in a treatment-3 cell operating while $H_2S$ levels alternated between 0 and 50 ppm in 24 h periods. The current density of 214 $mA \cdot cm^{-2}$ corresponded to fuel utilization of 16.7%. This test showed several hallmarks of sulfur poisoning [4,5,7,10]:

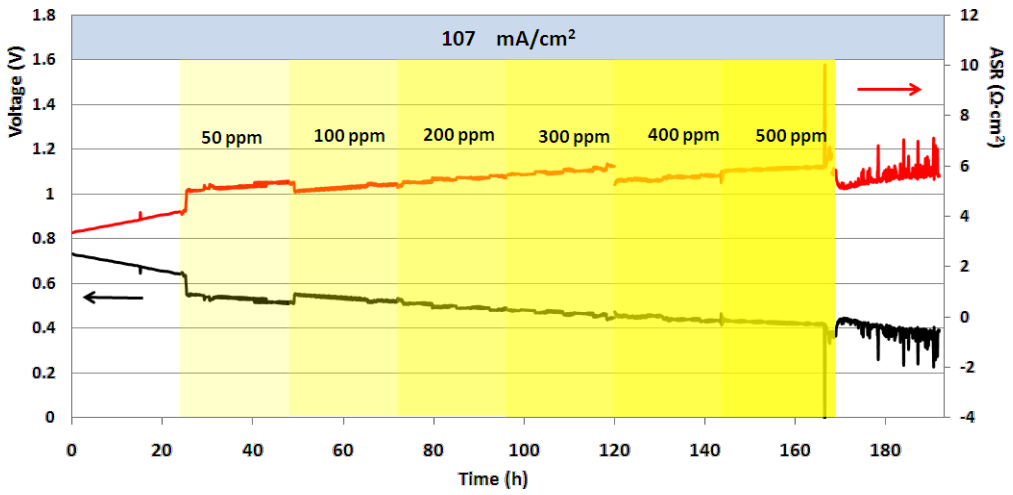


**Figure 1:** Output voltage and ASR at low current density, showing sulfur tolerance. Yellow shading denotes 24 h periods of $H_2S$ exposure in the anode stream at the concentration indicated. (Treatment-1 cell (no ceria coating) with no interlayer.)

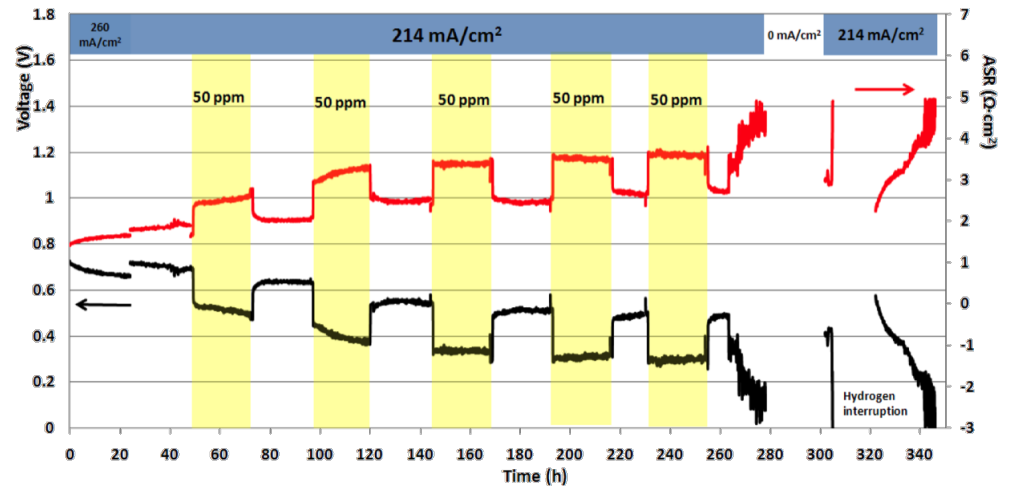


**Figure 2:** Output voltage and ASR, showing typical effects of partially reversible sulfur poisoning. Yellow bands denote periods of $H_2S$ exposure in the anode stream at the concentration indicated. (Treatment 3 cell, no interlayer.)

- a sharp initial drop in voltage on adding 50 ppm $H_2S$ to the fuel stream;
- a slower decrease in voltage on continued operation under constant atmosphere;
- recovery of most of the lost output voltage on reducing the $H_2S$ level to 0 ppm;
- overall decline in output voltage at constant current density, and a progressive rise in ASR (from 1.3 Ω·cm$^2$ to 4.8 Ω·cm$^2$) over the duration of the test.

This behavior was typical for many cells operated at current densities above about 200 mA·cm$^{-2}$ [12], whether ceria-coated or not. In general, exposure to $H_2S$ led to shorter operating lifetimes and/or lower power (see Figure 12 below), resulting in lower total lifetime energy output.

Figure 3 underscores the significance of current density in the appearance of sulfur poisoning in the present study. It shows the change in output voltage and ASR in a treatment-4 cell that exhibited both sulfur tolerance at a current density of 150 mA·cm$^{-2}$ (24–192 h) and partially reversible sulfur poisoning at 179–200 mA·cm$^{-2}$ (192–456 h).

Figure 4 shows the voltage output versus time of a treatment-2 cell that initially showed high sulfur tolerance, with little change in voltage or ASR on exposure to 50 ppm of $H_2S$ at high

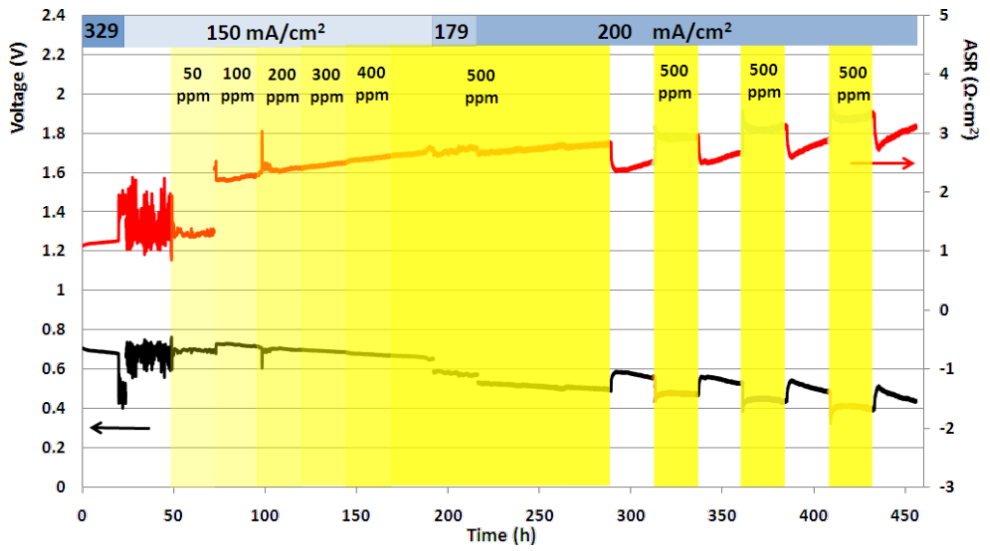


**Figure 3:** Output voltage and ASR, showing sulfur tolerance at a current density below 200 mA·cm$^{-2}$ (24–192 h) and partially reversible sulfur poisoning at 200 mA·cm$^{-2}$ (192–456 h). (Treatment-4 cell, no interlayer.)

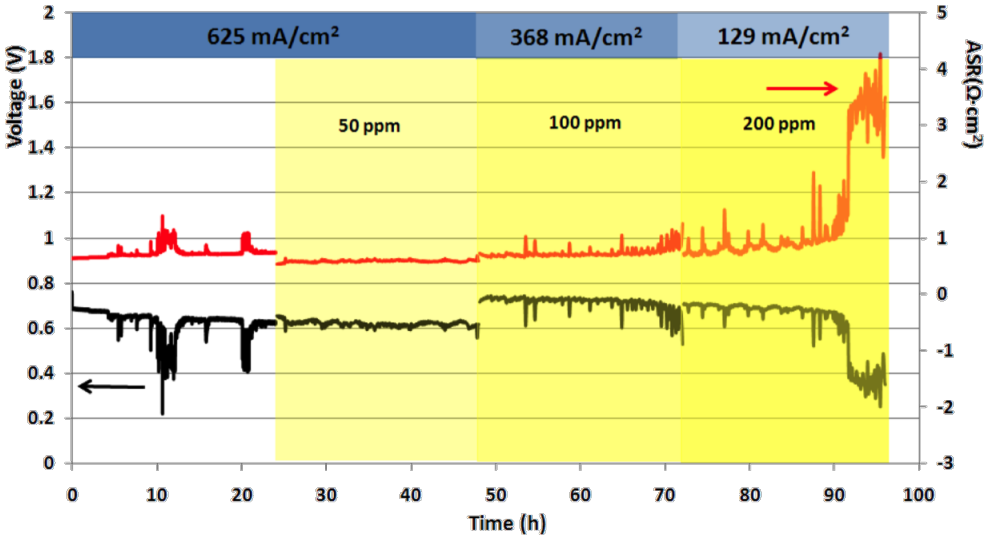


**Figure 4:** Output voltage and ASR, showing initial sulfur tolerance at high current density, and early cell failure. (Treatment-2 cell with GDC interlayer.)

current density (625 mA·cm$^{-2}$) for 24 h. Nevertheless, with each subsequent 24 h increase in $H_2S$ level (to 100 and 200 ppm) the current density had to be reduced sharply (to 368 and 129 mA·cm$^{-2}$, respectively) to maintain the same voltage as at the preceding $H_2S$ level. (After about 90 h of testing, the rapid failure of the cell resulted from inadequate removal of $H_2O$ from the anode atmosphere [12].)

## Microstructures of as-treated anodes

The microstructures of coatings of cells with gadolinia-doped ceria (GDC) interlayers between the anode and electrolyte (see Experimental section for details) were essentially the same as those observed on cells without GDC interlayers. All SEM images shown here, except Figure 9, are of cells without GDC interlayers.

The as-received anodes (i.e., before reduction of NiO to Ni) (Figure 5a) had a Ni:Ce atomic ratio of 3.47 (22.4 atom % Ce) (Table 1), in excellent agreement with the value of 3.43 computed from their nominal composition. (All reported Ni:Ce ratios and cerium concentrations were measured by using energy-dispersive X-ray spectroscopy (EDXS).) The NiO parti-

cles ranged in size from 0.5 to 1.5 μm and had faceted, polygonal faces (Figure 5a). The GDC particles were more rounded; many were sintered agglomerates ca. 3 μm long and ca. 1 μm wide.

Direct-treated ceria coatings (treatment 2) were mostly uniform and continuous (Figure 5b). The presence of a coating can be readily detected in the covering of the polygonal NiO grains, giving them a more rounded appearance. The untreated coating exhibited a few cracks at grain boundaries and occasional gaps (indicated by a circle in Figure 5b). The Ni:Ce atomic ratio was 2.60 (27.8 atom % Ce) (Table 1).

On thiol-treated anodes (treatment 3; Figure 5c) the ceria coating was uniform and continuous. Cracks in the coating were occasionally evident at the grain boundaries. The Ni:Ce atomic ratio was 2.01 (33.2 atom % Ce) (Table 1). On sulfonate-treated anodes (Figure 5d) the appearance of the anode was similar to that of the untreated anode, except that loose ceria clusters were evident. The Ni:Ce atomic ratio was 3.27 (23.4 atom % Ce) (Table 1).

Coating thicknesses were measured on cells with NiO/YSZ anodes that had been coated by using the same procedures as for the nickel-GDC anodes. Then cross-sections were prepared

**Table 1:** Summary of typical EDXS analyses of Ce and Ni (Ni + Ce = 100 atom %) from Ni/GDC anodes (without GDC interlayer) in cells before and after testing, by type of pre-treatment. Data in the "after testing" columns were taken from the surfaces and cross-sections of the anodes shown in Figures 7 through 10.

| treatment | | before testing | after testing | |
|---|---|---|---|---|
| | | | surface | cross-section |
| 1 | Ni, atom % | 77.6 | 69.4 | 69.2 |
| | Ce, atom % | 22.4 | 30.6 | 30.8 |
| | Ni:Ce | 3.47 | 2.27 | 2.25 |
| | Δ(Ni atom %)[a] | — | −8.2 | −8.4 |
| 2 | Ni, atom % | 72.2 | 64.2 | 64.4 |
| | Ce, atom % | 27.8 | 35.8 | 35.6 |
| | Ni:Ce | 2.60 | 1.79 | 1.81 |
| | Δ(Ni atom %)[a] | — | −8.0 | −7.8 |
| 3 | Ni, atom % | 66.8 | 65.3 | 67.5 |
| | Ce, atom % | 33.2 | 34.7 | 32.5 |
| | Ni:Ce | 2.01 | 1.88 | 2.08 |
| | Δ(Ni atom %)[a] | — | −1.5 | 0.7 |
| 4 | Ni, atom % | 76.6 | 76.8 | 69.2 |
| | Ce, atom % | 23.4 | 23.2 | 30.8 |
| | Ni:Ce | 3.27 | 3.30 | 2.25 |
| | Δ(Ni atom %)[a] | — | 0.2 | −7.4 |

[a]Change in atom % of nickel from start of testing to the end.

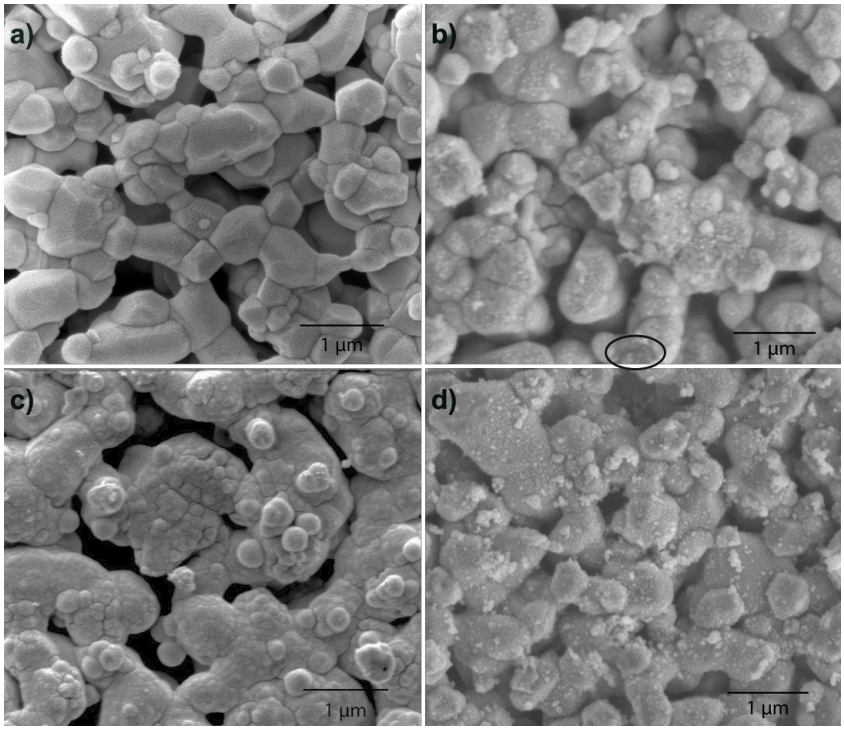


**Figure 5:** Top views of ceria deposition on NiO/GDC anodes. a) Treatment 1 (no coating). b) Treatment 2 (direct-treated). The ellipse indicates a gap in the coating. c) Treatment 3 (thiol-treated). d) Treatment 4 (sulfonate-treated).

by using a focused ion beam unit, and EDXS maps were superimposed on the cross-sectional images (Figure 6). With YSZ replacing the GDC as the ionically conducting phase in the anode, the ceria coating could easily be distinguished. All three cross-sections showed ceria coatings enveloping both the NiO and YSZ grains. Figure 6 shows that the coating extended into the porous anode. The thicknesses of the coatings were determined from 5–10 locations in the underlying SEM images (not shown). Typical thickness values ranged from 60 to 170 nm on the direct-treated anode (Figure 6a), 100–140 nm on the thiol-treated anode (Figure 6b), and 50–110 nm on the sulfonate-treated anode (Figure 6c). Coating thicknesses typically varied in the order: thiol (treatment 3) > direct (treatment 2) > sulfonate (treatment 4). The ceria contents of these samples, as determined from overall EDXS analysis of the SEM images, decreased in the same order (Table 1, Ce atom % before testing).

## Microstructural analysis of anodes after operation

**As-received cells (treatment 1):** Figure 7 shows the post-operation cross-sectional SEM images of the anode of an as-received cell (i.e., no ceria coating). The cell was tested at an average current of 71 $mA{\cdot}cm^{-2}$ for 98 h with a total $H_2S$ exposure of 28.8 $cm^3$. Even during this short test at low current density, some of the Ni particles had coarsened to over 2 µm in size (vs 0.5 to 1.5 µm before testing, Figure 5). At the top of the anode, coarsened Ni particles were spread on the surface. Both Ni particles and GDC particles were rounded without facets. The Ni:Ce atomic ratio was 2.27 at the surface and 2.25 at the cross-section, compared to 3.47 as received (Table 1). That is, Ni was depleted from the anode during operation, but had not preferentially segregated to the surface.

**Direct-coated cells (treatment 2):** Figure 8 shows the anode of a direct-treated cell that gave an average current density of 135 $mA{\cdot}cm^{-2}$ for 109 h, with a total $H_2S$ exposure of 28.9 $cm^3$. The testing conditions were comparable with the cell shown in Figure 7, but at nearly twice the current. The Ni:Ce atomic ratio was 1.79 at the surface, and 1.81 over the entire cross-section, compared to Ni:Ce = 2.60 at the surface of the coated anode before operation, i.e., depletion of Ni had occurred during operation, but Ni had not preferentially segregated to the surface.

**Thiol-treated cells (treatment 3):** Figure 9 shows the anode of the thiol-treated cell of Figure 2 after operation (average current

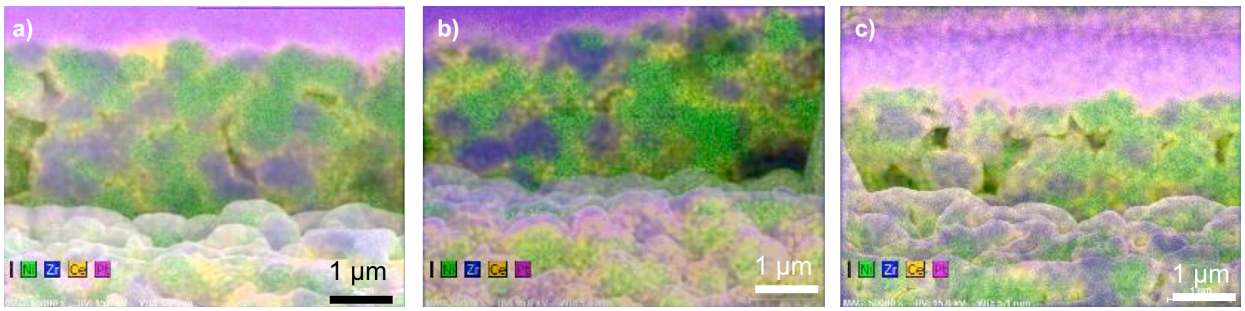


**Figure 6:** FIB cross-sections halfway through ceria-coated NiO/YSZ anodes, with superimposed EDXS maps (Ni: green; Zr: blue; Ce: yellow). a) Direct deposition (treatment 2). b) Deposition after thiol treatment (treatment 3). c) Deposition after sulfonate treatment (treatment 4). (Pink regions are the protective Pt layer applied as part of the FIB sectioning technique.)

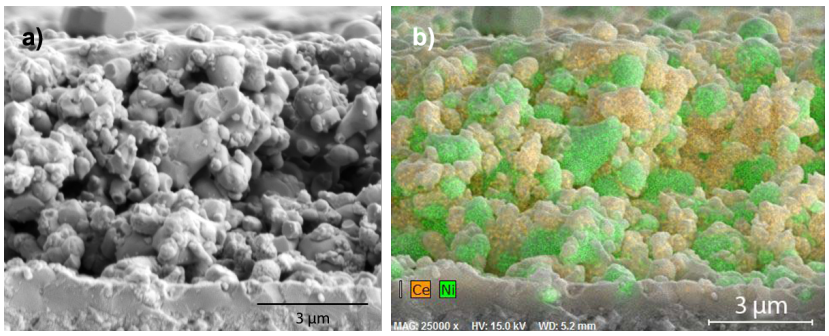


**Figure 7:** Cross-sectional view of an untreated Ni/GDC anode (treatment 1) after operation. a) SEM image; b) EDXS mapping of Ni (green) and Ce (yellow).

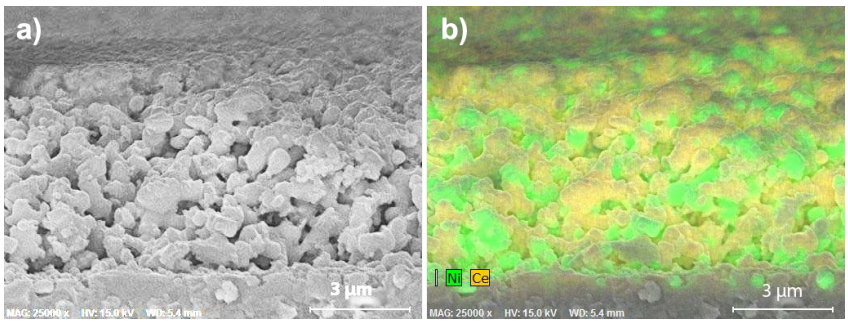


**Figure 8:** Cross-sectional view of a direct-treated anode (treatment 2) after cell operation. a) SEM image; b) EDXS mapping of Ni (green) and Ce (yellow).

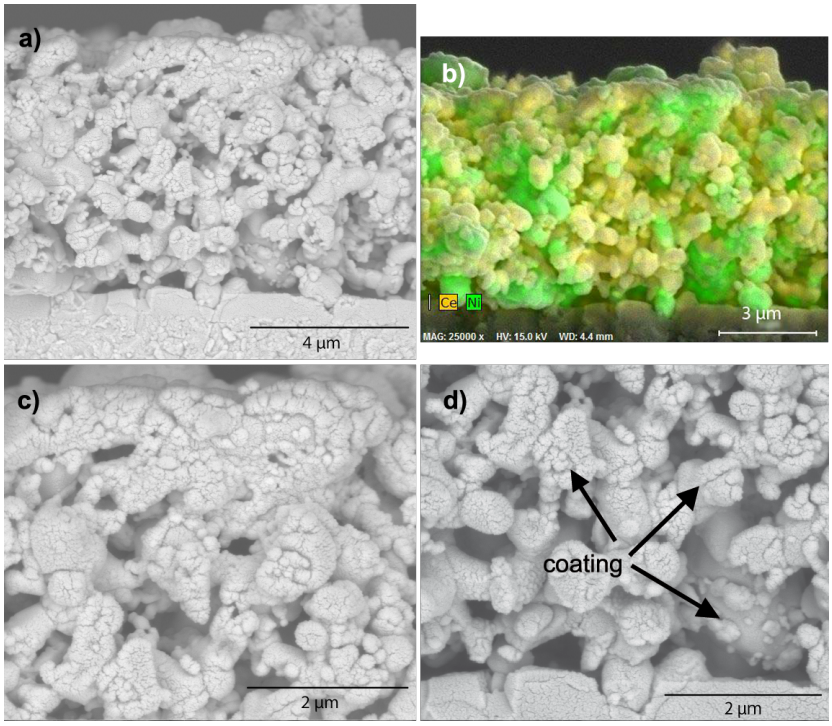


**Figure 9:** Cross-sectional views of the thiol-treated anode (treatment 3) of the cell shown in Figure 2 after operation. a) Whole anode thickness; b) EDXS mapping of Ni (green) and Ce (yellow); c) and d) higher magnification, c) near the anode surface and d) near the electrolyte (electrolyte is visible at bottom). Images c) and d) show that the ceria coating persisted throughout the anode. (Arrows in d point to coating edges or cracks).

density of 218 mA·cm$^{-2}$ for 305 h of actual operation, with a total $H_2S$ exposure of 36 cm$^3$). This test lasted nearly three times as long as that of the direct-treated cell (Figure 8). After operation, the remaining ceria film and film fragments could be observed at the anode surface and near the electrolyte (Figure 9). A few coarsened Ni particles over 2 µm in diameter, round with smooth surfaces, protruded from the anode surface. Pieces of the ceria film or of GDC particle fragments were observed on the coarsened Ni particles. The measured Ni:Ce ratio was 1.88 at the anode surface, and 2.08 over the cross-section (compared with 2.01 at the surface before operation). That is, a slight loss of Ni from the surface had occurred.

**Sulfonate-treated cells (treatment 4):** Figure 10 shows the anode of the sulfonate-treated cell of Figure 3 after testing (average current density of 187 mA·cm$^{-2}$ for 456 h, with a total $H_2S$ exposure of 367 cm$^3$). This was the longest test and the highest cumulative $H_2S$ exposure of the cells shown in Figures 1–4 and 7–10. Nickel and ceria phases were sintered into a porous two-phase network, with no signs of a ceria coating

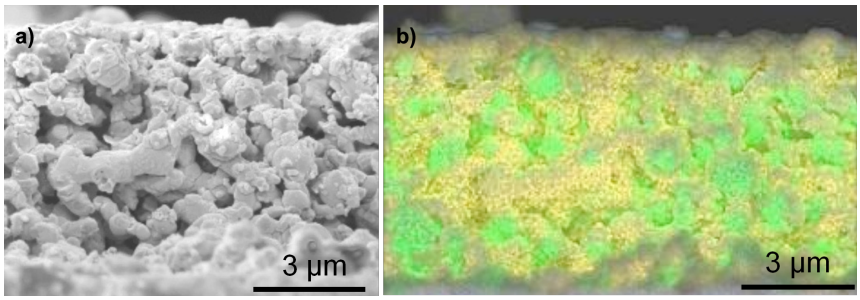


**Figure 10:** Cross-sectional view of a sulfonate-treated anode (treatment 4) after operation. a) SEM image; b) EDXS mapping of Ni (green) and Ce (yellow).

remaining. The measured Ni:Ce atomic ratio for the cross-section was 2.25, compared with 3.27 on the surface before operation, suggesting that nickel depletion from the interior had occurred during operation.

The loss of Ni from the anodes was especially noticeable for uncoated cells. Among the 17 anodes whose Ni distributions were analyzed after testing, on average, the trend for significance of this effect was: treatment 1 > treatment 4 ≈ treatment 2 > treatment 3. That is, the thicker the ceria coating, the less severe was loss of Ni from the anode.

## Overall cell performance

Because the test protocol (see Experimental section) subjected the cells to a wide range of current densities and $H_2S$ exposures of various concentrations and durations (compare, e.g., Figures 1–4), and because of the different pre-treatments to which the cells were subjected, as well as performance variations between nominally identical cells, the cells exhibited significant variation in their operating lifetimes and output. As fuel cells are essentially energy-conversion devices, one useful metric for assessing the relative performance of devices that differed not only in their anode structures, but also in the details of their operating history, is total electrical energy output over the life of the device. Figure 11 shows the average total energy output of the cells (with and without GDC interlayers), grouped by anode treatment, in tests entailing $H_2S$ exposure. On average, the direct-treated and thiol-treated cells provided 103% and 78.5% more energy over their lifetimes than did the untreated cells, whereas the sulfonate-treated cells provided 31% less energy than the untreated cells.

Plotting the average power over the lifetime of individual cells versus total $H_2S$ exposure for the four types of treatment (Figure 12, which includes all of the cells averaged in Figure 11, plus cells that underwent no $H_2S$ exposure) gives another perspective on the effectiveness of the ceria coatings at

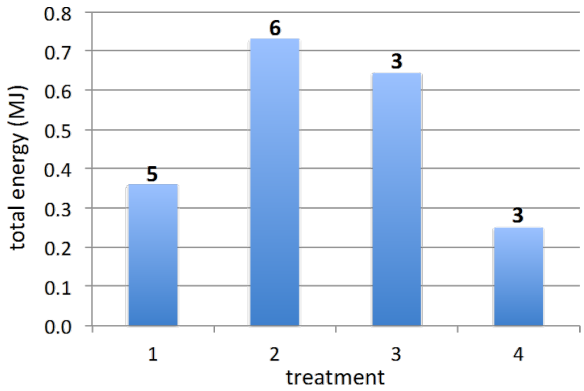


**Figure 11:** Average lifetime energy output of SOFCs (with and without GDC interlayers) tested in sulfur-containing fuel streams, grouped by treatment: 1, no coating; 2, direct ceria coating; 3, ceria coating after thiol treatment; 4, ceria coating after sulfonate treatment. The numeral above each column is the number of cells tested for each type of treatment.

improving sulfur tolerance. For cells with the same treatment, the average power mostly decreased with increasing cumulative sulfur exposure over the cell lifetime, but only ceria-coated cells (treatments 2, 3, and 4) survived total $H_2S$ exposure greater than 120 $cm^3$. Figure 12 also indicates that for cells that experienced no $H_2S$ exposure, all the ceria-coated cells exhibited higher average power than the uncoated cells (treatment 1). This suggests that the ceria coating, regardless of the details of the pre-treatment, improved the average power output of the cells over their lifetimes.

# Discussion

The microstructures of the anodes changed greatly during operation and depended strongly on the testing conditions. The most notable changes occurred in the nickel phase: coarsening (in almost all cases), and nickel depletion from the interior in most anodes. The effects of the coatings and of the surfactant treatments on these phenomena are discussed below.

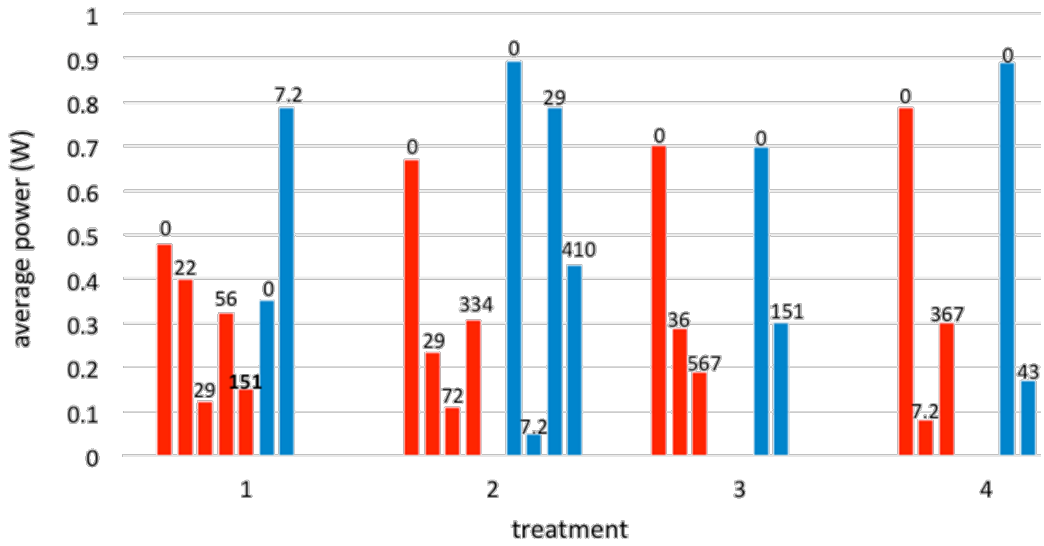


**Figure 12:** Average power over cell lifetime, grouped by anode treatment and anode type, ranked by cumulative $H_2S$ exposure within each group. Numbers at the top of each column indicate the cumulative $H_2S$ exposure over the lifetime of each cell. Blue columns: cells with GDC interlayers between anode and electrolyte. Red columns: cells without GDC interlayers.

## Dependence of coating characteristics on surfactant treatments

Whatever effects the organic surfactants had on the cell performance could have only been exerted during the deposition of the ceria coatings. Before cell operation, during the high-temperature reduction of NiO to Ni (see Experimental section), the surfactants were undoubtedly burnt out, as similar surfactant layers have been shown to pyrolyze below 400 °C, even in low-oxygen atmospheres [29].

During deposition, the solution parameters (concentration, temperature, and pH) can be expected mainly to dictate the particle size and ultimate crystalline form of the coating [30]. The effects of the surfactant layer will be seen primarily in the extent to which it promoted the attachment of the solid particles from the deposition medium and affected their distribution on the substrate (in this case, a NiO–GDC composite).

In previous studies of oxide film deposition on surfactant-treated surfaces, sulfonate surfaces strongly favored the formation of continuous films of $ZrO_2$, $TiO_2$, and $SnO_2$ [26]. This outcome is attributed to the high negative surface charge density of well-packed sulfonate surfaces under the acidic conditions at which these oxides precipitate from solution [31]. When the same treatments that we described here were used prior to applying ceria coatings to a different SOFC anode design than that used in the current work [27], the sulfonate surface gave the thickest and most continuous coatings.

In the present study, the fact that the sulfonate treatment gave the thinnest and least uniform ceria coatings can be attributed to the nature of the deposited surfactant layer. X-ray photoelectron spectroscopy (XPS) of the sulfonate-treated anodes (before ceria deposition) showed carbon and sulfur signals much higher than expected [32] from, e.g., a well-packed surfactant monolayer, and many times higher than the signals detected in the sulfonate-treated anodes of [27]. This indicates that the sulfonate treatment on the present anodes left large oligomers and cross-linked clusters of surfactant, which could have obscured or neutralized most of the sulfonate functionality and led to the thinner, less uniform ceria coatings.

Conversely, XPS measurements of the thiol-treated anodes before ceria deposition showed that most of the thiol functionality had oxidized to sulfonate. So it appears in the present work that the thiol surfactant provided a surface more like a well-packed sulfonate layer than did the sulfonate treatment (Figures 5c vs 5d; Figures 6b vs 6c), resulting in thicker and more uniform ceria coatings from the thiol treatment than from the sulfonate treatment.

## Relation of cell performance to coating characteristics and surfactant treatments

The effects of the surfactant treatments on the coatings are reflected in the sulfur tolerance of the variously treated anodes (Figure 11 and Figure 12). In light of the current thinking that sulfur blocks catalytic sites for the anode reaction on the nickel, the ceria coating may act to impede the sulfur adsorption on the

nickel while still allowing the anode reaction to proceed. The current results then suggest that a continuous coating (direct- or thiol-treated), but not necessarily the thickest (thiol-treated) provides best sulfur tolerance to the anode. Aspects of the sulfonate treatment, particularly the oxone oxidation step, may have adversely affected the anode surface chemistry. (As explained in the Experimental section, we observed chemical damage to the cathode if the oxone solution contacted it, and subsequently took steps to prevent such contact before testing began.)

### Nickel coarsening

Coarsening of nickel is often associated with performance degradation in cermet SOFC anodes [3,16,33,34]. One significant effect of the ceria coating in the current work was to hinder nickel coarsening. For example, compare the significantly coarsened nickel in Figure 7 (an untreated cell) to the nickel in Figure 8 (an direct-treated cell), tested for a similar time but at twice the current and power. Similarly, compare Figure 7b to Figure 9b and Figure 10b (thiol- and sulfonate-treated cells), which showed similar coarsening though the coated cells experienced many times longer and more intensive operation. Coarsening of the metallic phase reduces the density of three-phase boundaries between pore, electronic conductor, and ionic conductor, which are essential to cell operation [35]. Coarsening of Ni also leads to less interconnection of metal particles and therefore to a decrease of the electrical conductivity of the anode. This would be expected to result in loss of power over time, e.g., increased ASR.

The ceria coatings could not suppress nickel coarsening indefinitely. The coatings were readily observed after early stages of cell operation, but in the anodes of long-lived cells the ceria coating was visible mainly as small fragments on coarsened nickel particles. Most of the coating had presumably sintered into, and was indistinguishable from, the GDC phase of the anode. This suggests that eventually the ability of the coating to hinder coarsening broke down, allowing coarsening to proceed until the cell failed.

### Nickel depletion

Lussier et al. [8] reported Ni depletion from Ni/YSZ and Ni/GDC anodes during operation in sulfur-containing atmospheres. Likewise in the present work, by comparing the anode composition before and after cell operation, loss of nickel from the anode was detected for most cells, especially uncoated cells and cells running at high current for long times [32,36]. This suggests that the ceria coatings hindered Ni depletion. The mechanism of nickel depletion is believed to involve the formation of low-melting, volatile $Ni(OH)_2$ in the presence of the $H_2O$ formed at the anode [37]. A ceria shell around the metal network may act as a physical barrier to impede $Ni(OH)_2$ formation or evaporation, with the most continuous coatings being most effective.

## Conclusion

Overall, this work established that nanocrystalline ceria coatings could be deposited throughout porous cermet anodes of SOFCs 6 µm thick by using an aqueous infiltration technique at 50 °C in 48 h without subsequent heat treatment. The morphology of the coatings – specifically, their thickness and their continuity – could be affected through surfactant pretreatments. Lastly, continuous uniform coatings 60–170 nm thick, as deposited directly on the anodes without prior surfactant treatment, or 100–140 nm thick as deposited on thiol-treated anodes, significantly improveed the sulfur tolerance in the tested cells.

The improvements in sulfur tolerance in ceria-coated anodes were attributed to the ability of the coatings to suppress Ni coarsening and depletion in the anode, and this effect was most pronounced in the thiol-treated and the direct-treated cells. The protective effect of the ceria coating appeared to diminish in cells where the coating had not remained physically intact and continuous.

## Experimental

The cells used in this study were electrolyte-supported, circular "button" cells, 3.8 cm in diameter. The electrolyte was $Y_{0.03}Zr_{0.97}O_{2-\delta}$, 100 µm thick. The anode, 6 µm thick, consisted of 60 wt % NiO and 40 wt % $Gd_{0.1}Ce_{0.9}O_{2-\delta}$ (gadolinia-doped ceria, GDC). The NiO was reduced to Ni during the initial heat-up of the cell under a flowing $H_2/N_2$ stream before cell operation began.

Some anodes (the cell of Figure 4, cells included in the averages in Figure 11, and cells represented by blue columns in Figure 12) in addition contained a 2 µm-thick, porous GDC interlayer between anode and electrolyte. This interlayer had no discernible effect on the characteristics of the ceria coatings, either before or after testing, which are the focus of the current work; the conclusions presented here apply equally to both of these types of anodes.

The cathode, 12 µm thick, was composed of 50 wt % $Y_{0.08}Zr_{0.92}O_{2-\delta}$ and 50 wt % lanthanum strontium manganite with La:Sr ratio of 0.85:0.15. The area of each electrode was 2.8 $cm^2$.

### Surfactant treatment and ceria deposition

All cells were first cleaned with ethanol and dried in flowing argon. For the thiol treatment, the cleaned substrates were

immersed in 1-dodecanethiol ($CH_3C_{11}H_{22}SH$) for 5 h at room temperature in air, then washed in flowing ethanol for 2 min and in deionized water for 2 min.

For the sulfonate treatment, the cleaned cells were immersed in 1 vol % 1-bromo-11-(trichlorosilyl)undecane ($Cl_3SiC_{11}H_{22}Br$) in bicyclohexyl ($C_{12}H_{22}$) for 5 h at room temperature in air. The trichlorosilyl groups hydrolyze and undergo condensation reactions with oxide and hydroxide groups on the electrode surfaces, and with each other. The intended result is a siloxy-anchored, bromine-terminated, cross-linked organic monolayer on the pore walls of the electrode. Then the specimens were refluxed with 7% potassium thioacetate in ethanol at 80 °C for 16 h to replace the –Br end groups with thioacetate ($-SCOCH_3$). Lastly, the thioacetate was converted to sulfonate ($-SO_3H$) by exposing the anode to saturated oxone ($2KHSO_5{\cdot}KHSO_4{\cdot}K_2SO_4$) aqueous solution for 2.5 h at room temperature [31]. During this step, instead of immersing the cell into the oxone solution, a cotton pad saturated with oxone was used to cover only the anode side of the cell. This technique provides enough oxone to oxidize the thioacetate group to sulfonate, while preventing damage to the cathode by reaction with the oxone.

Prior to ceria deposition, the surfactant depositions were monitored with X-ray photoelectron spectroscopy (XPS, PHI Model 5600 MultiTechnique System), with particular attention to the presence of the characteristic functional groups and to the progress of the in situ transformations entailed by the sulfonate treatment.

To deposit the ceria coating, the cells (with or without surfactant pre-treatment) were immersed in an aqueous solution of 0.01 M cerium acetate and 0.005 M potassium chlorate [38] at 50 °C for 48 h. After the deposition, the cells were rinsed with deionized water then ethanol and dried with argon.

## Cell operation

Current collectors, consisting of a Pt wire (Alfa Aesar, 0.30 mm dia., 99.9% metals basis) spot-welded to Pt mesh (Alfa Aesar, 52 mesh, woven from 0.1 mm-diameter wire, 99.9% metals basis), were bonded to both electrodes with Pt-based ink (Heraeus). The cell was then sealed to the end of a 3.2 cm-diameter stabilized zirconia tube (by using a silicate-based paste fired at 1050 °C for 1 h) with the anode facing an alumina gas feed tube inside the zirconia tube. This assembly was then put into a vertical tube furnace for cell operation.

Cell operation was conducted at 900 °C. The cathode side of the cell was exposed to the air atmosphere of the furnace. Fuel of 25 sccm $H_2$ and 25 sccm $N_2$, humidified to 3% water vapor by passing through a water bubbler at room temperature, was fed to the anode through the alumina tube. For each tested cell, open circuit voltage (OCV) was checked at the start of operation and every 24 h thereafter to be between 1.0 and 1.1 V, and testing was ended if the OCV was below 1.0 V. Cells were operated galvanostatically (by using an Autolab electrochemical analyzer or an Amrel electronic load with a power supply) at a current that produced a cell voltage of 0.7 V. If the cell voltage dropped more than 5% in 24 h, the current was reduced until the voltage reached 0.7 V. If the cell voltage dropped less than 5% in the first 24 h, $H_2S$ was introduced to the fuel stream at 50 ppm for an additional 24 h. If the cell voltage dropped by less than 5% during this period, the level of $H_2S$ was raised to 100 ppm, 200 ppm, 300 ppm, 400 ppm, or 500 ppm in successive 24 h periods. If the voltage dropped by more than 5% during any of these stages, the cell was run in the original sulfur-free gas flow for 24 h. Testing was ended if the voltage dropped to 0.4 V or if the current density had dropped to <50 mA/cm$^2$ after a long decline in performance. After operation, the cells were cooled in flowing humidified $H_2/N_2$ to near room temperature. The current collectors were carefully peeled from the electrodes before analysis.

## Cell characterization

Scanning electron microscope (SEM) images of the anodes were taken (FEI xT Nova Nanolab) at 5 kV accelerating voltage. Energy-dispersive X-ray spectroscopy (EDXS) mapping at beam energy of 15 keV, combined with SEM images, was used to resolve the phases of anode particles qualitatively and to investigate the microstructure changes. The chemical compositions of the anode were analyzed (QUANTAX Esprit 1.8 software) on EDXS maps taken over an area of 190 μm$^2$ or greater. Cross-sectional images through the coated anodes were obtained by using the focused ion beam unit of the Nova Nanolab.

# Acknowledgements

The authors gratefully acknowledge the fabrication of the fuel cells by, and helpful discussions with, Dr. Zhien Liu of Rolls Royce Fuel Cell Systems U.S. (now LG Fuel Cell Systems, Inc.). At CWRU, the authors are grateful to Mirko Antloga for assistance with setting up the fuel cell test stations; Yen-Jung Huang for carrying out some of the cell performance tests; Craig Virnelson for assistance with the data acquisition software and hardware; and Dr. Amir Avishai for training in SEM and EDXS. The authors gratefully acknowledge financial support from the United States National Aeronautics and Space Administration under NASA Contract NNC06CA46C [39].

# References


1. Singhal, S. C.; Kendall, K. Introduction to SOFCs. In *High Temperature Solid Oxide Fuel Cells: Fundamentals, Design, and Applications;* Singhal, S. C.; Kendall, K., Eds.; Elsevier Inc.: New York, 2003; pp 1–22. doi:10.1016/B978-185617387-2/50018-0
2. Yokokawa, H.; Tu, H.; Iwanschitz, B.; Mai, A. *J. Power Sources* **2008,** *182,* 400–412. doi:10.1016/j.jpowsour.2008.02.016
3. Hansen, J. B.; Rostrup-Nielsen, J. Sulfur Poisoning on Ni Catalyst and Anodes. In *Handbook of Fuel Cells – Fundamentals, Technology and Applications;* Vielstich, W.; Yokokawa, H.; Gasteiger, H. A., Eds.; Advances in Electocatalysis, Materials, Diagnostics and Durability; Part 5: Performance Degradation; Chapter 65,, Vol. 6; John Wiley & Sons, Ltd., 2009; pp 1–13.
4. Cheng, Z.; Wang, J.-H.; Choi, Y.; Yang, L.; Lin, M. C.; Liu, M. *Energy Environ. Sci.* **2011,** *4,* 4380–4409. doi:10.1039/c1ee01758f
5. Matsuzaki, Y.; Yasuda, I. *Solid State Ionics* **2000,** *132,* 261–269. doi:10.1016/S0167-2738(00)00653-6
6. Sasaki, K.; Susuki, K.; Iyoshi, A.; Uchimura, M.; Imamura, N.; Kusaba, H.; Teraoka, Y.; Fuchino, H.; Tsujimoto, K.; Uchida, Y.; Jingo, N. *J. Electrochem. Soc.* **2006,** *153,* A2023–A2029. doi:10.1149/1.2336075
7. Cheng, Z.; Zha, S.; Liu, M. *J. Power Sources* **2007,** *172,* 688–693. doi:10.1016/j.jpowsour.2007.07.052
8. Lussier, A.; Sofie, S.; Dvorak, J.; Idzerda, Y. U. *Int. J. Hydrogen Energy* **2008,** *33,* 3945–3951. doi:10.1016/j.ijhydene.2007.11.033
9. Li, T. S.; Wang, W. G.; Chen, T.; Miao, H.; Xu, C. *J. Power Sources* **2010,** *195,* 7025–7032. doi:10.1016/j.jpowsour.2010.05.009
10. Li, T. S.; Wang, W. G. *Electrochem. Solid-State Lett.* **2011,** *14,* B35–B37. doi:10.1149/1.3526134
11. Brightman, E.; Ivey, D. G.; Brett, D. J. L.; Brandon, N. P. *J. Power Sources* **2011,** *196,* 7182–7187. doi:10.1016/j.jpowsour.2010.09.089
12. Wu, C. C.; De Guire, M. R. Performance of Solid Oxide Fuel Cells under Fuel-Side Operational Stresses. In *Proceedings of Energytech 2012,* Cleveland, OH, May 30–31, 2012; IEEE. doi:10.1109/EnergyTech.2012.6304695
13. McCarty, J. G.; Wise, H. *J. Chem. Phys.* **1980,** *72,* 6332. doi:10.1063/1.439156
14. Choi, Y. M.; Compson, C.; Lin, M. C.; Liu, M. *Chem. Phys. Lett.* **2006,** *421,* 179–183. doi:10.1016/j.cplett.2006.01.059
15. Dong, J.; Cheng, Z.; Zha, S.; Liu, M. *J. Power Sources* **2006,** *156,* 461–465. doi:10.1016/j.jpowsour.2005.06.016
16. Wang, J.-H.; Liu, M. *Electrochem. Commun.* **2007,** *9,* 2212–2217. doi:10.1016/j.elecom.2007.06.022
17. Kim, H.; Vohs, J. M.; Gorte, R. *Chem. Commun.* **2001,** 2334–2335. doi:10.1039/b105713h
18. He, H.; Gorte, R. J.; Vohs, J. M. *Electrochem. Solid-State Lett.* **2005,** *8,* A279–A280. doi:10.1149/1.1896469
19. Trembly, J. P.; Marquez, A. I.; Ohrn, T. R.; Bayless, D. *J. Power Sources* **2006,** *158,* 263–273. doi:10.1016/j.jpowsour.2005.09.055
20. Kurokawa, H.; Sholklapper, T. Z.; Jacobson, C. P.; De Jonghe, L. C.; Visco, S. J. *Electrochem. Solid-State Lett.* **2007,** *10,* B135–B138. doi:10.1149/1.2748630
21. Yun, J. W.; Yoon, S. P.; Han, J.; Park, S.; Kim, H. S.; Nam, S. W. *J. Electrochem. Soc.* **2010,** *157,* B1825–B1830. doi:10.1149/1.3499215
22. Gorte, R. J.; Park, S.; Vohs, J. M.; Wang, C. *Adv. Mater.* **2000,** *12,* 1465–1469. doi:10.1002/1521-4095(200010)12:19<1465::AID-ADMA1465>3.0.CO;2-9
23. Gorte, R. J.; Vohs, J. M.; McIntosh, S. *Solid State Ionics* **2004,** *175,* 1–6. doi:10.1016/j.ssi.2004.09.036
24. Chen, X. J.; Khor, K. A.; Chan, S. H. *Electrochem. Solid-State Lett.* **2005,** *8,* A79–A82. doi:10.1149/1.1843791
25. Yoon, S. P.; Han, J.; Nam, S. W.; Lim, T.-H.; Hong, S.-A. *J. Power Sources* **2004,** *136,* 30–36. doi:10.1016/j.jpowsour.2004.05.002
26. Parikh, H.; De Guire, M. R. *J. Ceram. Soc. Jpn.* **2009,** *117,* 228–235. doi:10.2109/jcersj2.117.228
27. Tang, L.; Salamon, M.; De Guire, M. R. *Sci. Adv. Mater.* **2010,** *2,* 1–11. doi:10.1166/sam.2010.1059
28. Garrels, M. The Interaction of Sulfur with Planar Solid Oxide Fuel Cell Cermet Anodes and the Role of Ceria. M. S. Thesis, Case Western Reserve University, U.S.A, 2005.
29. Shin, H.; Wang, Y.; Sampathkumaran, U.; De Guire, M.; Heuer, A.; Sukenik, C. N. *J. Mater. Res.* **1999,** *14,* 2116–2123. doi:10.1557/JMR.1999.0286
30. De Guire, M. R.; Pitta Bauermann, L.; Parikh, H.; Bill, J. Chemical Bath Deposition. In *Chemical Solution Deposition of Functional Oxide Thin Films;* Schneller, T.; Waser, R.; Kosec, M.; Payne, D., Eds.; Springer-Verlag: Vienna, Austria, 2013; pp 319–339. doi:10.1007/978-3-211-99311-8_14
31. Shyue, J.-J.; De Guire, M. R.; Nakanishi, T.; Masuda, Y.; Koumoto, K.; Sukenik, C. N. *Langmuir* **2004,** *20,* 8693–8698. doi:10.1021/la049247q
32. Tang, L. Modification of Solid Oxide Fuel Cell Anodes with Cerium Oxide Coatings. Ph.D. Thesis, Case Western Reserve University, U.S.A., 2009.
33. Wang, L. S.; Barnett, S. A. *J. Electrochem. Soc.* **2002,** *139,* 1134–1140. doi:10.1149/1.2069353
34. Hagen, A.; Barfod, R.; Hendriksen, P. V.; Liu, Y.-L.; Ramousse, S. *J. Electrochem. Soc.* **2006,** *153,* A1165–A1171. doi:10.1149/1.2193400
35. Simwonis, D.; Tietz, F.; Stöver, D. *Solid State Ionics* **2000,** *132,* 241–251. doi:10.1016/S0167-2738(00)00650-0
36. Wu, C.-C. Evaluation of Ceria-Based Anodes of Solid Oxide Fuel Cells and their Sulfur Tolerance. Ph.D. Thesis, Case Western Reserve University, U.S.A., 2011.
37. Du, K.; Ernst, F.; Garrels, M.; Payer, J. *Int. J. Mater. Res.* **2008,** *99,* 548–552. doi:10.3139/146.101663
38. Unuma, H.; Kanehama, T.; Yamamoto, K.; Watanabe, K.; Ogata, T.; Sugawara, M. *J. Mater. Sci.* **2003,** *38,* 255–259. doi:10.1023/A:1021197029004
39. De Guire, M. R.; Bayless, D. NASA Contract NNC06CA46C, Final Technical Report, June 2010.

BEILSTEIN JOURNAL OF NANOTECHNOLOGY

# Real-time monitoring of calcium carbonate and cationic peptide deposition on carboxylate-SAM using a microfluidic SAW biosensor

Anna Pohl[1,2] and Ingrid M. Weiss[*1]

Full Research Paper

Open Access

Address:
[1]INM – Leibniz Institute for New Materials, Campus D2 2, 66123 Saarbrücken, Germany and [2]Saarland University, Campus D2 2, 66123 Saarbrücken, Germany

Email:
Ingrid M. Weiss[*] - ingrid.weiss@inm-gmbh.de

* Corresponding author

Keywords:
biomineralization; calcium carbonate; love-type surface acoustic wave; poly-cationic peptide

*Beilstein J. Nanotechnol.* **2014,** *5,* 1823–1835.
doi:10.3762/bjnano.5.193

Received: 31 May 2014
Accepted: 28 September 2014
Published: 22 October 2014

This article is part of the Thematic Series "Towards multifunctional inorganic materials: biopolymeric templates".

Guest Editors: C. Steinem and J. Bill



## Abstract

A microfluidic biosensor with surface acoustic wave technology was used in this study to monitor the interaction of calcium carbonate with standard carboxylate self-assembled monolayer sensor chips. Different fluids, with and without biomolecular components, were investigated. The pH-dependent surface interactions of two bio-inspired cationic peptides, AS8 and ES9, which are similar to an extracellular domain of the chitin synthase involved in mollusc shell formation, were also investigated in a biological buffer system. A range of experimental conditions are described that are suitable to study non-covalent molecular interactions in the presence of ionic substances, such as, mineral precursors below the solubility equilibrium. The peptide ES9, equal to the mollusc chitin synthase epitope, is less sensitive to changes in pH than its counterpart AS8 with a penta-lysine core, which lacks the flanking acidic residues. This study demonstrates the extraordinary potential of microfluidic surface acoustic wave biosensors to significantly expand our experimental capabilities for studying the principles underlying biomineralization in vitro.

## Introduction

Biomineralization is a natural process of global significance that involves the deposition of mineral ions under the control of biological organisms [1-7]. The interaction of proteins with minerals is one of the key regulatory elements in biomineralization processes, and many proteins involved in biomineralization exhibit molecular features that make them attractive models for materials science and nanotechnology [8-10]. Especially the protein fraction of mollusc shells is of interest for studying protein–mineral interactions because each mollusc shell contains a species-specific set of proteins which, in a collective manner, achieve superior materials properties in the final ceramic composite [11-13]. Molecular and phylogenetic investi-

gations report that the differences between the assemblies of shell proteins from one species to another species can be tremendous [14-16]. This observation suggests that multiple interactions between the proteins are fine-tuned in relationship to the forming mineral phases [17-20].

Dissecting each single interaction event in a given biomineralization process poses some experimental challenges [21-24]. An investigation of biomolecular interactions, in such a process, requires quantifying the impact of different parameters under well-defined conditions [25,26]. Especially in the case of mineral precipitation, the required control over the process is limited when the reaction takes place closer to the solubility equilibria regime [27]. This could be one of the reasons why mechanistic insights into the functions of many biomineralization proteins are difficult to establish [9,28]. Mineral precipitates obtained in the presence of organic additives have been analyzed using an arsenal of characterization techniques including high-resolution X-ray and electron microscopy techniques [25]. However, many details about the dynamics of interfacial interactions – an intrinsic design feature of enzymatic catalysis common to all biological systems [4,26] – are still poorly understood as far as the design features of biomineralization proteins are concerned [14,19]. Especially in the field of biomineralization it is therefore of major importance to quantify biomolecular interactions as a solid–liquid system with high sensitivity.

Recent progress in the field of biosensors based on surface acoustic wave (SAW) technology has made it possible to perform experiments with very high sensitivity in extremely small volumes of liquid media [29]. Surface acoustic wave biosensors operate with different types of waves [30]. Not all of them are useful for fluidic applications due to an enormous energy loss [31]. The propagation of the surface acoustic wave is influenced by the adjacent medium. Phase and amplitude of the propagating wave vary as a function of viscosity changes related to mass deposited on the surface [32]. Advanced microfluidic biosensor technology is based on the propagation of a surface acoustic wave within a thin film [33]. Interdigital transducers on both sides of the sensor area give rise to an electrical field when alternating voltage is applied [34]. The electrical field is converted into mechanical stress that propagates through the material and generates the surface acoustic wave, which is converted at the opposite side of the sensor to an electrical signal by the direct piezoelectric effect. The ability to easily calibrate the system with high performance [35] is essential to ensure the observed changes in the acoustic wave are indicative of changes in the system free energy which changes as a function of mass transfer between the fluid and the sensor [33]. This opens the possibility to analyze the deposition of mass in real-time and as a function of organic additives under marker-free conditions [29].

The sensitivity of the new generation of microfluidic SAW sensors is about 4–5 times higher than that of quartz crystal microbalances with dissipation QCM-D [35]. Mass and viscosity changes can be continuously and simultaneously monitored in standardized systems, as long as the amplitude signal is strongly correlated with the viscosity of the fluid [36]. Recently, multichannel experiments became possible, enhancing the efficiency while expanding the experimental design options [37,38].

So far, the most common real-time assays with respect to the function of macromolecules involved in biomineralization are based on calcium titration in bulk environments [23,39]. Although these assays are perfectly suited to monitor the onset of early mineralization events including the formation of prenucleation clusters, the assay is restricted to comparably large volumes, which poses a problem for the study of biomineralization, where the amount of organic compounds is rather limited because of the low yield after purification, especially from native shell extracts [40], but even from recombinant sources [41,42].

The aim of the present study was to evaluate the suitability of microfluidic SAW biosensor systems with respect to elucidating the interaction between small biomolecules and calcium carbonate, one of the most common minerals in biomineralization processes. Acidic macromolecules comprise a significant fraction of the organic matrix of many mollusc shells [43-45], therefore a carboxylate-terminated self-assembled monolayer (COO-SAM) sensor chip was used to investigate under which conditions interactions related to organic biomolecules and calcium carbonate in the presence of carboxylate surfaces could be reproducibly quantified in real-time assays.

Here, we report a case study with calcium carbonate, both in pure aqueous systems and in the presence of citric acid. We also investigated the two cationic peptides ES9 (sequence, N→C: EEKKKKKES) and AS8 (sequence, N→C: AKKKKKAS) [46]. The ES9 peptide is derived from E22, one of four major extracellular loops of an enzyme involved in biomineralization [20,47]. Previous experiments suggest that self-assembly of E22 is fine-tuned in accordance with pH changes that may occur as a function of the mineral precipitation and dissolution [48]. Since no equivalent real-time information regarding the deposition of calcium carbonate on carboxylate-SAMs below the equilibrium solubility is available from the literature, we started our investigation and described our results in detail with the particular aim to inspire similar investigations in biomineralization

research in the future. A standard database of the function of organic molecules, peptides and proteins in mineralizing systems will be a major achievement of global significance for materials science, biomedical engineering and bioinspired nanotechnology.

## Results and Discussion

Using a standard microfluidic surface acoustic wave (SAW) biosensor system equipped with commercially available $COO^-$/$H_3O^+$-SAM (COOH-SAM, in the following is termed COO-SAM) sensor chips, we monitored the phase and amplitude signals as a function of time. The influence of the concentration of calcium carbonate relative to the solubility equilibrium and the flow rate on the SAW biosensor phase and amplitude signals was investigated in real-time. The influence of organic molecules is studied in two different systems: First, citric acid in aqueous solution was investigated in a flow channel pre-incubated with calcium carbonate. Second, two peptides (pI 10 and pI 9) in glycylglycine buffer (Gly–Gly) were investigated at three different pH values between pH 7.75 and pH 9.0 in order to learn about their interaction with charged surfaces. The aim of this study was to evaluate the competitive non-covalent interactions of peptides and buffer substances at the liquid–solid interface. For standardization, commercially available COO-SAMs were used to mimic negatively charged surfaces, which similarly occur in natural biomineralization processes. The sequence of injections into the respective flow channels is an essential part of each experiment and the tables are presented in Supporting Information File 1.

### Calcium carbonate in water

The first series of experiments are designed to test whether dynamic interactions between calcium and (bi)carbonate ions (hydrogen carbonate and/or carbonate) with a COO-SAM surface can be monitored in real-time and whether or not the interaction depends on the concentration, which was adjusted to fractions of the solubility equilibrium concentration. Therefore, 140 µmol/L calcium carbonate in pure water was diluted to 105 µmol/L, 70 µmol/L, 35 µmol/L, 17.5 µmol/L. Deionized water was used as the running buffer in these experiments and calcium carbonate solutions were sequentially injected, all into the same channels of a four-channel sensor chip, starting with the lowest concentration (Supporting Information 1, Table S1). In between the injections, deionized water (the "running buffer" in this case) was supplied to all channels of the sensor chip for five minutes. Figure 1 shows the phase and amplitude signals of the SAW sensor in response to the calcium carbonate injections at different concentrations.

The phase signal as a function of time (Figure 1A) was nearly the same for all concentrations tested in this experiment. At time = 0 seconds the injection started, lasting for 600 seconds in this case. After an initial fast increase, the signal remained more or less constant at maximum values, dependant on the different calcium carbonate concentrations. The 140 µmol/L solution reaches 0.44°, whereas the 17.5 µmol/L solution achieves the lowest maximum phase value with only 0.05°. The baseline noise, according to the manufacturer of the instrument, is <0.05° phase (RMS), the baseline drift typically <0.01° phase/min. The signal decreased when the channel is flushed with an injection of water and reached a nearly constant value, which differed from the starting conditions up to about 0.04°, corresponding to about 10% of the maximum phase value reached during the continuous calcium carbonate flow. It is unclear, how stable the interaction with the COO-SAM during the calcium carbonate injection would be. The obtained value could just indicate a more or less stable equilibrium between precipitation and dissolution from the surface. The final value, which is reached after pure water is injected, very likely represents the complete dissolution of a precipitate temporarily attached to the COO-SAM. If this is indeed true, it would represent a calcium carbonate precipitate reversibly formed under conditions far below the solubility equilibrium, thus providing an opportunity to study the function of biomineralization proteins under conditions where spontaneous mineral nucleation should not occur. This would, in turn, represent a new degree of freedom in biomineralization research.

The response of the amplitude signal to the injection of calcium carbonate solutions is in the range of 0.998–1.001 a.u. (compare also with citrate experiments described in the following section). The amplitude data presented in Figure 1B are evaluated with respect to significant differences before and after the injection of calcium carbonate (Figure 1C). The amplitude signals decrease with increasing calcium carbonate concentrations of at least 35 µmol/L. The data sets of the different calcium carbonate concentrations were compared after the injections were followed by a constant flow of deionized water (Figure 1D). After equilibration, amplitude signals of 105 µmol/L and 140 µmol/L remain low, whereas the 70 µmol/L reaches the same range as the 17.5 µmol/L (Figure 1D). The relatively high amplitude signal corresponding to 35 µmol/L indicates additional drift effects. In summary, it can be concluded that the temporary interaction with the sensor chip is concentration dependent. A minimum concentration of 35 µmol/L is required. After the injection of deionized water (Figure 1A, 600–1000 s), the 105 µmol/L or 140 µmol/L calcium carbonate injections apparently lead to stable calcium deposits on top of the COO-SAM. The lower concentrations are similar to 17.5 µmol/L calcium carbonate, which appears inert during the injection. There is no long-term effect. This observation raises the question of whether there is a

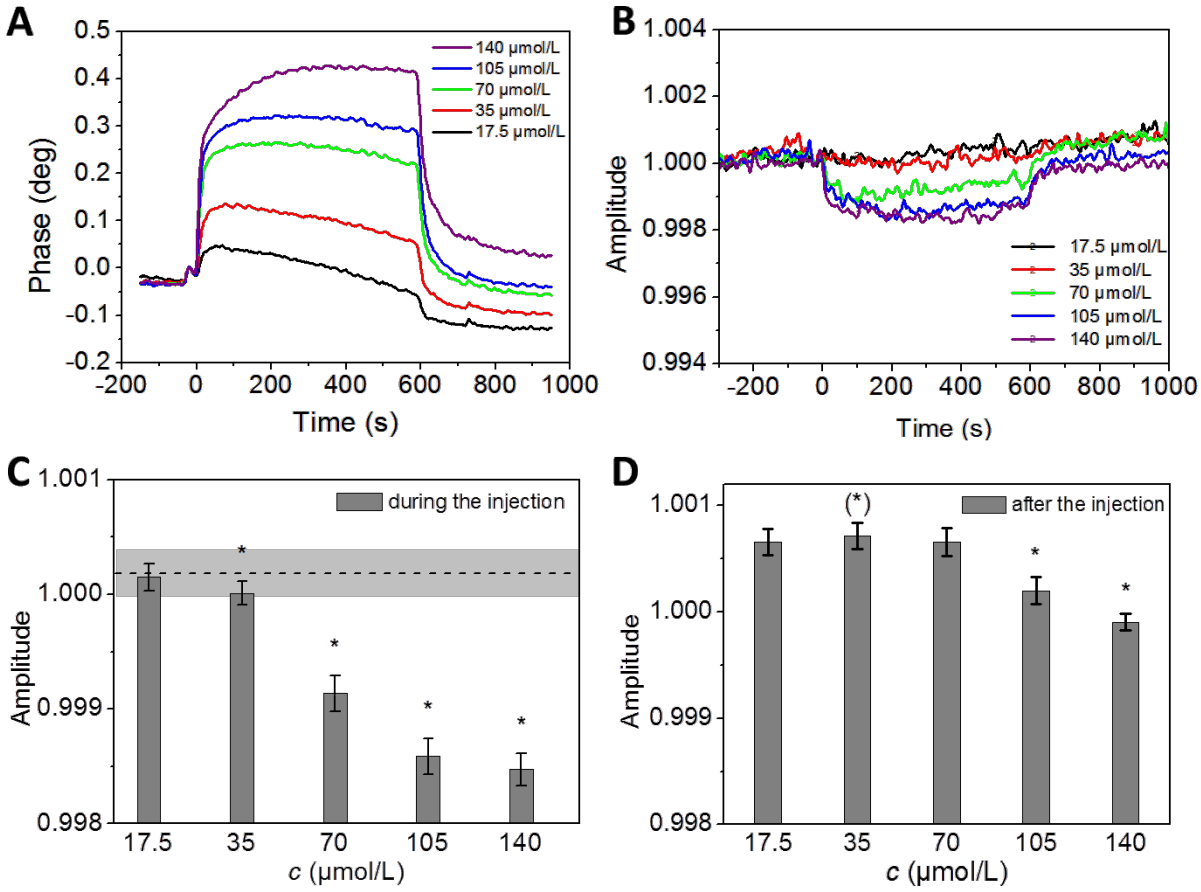


**Figure 1:** Phase and amplitude signal of microfluidic experiments on COO-SAM with calcium carbonate in pure water at different concentrations. Calcium carbonate solutions of 140 µmol/L (equilibrium saturation level, violet), 105 µmol/L (blue), 70 µmol/L (green), 35 µmol/L (red), 17.5 µmol/L (black) were injected in a sam®X system and interactions with a COO-SAM sensor chip were monitored in real-time. The phase vs -time plot visualizes the change of the phase signals (A) and the corresponding amplitude signals (B) of the sensor during the injection of the calcium carbonate solutions (0–600 s) and pure water (600–1000 s). (C), Statistical evaluation of averaged amplitudes prior to (shaded box) and during injections as shown in (B). (D), Comparison between the amplitude signals after the injections as shown in (B). There is a significant difference between the lowest concentration ($c$ = 17.5 µmol/L) and $c$ = 105 µmol/L or, $c$ = 140 µmol/L, indicating that long-lasting residence of calcium carbonate at the carboxylate-SAM interface occurs at $c$ > 70 µmol/L but far below the calculated equilibrium in solution. Note that the amplitude signal during the injections (C) remained unchanged only for the lowest concentration ($c$ = 17.5 µmol/L).

structural difference between calcium deposits on COO-SAMs obtained at higher versus lower concentration levels. Such structural differences could account for the sustained stability of the layer as indicated by both the phase and the amplitude signals.

Since even the smallest change in concentration causes a discernable change in the phase signal (Figure 1A), this biosensor system is suitable to detect biomolecular interactions with calcium carbonate in the range of $n(CaCO_3)$ ~$10^{-12}$ mol to $10^{-11}$ mol. One microfluidic channel has a flow cell height of $2 \times 10^5$ nm and a volume of 1.2 µL. The sensitive area of the chip is $5 \times 10^6$ nm × $1.2 \times 10^6$ nm and the cross-sectional area of the flow channel is 0.24 mm$^2$. This would correspond to ~$2 \times 10^{13}$ to $3 \times 10^{13}$ elementary cells of calcite, assuming that these would form a homogeneous monolayer on the sensitive area of one sensor channel. The commercial SAM's used here were not specifically characterized with respect to the molecular ordering. It would have exceeded the scope of the present study to investigate the growth kinetics of differently oriented calcium carbonate crystals [44,45], and to evaluate the homogeneity of the calcium carbonate films deposited on the sensor chip.

The injection of pure water did not result in a complete reduction of the phase signal. This suggests that calcium ions and/or calcium carbonate are not completely removed from the sensor chip surface. It seems that part of the previously formed layer is stable with respect to the water interface at a given flow rate, depending on how closely the concentration of the dissolved

calcium carbonate matches the solubility equilibrium during deposition. The relatively small changes in the amplitude signals during the injection indicate that the overall viscosity effect on a COO-SAM is small in the case of calcium and (bi)carbonate ions in aqueous solution.

## Flow rate dependence

The sam®X microfluidic system was designed for flow rates in the range between 12.5 µL/min and 300 µL/min. The influence of different flow rates on the interaction between ions derived from calcium carbonate in aqueous solution and the sensor chip surface was tested at flow rates of 200 µL/min, 100 µL/min, 50 µL/min, 25 µL/min and 12.5 µL/min. At each time, 400 µL of the calcium carbonate solution was injected. The system was allowed to equilibrate for 5 minutes between individual experiments with pure water at the respective flow rates (Supporting Information 1, Table S2). Figure 2 shows the phase vs time and amplitude vs time plots obtained when a calcium carbonate solution at solubility equilibrium was injected at different flow rates.

The initial slope and overall shape of the phase signal vs time is independent of the flow rate. A maximum phase value of ~0.7° is reached at flow rates up to 50 µL/min. When the experiments are performed at flow rates 100 µL/min and 200 µL/min, the maximum phase values are in the range 0.5–0.6°, which indicates that the threshold for flow rate independence is between 50 µL/min and 100 µL/min. The little irregular peaks in the phase signal obtained for 200 µL/min flow rates can be attributed to the pumping procedure which is a common phenomenon when the flow rate is high. The volume of the pump is 250 µL, and each time when this volume is refilled it causes artifacts in the signal as observed here.

Since the flow rate determines the duration of the injection, we chose to keep the injection volume and thus the total amount of injected calcium carbonate constant. If the phase signal at flow rates up to 50 µL/min, as shown in Figure 2A, were displayed at stretched time intervals, they would correspond to each other in terms of maximum height and curvature. There is no flow rate dependency as long as flow rates are kept below 50 µL/min. The highest flow rate tested (200 µL/min) yields the lowest phase signal at approximately 0.5°. Flow rates below 50 µL/min reach the maximum phase at values between 0.6 and 0.7°. In accordance with these observations, all subsequent experiments are performed at flow rates equal to or less than 50 µL/min. The maximum phase values are reached after approximately 200 µL injection volume. This observation suggests that the time course of the interaction depends also on the total amount of calcium and/or (bi)carbonate ions introduced to the sensor surface. It is interesting to note that calcium carbonate surface interactions seem to be less well controlled at flow rates higher than 50 µL/min. One can assume that, at higher flow rates, the interaction of calcium and/or (bi)carbonate does not reach the maximum capacity of the sensor surface.

## Calcium carbonate and citric acid interactions

In order to explore the possibility of calcium carbonate removal from the sensor chips as seen in the previous experiments, the COO-SAM surfaces of the sensor chip were treated with different volumes of 1 mM citric acid. A solution of calcium carbonate at solubility equilibrium (140 µmol/L) was used as the running buffer and different amounts of citric acid (100 µL, 200 µL, 400 µL) were injected successively. The flow rate was kept constant at 50 µL/min. Pure water was also injected for comparison. Table S3 (Supporting Information File 1) shows the sequence of injections and experimental details.

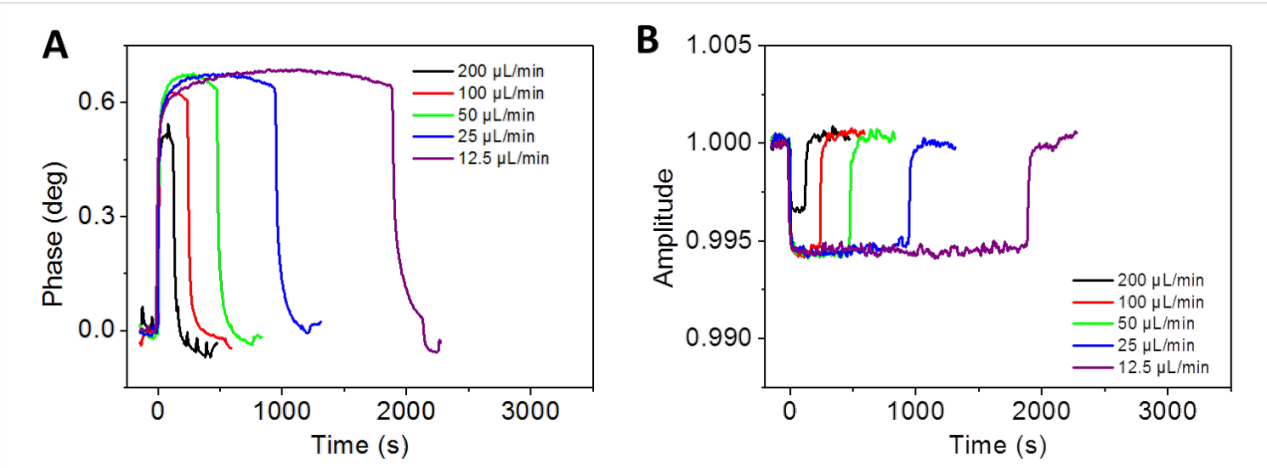


**Figure 2:** Flow-rate dependency of calcium carbonate interactions with COO-SAM chip. Phase vs time plot (A) and corresponding amplitude vs time plot (B) for different flow rates. A constant volume of 400 µL calcium carbonate in pure water (140 µmol/L) was injected, followed by pure water for 5 minutes.

The time course of the phase signal for the duration of each injection volume was similar for all injected volumes of 1 mM citric acid (Figure 3A).

The phase signals of pure water and citric acid experiments are displayed in an overlay, adjusted to phase = 0° and time of injection = 0 seconds. The injected volume determined the length of each injection. There is almost no change in the phase signal of the three injections of pure water (Figure 3A), all of them have the same negative gradient during the injection. The phase signal decreases with time in an almost parabolic shape. As soon as the injection ends there is a fast increase in the phase signal until it reaches the original value. Phase signals at the end of the injection period reach a certain minimum value, depending on the volume and hence the duration of the injection. Nevertheless, all phase signals of the citric acid injections decrease very rapidly with nearly the same negative slope, which decreases with time until a constant minimum value is reached (Figure 3A, 200 µL and 400 µL citric acid). As soon as the injection is finished, the phase signal increases very rapidly until the original value close to 0° is reached. In the case of pure water, an injection volume of 400 µL is required to reach the minimum phase value of the citric acid experiment.

Figure 3B shows the corresponding amplitude vs time plot. Almost no amplitude changes occur when different volumes of pure water are injected. In contrast, the amplitude signals for the injections of citric acid decrease immediately after injection and remain at a constant minimum value as long as citric acid is injected. When the injections stop, the amplitude signals return quickly to the original value of 1.00 (a.u.). The volume of citric acid and thus the total amount of organic molecules has little effect in this case. The volume of the injected solution changes only the duration of the injection period and does not change anything in the behavior of the amplitude signal. Experiments with 10 mM citric acid show that the phase signal behave more or less the same, but the minimum phase value attained during the injection is much lower than the phase shifts caused by 1 mM citric acid solution.

The decrease in the phase signals observed for citric acid and pure water corresponds to a loss of mass on the surface of the sensor chip. Based on the time-course of the phase signals we assume that calcium carbonate originating from the running buffer is removed from the sensor surface by pure water and, even faster, by citric acid. Furthermore the time-course of the removal of calcium carbonate from the surface depends on the total volume of the citric acid injected. A certain amount of citric acid is required to reach the equilibrium level that leads to a depletion of mass, represented by the phase signal. A maximum turn-over is reached at 200 µL of citric acid or 400 µL of pure water. The observation that the changes of the phase signals caused by citric acid occur much faster than the changes of those induced by pure water injections indicates the removal by citric acid is more efficient. This is in perfect agreement with expectations, confirming that an online monitoring of the sequence of events in the removal of calcium and/or (bi)carbonate ions from COO-SAM surfaces by citric acid in comparison to water is possible. However, as shown in Figure 3B, the viscosity effect was not observed to follow the trend of the observed mass loss for the two different solvents (phase signal, Figure 3A). Citric acid and pure water induce a mass loss from the calcium carbonate treated COO-SAM sensor chip, but only citric acid shows a significant viscosity effect.

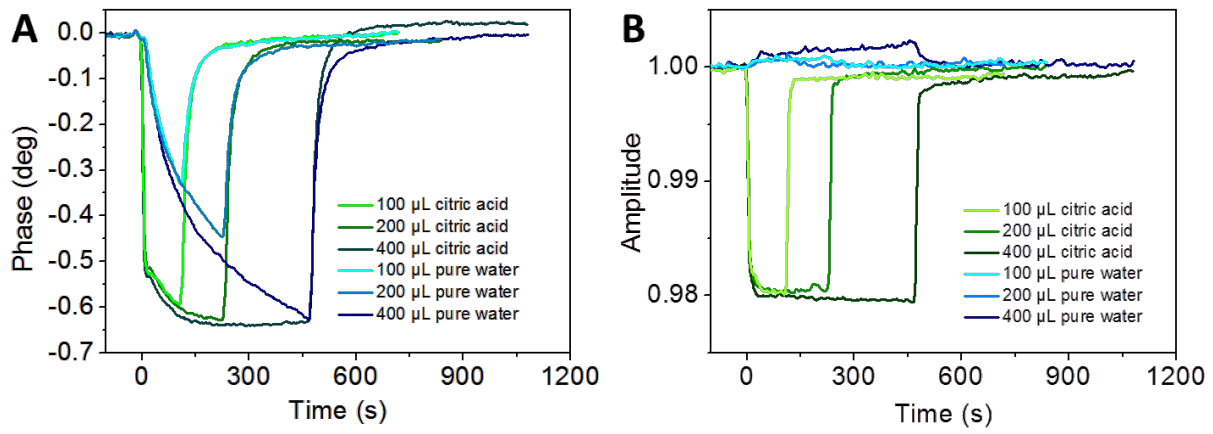


**Figure 3:** Monitoring of citric acid on calcium carbonate treated sensor surfaces. Phase (A) and corresponding amplitude (B) signal versus time for different injection volumes of 1 mM citric acid. Citric acid and pure water differ in their interaction with sensor chip surfaces in the presence of calcium carbonate.

Whether the temporary residence of citric acid molecules on the calcium carbonate layer can explain this behavior remains subject to further investigations. When 10 mM citric acid was used, the viscosity effect was even more pronounced and prevented reliable phase measurements (data not shown). We also tested the applicability of mass normalization based on integrated features provided by the commercial biosensor sam®X and the software SenseMaster [49]. An example for the experimental procedure is described in Supporting Information File 2. The phase vs time and amplitude vs time plots are shown in Figure 4.

Experimentally, the procedure is very fast and easy to perform, since the experiment is simply followed by an injection of an appropriate viscous substance. In this case, 5% aqueous glycerol was used. The calculation of the normalized mass signal is shown in Figure 5.

First, the "SenseMaster" software calculates a correction factor based on the phase difference between two values prior to and after the injection of the reference substance, arbitrarily selected by the user. For example, in the case of $t_1$ = 4200 s, and $t_2$ = 4700 s (Figure 4A), the phase difference for glycerol is 5.4° (Figure 5A). In the second step, this factor is used for calculating the normalized phase where, in principle, the "viscosity effect" should be eliminated. In the case of glycerol, the phase is normalized to −0.075° ± 0.074° ($\Delta t$ = −100–400 s, Figure 5B). The calculated phase ("mass normalized", Figure 5B) for calcium carbonate is decreased by the injection of citrate from −0.439° ± 0.015° to −1.363° ± 0.015° (mean values of 4 individual injections between 30–100 seconds). The respective amplitude signals are shown in Supporting Information File 2. These observations would be consistent with a relative mass loss, which is induced by the injection of citrate. This experiment provides first evidence that calcium carbonate interacts with the COO-SAM surface in the range of the solubility equilibrium, and that the molecular interactions could be quantified to some extent.

The procedure was experimentally established for biomolecular systems in order to evaluate the underlying theoretical calculations [49]. The same procedure, however, must not be used for calculating viscosity and mass effects in mineral systems, unless further experiments provide the evidence that interference with density and/or viscosity effects in such complex systems are negligible. Unless specifically mentioned, all data

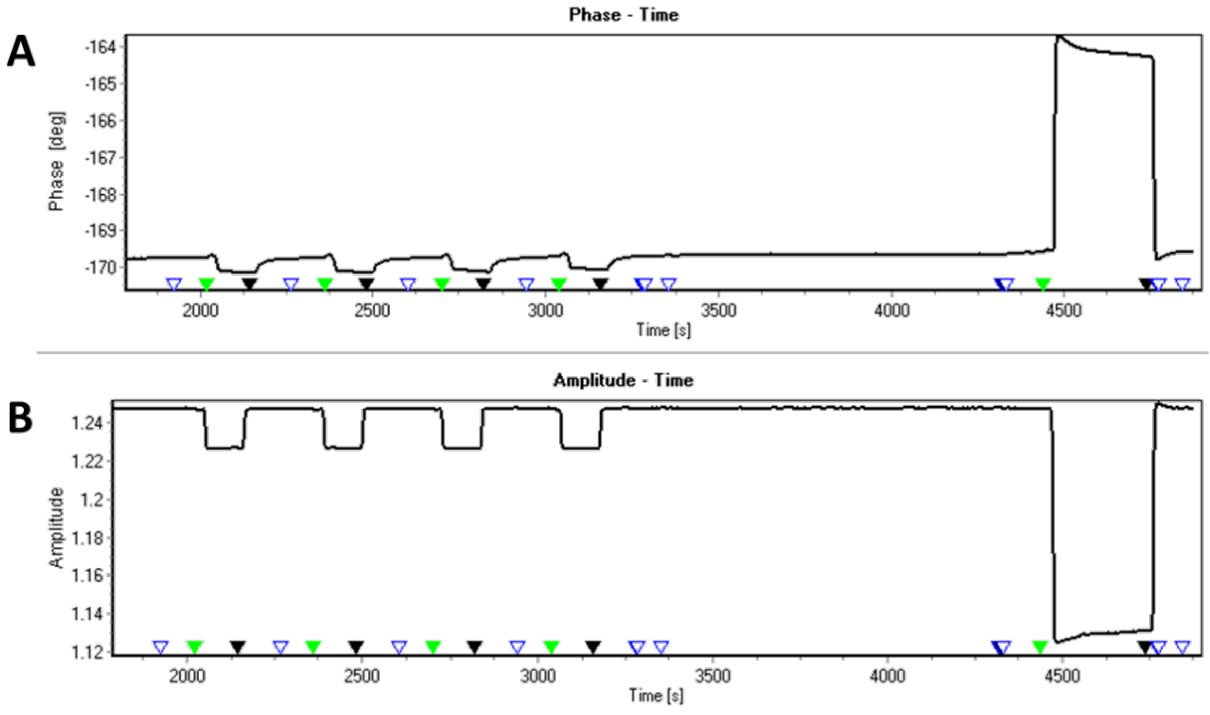


**Figure 4:** Experimental determination of the mass normalized phase signal in a citric acid/calcium carbonate system. A calcium carbonate running buffer was used here. Citric acid was injected for 120 seconds, followed by regeneration intervals of several minutes. Finally, 5% glycerol were injected. Green triangles, injection start; black triangle, end of injection.

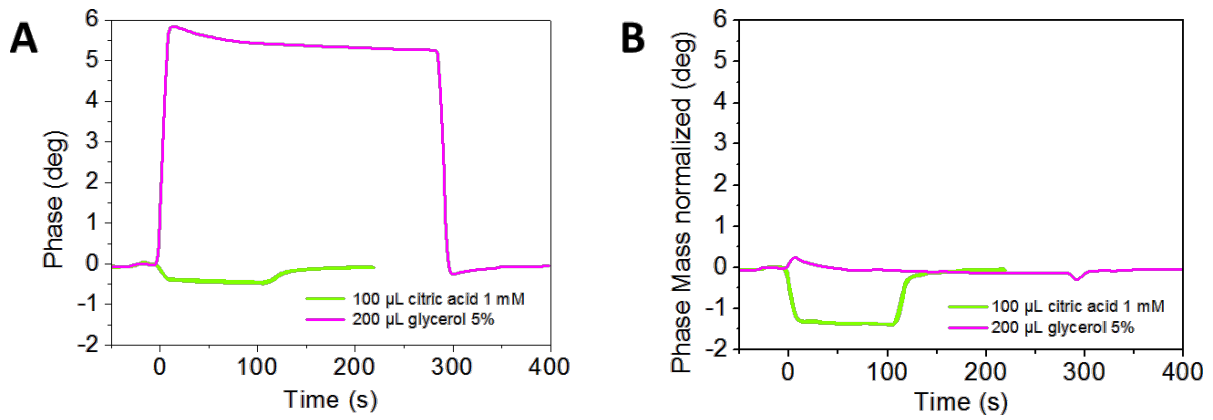


**Figure 5:** Comparison between the original phase signal and calculated mass normalized phase signal. The time-courses of all signals are aligned according to the injection start. The green lines represent an overlay of 4 citric acid injections as indicated in Figure 4. Note that these signals are extremely reproducible. The line in magenta represents the glycerol injection. (A), original phase signal; (B), calculated mass normalized phase signal. The glycerol signal in (A) was used for the software-automated calculation of all signals shown in (B).

sets shown in this paper represent the original measurements for both, phase and amplitude obtained without viscosity correction procedures.

## Cationic peptide interactions on COO-SAM

Two positively charged peptides, AS8 and ES9, were previously shown to produce calcium carbonate precipitates with characteristic complex morphologies as a function of pH [46]. We are interested to see whether these peptides also interact with negatively charged surfaces such as COO-SAM as a function of pH. We are also interested to see whether the molecular features of these peptides (pI 9, pI 10) could be differentiated by using the microfluidic biosensor system sam®X. The buffer substance glycylglycine (Gly–Gly) is used to maintain the pH values 7.75, 8.2 and 9.0, similar to the previous studies [46,48]. The peptide AS8 represents a modified version of the peptide ES9 with only two differences in the length and in the substitution of two glutamic acid residues by alanines [46]. Different concentrations of peptides (0 µM, 50 µM, 100 µM, 200 µM) are dissolved in Gly–Gly buffers and adjusted to pH values 7.75, 8.2 and 9.0. The highest concentration (200 µM) was used for the experiments presented here. In Table S4 (Supporting Information File 1), a representative experiment with peptides ES9 and AS8 in Gly–Gly buffer is listed. Experiments at pH 7.75, pH 8.2 and pH 9.0 were performed analogous on the same biosensor chip using separate channels. The flow rate was 40 µL/min and the running buffer was the respective Gly–Gly buffer. Between the injections of the peptides EDTA was injected. Volumes of 200 µL were injected if not otherwise indicated.

The three experiments with the different pH values are performed sequentially on separate channels of the same sam®X sensor chip. It was necessary to adjust the entire system to the same buffer conditions for Gly–Gly buffers pH 7.75, pH 8.2 or pH 9.0, in order to avoid uncontrolled response of the SAW sensor system when switching from the running buffer to injection mode. The peptide solutions were sequentially injected on the same channel, first ES9 and then AS8. The phase signals for 200 µM peptide injections according to Table S4 (Supporting Information File 1) are shown in Figure 6.

The observed maximum phase shift values depend on the pH. For both peptides, the maximum phase shifts are observed for pH 8.2. Taking all experiments into account, it is 1.4° ± 0.3° in the case of AS8 and 0.6° ± 0.5° in the case of ES9. The latter only reaches 0.24° ± 0,03 at pH 7.75 and 0.25° ± 0.03° at pH 9.0. Peptide AS8 reaches maximum values of approximately 0.78° ± 0.03° at pH 7.75 and 0.96° ± 0.09° at pH 9.0. These observations suggest that pH 8.2 provides conditions for both, the cationic peptides and the carboxylate-terminated COO-SAM, to have the maximum surface interaction. However, the maximum value represents steady-state conditions as long as peptide is continuously supplied. We also evaluated the difference between the initial phase value (setpoint: 0°) and the phase values at the time = 310 seconds, 10 seconds after the injections finished (Figure 6D). This difference indicates the amount of peptide that remains stably adsorbed to the surface. As shown in Figure 7, there is a trend for peptide ES9 indicating the peptide interaction is decreasing with increasing pH.

At pH 9, the interaction is lowest for both peptides. This is in agreement with simple calculations according to the Henderson–Hasselbalch equation [48], since most of the lysine residues are neutral under these conditions. The presence of negatively charged glutamic acid residues in peptide ES9 leads

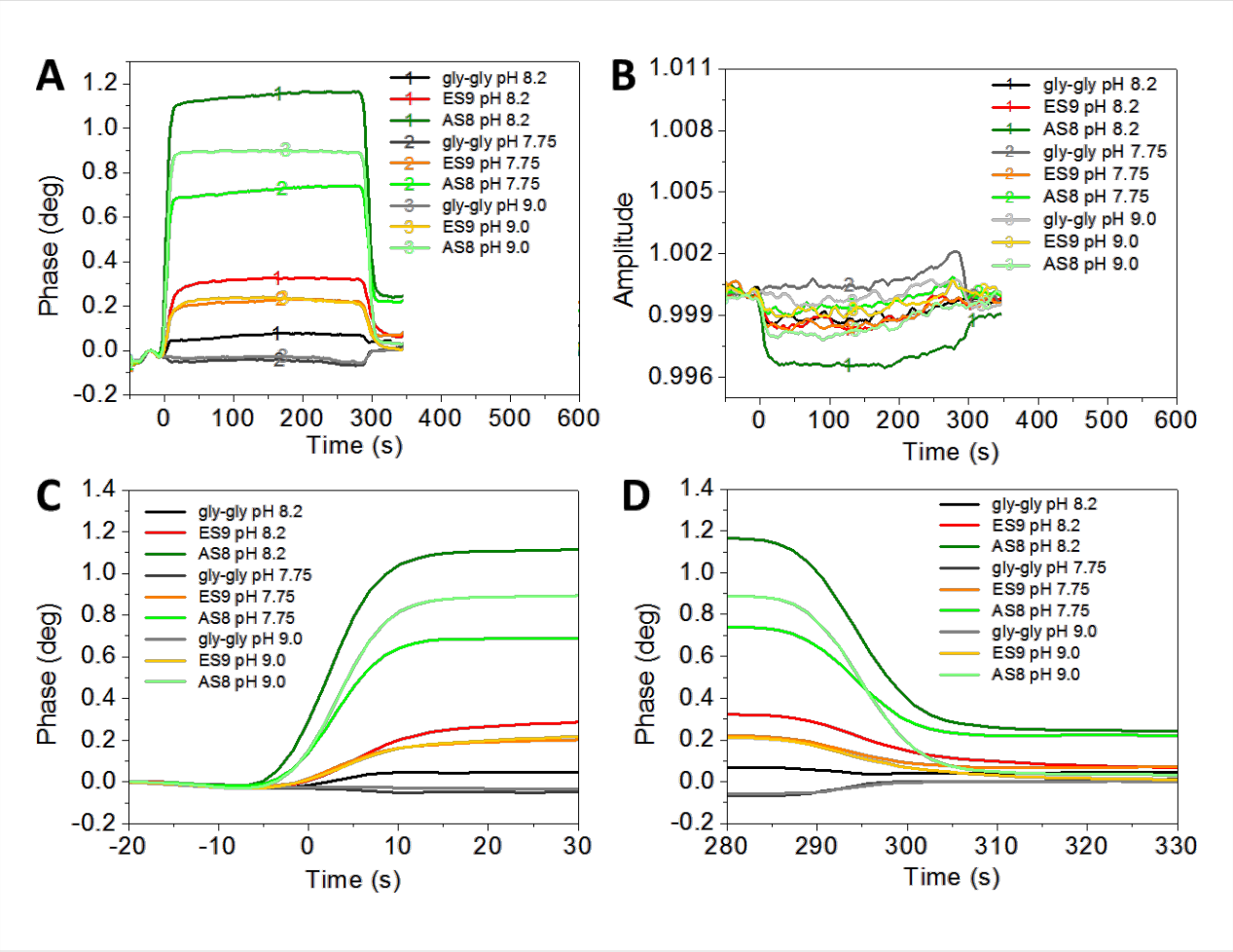


**Figure 6:** Monitoring of cationic peptides ES9 and AS8 on COO-SAM sensor surfaces. Phase (A) and corresponding amplitude (B) signal vs time for Gly–Gly pH 7.75, pH 8.2, or pH 9.0 with 200 µM peptides ES9 and AS8 (injection: 0–300 s). Graphs were produced by an overlay of data-sets (rows 2, 4, 6 of Table S4, Supporting Information File 1) at the time of injection (setpoint: 0 s). For clarity, the phase signals at the onset (C) and offset (D) of peptide injections are shown in time intervals of 50 seconds.

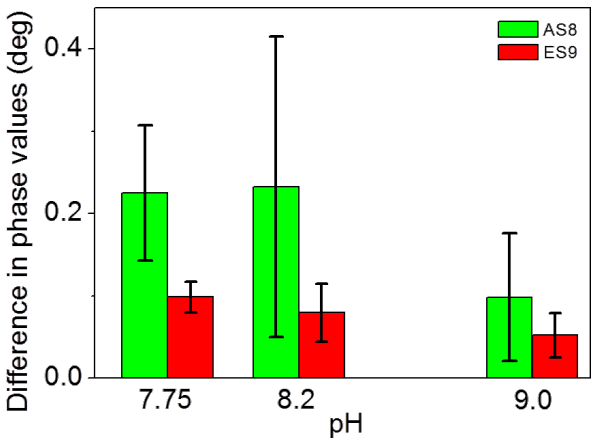


**Figure 7:** Evaluation of the phase difference prior and after injection of peptides as shown in Figure 6 A,C,D. For experimental values, see Supporting Information File 3.

to a reduction in the interaction with carboxyl-terminated SAM. As Figure 7 also shows, the AS8 has a larger variation in the phase difference, especially at pH 8.2. Previous results suggested that the peptide AS8 is not as well suited to gain control over calcium carbonate precipitation and crystal growth as the peptide ES9 [46]. Further work is required to elucidate the exact mechanisms in the case of AS8/$CaCO_3$ or ES9/$CaCO_3$ composites. However, the results as presented here suggest that the previously predicted pH-dependent interfacial interactions of each peptide species, which is intimately related to its sequence and pI, can be quantified by comparative sam®X biosensor experiments in order to predict which peptide sequences are more suitable to gain control over biomineralization in vitro and in vivo.

The initial slope prior to reaching the steady-state level (Figure 6A,C) is steeper for peptide AS8 (calculated pI ~10.4) as compared to the peptide ES9 (calculated pI ~9.2). We evalu-

ated both, the slopes at the time of injection (Figure 6C), and after the injection is finished (Figure 6D). The results for the injection of the peptides are shown in Figure 8.

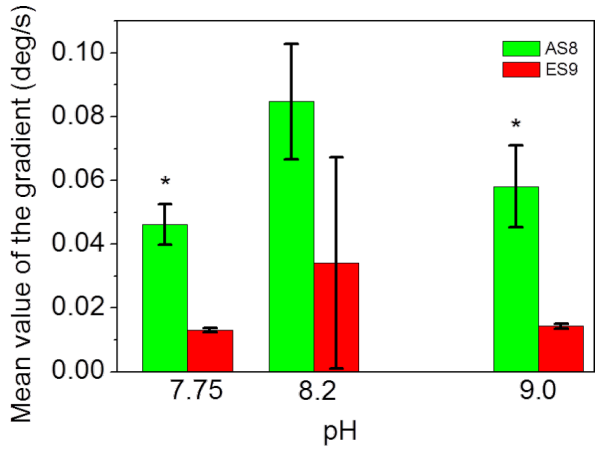


**Figure 8:** Evaluation of the slope observed in peptide experiments as shown in Figure 6C. For experimental values, see Supporting Information File 4.

This graph demonstrates that the two peptides, which differ in pI due to the exchange of glutamic acid residues (glu, E) against alanine residues (ala, A), flanking the penta-lysine core (N-EEKKKKKES-C vs N-AKKKKKAS-C) interact with carboxylates on the SAM-biosensor chip surface in a different way. The presence of the glutamic acid residues stabilizes the mode of interaction with the charged surface. When lysine residues are flanked by neutral amino acids, the interaction seems more likely to depend on pH. In the case of ES9, which represents the evolutionary optimized conserved sequence derived from the natural biomineralization system, the interaction seems to be less dependent on pH, suggesting a more robust control mechanism for the interfacial interaction of the tissue with the forming biomineral.

It remains subject to speculations whether, for example, pH-dependent peptide folding could favor interpeptide or intrapeptide interactions, which could also reduce the potential for interaction with the negatively charged COO-SAM surface. It was clearly shown in this experiment that the Gly–Gly buffer does not interfere significantly with the interfacial interactions of the positively charged penta-K (penta-lysine) peptides, and can therefore be regarded as a neutral agent which mainly serves for maintaining the pH. The fact that phase signals differed relatively to each other as function of pH further demonstrates that the buffer capacity of the chosen Gly–Gly system is sufficient to probe various environmental conditions in a convenient way.

## Conclusion

Biomineralization processes are very complex systems. They depend on evolutionary conserved, collective biomolecular interactions in fluidic systems, which are even more difficult to mimic when minerals are deposited or dissolved. Recently developed microfluidic biosensor systems provide promising perspectives for quantifying such biomolecular interactions under defined conditions. The biosensor sam®X (SAW Instruments, Bonn, Germany) used in this study combines a four channel microfluidic system with SAW detection and is equipped with an efficient software-driven access for automated sample processing and data analysis. The injection of a glycerol reference is a useful technique to separate the mass signal from the viscosity effect of the surrounding medium. In most cases the latter is represented by the amplitude signal. The mass deposited at the surface can be calculated from the viscosity normalized phase signal. As demonstrated here, this effect was marginal in the case of the purely aqueous calcium carbonate system. However, in the case of organic additives this may as well change. As a case study for a more complex system in biological buffers at various pH, we chose a peptide which was taken from an extracellular domain of the chitin synthases involved in biomineralization. A control peptide was designed with a slightly higher pI from glutamic acid residues, flanking a penta-lysine motif, were replaced by alanines. The pH-dependency of these peptides' interactions with calcium carbonate precipitation was previously demonstrated [46]. The in vitro systems tested so far were operated under saturated conditions by means of sodium bicarbonate and calcium chloride, thus suffering from additional salt effects. Only the finally obtained precipitate was analyzed further. The microfluidic biosensor experiments, in contrast to the previous study [46], bear the advantage of detecting mineral interactions prior to reaching the solubility equilibrium, as demonstrated here for the first time. So far, there are not many studies on biomineralization performed using microfluidic SAW sensor techniques [25]. We therefore started with calcium carbonate deposition on negatively charged standard SAMs. Our present results confirm that there are many parameters that determine the interaction of dissolved calcium carbonate with the carboxylate surface. The investigation of the cationic peptides AS8 and ES9 was therefore limited to the evaluation of the pH-dependency of COO-SAM interaction, but still in the absence of calcium carbonate. This system provides the chance to fine-tune parameters such as temperature, which also influences the solubility equilibrium, and flow rates. The influence of the buffer system can be monitored along with the samples of interest for direct comparison on the same chip. On the other hand, further experiments are necessary to interpret, for example, the difference in the dissolution of calcium carbonate by citric acid versus pure water. One has to be careful in terms of interpreting the large negative

amplitude signal of the citric acid experiments mainly as a viscosity effect as suggested by the manufacturer (SAW Instruments). The normalized mass signals presented in this study certainly require additional work to establish a reliable sensitivity factor ($\Delta S$, [$\mu g^{-1} \cdot cm^{2} \cdot °$]). As demonstrated here, the calcium carbonate concentration plays a significant role in the interaction with the carboxylate SAM, whereas the flow rate does not really matter unless it is very high. The possibility to investigate calcium carbonate solutions at much lower concentrations than the solubility equilibria of the respective mineral phase is particularly appealing to study the influence of peptides on mineral deposition in a buffer system similar to biomineralizing compartments. It can be concluded that multichannel microfluidic SAW sensor systems are highly attractive for biomimetic mineralization studies in liquids and in real-time. It remains subject to further investigations whether this technique will bring the desired break-through in terms of elucidating the structure–function relationships in biomineralization. Our possiblities to replicate biominerals, to create sustainable processes and to design bio-inspired new biocompatible materials with sophisticated structures and functions will certainly expand.

# Experimental

## Biosensor measurements

A commercial biosensor system sam®X (SAW Instruments, Bonn, Germany) equipped with carboxyl-terminated self-assembled monolayer (SAM) coated Au sensor chips (SAW Instruments, Bonn, Germany) was used in this study. The surface acoustic wave phase signal as well as the amplitude signal was recorded for each experiment. Calibration procedures followed exactly as described according to the manufacturer's instructions. The instrument was operated at 22 ± 1 °C.

The software packages SensMaster und SequenceMaster (SAW Instruments, Bonn, Germany) were used to control the biosensor sam®X. Automated features were used for programming and documentation of the experimental conditions. The software package FitMaster (SAW Instruments, Bonn, Germany) was used to analyze the collected data and to electronically align, for example, the time of injection for comparative analyses of different experiments.

The phase signal is sensitive to both, mass changes on the surface as well as viscosity changes in the adjacent medium. Since the amplitude signal is influenced almost exclusively by the viscosity effect, a corrected phase signal can be calculated using the software SensMaster (SAW Instruments, Bonn, Germany). For this purpose, the phase signal is recorded after injection of 5% glycerin in the respective running buffer. The software extracts the corrected phase signal based on the assumption that glycerin induces a change in viscosity only, but does not affect the mass signal. All data as shown in this paper represent the original raw data, unless otherwise indicated.

## Statistics

OriginPro 8.6G (OriginLab Corporation, Additive GmbH, Friedrichsdorf, Germany) was used for data handling and statistics. Data from 5 measurements (120 measured values) in the time interval prior to the injection (−140 seconds to −100 seconds) were avaraged in order to account for deviations caused by the instrument and initial alignment procedures (e.g., shaded box in Figure 1C). For individual experiments, 120 values measured during injections, between 100–300 seconds, and after injections, between 700–900 seconds were averaged. The Wilcoxon signed-rank test and sign test were used to determine statistical significance (p-value 0.05).

## Solutions and buffers

Ultra-pure water with a conductivity of <0.026 µS (Barnstead™ GenPure™ Pro; Thermo Fisher Scientific) was used for all experiments including the preparation of solutions and buffers. The latter were prepared at room temperature (20 ± 3 °C).

### Calcium carbonate solutions

Solid calcium carbonate (minimum 99.0%, Sigma-Aldrich, USA) was freshly dissolved at 100× the solubility product of 1.4 mg/L (20 °C) in pure water or in Gly–Gly buffers, which were previously adjusted to three different pH values pH 7.75, pH 8.2, or pH 9.0. The solid-free supernatant was used for experiments at 140 µmol/L and served as a stock solution for the respective dilution series.

### Peptides in Gly–Gly buffer

A 10 mM stock solution of peptides AS8 and ES9 (99% purity; GeneCust, Dudelange, Luxembourg) [46] was prepared in Gly–Gly buffers (20 mM glycylglycine, 350 mM NaCl, 10 mM KCl), previously adjusted to either pH 7.75, 8.2 or 9.0. Each peptide was diluted in the respective buffers to final concentrations of 50 µM, 100 µM or 200 µM.

### Citric acid

A 10 mM citric acid solution was prepared using 0.9% NaCl in pure water as the solvent. The pH was adjusted to pH 5.5 and diluted to a final concentration of 1 mM citric acid in order to reduce viscosity effects. This solution was also used in some experiments for regenerating the sensor chip after exposure to calcium carbonate.

### Ethylendiamintetraacetate (EDTA) solution

For regenerating the sensor chip after exposure to calcium carbonate, 1 mM and 10 mM EDTA solutions were prepared from a 0.5 M EDTA stock solution, pH 8.0 (146 g/L).

### Glycerol solution

For determining viscosity effects, a 5% glycerol solution was prepared in aqueous buffer.

## Supporting Information

### Supporting Information File 1

Experimental details.
[http://www.beilstein-journals.org/bjnano/content/supplementary/2190-4286-5-193-S1.pdf]

### Supporting Information File 2

Phase signal calculation using glycerol as reference.
[http://www.beilstein-journals.org/bjnano/content/supplementary/2190-4286-5-193-S2.pdf]

### Supporting Information File 3

Monitoring cationic peptides ES9 and AS8 on COO-SAM, experimental values, Table S5.
[http://www.beilstein-journals.org/bjnano/content/supplementary/2190-4286-5-193-S3.pdf]

### Supporting Information File 4

Monitoring cationic peptides ES9 and AS8 on COO-SAM, experimental values, Table S6.
[http://www.beilstein-journals.org/bjnano/content/supplementary/2190-4286-5-193-S4.pdf]

## Acknowledgements

The authors thank Miguel Jimenez, Thomas Gronewold and Mihaela Stumbaum for constructive comments during the initial experimental phase. The expert technical assistance of Christina Muth is kindly acknowledged. The authors acknowledge Jennifer Atchison, Tobias Kraus, and Andreas Schütze for valuable discussions and advice. This work would have been impossible without the continuous support of Eduard Arzt.

## References

1. Lowenstam, H. A.; Weiner, S. *On Biomineralization;* Oxford Univ. Press: New York, 1989.
2. Weiner, S.; Addadi, L. *Annu. Rev. Mater. Res.* **2011,** *41,* 21. doi:10.1146/annurev-matsci-062910-095803
3. Addadi, L.; Vidavsky, N.; Weiner, S. *Z. Kristallogr. – Cryst. Mater.* **2012,** *227,* 711. doi:10.1524/zkri.2012.1524
4. Alberts, B.; Johnson, A.; Lewis, J.; Raff, M.; Roberts, K.; Walter, P. *Molecular Biology of the Cell: Reference Edition,* 5th ed.; Garland Science: New York, 2007.
5. Mann, S. *Biomineralization: Principles and Concepts in Bioinorganic Materials Chemistry;* Oxford University Press: Oxford, 2001.
6. Knoll, A. H. *Rev. Mineral. Geochem.* **2003,** *54,* 329. doi:10.2113/0540329
7. Raven, J. A.; Knoll, A. H. *Geomicrobiol. J.* **2010,** *27,* 572. doi:10.1080/01490451003702990
8. Gao, H.; Ji, B.; Jäger, I. L.; Arzt, E.; Fratzl, P. *Proc. Natl. Acad. Sci. U. S. A.* **2003,** *100,* 5597. doi:10.1073/pnas.0631609100
9. Weiss, I. M.; Marin, F. In *Met. Ions Life Sci. - Biomineralization: From Nature to Application;* Sigel, A.; Sigel, H.; Sigel, R. K. O., Eds.; John Wiley & Sons: West Sussex, UK, 2008; Vol. 4.
10. Meldrum, F. C.; Cölfen, H. *Nanoscale* **2010,** *2,* 2326. doi:10.1039/c0nr90029j
11. Addadi, L.; Joester, D.; Nudelman, F.; Weiner, S. *Chem. – Eur. J.* **2006,** *12,* 980. doi:10.1002/chem.200500980
12. Addadi, L.; Politi, Y.; Nudelman, F.; Weiner, S. Biomineralization design strategies and mechanisms of mineral formation: operating at the edge of instability. In *Engineering of Crystalline Materials Properties State of the Art in Modeling, Design and Applications;* Novoa, J. J.; Braga, D.; Addadi, L., Eds.; NATO Science for Peace and Security Series B: Physics and Biophysics; Springer: Dordrecht, The Netherlands, 2008; pp 1–15. doi:10.1007/978-1-4020-6823-2
13. Falini, G.; Albeck, S.; Weiner, S.; Addadi, L. *Science* **1996,** *271,* 67. doi:10.1126/science.271.5245.67
14. Suzuki, M.; Iwashima, A.; Kimura, M.; Kogure, T.; Nagasawa, H. *Mar. Biotechnol.* **2013,** *15,* 145. doi:10.1007/s10126-012-9471-2
15. Marin, F.; Le Roy, N.; Marie, B. *Front. Biosci., Scholar Ed.* **2012,** *4S,* 1099. doi:10.2741/S321
16. Marie, B.; Joubert, C.; Tayalé, A.; Zanella-Cleón, I.; Belliard, C.; Piquemal, D.; Cochennec-Laureau, N.; Marin, F.; Gueguen, Y.; Montagnani, C. *Proc. Natl. Acad. Sci. U. S. A.* **2012,** *109,* 20986. doi:10.1073/pnas.1210552109
17. Marie, B.; Ramos-Silva, P.; Marin, F.; Marie, A. *Proteomics* **2013,** *13,* 3109. doi:10.1002/pmic.201300162
18. Levi-Kalisman, Y.; Falini, G.; Addadi, L.; Weiner, S. *J. Struct. Biol.* **2001,** *135,* 8. doi:10.1006/jsbi.2001.4372
19. Miyamoto, H.; Endo, H.; Hashimoto, N.; Limura, K.; Isowa, Y.; Kinoshita, S.; Kotaki, T.; Masaoka, T.; Miki, T.; Nakayama, S.; Nogawa, C.; Notazawa, A.; Ohmori, F.; Sarashina, I.; Suzuki, M.; Takagi, R.; Takahashi, J.; Takeuchi, T.; Yokoo, N.; Satoh, N.; Toyohara, H.; Miyashita, T.; Wada, H.; Samata, T.; Endo, K.; Nagasawa, H.; Asakawa, S.; Watabe, S. *Zool. Sci.* **2013,** *30,* 801. doi:10.2108/zsj.30.801
20. Weiss, I. M. *Z. Kristallogr. – Cryst. Mater.* **2012,** *227,* 723. doi:10.1524/zkri.2012.1530
21. Meldrum, F. C.; Cölfen, H. *Chem. Rev.* **2008,** *108,* 4332. doi:10.1021/cr8002856
22. Yang, X.; Xie, B.; Wang, L.; Qin, Y.; Henneman, Z. J.; Nancollas, G. H. *CrystEngComm* **2011,** *13,* 1153. doi:10.1039/c0ce00470g
23. Borah, B. M.; Halter, T. J.; Xie, B.; Henneman, Z. J.; Siudzinski, T. R.; Harris, S.; Elliott, M.; Nancollas, G. H. *J. Colloid Interface Sci.* **2014,** *425,* 20. doi:10.1016/j.jcis.2014.03.029
24. Nielsen, M. H.; Li, D.; Zhang, H.; Aloni, S.; Han, T. Y.-J.; Frandsen, C.; Seto, J.; Banfield, J. F.; Cölfen, H.; De Yoreo, J. J. *Microsc. Microanal.* **2014,** *20,* 425. doi:10.1017/S1431927614000294
25. De Yoreo, J. J., Ed. *Research Methods in Biomineralization Science;* Academic Press: Waltham, San Diego, USA, 2013; Vol. 532.
26. Israelachvili, J. N. *Intermolecular and Surface Forces;* Academic Press: Waltham, San Diego, USA, 2011.
27. Gebauer, D.; Kellermeier, M.; Gale, J. D.; Bergström, L.; Cölfen, H. *Chem. Soc. Rev.* **2014,** *43,* 2348. doi:10.1039/c3cs60451a
28. Verch, A.; Gebauer, D.; Antonietti, M.; Cölfen, H. *Phys. Chem. Chem. Phys.* **2011,** *13,* 16811. doi:10.1039/c1cp21328h

29. Perpeet, M.; Glass, S.; Gronewold, T.; Kiwitz, A.; Malavé, A.; Stoyanov, I.; Tewes, M.; Quandt, E. *Anal. Lett.* **2006,** *39,* 1747. doi:10.1080/00032710600671406
30. Ruppel, C. C. W.; Fjeldly, T. A. *Advances in Surface Acoustic Wave Technology, Systems and Applications;* World Scientific Publishing Co. Pte. Ltd.: Singapore, 2001.
31. Jung, A.; Gronewold, T. M. A.; Tewes, M.; Quandt, E.; Berlin, P. *Sens. Actuators, B* **2007,** *124,* 46. doi:10.1016/j.snb.2006.11.040
32. Hoummady, M.; Campitelli, A.; Wlodarski, W. *Smart Mater. Struct.* **1997,** *6,* 647. doi:10.1088/0964-1726/6/6/001
33. Freund, L. B.; Suresh, S. *Thin Film Materials: Stress, Defect Formation and Surface Evolution;* Cambridge University Press: Cambridge, UK, 2009.
34. Andle, J. C.; Vetelino, J. F. *Sens. Actuators, A* **1994,** *44,* 167. doi:10.1016/0924-4247(94)00801-9
35. Gronewold, T. M. A. *Anal. Chim. Acta* **2007,** *603,* 119. doi:10.1016/j.aca.2007.09.056
36. Cui, J.; Iturri, J.; Götz, U.; Jimenez, M.; del Campo, A. *Langmuir* **2013,** *29,* 6582. doi:10.1021/la401014q
37. Länge, K.; Rapp, B. E.; Rapp, M. *Anal. Bioanal. Chem.* **2008,** *391,* 1509. doi:10.1007/s00216-008-1911-5
38. Joseph, S.; Gronewold, T. M. A.; Schlensog, M. D.; Olbrich, C.; Quandt, E.; Famulok, M.; Schirner, M. *Biosens. Bioelectron.* **2005,** *20,* 1829. doi:10.1016/j.bios.2004.07.014
39. Kellermeier, M.; Cölfen, H.; Gebauer, D. *Methods Enzymol.* **2013,** *532,* 45. doi:10.1016/B978-0-12-416617-2.00003-5
40. Weiss, I. M.; Kaufmann, S.; Mann, K.; Fritz, M. *Biochem. Biophys. Res. Commun.* **2000,** *267,* 17. doi:10.1006/bbrc.1999.1907
41. Weber, E.; Guth, C.; Weiss, I. M. *PLoS One* **2012,** *7,* e46653. doi:10.1371/journal.pone.0046653
42. Weber, E.; Bloch, L.; Guth, C.; Fitch, A. N.; Weiss, I. M.; Pokroy, B. *Chem. Mater.* **2014,** *26,* 4925. doi:10.1021/cm500450s
43. Gotliv, B.-A.; Addadi, L.; Weiner, S. *ChemBioChem* **2003,** *4,* 522. doi:10.1002/cbic.200200548
44. Pokroy, B.; Aizenberg, J. *CrystEngComm* **2007,** *9,* 1219. doi:10.1039/b710294a
45. Pokroy, B.; Chernow, V. F.; Aizenberg, J. *Langmuir* **2009,** *25,* 14002. doi:10.1021/la902739q
46. Sengupta Ghatak, A.; Koch, M.; Guth, C.; Weiss, I. M. *Int. J. Mol. Sci.* **2013,** *14,* 11842. doi:10.3390/ijms140611842
47. Weiss, I. M.; Schönitzer, V.; Eichner, N.; Sumper, M. *FEBS Lett.* **2006,** *580,* 1846. doi:10.1016/j.febslet.2006.02.044
48. Weiss, I. M.; Lüke, F.; Eichner, N.; Guth, C.; Clausen-Schaumann, H. *J. Struct. Biol.* **2013,** *183,* 216. doi:10.1016/j.jsb.2013.04.011
49. Tewes, M.; Glaß, S.; Schlensog, M. D.; Quandt, E. Mass determination method for measuring the mass acting on a surface acoustic wave sensor, e.g., for use in micro-weighing scales, whereby a calibration is first carried out using an analyte. Ger. Pat. Appl. DE102004006823A1, Sept 1, 2005.

## License and Terms

BEILSTEIN JOURNAL OF NANOTECHNOLOGY

# Electrostatic interplay: The interaction triangle of polyamines, silicic acid, and phosphate studied through turbidity measurements, silicomolybdic acid test, and $^{29}$Si NMR spectroscopy

Anne Jantschke, Katrin Spinde and Eike Brunner*

Full Research Paper

Open Access

Address:
TU Dresden, Fachrichtung Chemie und Lebensmittelchemie, Bioanalytische Chemie, 01062 Dresden, Germany

Email:
Eike Brunner* - eike.brunner@chemie.tu-dresden.de

* Corresponding author

Keywords:
phosphate; self-assembly; silica–polyamine interactions; silicomolybdic acid test; $^{29}$Si NMR; turbidity measurements

*Beilstein J. Nanotechnol.* **2014,** *5,* 2026–2035.
doi:10.3762/bjnano.5.211

Received: 10 June 2014
Accepted: 14 October 2014
Published: 06 November 2014

This article is part of the Thematic Series "Towards multifunctional inorganic materials: biopolymeric templates".

Guest Editors: C. Steinem and J. Bill



## Abstract

The discovery of long-chain polyamines as biomolecules that are tightly associated to biosilica in diatom cell walls has inspired numerous in vitro studies aiming to characterize polyamine–silica interactions. The determination of these interactions at the molecular level is of fundamental interest on one hand for the understanding of cell wall biogenesis in diatoms and on the other hand for designing bioinspired materials synthesis approaches. The present contribution deals with the influence of amines and polyamines upon the initial self-assembly processes taking place during polyamine-mediated silica formation in solution. The influence of phosphate upon these processes is studied. For this purpose, sodium metasilicate solutions containing additives such as polyallylamine, allylamine and others in the presence/absence of phosphate were investigated. The analyses are based mainly on turbidity measurements yielding information about the early aggregation steps which finally give rise to the formation and precipitation of silica.

## Introduction

Long-chain polyamines (LCPAs) were previously found biomolecules that are tightly associated to the biosilica of various diatom species [1-5]. They consist of linear oligopropyleneimine chains attached to putrescine or spermine [5,6]. Biosilica-associated LCPAs occur either as free molecules [1,4] or covalently attached to the ε-amino groups of certain lysine-residues [7,8] in highly post-translationally modified peptides, so-called silaffins [7-10]. It is, furthermore, remarkable that the

amine moieties in LCPAs from diatoms are partially methylated. The degree of methylation depends on the diatom species. LCPAs have also been identified in the silica spicules of sponges [11] and thus appear to be a general component for biological silica formation. In vitro experiments with LCPAs extracted from diatom biosilica revealed that these molecules are capable of enhancing the silica precipitation from silicic acid solutions [2,5]. It is very remarkable that the silica precipitation process is extremely rapid if the solutions contain phosphate or other suitable counterions in addition to LCPAs and silicic acid [2,3,12]. These observations have inspired numerous in vitro investigations to understand the underlying self-assembly processes and interactions [13-30]. Corresponding in vitro investigations using polyallylamine (in form of polyallylamine hydrochloride, PAH) as a synthetic analogue [15] for native LCPAs revealed that phosphate is capable of inducing the self-assembly of PAH into large aggregates that could be detected by dynamic light scattering (DLS) experiments [16,17]. Self-assembled PAH aggregates were shown to strongly enhance the speed of silica precipitation, which takes place at a time scale of seconds or minutes. In the absence of phosphate, solutions containing polyallylamine and silicic acid are capable of forming so-called polyamine-stabilized silica sols [18]. These stabilized sols exhibit particles of 30–50 nm diameter, which remain stable up to 24 h. In the relevant pH range of 5–7, monosilicic acid is an uncharged molecule, $Si(OH)_4$ [31]. However, monosilicic acid ($pK_a \approx 9.8$) spontaneously transforms into higher oligomers and silica particles ($pK_a \approx 6–7$) [19] which exhibit a negative surface charge in solution. It was, therefore, suggested that the stabilized sol consists of polyamine–silica nanoparticle superstructures resulting from a self-assembly process driven by attractive interactions between positively charged polyamines and negatively charged silica particles [18,20]. Subsequent in vitro studies support the idea of polyamine-stabilized sols [21,22]. In contrast to the charged PAH, uncharged polymers such as polyvinylpyrrolidone or polyethylene glycol cannot undergo such a self-assembly process driven by electrostatic interactions [23,24]. However, they interact with the silicic acid/silica species via hydrogen bonding and possibly hydrophobic interactions. These interactions even result in the stabilization of mono- and disilicic acid species [22,23]. The described observations have meanwhile lead to numerous biomimetic or bioinspired silica synthesis approaches [21,25-32].

The addition of negatively charged phosphate ions (see above) to pure LCPA solutions has already been studied in detail. Phosphate results in a cross-linking of the positively charged LCPAs. The resulting self-assembly processes give rise to the formation of a microemulsion finally leading to macroscopic phase separation. It was concluded that the phosphate-driven self-assembly processes are accelerating the silica-precipitation processes. However, the self-assembly processes going on in LCPA/silicic acid/phosphate solutions have not yet been studied in detail — in contrast to the pure LCPA/phosphate system [12,16,17]. Further understanding of the molecular interactions between polyamines, silicic acid/silica species and phosphate is, therefore, a rewarding research topic. The aim of the present study is the analysis of the influence of the polyamine structure and charge upon the polycondensation of silicic acid in the absence and presence of phosphate. The kinetics of the aggregation and silica polycondensation processes were studied by a combination of turbidity measurements and silicomolybdic acid test [31,33,34]. The study includes the monomeric allylamine, its fully methylated analogue allyltrimethylammonium bromide (allylamineQ) and the widely used long-chain model polyamine poly(allylamine) hydrochloride (PAH). Moreover, a homologous series of diamines with different degree of methylation was studied in order to visualize the possible influence of hydrophobic interactions. For $^{29}$Si NMR spectroscopy aqueous solutions of isotope-labelled sodium [$^{29}$Si] metasilicate as precursor compound were used. Different silica precursors, such as toxic TMOS (tetramethyl orthosilicate) or TEOS (tetraethyl orthosilicate), have been used for previous in vitro experiments. Here we used the biorelevant sodium metasilicate as silicic acid precursor. Sodium metasilicate dissolves in water to silicic acid ($Na_2SiO_3 + 3H_2O \rightarrow Si(OH)_4 + NaOH$) at a pH value of 11.5–12.5 and can subsequently be acidified. Another benefit of using sodium metasilicate is the relatively high sodium concentration since it is known that silicon uptake and transport are connected with the sodium metabolism of diatoms [35,36].

## Results and Discussion

Two of the most important parameters influencing the polycondensation reaction of silicic acid [31] are concentration [37] and pH value [38]. The maximum polycondensation rates occur around pH 7 [31,38]. It should be noted that the formation of diatom cell walls takes place in the so-called silica deposition vesicle (SDV) with an internal pH of 5–6 [39-42]. Previous in vitro experiments were carried out by Sumper et al. at pH 6.8 [3,27]. Other experimentalists have chosen pH 5.5 [2,23,24]. We have therefore carried out experiments at both pH values, ca. 7 and 5.5.

At pH > 12, the silicic acid solutions (in the form of silicate) remain stable even at high concentrations [23,31]. The same is true under very acidic conditions. However, $^{29}$Si HR NMR measurements (Figure 1) of sodium metasilicate solutions without any additive reveal that the state of the silicic acid is different for the basic (pH 12.5) and the acidic environment (pH 1.95). In the basic environment, the signals of $Q_0$ and $Q_1$

are dominating the spectrum ($Q_n$ = $Si(OSi)_n(OH)_{4-n}$, $n$ = 0–4) [43]. Note that highly mobile species exhibit narrow signals as observed in basic solution. In contrast, the spectrum of the acidic solution already exhibits the $Q_2$, $Q_3$, and $Q_4$ signals characteristic for higher oligomers which are broadened due to an increasing degree of immobilization. That means the condensation reaction is more advanced in the acidic solution whereas the basic solution mainly consists of $Q_0$ and $Q_1$ species. It should be noted that these two species are rapidly interconverting. The sum of $Q_0$ and $Q_1$ represents the so-called "soluble silica" and can be detected by the silicomolybdic acid test reaction [31,33,34]. In the basic solution, practically all silica is soluble, i.e., molybdate-reactive. For this reason, our experiments were carried out starting from a basic sodium metasilicate solution.

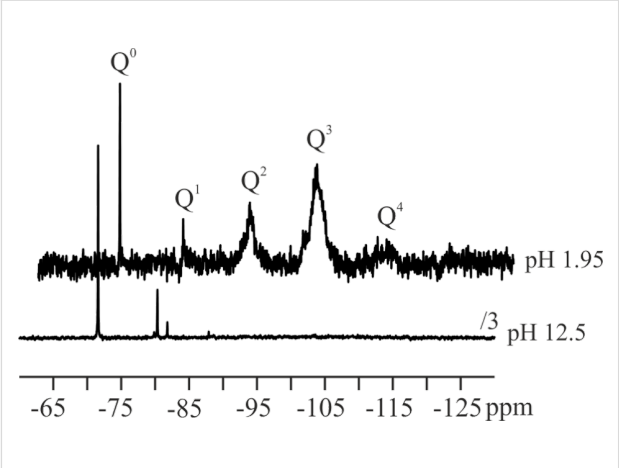


**Figure 1:** $^{29}Si$ HR NMR spectra of the control stock solution (75 mM $SiO_2$) in acidic and basic solution.

Figure 2 shows the concentration of soluble silica as a function of pH determined by the silicomolybdic acid test. A pure sodium metasilicate solution and a solution containing sodium metasilicate and PAH are compared. The interaction between silicic acid/silica species and PAH is assumed to be mediated by the $NH_2$ groups. Therefore, the PAH concentration was chosen to obtain a Si/N ratio of 1:1. In the pure sodium metasilicate solution, all silica is detected by the silicomolybdic acid test reaction at pH 11.5. However, the amount of soluble silica steadily decreases with decreasing pH. In the pH range of 5–7, more than 95% of the initial silicic acid are present in the form of insoluble silica. This is the result of the silica polycondensation reaction, which transforms soluble silica species into insoluble silica species, i.e., higher oligomers or silica nanoparticles. Such insoluble silica species are not detected by the silicomolybdic acid test. It is remarkable that the presence of PAH strongly influences the amount of soluble silica, i.e., the silica polycondensation reaction. The concentration of soluble silica in the PAH-containing sample is always lower than in the PAH-free control. The most pronounced difference between the pure and the PAH-containing sodium metasilicate solution occurs in the pH range between 11.5 and 8.5. The p$K_a$ of PAH amounts to ca. 9.7 [44,45] and the p$K_a$ of $Si(OH)_4$ to circa 9.8. That means PAH is positively charged for pH < 9.7 and $Si(OH)_4$ is negatively charged for pH > 9.8. Hence, purely electrostatic interactions between the polyamine and monosilicic acid cannot be expected.

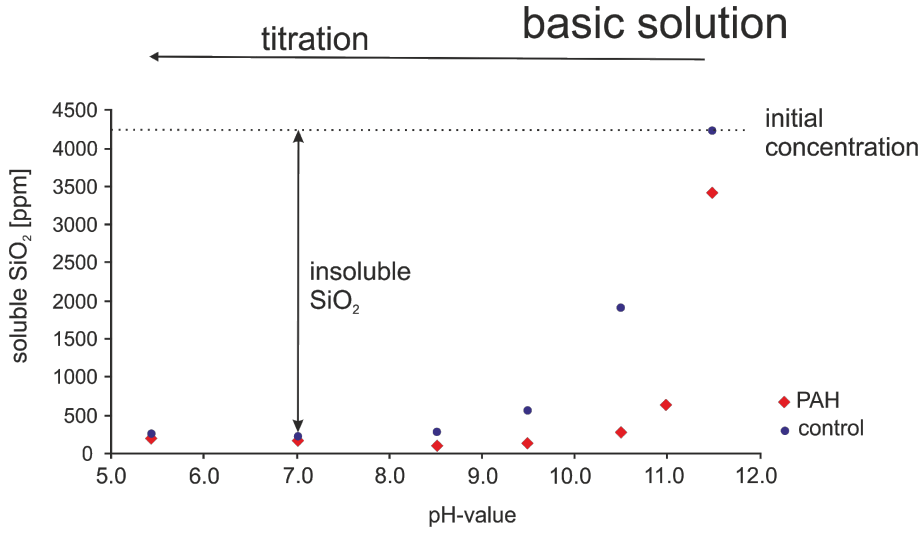


**Figure 2:** Soluble silicic acid concentration at different pH values in the presence (red rhombuses) and absence (control, blue circles) of PAH. $SiO_2$ concentration 70 mM (4200 ppm); PAH concencation 0.45 mM. The silicomolybdic acid test reaction was performed 30 min after sample preparation/pH titration.

In contrast to monosilicic acid, higher silicic acid oligomers/silica nanoparticles exhibit lower p$K_a$ values. For fumed silica, two different types of silanol groups are reported with p$K_a$ values of ca. 8 and 4.5 [46,47]. It can therefore be assumed that, in the relevant pH range of 5–7, the silica nanoparticles exhibit a negative surface charge. Electrostatic interactions will, therefore, occur between the positively charged polyamine and negatively charged higher silicic acid oligomers/silica nanoparticles below the p$K_a$ of PAH. The resulting immobilization of higher silicic acid oligomers could indeed be observed by $^{29}$Si NMR spectroscopy previously [23]. The soluble silica (mono- and disilicic acid) is almost completely polycondensed into insoluble species (higher silica oligomers/nanoparticles) below pH 9 after 30 min in pure sodium metasilicate as well as the PAH containing sample (see Figure 2). The PAH-containing sample exhibits a white precipitate whereas the pure sodium metasilicate solution has formed a gel.

## Turbidity measurements

Turbidity measurements provide a simple possibility for the time-resolved study of self-assembly processes in solutions containing organic molecules and silicic acid as has been demonstrated by Robinson et al. [48]. The process of self-assembly and silica polycondensation reaction increases the turbidity of the solution, which causes an increasing absorption. This property can easily be determined with a spectrophotometer and provides a measure for the speed of the ongoing aggregation processes [48,49]. Moreover, the turbidity, i.e., the absorbance is influenced by the size and number of aggregates formed in solution. We chose 90 mM silicic acid concentration for measurements at a reasonable timescale (up to 800 min) following Robinson et al. [48]. The silica polycondensation is very fast at the PAH concentrations applied in the experiments as shown in Figure 2 (0.45 mM) in the relevant pH range between 5 and 7. Hence, we have decreased the PAH concentration down to 31.25 µM in order to prevent rapid silica precipitation at the timescale of the turbidity measurements. The results are shown in Figure 3.

Figure 3 displays the absorbance of a solution with pure sodium metasilicate solution (90 mM silicic acid) and a solution with 90 mM silicic acid plus 31.25 µM PAH at pH values of 5.5 and 6.8. The absorbance of the pure sodium metasilicate solution increases much faster at pH 6.8 than at pH 5.5. This is obviously due to the fact that the maximum speed of silica polycondensation is expected around pH 7. The addition of PAH to the sodium metasilicate solutions strongly enhances the absorbance at pH 6.8. That means the polyamine additive pronouncedly accelerates the aggregation process, which can be explained by the electrostatic interactions between the positively charged PAH and negative surface charges of higher silica oligomers/silica nanoparticles rapidly forming at pH 6.8. At pH 5.5, the absorbance for both samples slowly increases after an induction period of ca. 100 min. In contrast to the behavior found at pH 6.8, the addition of PAH has almost no effect at pH 5.5, the absorption of the PAH-containing sample is even slightly smaller than in the control solution. It is remarkable that this rather small change of pH by 1.3 units gives rise to such a pronounced change in the aggregation behavior. The two samples exhibit an identical overall composition except for the pH and amount of chloride resulting from the titration with HCl. With respect to the charges of the aggregating molecules, the change in pH will result in the following: The total charge of PAH may become slightly more positive. For monomeric allylamine, the p$K_a$ value is known to be 9.49. That means allylamine would be positively charged at both pH values, 5.5. and 6.8. However, the p$K_a$ values of polyallylamine, i.e., of allylamine in its polymeric form, are likely to be different from the

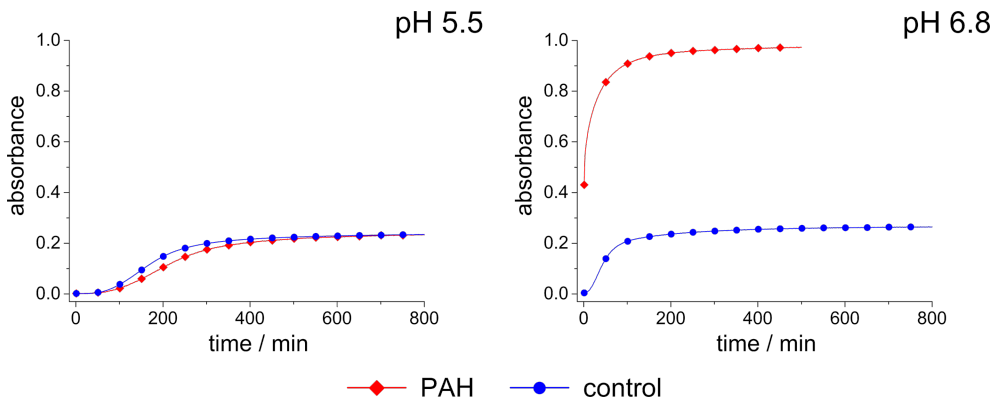


**Figure 3:** Absorbance of a 90 mM sodium metasilicate solution with 31.25 µM PAH (red rhombuses) and of a pure sodium metasilicate solution (control, blue circles) measured as a function of time up to 800 min.

monomer. Kobayashi et al. and Rao et. al. estimated a p$K_a$ value of 9.7 for polyallylamine [44,45]. The real charge state of PAH is yet hardly predictable, but it should be supposed that a decreasing pH results in an increasingly positive charge. Moreover, the silica oligomers/nanoparticles in solution are supposed to exhibit a decreasingly negative surface charge at decreasing pH. If so, the repulsion among the increasingly positive PAH molecules would not be compensated by attractive forces with the negatively charged silica oligomers/nanoparticles. Consequently, the aggregation process would be suppressed below a certain pH, as is indeed observed for pH 5.5. If the lack of negative charges is indeed the problem, the capability of the system to self-aggregate should be restored by the introduction of negatively charged ions that themselves do not destructively interfere with the PAH/silica system. This should be the case for phosphate, which is already known to enhance silica precipitation from polyamine/silicic acid solutions. The influence of phosphate upon the sample at pH 5.5 is demonstrated in Figure 4. As predicted, the phosphate-containing solution exhibits a rapidly increasing, strong absorbance which indicates aggregate formation. In the case of the PAH-free control sample, the negatively charged phosphate has the opposite effect: The aggregation becomes even slower than in the phosphate-free sodium metasilicate solution (cf. Figure 3). This can be explained by the fact that the repulsion among the silica oligomers/nanoparticles with their negative surface charge and the phosphate ions further retards the aggregation processes. It can, therefore, be concluded that charge balance is one major parameter determining the speed of aggregation in the polyamine–silica system. Perturbed charge balance can be restored at decreasing pH by introducing phosphate or other appropriate anions into the solutions.

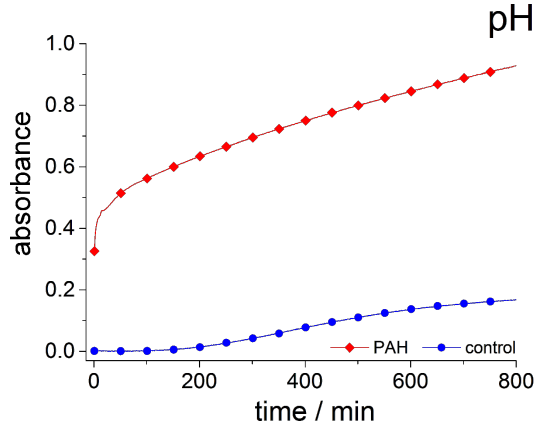


**Figure 4:** Absorbance of a 90 mM sodium metasilicate solution with 31.25 μM PAH and 180 mM hydrogen phosphate (red rhombuses) and of a sodium metasilicate solution 90 mM containing 180 mM hydrogen phosphate (control, blue circles) measured as a function of time up to 800 min.

We have also studied sodium metasilicate solutions containing monomeric allylamine (p$K_a$ ≈ 9.5) at the same Si/N ratio as in the PAH-containing solutions shown in Figure 3 and Figure 4 in order to elucidate possible differences between the polymeric and monomeric compounds. Moreover, monomeric allylamineQ was also used in order to analyse the influence of a quaternary ammonium group with its pH-independent, permanently positive charge surrounded by three hydrophobic methyl groups. The result of the corresponding turbidity measurements at pH 6.8 is shown in Figure 5. First of all, it is evident that the monomeric compounds are much less efficient than the polymer, PAH, in inducing the aggregation process at pH 6.8. This observation agrees with previous studies performed by Behrens et al. [50] on other polyamines. It should be noted that allylamineQ is slightly more efficient than allylamine at pH 6.8 although the charge state of both molecules should be the same (+1 elementary charges).

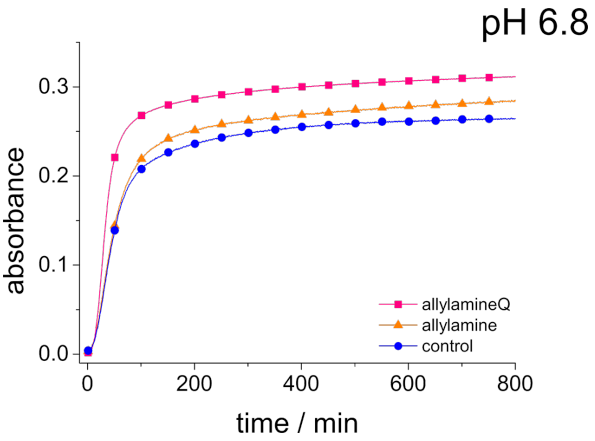


**Figure 5:** Absorbance of a 90 mM sodium metasilicate solution with 10 mM allylamine (orange triangles), 10 mM allylamineQ (pink squares) and of a sodium metasilicate solution (control, blue circles) measured as a function of time up to 800 minutes.

An explanation for the higher turbidity induced by allylamineQ compared with allylamine could be the influence of hydrophobic interactions induced by the methyl groups. This effect has already been described by Robinson et al. [48] when studying the turbidity of polyamines with different degree of methylation in solution. Interestingly, long-chain polyamines in diatoms are sometimes methylated and lysine residues in silaffins occur as trimethyllysine. It is, therefore, likely that methylation of amine moieties is an important parameter for self-assembly processes. In order to further substantiate this effect, a series of diamines with different degree of methylation was studied, the compounds and their charge state are described in Table 1. The absorbance of sodium metasilicate solutions containing these additives are displayed in Figure 6. The solution containing the compound TMEDA with two methyl groups

**Table 1:** Diamines used in the turbidity measurements and their calculated fractions of the charge states at pH 7.

| pH 7 | fraction of charge states [%] | | |
|---|---|---|---|
| EN | 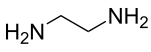 | 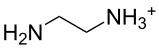 | 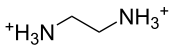 |
| | 0.04 | 50.56 | 49.40 |
| MEEN | 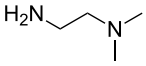 | 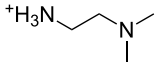 | 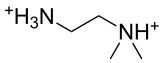 |
| | 0.21 | 69.95 | 29.84 |
| ENQ | 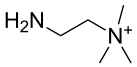 | 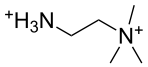 | — |
| | 40.34 | 59.66 | |
| TMEDA | 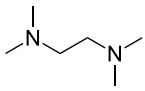 | 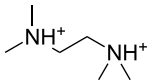 | 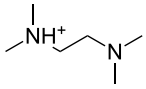 |
| | 0.75 | 94.51 | 4.74 |

on each of the two nitrogen atoms exhibits by far the largest turbidity. In contrast, the non-methylated compound EN exhibits the lowest absorption, even slightly below the control. The absorbance curves for two partly methylated substances MEEN and ENQ are found in between.

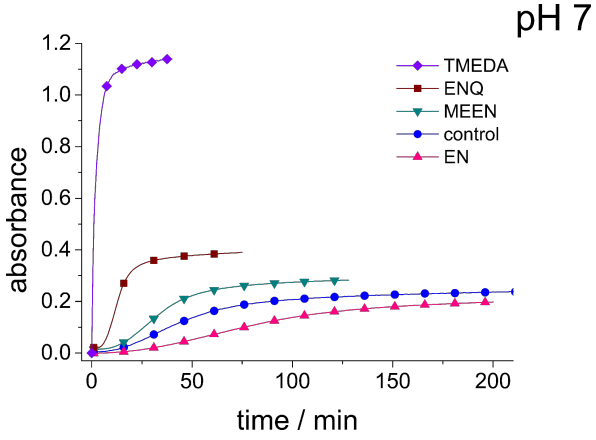


**Figure 6:** Absorbance of a 90 mM sodium metasilicate solution with 10 mM TMEDA, ENQ, MEEN, and EN (cf. Table 1) and of a pure sodium metasilicate solution (control, blue circles) measured as a function of time up to 800 min.

It can, therefore, be stated that hydrophobic interactions can very strongly influence self-assembly processes taking place in silicic acid solutions. It is interesting to note in this context that Belton et al. [25] observed an increasing third order reaction rate for the monosilicic acid condensation reaction in methylated triamines compared with the non-methylated substance. It is possible, that this enhanced reaction rate is coupled with the enhanced efficiency of the self-assembly processes observed here. For polyallylamine, efficient aggregation under the chosen conditions and at pH 5.5 only occurred in the presence of phosphate (Figure 4). The final question to be answered is therefore related to the influence of phosphate upon the monomer-containing solutions.

Figure 7 shows the absorbance curves for phosphate-containing sodium metasilicate solutions in the presence allylamine and allylamineQ as well as for the pure phosphate-containing

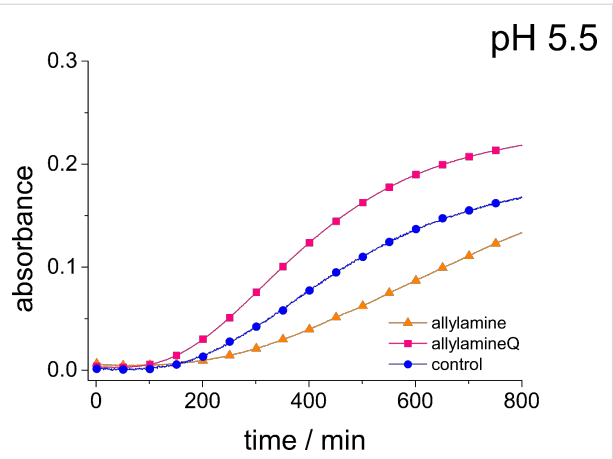


**Figure 7:** Absorbance of a 90 mM sodium metasilicate solution with 180 mM hydrogen phosphate in the presence of 10 mM allylamine and allylamineQ and of a pure sodium metasilicate solution with 180 mM hydrogen phosphate (control, blue circles) measured as a function of time up to 800 min.

sodium metasilicate (control). In contrast to the behavior observed for PAH, phosphate does not enhance the aggregate formation in these solutions. The influence of phosphate is even slightly retarding the aggregation. This observation again emphasizes the need to use polymeric additives such as PAH in order to obtain an enhanced aggregation in silicic acid containing solutions.

## Conclusion

The self-assembly processes taking place in sodium metasilicate solutions containing polyamines as well as monomeric amine compounds were studied in the presence and absence of phosphate ions. The present study was especially devoted to the characterization of the initial aggregation steps taking place in such solutions. For this purpose, turbidity measurements were employed as a simple method to detect self-assembly before silica precipitation starts. The following conclusions can be drawn from our studies:

(i) Polyallylamine (PAH) is by far more efficient in inducing self-assembly processes in silicic-acid containing solutions than equivalent amounts of its monomer, allylamine. That means efficient self-assembly necessarily requires the polymeric state of the amine as already pointed out by Behrens et al. [50]. PAH strongly reduces the concentration of soluble silica especially at elevated pH above 8.5. It is tempting to speculate that PAH catalyzes the silicic acid polycondensation reaction as suggested by Kröger et al. [1] – in particular at elevated pH. Belton et al. [25] indeed observed an enhanced reaction rate for the silicic acid polycondensation reaction in the presence of different amines at pH 6.8 whereas Behrens et al. [50] did not observe such an effect at pH 5.5. Elucidation of this possible catalytic effect and its dependence on the experimental parameters should be subject of future research.

(ii) Efficient self-assembly takes place in the pure PAH/silicic acid solution at pH 6.8. This can be explained by the electrostatic interactions between positively charged polyamines and negatively charged silicic acid oligomers/silica nanoparticles. However, changes of the pH strongly influence these processes. At pH 5.5, self-assembly in the pure silicic acid/PAH solutions is totally suppressed at the concentrations chosen here. This is explained by the perturbed charge balance caused by the decreasing negative surface charge of the silica nanoparticles at lower pH. However, the introduction of negatively charged phosphate restores the ability of the system to self-assemble. This highlights the necessity of a proper charge balance in the formed aggregates.

(iii) Methylation of the amine groups strongly enhances the tendency for self-assembly in amine-containing silicic acid solutions (see also [48]). The enhanced reactivity of methylated polyamines in the silicic acid polycondensation reaction observed by Belton et al. [25] may be related to this fact. That means the degree of methylation provides a further important "tuning" parameter for bioinspired silica synthesis approaches based on the use of LCPAs which should be further exploited in future in vitro studies.

## Experimental

### Reagents and chemicals

Polyallylamine hydrochloride (PAH; $(C_3H_8ClN)_n$; $M$ = 15000 g/mol, $n \approx 160$), allylamine ($C_3H_7N$; $M$ = 57.09 g/mol), ethylenediamine dihydrochloride (EN; $C_2H_8N_2{\cdot}2HCl$; $M$ = 133.02 g/mol), *N*,*N*-dimethylethylenediamine (MEEN; $C_4H_{12}N_2$; $M$ = 88.15 g/mol), (2-aminoethyl)trimethylammonium chloride hydrochloride (ENQ; $C_5H_{15}N_2Cl{\cdot}HCl$; $M$ = 175.10 g/mol), *N*,*N*,*N*′,*N*′-tetramethylethylenediamine (TMEDA; $C_6H_{16}N_2$; $M$ = 116.20 g/mol), sodium metasilicate ($Na_2SiO_3{\cdot}9H_2O$; $M$ = 284.2 g/mol), as well as the reagents used for the silicomolybdic acid test (ammonium molybdate ($(NH_4)_6Mo_7O_{24}{\cdot}4H_2O$), oxalic acid ($C_2H_2O_4{\cdot}2H_2O$)) were purchased from Sigma-Aldrich (Germany). The allyltrimethylammonium bromide (allylamineQ; $C_6H_{14}BrN$; $M$ = 180.09 g/mol) was obtained from ABCR (Germany).

The samples studied in this work were prepared by using purified distilled water (filtersystem: Elga – Purelab Classic, Germany; filter: Gelman Sciences – Supor® DCF™ 0.2 μm). In the following, this deionized water will be called ultrapure water.

### Silicomolybdic acid test

The solutions for the silicomolybdic acid test were prepared and used by following the protocol developed by Spinde et al. [23].

### $^{29}$Si NMR measurements

To obtain $^{29}$Si-enriched sodium metasilicate ($Na_2{}^{29}SiO_3$), $^{29}SiO_2$ was melted with sodium carbonate (Fluka), thus forming $Na_2{}^{29}SiO_3$ in a solid-state reaction.

For liquid-state $^{29}$Si NMR measurements, 24.2 mg of $Na_2{}^{29}SiO_3$ were dissolved in 2 mL of $D_2O/H_2O$ (1:1) and placed in a container with a Teflon-covered magnetic stirring bar, resulting in a 6030 ppm $SiO_2$ stock solution at pH 12. For the acidic sample, 24.2 mg of $Na_2{}^{29}SiO_3$ were dissolved in 2 mL 0.25 M hydrochloric acid and hydrolyzed for 15 min. Ultrapure water was added to both stock solutions giving a final silicic acid concentration of 4350 ppm.

$^{29}$Si NMR experiments were performed on a Bruker Avance 300 spectrometer operating at a resonance frequency of

59.63 MHz. For liquid-state $^{29}$Si NMR measurements, a commercial 10 mm HR probe (56° flip angle, number of scans 180, 60 s repetition time) was used. Typical $T_1$ values for samples in solution were 8–13 s. Waltz16 $^1$H decoupling was applied during signal acquisition. The chemical shift was referenced relative to tetramethylsilane (TMS).

## pH Titration

The starting solutions were prepared by mixing 2.1 mL of orthosilicic acid solution (100 mM, $Na_2SiO_3$) with 0.6 mL of a PAH containing solution (2 mM) or ultrapure water (control). The final ratio of silicon and nitrogen atoms in the polymer-containing sample was 1:1 and the starting pH was 12.7. The desired pH values were adjusted by titration with a 2.4 M HCl stock solution under continuous stirring. The final $SiO_2$ concentration was 70 mM. The resulting solution (control) or precipitate (PAH) were transferred into Eppendorf vials and set aside without stirring. The concentration of soluble silicic acid was determined using the well-established silicomolybdic acid test 40 min after titration.

## Turbidity measurements

To slow down the reaction, the final ratio of silicon and nitrogen atoms in the turbity measurements was changed to 9:1. Turbidity measurements were performed by mixing a silicate-containing solution A with different amines (solution B).

**Preparation of solution A without phosphate:** Solution A was prepared by titration of a stock solution of sodium metasilicate (ca. 250 mM) to pH 6.8 or 5.5 with 2.5 M hydrochloric acid (see final concentrations in Table 2). Finally, the samples were diluted to a Si-concentration of 120 mM.

**Table 2:** Final concentrations of stock solution A without phosphate.

| final concentration (solution A without phosphate) | pH 5.5 | pH 6.8 |
|---|---|---|
| silica | 120 mM | 120 mM |
| chloride | 220 mM | 180 mM |

**Preparation of solution A with phosphate:** Solution A was prepared as described by using 0.5 M phosphoric acid for titration (see final concentration in Table 3). Finally, the samples were diluted to a Si-concentration of 120 mM.

**Preparation of solution B:** The amine-containing solution B was prepared by titration of an amine stock solution (ca. 40 mM or ca. 0.25 mM for PAH) with 2.5 M hydrochloric acid. Afterwards, the solutions were diluted to the final concentrations shown in Table 4.

**Table 3:** Final concentrations of stock solution A with phosphate.

| final concentration (solution A with phosphate) | pH 5.5 | pH 6.8 |
|---|---|---|
| silica | 120 mM | 120 mM |
| phosphate | 240 mM | 160 mM |

**Table 4:** Final concentrations of stock solution B.

| final concentration (solution B) | | pH 5.5 | pH 6.8 |
|---|---|---|---|
| amine | monomer | 20 mM | 20 mM |
| | polymer | 125 µM | 125 µM |
| HCl | | depending on amine | |

**Measurements:** All solutions were prepared immediately before use. Both solutions were stored in an ice bath to slow down further reactions. Before starting the measurements, the samples were warmed in a water bath at room temperature for 5 min. Mixing of 1.2 mL solution A with 0.4 mL of solution B resulted in the final concentrations displayed in Table 5 and Table 6.

**Table 5:** Final concentration of turbidity measurement samples without phosphate.

| final concentration (without phosphate) | | pH 5.5 | pH 6.8 |
|---|---|---|---|
| silica | | 90 mM | 90 mM |
| amine | monomer | 10 mM | 10 mM |
| | polymer | 31.25 µM | 31.25 µM |
| chloride | | 165 mM | 135 mM |

**Table 6:** Final concentration of turbidity measurements with phosphate.

| final concentration (with phosphate) | | pH 5.5 | pH 6.8 |
|---|---|---|---|
| silica | | 90 mM | 90 mM |
| amine | monomer | 10 mM | 10 mM |
| | polymer | 31.25 µM | 31.25 µM |
| phosphate | | 180 mM | 120 mM |

An initial absorption spectrum was taken from 400 to 500 nm on a Varian Cary 50 spectrometer. The solutions were directly mixed in a glass cuvette, shortly shaken and the measurement started immediately. For rapidly reacting solutions (such as with PAH) solution B was given directly into the cuvette, which already contained solution A and was placed in the spectrom-

eter by moving the pipette from the bottom upwards. The resulting mixture was homogenous and no air bubbles, gradient or sedimentation could be observed. The absorbance was measured as a function of time ($t_{max}$ = 800 min) in continuous mode every minute. Measurements were run overnight. The absorbance at 480 nm was taken as a measure of turbidity.

## Acknowledgements

Financial support from the Deutsche Forschungsgemeinschaft (grants no. Br 1278/24-1 within the Research Unit FOR 2038 "Nanopatterned Organic Matrices in Biological Silica Mineralization" and Br 1278/ 25-2 within the SPP 1562 "Generation of Multifunctional Inorganic Materials by Molecular Bionics").

## References

1. Kröger, N.; Deutzmann, R.; Bergsdorf, C.; Sumper, M. *Proc. Natl. Acad. Sci. U. S. A.* **2000,** *97,* 14133–14138. doi:10.1073/pnas.260496497
2. Sumper, M.; Lorenz, S.; Brunner, E. *Angew. Chem., Int. Ed.* **2003,** *42,* 5192–5195. doi:10.1002/anie.200352212
3. Sumper, M.; Brunner, E. *Adv. Funct. Mater.* **2006,** *16,* 17–26. doi:10.1002/adfm.200500616
4. Sumper, M.; Brunner, E.; Lehmann, G. *FEBS Lett.* **2005,** *579,* 3765–3769. doi:10.1016/j.febslet.2005.06.001
5. Sumper, M.; Lehmann, G. *ChemBioChem* **2006,** *7,* 1419–1427. doi:10.1002/cbic.200600184
6. Sumper, M.; Brunner, E. *ChemBioChem* **2008,** *9,* 1187–1194. doi:10.1002/cbic.200700764
7. Kröger, N.; Deutzmann, R.; Sumper, M. *Science* **1999,** *286,* 1129–1132. doi:10.1126/science.286.5442.1129
8. Kröger, N.; Lorenz, S.; Brunner, E.; Sumper, M. *Science* **2002,** *298,* 584–586. doi:10.1126/science.1076221
9. Poulsen, N.; Kröger, N. *J. Biol. Chem.* **2004,** *279,* 42993–42999. doi:10.1074/jbc.M407734200
10. Richthammer, P.; Börmel, M.; Brunner, E.; van Pée, K.-H. *ChemBioChem* **2011,** *12,* 1362–1366. doi:10.1002/cbic.201000775
11. Matsunaga, S.; Sakai, R.; Jimbo, M.; Kamiya, H. *ChemBioChem* **2007,** *8,* 1729–1735. doi:10.1002/cbic.200700305
12. Gröger, C.; Lutz, K.; Brunner, E. *Cell Biochem. Biophys.* **2008,** *50,* 23–39. doi:10.1007/s12013-007-9003-2
13. Zhang, B.-R.; Chen, Y.-N.; Li, F.-T. *Colloids Surf., A* **2011,** *385,* 11–19. doi:10.1016/j.colsurfa.2011.03.062
14. Demadis, K. D.; Neofotistou, E. *Chem. Mater.* **2007,** *19,* 581–587. doi:10.1021/cm062370d
15. Mizutani, T.; Nagase, H.; Fujiwara, N.; Ogoshi, H. *Bull. Chem. Soc. Jpn.* **1998,** *71,* 2017–2022. doi:10.1246/bcsj.71.2017
16. Brunner, E.; Lutz, K.; Sumper, M. *Phys. Chem. Chem. Phys.* **2004,** *6,* 854–857. doi:10.1039/b313261g
17. Lutz, K.; Gröger, C.; Sumper, M.; Brunner, E. *Phys. Chem. Chem. Phys.* **2005,** *7,* 2812–2815. doi:10.1039/b505945c
18. Sumper, M. *Angew. Chem., Int. Ed.* **2004,** *43,* 2251–2254. doi:10.1002/anie.200453804
19. Annenkov, V. V.; Danilovtseva, E. N.; Likhoshway, Y. V.; Patwardhan, S. V.; Perry, C. C. *J. Mater. Chem.* **2008,** *18,* 553–559. doi:10.1039/b716367n
20. Coradin, T.; Lopez, P. J. *ChemBioChem* **2003,** *4,* 251–259. doi:10.1002/cbic.200390044
21. Annenkov, V. V.; Danilovtseva, E. N.; Pal'shin, V. A.; Aseyev, V. O.; Petrov, A. K.; Kozlov, A. S.; Patwardhan, S. V.; Perry, C. C. *Biomacromolecules* **2011,** *12,* 1772–1780. doi:10.1021/bm2001457
22. Danilovtseva, E. N.; Pal'shin, V. A.; Likhoshway, Y. V.; Annenkov, V. V. *Adv. Sci. Lett.* **2011,** *4,* 616–621. doi:10.1166/asl.2011.1262
23. Spinde, K.; Pachis, K.; Antonakaki, I.; Paasch, S.; Brunner, E.; Demadis, K. D. *Chem. Mater.* **2011,** *23,* 4676–4687. doi:10.1021/cm201988g
24. Preari, M.; Spinde, K.; Lazic, J.; Brunner, E.; Demadis, K. D. *J. Am. Chem. Soc.* **2014,** *136,* 4236–4244. doi:10.1021/ja411822s
25. Belton, D. J.; Patwardhan, S. V.; Annenkov, V. V.; Danilovtseva, E. N.; Perry, C. C. *Proc. Natl. Acad. Sci. U. S. A.* **2008,** *105,* 5963–5968. doi:10.1073/pnas.0710809105
26. Bernecker, A.; Wieneke, R.; Riedel, R.; Seibt, M.; Geyer, A.; Steinem, C. *J. Am. Chem. Soc.* **2010,** *132,* 1023–1031. doi:10.1021/ja9061163
27. Wieneke, R.; Bernecker, A.; Riedel, R.; Sumper, M.; Steinem, C.; Geyer, A. *Org. Biomol. Chem.* **2011,** *9,* 5482–5486. doi:10.1039/c1ob05406f
28. Patwardhan, S. V.; Clarson, S. J. *Silicon Chem.* **2002,** *1,* 207–214. doi:10.1023/A:1021243810915
29. Patwardhan, S. V.; Mukherjee, N.; Clarson, S. J. *Silicon Chem.* **2002,** *1,* 47–54. doi:10.1023/A:1016026927401
30. Menzel, H.; Horstmann, S.; Behrens, P.; Bärnreuther, P.; Krueger, I.; Jahns, M. *Chem. Commun.* **2003,** 2994–2995. doi:10.1039/b310201g
31. Iler, R. K. *The chemistry of silica : solubility, polymerization, colloid and surface properties, and biochemistry;* Wiley: New York, 1979; p 866.
32. Bäuerlein, E.; Behrens, P.; Epple, M. *Handbook of Biomineralization;* Wiley-VCH: Weinheim, 2007; Vol. 1–3, pp 1269 ff. doi:10.1002/9783527619443
33. Mullin, J. B.; Riley, J. P. *Anal. Chim. Acta* **1955,** *12,* 162–176. doi:10.1016/S0003-2670(00)87825-3
34. Coradin, T.; Eglin, D.; Livage, J. *Spectroscopy* **2004,** *18,* 567–576. doi:10.1155/2004/356207
35. Chisholm, S. W.; Azam, F.; Eppley, R. W. *Limnol. Oceanogr.* **1978,** *23,* 518–529. doi:10.4319/lo.1978.23.3.0518
36. Kinrade, S. D.; Hamilton, R. J.; Schach, A. S.; Knight, C. T. G. *J. Chem. Soc., Dalton Trans.* **2001,** 961–963. doi:10.1039/b010111g
37. Amjad, Z.; Zuhl, B. *Mater. Perform.* **2009,** *48,* 48–52.
38. Ketsetzi, A.; Stathoulopoulou, A.; Demadis, K. D. *Desalination* **2008,** *223,* 487–493. doi:10.1016/j.desal.2007.01.230
39. Vrieling, E. G.; Beelen, T. P. M.; van Santen, R. A.; Gieskes, W. W. C. *Prog. Ind. Microbiol.* **1999,** *35,* 39–51. doi:10.1016/S0079-6352(99)80096-4
40. Vrieling, E. G.; Beelen, T. P. M.; van Santen, R. A.; Gieskes, W. W. C. *Angew. Chem., Int. Ed.* **2002,** *41,* 1543–1546. doi:10.1002/1521-3773(20020503)41:9<1543::AID-ANIE1543>3.0.CO;2-B
41. Hazelaar, S.; Van Der Strate, H. J.; Gieskes, W. W. C.; Vrieling, E. G. *J. Phycol.* **2005,** *41,* 354–358. doi:10.1111/j.1529-8817.2005.04131.x
42. Gordon, R.; Drum, R. W. In *The Chemical Basis of Diatom Morphogenesis;* Jeon, K. W.; Jarvik, J., Eds.; International Review of Cytology, Vol. 150; Academic Press, 1994; pp 243–372.
43. Nagy, J. B.; Engelhardt, G.; Michel, D. *Adv. Colloid Interface Sci.* **1985,** *23,* 67–128. doi:10.1016/0001-8686(85)80017-8
44. Kobayashi, S.; Tokunoh, M.; Saegusa, T.; Mashio, F. *Macromolecules* **1985,** *18,* 2357–2361. doi:10.1021/ma00154a004
45. Rao, G. V. R.; Konishi, T.; Ise, N. *Macromolecules* **1999,** *32,* 7582–7586. doi:10.1021/ma990851v

46. Ong, S.; Zhao, X.; Eisenthal, K. B. *Chem. Phys. Lett.* **1992,** *191,* 327–335. doi:10.1016/0009-2614(92)85309-X
47. Leung, K.; Nielsen, I. M. B.; Criscenti, L. J. *J. Am. Chem. Soc.* **2009,** *131,* 18358–18365. doi:10.1021/ja906190t
48. Robinson, D. B.; Rognlien, J. L.; Bauer, C. A.; Simmons, B. A. *J. Mater. Chem.* **2007,** *17,* 2113–2119. doi:10.1039/b700514h
49. Trompette, J. L.; Meireles, M. *J. Colloid Interface Sci.* **2003,** *263,* 522–527. doi:10.1016/S0021-9797(03)00397-7
50. Behrens, P.; Jahns, M.; Menzel, H. The Polyamine Silica System: A Biomimetic Model for the Biomineralization of Silica. In *Handbook of Biomineralization;* Bäuerlein, E.; Behrens, P., Eds.; Wiley-VCH Verlag GmbH, 2007; pp 2–18. doi:10.1002/9783527619443.ch25

## License and Terms

BEILSTEIN JOURNAL OF NANOTECHNOLOGY

# Biopolymer colloids for controlling and templating inorganic synthesis

Laura C. Preiss, Katharina Landfester and Rafael Muñoz-Espí*

Review

Open Access

Address:
Max Planck Institute for Polymer Research, Ackermannweg 10, 55128 Mainz, Germany

Email:
Rafael Muñoz-Espí* - munoz@mpip-mainz.mpg.de

* Corresponding author

Keywords:
biomacromolecules; biopolymer; colloid; nanoparticle; organic–inorganic hybrid; template

*Beilstein J. Nanotechnol.* **2014,** *5,* 2129–2138.
doi:10.3762/bjnano.5.222

Received: 20 July 2014
Accepted: 29 October 2014
Published: 17 November 2014

This article is part of the Thematic Series "Towards multifunctional inorganic materials: biopolymeric templates".

Guest Editors: C. Steinem and J. Bill



## Abstract

Biopolymers and biopolymer colloids can act as controlling agents and templates not only in many processes in nature, but also in a wide range of synthetic approaches. Inorganic materials can be either synthesized ex situ and later incorporated into a biopolymer structuring matrix or grown in situ in the presence of biopolymers. In this review, we focus mainly on the latter case and distinguish between the following possibilities: (i) biopolymers as controlling agents of nucleation and growth of inorganic materials; (ii) biopolymers as supports, either as molecular supports or as carrier particles acting as cores of core–shell structures; and (iii) so-called "soft templates", which include on one hand stabilized droplets, micelles, and vesicles, and on the other hand continuous scaffolds generated by gelling biopolymers.

## Introduction

During the natural synthesis of inorganic matter in living organisms, referred to as biomineralization, biogenic macromolecules are not only present in the crystallization medium, but play a crucial role in the mineral formation. Biomacromolecules, (e.g., polysaccharides, proteins, and nucleic acids) can have thereby two main functions: (i) a controlling effect on nucleation and growth of the inorganic material, and (ii) a structuring function, either confining spaces or acting as supports or as scaffolds for the growth. As a result of the interaction of organic and inorganic matter, nature is able to create hybrid materials whose exquisite structures and properties continue to impress humankind [1]. Egg shells, nacre, corals, or biosilica in sponges are still nowadays fascinating materials for scientists, who try to imitate natural strategies in the laboratory with only limited success.

It is clear that all synthetic routes based on the use of (bio)polymers as controlling and templating agents in inorganic syn-

thesis have in one or other way their origin or inspiration in natural strategies. We do not wish, however, to insist once more on the well-known ditty on the use of nature as "bioinspiration" for science. Our aim, probably more modest, is to classify and review here some of the recent – and in our opinion most representative – synthetic works involving the use of biopolymer and biopolymer colloids for the design of inorganic and inorganic/organic materials, with special emphasis on particles and particle synthesis.

In the formation of polymer/inorganic hybrid materials, both the inorganic and the polymer component can be formed either in situ or ex situ (i.e., prepared independently before the formation of the hybrid final material), leading to four combinatorial possibilities: in situ/in situ, in situ/ex situ, ex situ/ex situ, and in situ/in situ. These different strategies for the formation of hybrid materials have been recently reviewed elsewhere in detail [2]. In the present review, we will describe the use of biopolymers as controlling agents and templates, which implies that the polymer is almost always formed beforehand. Nevertheless, cross-linking processes of the polymer can occur simultaneously to the inorganic precipitation/crystallization. With these considerations in mind, and centering our attention on the formation of the inorganic materials and not of the biopolymer, we should distinguish two possibilities:

1. Approaches in which the inorganic component is formed ex situ and later combined with the polymer
2. Approaches in which the formation of the inorganic material takes place in situ, that is, while the biopolymers are already present in the system

In the first situation, with the inorganic material being formed ex situ, biopolymers can probably be considered neither as controlling agents nor as templates in a strict sense, at least not for the synthesis. However, before entering to describe the in situ formation, we will briefly refer to the ex situ case for the sake of completeness. Figure 1 represents schematically the ways in which biopolymers can be useful for designing inorganic and inorganic/organic materials, including the ex situ synthesis and the different cases of the in situ formation, further classified in the corresponding section below.

# Review

## Ex situ formation of the inorganic material

Hydrogels, such as those based on the polyaminosaccharide chitosan, are probably the most commonly used scaffolds for the preparation of bipolymer/inorganic composites, very especially for biomedical applications. Aimé and Coradin have reviewed the topic in a recent publication [3]. By mixing

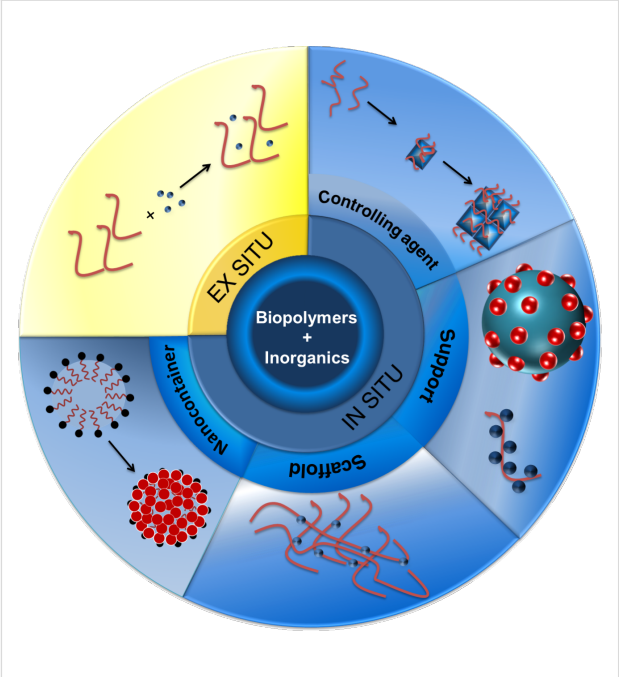


**Figure 1:** Different roles of biopolymers as controlling agents and templates in the formation of inorganic materials.

colloidal inorganic particles formed ex situ with a biopolymer sol, followed by a gelation process, porous hybrid structures can be obtained. Starting from a colloidal suspension of laponite particles, Shi et al. [4] reported the preparation of a nanocomposite matrix of chitosan and clay that was applied as a glucose biosensor. Very recently, da Costa Neto et al. [5] prepared chitosan/silica composite microspheres by mixing an aqueous solution of the biopolymer with commercial nanosized silica particles. The obtained microparticles were dried afterwards. In further examples, chitosan matrices have also been used to immobilize CdSe quantum dots [6] and γ-$Fe_2O_3$ nanoparticles [7].

In a different approach, biopolymers can also be applied to modify surfaces and induce the deposition of nanoparticles. For instance, Nochomovitz et al. [8] described the deposition and patterning of gold colloidal nanoparticles and carbon nanotubes on surfaces previously modified with peptides.

## In situ formation of the inorganic material

After having briefly discussed a few examples in which the inorganic material is formed ex situ and combined a posteriori with biopolymers, we will revise now in situ strategies, with biopolymers playing an active role during the formation of inorganic materials. We propose the following classification, being aware that all divisions are arbitrary to some degree and it may be difficult to place some of the examples in one or other group without ambiguity:

A. The use of biopolymers and biopolymer colloids as controlling agents for the precipitation and crystallization of inorganic materials, which is typically referred to as "polymer-assisted" or "polymer-controlled" formation and is intimately related to the (bio)mineralization field.

B. Biopolymers as "supports" for precipitation/crystallization processes. We distinguish depending on whether the formation of inorganic nanoparticles takes places on biopolymer molecules or on particles: (B1) Nanoparticle formation on biopolymer molecules (often referred to as "metallization" and "mineralization" of biopolymers). (B2) Biopolymer particles as support, with the formation of the inorganic nanoparticles taking place on the surface.

C. Biopolymers as so-called "soft templates". Differently from the previous case, here the precipitation/crystallization of the inorganic materials does not take place merely on the surface, but *within* the supramolecular structure formed by the biopolymer (polymer matrix). Among the "soft templates", two subgroups can be considered: (C1) Biopolymer-stabilized spherical geometries (stabilized droplets, micelles, and vesicles) that confine the inorganic formation. (C2) Biopolymer structures acting as "scaffolds", with more complex geometries than simple spheres. This is typically the case for gels and microgels. Microgels can also be prepared in the form of nanoparticles, which can be considered a kind of intermediate case between C1 and C2.

## A. Biopolymers and biopolymer colloids as controlling agents: polymer-controlled crystallization

Many types of polymers, both of natural origin and synthetic, have been used as controlling agents for crystallization. This field of the so-called "polymer-controlled crystallization" has been reviewed in detail in several publications of Cölfen and collaborators [9-12].

Among the different natural or biomimetic polymers studied, we find starch [13,14], different cellulose derivatives [15], dextran [16], pectin [17], alginate [18], and poly(amino acids) or proteins [19-29]. Researchers in the biomineralization field very often extract proteins from biological matter and use them for the ex vivo mineralization, trying to study the effects of natural macromolecules [30]. Silicateins, for instance, are proteins not only used ex vivo for understanding mineralization processes in sponges, but also applied to prepare novel biomimetic hybrid materials, as nicely revised in a recent publication by Müller et al. [31].

From the mineral side, the most investigated systems are by far the calcium minerals because of their biological importance: calcium carbonate [16-18,20,32], calcium oxalate [23-26,33], and calcium phosphates (including hydroxyapatite) [22]. Nevertheless, biopolymers have also been used as controlling agents or additives in the precipitation/crystallization of other inorganic systems, such as ZnO [34], metal particles [13], silica [35], or $Fe_2O_3$ [15].

To investigate the effects of proteins in mineralization, synthetic oligopeptides with sequences of defined lengths and composition are sometimes used [23,24,36,37]. A previous work from our research group showed that an increasing length of oligo(L-glutamic acid) chains is able to change not only the morphology of the obtained crystals, but also to stabilize the metastable calcium oxalate dihydrate (Figure 2) [38]. In a more recent work, we have also shown that charged acidic peptides are able to stabilize vaterite, and we studied the effect of the acidity of the amino acid residues on this stabilization [39].

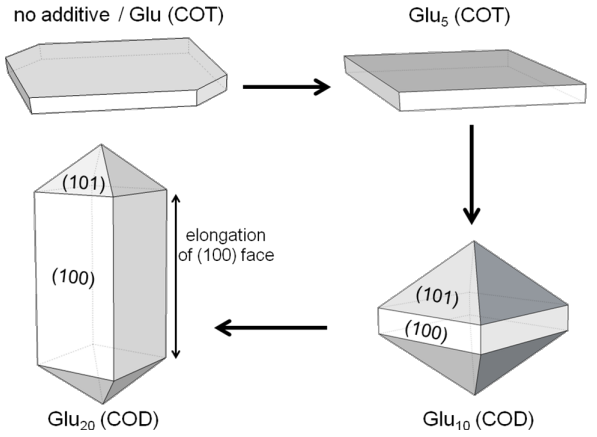


**Figure 2:** Schematic representation of the evolution of the morphology of calcium oxalate crystals prepared in the presence of oligo(L-glutamic acid)s of different lengths, ranging from the monomer (Glu) to the eicosamer ($Glu_{20}$). COD: calcium oxalate dihydrate; COT: calcium oxalate trihydrate. Reprinted with permission from [38]. Copyright 2010 American Chemical Society.

In a previous work, synthetic polymer colloidal particles functionalized with different groups were shown to have an effect on the growth and on the final properties of inorganic materials such as zinc oxide [40,41], calcium oxalate [38], or calcium carbonate [42,43]. It is expectable that analogous effects should be obtained when biopolymeric (or synthetic biomimetic chains) are attached to the surface of colloidal particles. In this sense, Krattiger et al. [44] reported the morphogenesis of $CaCO_3$ and DL-alanine crystals in the presence of polystyrene beads functionalized with synthetic peptides with different amino acids and oligopeptides.

## B. Biopolymers as "supports"

**B1. Molecular templates:** Biomacromolecules contain often functional groups (such as phosphates in DNA or carboxylic and amino groups in proteins) that are able to complex metal ions and act as nucleation centers for the growth of metal or mineral nanoparticles. The use of molecular templates as a support for inorganic nanoparticles may be referred to as "metallization" or "mineralization" (depending on whether metal or mineral particles are formed) of biopolymers. Zinchenko [45] reviewed the advances in the field, with special emphasis on DNA and its assemblies, but going also through the use of proteins. Although there are common points between such molecular templating and the polymer-controlled crystallization described above, and in some cases the distinction may be unclear, the main difference lies on the size of the formed particles and the polymer. In the case of molecular supports, tiny inorganic nanoparticles are formed on the biomacromolecular chain, while in polymer-controlled crystallization processes the inorganic material is significantly larger than the macromolecules, which may get engulfed by the growing crystals.

DNA chains have been coated by in situ deposition with different metals, metal oxides, and metal chalcogenides, including metallic silver [46], Pt [47], $Fe_2O_3$ [48], and CdS [49-52]. Pu et al. [52] reported the deposition of DNA chains on silica particles. After mineralization of the DNA to CdS as shell and subsequent removal of the silica core by dissolution with HF, hollow inorganic particles were obtained (Figure 3). Analogous to the DNA case, peptidic supports have also been used for the deposition of metals [53] and semiconductor chalcogenide quantum dots [54-65].

**B2. Biopolymer particles as "supports":** In the area of preparation of hollow particles it is common to distinguish between "hard" and "soft" templates [57-59]. This nomenclature can also be extended to the formation of polymer/inorganic particles. "Soft templates" will be reviewed in Section C; here, we will consider the case of so-called "hard templates", which typically involves the deposition of an inorganic material on the surface of "hard" spheres (silica or polymer) that act as sacrificial cores. The core can be eventually removed by calcination or dissolution, if the aim is the formation of hollow structures. Such strategies have been widely used for templates with synthetic polymers (see Section 4 in [60] for a review), but only a limited number of works are found for biopolymers.

Li et al. [61] prepared cross-linked chitosan microspheres and immobilized bovine serum albumin covalently on their surface. On the resulting particles, silica was formed by a sol–gel process from 3-aminopropyltrimethyoxysilane (APTMS) or tetraethoxysilane (TEOS). The structures after the removal of the template were proven to be suited for protein recognition. The synthesis process is depicted in Figure 4.

When referring to polymer particles, the denomination "hard template" may sound somehow odd, even more in the case of microgel particles, which are definitely not "hard". However, in our classification we consider within this group all approaches in which a shell is formed on the surface of a particle. As an example, Boissière et al. [62] synthesized poly(L-lysine)/alginate microparticles through a microgel route and coated them with silica to obtain core–shell composites. In an alternative method, spray-drying of biopolymer and biopolymer/silica solutions was conducted. Magnetic cobalt silicate could be also generated by introducing a cobalt salt during the process.

## C. Biopolymers as "soft templates"

**C1. Biopolymer-stabilized simple geometries (droplets, micelles, and vesicles):** Surface-active polymers can assemble in solution and in heterophase systems to form defined geome-

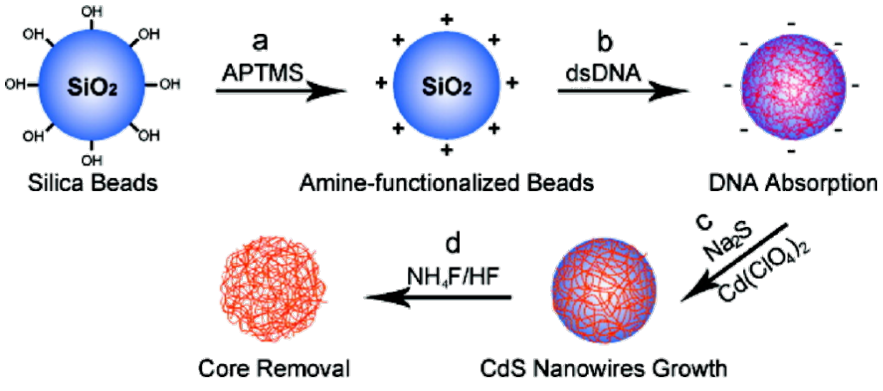


**Figure 3:** DNA-templated preparation of porous CdS shells on the surface of silica beads: (a) surface modification with (3-aminopropyl)trimethoxysilane (APTMS), (b) DNA deposition on the cationic particle surface, (c) CdS precipitation, and (d) dissolution of the $SiO_2$ core to form hollow structures. Reprinted with permission from [52]. Copyright 2011 American Chemical Society.

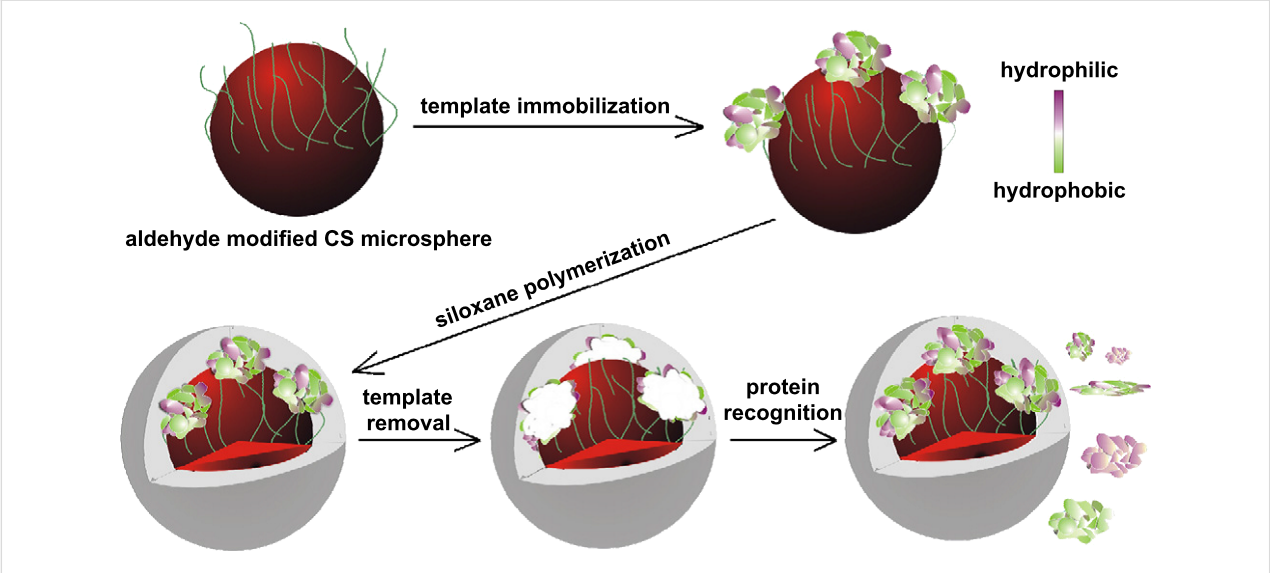


**Figure 4:** Siloxan polymerization on chitosan microspheres by using immobilized protein templates. Reprinted with permission from [61]. Copyright 2008 Elsevier.

tries, most typically spherical, such as micelles, vesicles, or even stabilized droplets. As in the case of "hard templates" stated above, the approach has been very productive with synthetic polymers [2,60], but only explored in a limited way with biopolymers. The main reason for this is that the assembly of many biopolymers results in a rather continuous network and not necessarily in "discrete" geometries.

In a very recent work, Taheri et al. [63] have presented the formation of potato starch capsules decorated with silver nanoparticles, which could have applications as drug carriers or antibacterial coatings. The capsules are prepared in an inverse (water-in-oil) miniemulsion and the surfactant polyglycerine-polyricinoleate (PGPR) is used to stabilize the system. Interestingly, a polyaddition process of the starch, driven by the addition of 2,4-toluene diisocyanate (TDI), occurs simultaneously to the reduction of $Ag^+$ ions to metallic silver without addition of any additional reducing agent (Figure 5). Since polyaddition and silver precipitation occur both at the same time, the approach could be considered as an "in situ/in situ" or "all in situ" strategy, which is a rather rare case in literature. We have decided to include it within this subsection mainly due to the spherical geometry and the presence of a heterophase system, but probably the example could have been included as well in the next subsection, as the silver precipitation takes place within the polymer scaffold.

As an extension of the metallization examples presented in Section B1, structures formed by DNA or proteins can also be used for templating. The toroidal structures formed by DNA condensates were used as soft templates for the formation of silver [64,65] and gold [66] nanoparticles by reduction of the metal salts (Figure 6). Rings resulting from the assembly of a bolaamphiphilic peptide molecule were reported as templates for the growth of conductive indium tin oxide (ITO) nanoparticles [67].

**C2. Biopolymers as "scaffolds":** As mentioned above, gelling biopolymers are very common templates in inorganic syntheses [3,68]. Since the precipitation/crystallization of the inorganic nanoparticles takes place within the network generated by the polymer and not on the surface or edges (as it is the case of the "supports" of the previous subsection), we label this type of templating as "scaffold", being aware that the term is also used in a more general way – almost as a simple synonym for "template" – by other authors.

Because of the biodegradability and biocompatibility, chitosan can be considered as a "green material". In addition to the common applications in food and biotechnology, chitosan can also be used as a support for catalysts. Chitosan–silica [69] and chitosan–titania [70] catalysts were prepared by applying conventional sol–gel methods. The preparation of sol–gel silicates have been reported by several research groups [71,72]. Nevertheless, the use of chitosan is not limited to silicates and titanates. El Kadib et al. [73] demonstrated the use of chitosan microspheres as templates for vanadium, tungsten, and molybdenum oxide clusters, which were shown to be active as catalysts for selective alcohol oxidation. Similarly, Ganesan and Gedanken [74] had prepared tungsten(VI) oxide nanoparticles through the encapsulation of ammonium metatungstate on chitosan and the subsequent calcination. These particles showed a higher catalytic activity than bulk tungsten trioxide. Other ma-

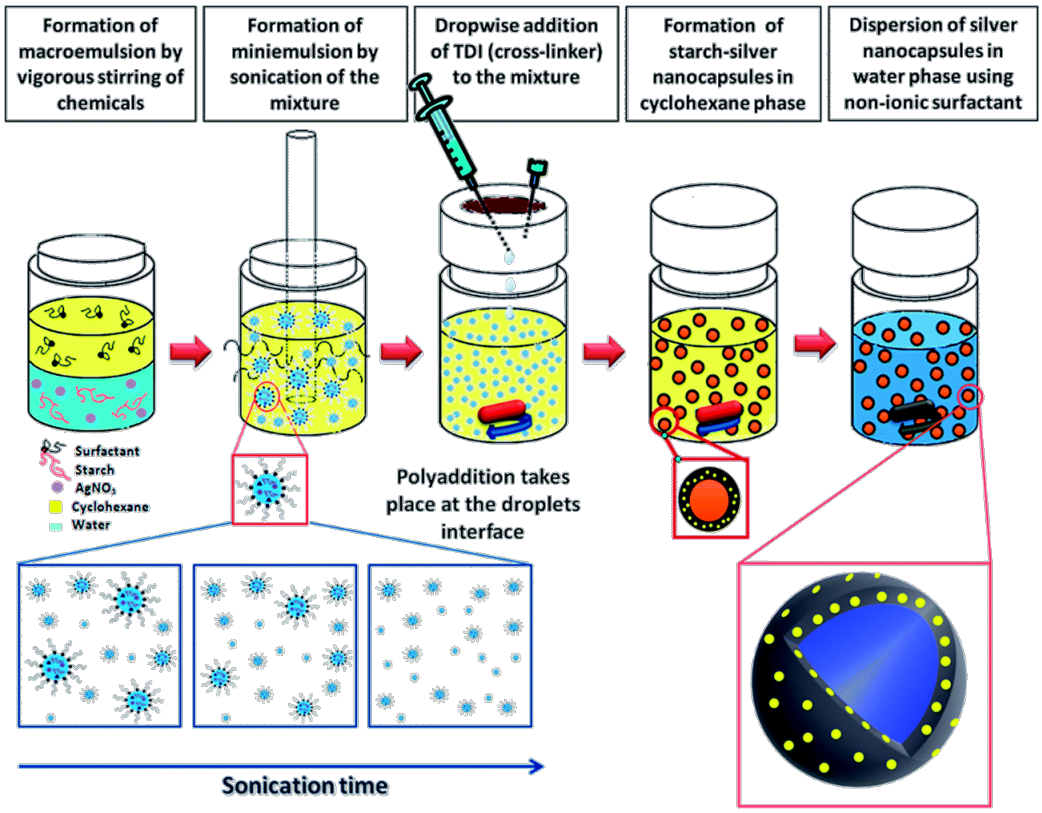


**Figure 5:** Schematic representation of the procedure applied for synthesizing starch/Ag nanocapsules. Reprinted with permission from [63]. Copyright 2014 The Royal Society of Chemistry.

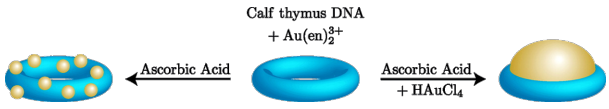


**Figure 6:** Products obtained when gold(III) is reduced in the presence of DNA toroids formed with bis(ethylenediamine)gold(III). Reprinted with permission from [66]. Copyright 2010 American Chemical Society.

terials, such as cobalt-Prussian blue nanoparticles [75], Zn–Al layered double hydroxide [76], hydroxyapatite [77], and calcium carbonate [78], were also prepared within, or in the presence of, chitosan gels. In a biological approach, calcium phosphate/chitosan composite films were shown to influence the behavior of human mesenchymal stem cells. Lee et al. [79] studied the scaffold–cell interaction by changing the crystallinity and ratio of the calcium phosphate.

Alginate is another of the gelling biopolymers used as a scaffold. An alginate-influenced growth of Co, Ni, and CoNi nanoparticles was reported by Coradin et al. [80]. The same research group also studied the in situ growth of gold colloids with alginate films [81,82]. Gel frameworks have been shown to be able to control the size distribution of particles. Hernández et al. [83] demonstrated the synthesis of iron oxide nanoparticles in a semi-interpenetrating polymer network of alginate and poly(*N*-isopropylacrylamide).

Gold and AuNi alloy gelatin nanocomposites were developed by Brayner et al. [84]. A gelatin network incorporating metallic nanoparticles was obtained after reduction of gold salts. Like other gel biopolymer templates, gelatin has also been used in silicate sol–gel processes [72,85,86]. Ethirajan et al. [87] used the confinement provided by gelatin particles prepared through a miniemulsion to template the crystallization of hydroxyapatite (Figure 7).

A further example of a heterogeneous catalyst was reported by Taubert's group with gold/cellulose nanocrystal hybrids

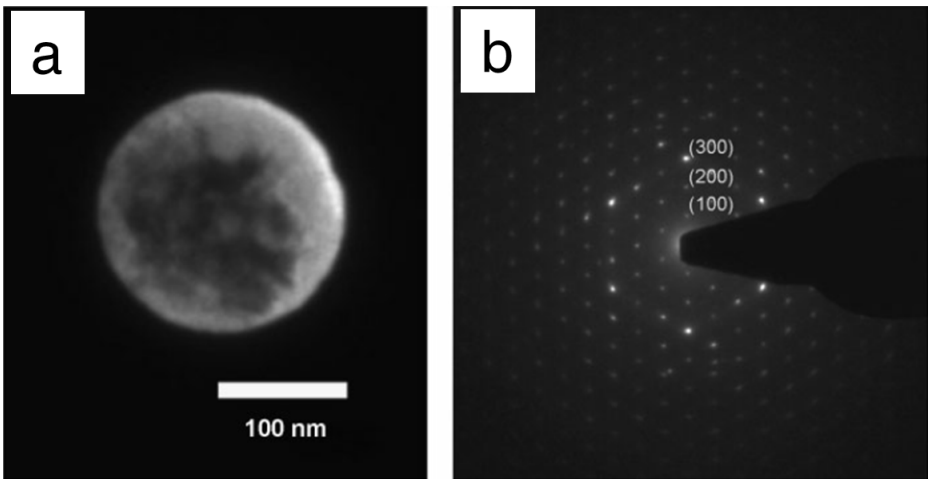


**Figure 7:** Dark-field TEM micrograph (a) and corresponding electron diffraction pattern (b) of hydroxyapatite/gelatin particles. Reprinted with permission from [87]. Copyright 2008 John Wiley & Sons.

produced in the presence of ionic liquids [88]. Also for catalytic applications, nanoparticles of silver, gold, and platinum were synthesized by using a cellulose aerogel [89]. Cellulose has been further used for silicates. Zhang et al. [90] presented the in situ formation of silica in a cellulose aerogel (Figure 8). The addition of the silicate precursor (TEOS) takes place first, followed by a sol–gel process and the cellulose/silica composite formation. The aerogel is formed by drying with supercritical $CO_2$ and subsequent calcination.

Scaffold templating can also be achieved with starch and even with peptides. Thakore et al. [13] synthesized Cu, Ag, and Cu–Ag alloy nanoparticles in a matrix of starch through a green route and studied the antibacterial activity. Hexagonal silica platelets were prepared through a polypeptide-templated synthesis by using the interactions of a polypeptide of L-lysine with silicate [35].

## Conclusion

The application of biopolymers (polysaccharides, peptides, and nucleic acids) as controlling agents or as templates of inorganic precipitation and crystallization is not only present in nature (biomineralization), but is also a versatile strategy for the design of inorganic and inorganic/organic hybrid materials in the laboratory. On one hand, biopolymers may assemble forming structures that serve as confining spaces or scaffolds in which the formation of the inorganic component takes place. On the other hand, the presence of functional groups such as

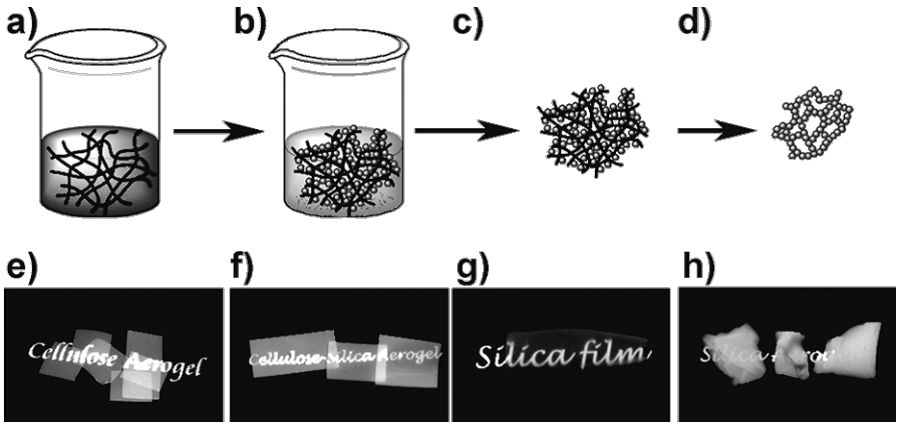


**Figure 8:** Schematic representation of aerogel preparation. A nanoporous cellulose gel is impregnated with the silica precursor TEOS (a). Afterwards, the silica formation takes place by sol–gel process (hydrolysis and condensation), yielding a cellulose–silica composite gel (b). Drying with supercritical $CO_2$ gives a composite aerogel (c). Macroscopic views of the prepared samples are shown in panels (e–h). Reprinted with permission from [90]. Copyright 2012 John Wiley & Sons.

carboxylic, amino or phosphate groups can provide a high ability to bind metal ions or to interact with growing crystal faces, influencing nucleation and growth.

Hydrogels, such as those formed with chitosan or gelatin, are very commonly used as polymer matrices for the synthesis of porous structures. Although in general the inorganic material is formed in situ (i.e., while the biopolymer is present in the system), there are also some examples in which previously formed nanoparticles are combined with the biopolymer and incorporated into the matrix after gelation.

In most cases, biopolymers have been either used in bulk solutions or applied to surfaces, so that the resulting material is a continuous hybrid structure. However, they can also be used to generate "discrete" structures either by using single molecular chains as supports (e.g., metallization or mineralization of DNA) or by using particle systems. Hydrogel approaches can also be confined to the spaces of particles.

Clearly, synthetic polymers are often a more economic and versatile alternative, but biopolymers can be especially interesting in those applications in which biocompatibility or biodegradability are an issue, such as biomedical applications. In addition, biopolymers may be also good model systems. In this sense, for instance, peptides or nucleic acids of defined length and structure can be very convenient models for studying polyelectrolyte systems. Furthermore, the high ability of biopolymers to form complex hierarchical structures is a major feature to be explored in the upcoming years. A better understanding of the interface between the biopolymeric component and the growing inorganic matter will continue to be the crucial issue in the design of novel and more sophisticated materials.

## References


1. Sotiropoulou, S.; Sierra-Sastre, Y.; Mark, S. S.; Batt, C. A. *Chem. Mater.* **2008,** *20,* 821–834. doi:10.1021/cm702152a
2. Hood, M. A.; Mari, M.; Muñoz-Espí, R. *Materials* **2014,** *7,* 4057–4087. doi:10.3390/ma7054057
3. Aimé, C.; Coradin, T. *J. Polym. Sci., Part B: Polym. Phys.* **2012,** *50,* 669–680. doi:10.1002/polb.23061
4. Shi, Q.; Li, Q.; Shan, D.; Fan, Q.; Xue, H. *Mater. Sci. Eng., C* **2008,** *28,* 1372–1375. doi:10.1016/j.msec.2008.03.001
5. da Costa Neto, B. P.; da Mata, A. L. M. L.; Lopes, M. V.; Rossi-Bergmann, B.; Ré, M. I. *Powder Technol.* **2014,** *255,* 109–119. doi:10.1016/j.powtec.2013.10.046
6. Wu, W.; Shen, J.; Banerjee, P.; Zhou, S. *Biomaterials* **2010,** *31,* 8371–8381. doi:10.1016/j.biomaterials.2010.07.061
7. Zvarec, O.; Purushotham, S.; Masic, A.; Ramanujan, R. V.; Miserez, A. *Langmuir* **2013,** *29,* 10899–10906. doi:10.1021/la401858s
8. Nochomovitz, R.; Amit, M.; Matmor, M.; Ashkenasy, N. *Nanotechnology* **2010,** *21,* 145305. doi:10.1088/0957-4484/21/14/145305
9. Xu, A.-W.; Ma, Y. R.; Cölfen, H. *J. Mater. Chem.* **2007,** *17,* 415–449. doi:10.1039/b611918m
10. Cölfen, H. *Top. Curr. Chem.* **2007,** *271,* 1–77. doi:10.1007/128_056
11. Meldrum, F. C.; Cölfen, H. *Chem. Rev.* **2008,** *108,* 4332–4432. doi:10.1021/cr8002856
12. Song, R.-Q.; Cölfen, H. *CrystEngComm* **2011,** *13,* 1249–1276. doi:10.1039/c0ce00419g
13. Valodkar, M.; Modi, S.; Pal, A.; Thakore, S. *Mater. Res. Bull.* **2011,** *46,* 384–389. doi:10.1016/j.materresbull.2010.12.001
14. Taubert, A.; Wegner, G. *J. Mater. Chem.* **2002,** *12,* 805–807. doi:10.1039/b110424c
15. Bakandritsos, A.; Mattheolabakis, G.; Chatzikyriakos, G.; Szabo, T.; Tzitzios, V.; Kouzoudis, D.; Couris, S.; Avgoustakis, K. *Adv. Funct. Mater.* **2011,** *21,* 1465–1475. doi:10.1002/adfm.201002112
16. Hardikar, V. V.; Matijević, E. *Colloids Surf., A* **2001,** *186,* 23–31. doi:10.1016/S0927-7757(01)00479-4
17. Butler, M. F.; Frith, W. J.; Rawlins, C.; Weaver, A. C.; Heppenstall-Butler, M. *Cryst. Growth Des.* **2008,** *9,* 534–545. doi:10.1021/cg8008333
18. Olderøy, M. Ø.; Xie, M.; Strand, B. L.; Flaten, E. M.; Sikorski, P.; Andreassen, J.-P. *Cryst. Growth Des.* **2009,** *9,* 5176–5183. doi:10.1021/cg9005604
19. Njegić-Džakula, B.; Brečević, L.; Falini, G.; Kralj, D. *Cryst. Growth Des.* **2009,** *9,* 2425–2434. doi:10.1021/cg801338b
20. Volkmer, D.; Fricke, M.; Huber, T.; Sewald, N. *Chem. Commun.* **2004,** 1872–1873. doi:10.1039/b405613b
21. Aschauer, U.; Ebert, J.; Aimable, A.; Bowen, P. *Cryst. Growth Des.* **2010,** *10,* 3956–3963. doi:10.1021/cg1005105
22. Diegmueller, J. J.; Cheng, X.; Akkus, O. *Cryst. Growth Des.* **2009,** *9,* 5220–5226. doi:10.1021/cg900750z
23. Wang, L.; Qiu, S. R.; Zachowicz, W.; Guan, X. Y.; DeYoreo, J. J.; Nancollas, G. H.; Hoyer, J. R. *Langmuir* **2006,** *22,* 7279–7285. doi:10.1021/la060897z
24. Wang, L.; Guan, X.; Tang, R.; Hoyer, J. R.; Wierzbicki, A.; De Yoreo, J. J.; Nancollas, G. H. *J. Phys. Chem. B* **2008,** *112,* 9151–9157. doi:10.1021/jp804282u
25. Cerini, C.; Geider, S.; Dussol, B.; Hennequin, C.; Daudon, M.; Veesler, S.; Nitsche, S.; Boistelle, R.; Berthézène, P.; Dupuy, P.; Vazi, A.; Berland, Y.; Dagorn, J.-C.; Verdier, J.-M. *Kidney Int.* **1999,** *55,* 1776–1786. doi:10.1046/j.1523-1755.1999.00426.x
26. Wesson, J. A.; Worcester, E. M.; Kleinman, J. G. *J. Urol.* **2000,** *163,* 1343–1348. doi:10.1016/S0022-5347(05)67775-0
27. Gotliv, B.-A.; Addadi, L.; Weiner, S. *ChemBioChem* **2003,** *4,* 522–529. doi:10.1002/cbic.200200548
28. Suzuki, M.; Saruwatari, K.; Kogure, T.; Yamamoto, Y.; Nishimura, T.; Kato, T.; Nagasawa, H. *Science* **2009,** *325,* 1388–1390. doi:10.1126/science.1173793
29. Michenfelder, M.; Fu, G.; Lawrence, C.; Weaver, J. C.; Wustman, B. A.; Taranto, L.; Evans, J. S.; Morse, D. E. *Biopolymers* **2003,** *70,* 522–533. doi:10.1002/bip.10536
30. Pokroy, B.; Fitch, A. N.; Marin, F.; Kapon, M.; Adir, N.; Zolotoyabko, E. *J. Struct. Biol.* **2006,** *155,* 96–103. doi:10.1016/j.jsb.2006.03.008
31. Müller, W. E. G.; Schröder, H. C.; Burghard, Z.; Pisignano, D.; Wang, X. *Chem. – Eur. J.* **2013,** *19,* 5790–5804. doi:10.1002/chem.201204412
32. Butler, M. F.; Glaser, N.; Weaver, A. C.; Kirkland, M.; Heppenstall-Butler, M. *Cryst. Growth Des.* **2006,** *6,* 781–794. doi:10.1021/cg050436w
33. Akin, B.; Öner, M.; Bayram, Y.; Demadis, K. D. *Cryst. Growth Des.* **2008,** *8,* 1997–2005. doi:10.1021/cg800092q

34. Gao, S.; Zhang, H.; Wang, X.; Deng, R.; Sun, D.; Zheng, G. *J. Phys. Chem. B* **2006,** *110,* 15847–15852. doi:10.1021/jp062850s
35. Tomczak, M. M.; Glawe, D. D.; Drummy, L. F.; Lawrence, C. G.; Stone, M. O.; Perry, C. C.; Pochan, D. J.; Deming, T. J.; Naik, R. R. *J. Am. Chem. Soc.* **2005,** *127,* 12577–12582. doi:10.1021/ja0524503
36. Elhadj, S.; De Yoreo, J. J.; Hoyer, J. R.; Dove, P. M. *Proc. Natl. Acad. Sci. U. S. A.* **2006,** *103,* 19237–19242. doi:10.1073/pnas.0605748103
37. Levi, Y.; Albeck, S.; Brack, A.; Weiner, S.; Addadi, L. *Chem. – Eur. J.* **1998,** *4,* 389–396. doi:10.1002/(SICI)1521-3765(19980310)4:3<389::AID-CHEM389>3.0.CO;2-X
38. Fischer, V.; Landfester, K.; Muñoz-Espí, R. *Cryst. Growth Des.* **2011,** *11,* 1880–1890. doi:10.1021/cg200058d
39. Hood, M. A.; Landfester, K.; Muñoz-Espí, R. *Cryst. Growth Des.* **2014,** *14,* 1077–1085. doi:10.1021/cg401580y
40. Muñoz-Espí, R.; Qi, Y.; Lieberwirth, I.; Gómez, C. M.; Wegner, G. *Chem. – Eur. J.* **2006,** *12,* 118–129. doi:10.1002/chem.200500860
41. Muñoz-Espí, R.; Chandra, A.; Wegner, G. *Cryst. Growth Des.* **2007,** *7,* 1584–1589. doi:10.1021/cg060858l
42. Wegner, G.; Demir, M. M.; Faatz, M.; Gorna, K.; Muñoz-Espí, R.; Guillemet, B.; Gröhn, F. *Macromol. Res.* **2007,** *15,* 95–99. doi:10.1007/BF03218759
43. Kim, Y.-Y.; Ribeiro, L.; Maillot, F.; Ward, O.; Eichhorn, S. J.; Meldrum, F. C. *Adv. Mater.* **2010,** *22,* 2082–2086. doi:10.1002/adma.200903743
44. Krattiger, P.; Nassif, N.; Völkel, A.; Mastai, Y.; Wennemers, H.; Cölfen, H. *Colloids Surf., A* **2010,** *354,* 218–225. doi:10.1016/j.colsurfa.2009.09.031
45. Zinchenko, A. *Polym. Sci., Ser. C* **2012,** *54,* 80–87. doi:10.1134/S1811238212070077
46. Braun, E.; Eichen, Y.; Sivan, U.; Ben-Yoseph, G. *Nature* **1998,** *391,* 775–778. doi:10.1038/35826
47. Mertig, M.; Colombi Ciacchi, L.; Seidel, R.; Pompe, W.; De Vita, A. *Nano Lett.* **2002,** *2,* 841–844. doi:10.1021/nl025612r
48. Kinsella, J. M.; Ivanisevic, A. *J. Am. Chem. Soc.* **2005,** *127,* 3276–3277. doi:10.1021/ja043865b
49. Torimoto, T.; Yamashita, M.; Kuwabata, S.; Sakata, T.; Mori, H.; Yoneyama, H. *J. Phys. Chem. B* **1999,** *103,* 8799–8803. doi:10.1021/jp991781x
50. Dong, L.; Hollis, T.; Connolly, B. A.; Wright, N. G.; Horrocks, B. R.; Houlton, A. *Adv. Mater.* **2007,** *19,* 1748–1751. doi:10.1002/adma.200602543
51. Wang, Z.; Liu, J.; Zhang, K.; Cai, H.; Zhang, G.; Wu, Y.; Kong, T.; Wang, X.; Chen, J.; Hou, J. *J. Phys. Chem. C* **2009,** *113,* 5428–5433. doi:10.1021/jp810274k
52. Pu, S.; Zinchenko, A. A.; Murata, S. *Langmuir* **2011,** *27,* 5009–5013. doi:10.1021/la104984x
53. Reches, M.; Gazit, E. *Science* **2003,** *300,* 625–627. doi:10.1126/science.1082387
54. Mao, C.; Flynn, C. E.; Hayhurst, A.; Sweeney, R.; Qi, J.; Georgiou, G.; Iverson, B.; Belcher, A. M. *Proc. Natl. Acad. Sci. U. S. A.* **2003,** *100,* 6946–6951. doi:10.1073/pnas.0832310100
55. Kumara, M. T.; Tripp, B. C.; Muralidharan, S. *J. Phys. Chem. C* **2007,** *111,* 5276–5280. doi:10.1021/jp067479n
56. Padalkar, S.; Hulleman, J. D.; Kim, S. M.; Rochet, J. C.; Stach, E. A.; Stanciu, L. A. *Nanotechnology* **2008,** *19,* 275602. doi:10.1088/0957-4484/19/27/275602
57. Caruso, F. *Top. Curr. Chem.* **2003,** *227,* 145–168. doi:10.1007/3-540-36412-9_6
58. Lou, X. W.; Archer, L. A.; Yang, Z. C. *Adv. Mater.* **2007,** *20,* 3987–4019. doi:10.1002/adma.200800854
59. Liu, J.; Liu, F.; Gao, K.; Wu, J. S.; Xue, D. F. *J. Mater. Chem.* **2009,** *19,* 6073–6084. doi:10.1039/b900116f
60. Muñoz-Espí, R.; Mastai, Y.; Gross, S.; Landfester, K. *CrystEngComm* **2013,** *15,* 2175–2191. doi:10.1039/C3CE26657E
61. Li, F.; Li, J.; Zhang, S. *Talanta* **2008,** *74,* 1247–1255. doi:10.1016/j.talanta.2007.08.032
62. Boissière, M.; Meadows, P. J.; Brayner, R.; Hélary, C.; Livage, J.; Coradin, T. *J. Mater. Chem.* **2006,** *16,* 1178–1182. doi:10.1039/b515797h
63. Taheri, S.; Baier, G.; Majewski, P.; Barton, M.; Förch, R.; Landfester, K.; Vasilev, K. *J. Mater. Chem. B* **2014,** *2,* 1838–1845. doi:10.1039/c3tb21690j
64. Zinchenko, A. A.; Yoshikawa, K.; Baigl, D. *Adv. Mater.* **2005,** *17,* 2820–2823. doi:10.1002/adma.200501549
65. Chen, N.; Zinchenko, A. A.; Yoshikawa, K. *Nanotechnology* **2006,** *17,* 5224. doi:10.1088/0957-4484/17/20/030
66. Preston, T. C.; Signorell, R. *Langmuir* **2010,** *26,* 10250–10253. doi:10.1021/la100402j
67. Lee, I.; Lee, S.-Y. *J. Phys. Chem. C* **2009,** *113,* 17372–17377. doi:10.1021/jp905869b
68. El Kadib, A.; Bousmina, M. *Chem. – Eur. J.* **2012,** *18,* 8264–8277. doi:10.1002/chem.201104006
69. Molvinger, K.; Quignard, F.; Brunel, D.; Boissière, M.; Devoisselle, J.-M. *Chem. Mater.* **2004,** *16,* 3367–3372. doi:10.1021/cm0353299
70. El Kadib, A.; Molvinger, K.; Guimon, C.; Quignard, F.; Brunel, D. *Chem. Mater.* **2008,** *20,* 2198–2204. doi:10.1021/cm800080s
71. Silva, S. S.; Ferreira, R. A. S.; Fu, L.; Carlos, L. D.; Mano, J. F.; Reis, R. L.; Rocha, J. *J. Mater. Chem.* **2005,** *15,* 3952–3961. doi:10.1039/b505875a
72. Watzke, H. J.; Dieschbourg, C. *Adv. Colloid Interface Sci.* **1994,** *50,* 1–14. doi:10.1016/0001-8686(94)80021-9
73. El Kadib, A.; Primo, A.; Molvinger, K.; Bousmina, M.; Brunel, D. *Chem. – Eur. J.* **2011,** *17,* 7940–7946. doi:10.1002/chem.201003740
74. Ganesan, R.; Gedanken, A. *Nanotechnology* **2008,** *19,* 025702. doi:10.1088/0957-4484/19/02/025702
75. Collins, A. M.; Mann, S.; Hall, S. R. *Nanoscale* **2010,** *2,* 2370–2372. doi:10.1039/c0nr00382d
76. Depan, D.; Singh, R. P. *J. Appl. Polym. Sci.* **2010,** *115,* 3636–3644. doi:10.1002/app.31463
77. Fernández, M. S.; Arias, J. I.; Martínez, M. J.; Saenz, L.; Neira-Carrillo, A.; Yazdani-Pedram, M.; Arias, J. L. *J. Tissue Eng. Regener. Med.* **2012,** *6,* 497–504. doi:10.1002/term.455
78. Neira-Carrillo, A.; Yazdani-Pedram, M.; Retuert, J.; Diaz-Dosque, M.; Gallois, S.; Arias, J. L. *J. Colloid Interface Sci.* **2005,** *286,* 134–141. doi:10.1016/j.jcis.2004.12.046
79. Lee, Y.-T.; Yu, B.-Y.; Shao, H.-J.; Chang, C.-H.; Sun, Y.-M.; Liu, H.-C.; Hou, S.-M.; Young, T.-H. *J. Biomater. Sci., Polym. Ed.* **2011,** *22,* 2369–2388. doi:10.1163/092050610X540431
80. Brayner, R.; Vaulay, M.; Fiévet, F.; Coradin, T. *Chem. Mater.* **2007,** *19,* 1190–1198. doi:10.1021/cm062580q
81. Jaouen, V.; Brayner, R.; Lantiat, D.; Steunou, N.; Coradin, T. *Nanotechnology* **2010,** *21,* 185605. doi:10.1088/0957-4484/21/18/185605
82. Perullini, M.; Amoura, M.; Jobbágy, M.; Roux, C.; Livage, J.; Coradin, T.; Bilmes, S. A. *J. Mater. Chem.* **2011,** *21,* 8026–8031. doi:10.1039/c1jm10684h

83. Hernández, R.; Sacristán, J.; Nogales, A.; Ezquerra, T. A.; Mijangos, C. *Langmuir* **2009,** *25,* 13212–13218. doi:10.1021/la902441s
84. Brayner, R.; Coradin, T.; Vaulay, M.; Mangeney, C.; Livage, J.; Fiévet, F. *Colloids Surf., A* **2005,** *256,* 191–197. doi:10.1016/j.colsurfa.2005.01.018
85. Smitha, S.; Shajesh, P.; Mukundan, P.; Warrier, K. G. K. *J. Sol-Gel Sci. Technol.* **2007,** *42,* 157–163. doi:10.1007/s10971-007-1535-9
86. Smitha, S.; Shajesh, P.; Mukundan, P.; Nair, T. D. R.; Warrier, K. G. K. *Colloids Surf., B* **2007,** *55,* 38–43. doi:10.1016/j.colsurfb.2006.11.008
87. Ethirajan, A.; Ziener, U.; Chuvilin, A.; Kaiser, U.; Cölfen, H.; Landfester, K. *Adv. Funct. Mater.* **2008,** *18,* 2221–2227. doi:10.1002/adfm.200800048
88. Li, Z.; Taubert, A. *Molecules* **2009,** *14,* 4682–4688. doi:10.3390/molecules14114682
89. Cai, J.; Kimura, S.; Wada, M.; Kuga, S. *Biomacromolecules* **2008,** *10,* 87–94. doi:10.1021/bm800919e
90. Cai, J.; Liu, S.; Feng, J.; Kimura, S.; Wada, M.; Kuga, S.; Zhang, L. *Angew. Chem., Int. Ed.* **2012,** *51,* 2076–2079. doi:10.1002/anie.201105730

## License and Terms

BEILSTEIN JOURNAL OF NANOTECHNOLOGY

# Chemoselective silicification of synthetic peptides and polyamines

Maryna Abacilar, Fabian Daus and Armin Geyer*

Full Research Paper

Open Access

Address:
Faculty of Chemistry, Philipps-Universität Marburg, 35032 Marburg, Germany

Email:
Armin Geyer* - geyer@staff.uni-marburg.de

* Corresponding author

Keywords:
biomineralisation; biosilicification; NMR spectroscopy; polyamines; silaffin

*Beilstein J. Nanotechnol.* **2015,** *6,* 103–110.
doi:10.3762/bjnano.6.10

Received: 15 August 2014
Accepted: 03 December 2014
Published: 08 January 2015

This article is part of the Thematic Series "Towards multifunctional inorganic materials: biopolymeric templates".

Guest Editors: C. Steinem and J. Bill



## Abstract

Biosilicification sets the standard for the localized in vitro precipitation of silica at low orthosilicate concentrations in aqueous environment under ambient conditions. Numerous parameters must be controlled for the development of new technologies in designing inventive nanosilica structures, which are able to challenge the biological templates. A long neglected requirement that came into focus in the recent years are the cellular techniques of preventing unintentional lithification of cellular structures since numerous cellular components such as membranes, DNA, and proteins are known to precipitate nanosilica. The diatom metabolism makes use of techniques that restrict silicification to an armor of silica around the cell wall while avoiding the petrifying gaze of Medusa, which turns the whole cell into stone. Step by step, biochemistry unveils the hierarchical interplay of an arsenal of low-molecular weight molecules, proteins, and the cytoskeletal architecture and it becomes clearer why the organisms invest much metabolic effort for an obviously simple chemical reaction like the precipitation of amorphous silica. The discrimination between different soluble components in the silicification process (chemoselective silicification) is not only vitally important for the diatom but poses an interesting challenge for in vitro experiments. Until now, silica precipitation studies were mainly focused on the amount, the morphology, and composition of the precipitate while disregarding a quantitative analysis of the remaining soluble components. Here, we turn the tables and quantify the soluble components by $^{1}$H NMR in the progress of precipitation and present experiments which quantify the additivity, and potential cooperativity of long chain polyamines (LCPAs) and cationic peptides in the silicification process.

## Introduction

Modifications of the Stöber method [1] are in use today for the synthesis of largely monodisperse silica particles with entrapped enzymes for NMR studies [2] or numerous other applications [3]. Generally, one or more molecular species are exposed to orthosilicic acid at pH 7 or higher. Slow or inefficient precipitation is accompanied by gelation of the remainig

silicic acid but the primary aim of such experiments is the formation of precipitates with well-defined shapes such as spheres (grey ball in Figure 1) or other morphologies. The unmitigated silicification entraps the dissolved molecules as far as possible in the silica precipitate. Biosilicification however, relies on the sharp differentiation between soluble and entrapped molecules, a sophisticated form of chemoselective silicification. Currently accepted models are the LCPA–phosphate model [4] and the silaffin-matrix hypothesis [5]. Both formulate varying concentrations of soluble components at the surface of the forming silica beads. Poulsen et al. investigated the mutual influence of peptides and LCPAs. Here we investigate the simplest scenario of chemoselective precipitation, which is the differentiation between two dissolved components, a cationic peptide and an oligoamine, that are both capable of precipitating silica on their own (Figure 1). Observing dissolved molecules next to the precipitate gives answers to questions such as these: Is the amine completely consumed by the precipitate formed or is there a fixed N/Si ratio leaving the surplus amine untouched? What happens with the less capable Si precipitator in the presence of the better precipitator? Is there a measurable cooperativity between peptides and amines?

Silica precipitation experiments are time consuming and error-prone because many actions are needed to separate the precipitate of amorphous silica, to dry it, and to weigh it. NMR is no substitute for other analytical methods but $^1$H NMR is a single technology that simultaneously monitors the pH value, viscosity, and amount of dissolved molecules. $^1$H NMR is advantageous for optimizing the experimental settings of silica precipitation process because of the many parameters that are visible in a single spectrum. The consumption of molecules during the precipitation process is quantified as a function of time while constantly monitoring the change in pH from the signal splitting of imidazole and the viscosity of the solution from the half-width of a selected singlet. The greatest benefit lies in the conduction of competition experiments between different types of molecules. By using only a small excess of TMOS, there is no need for stopping the precipitation experiment by addition of HCl after a few minutes. Instead, a molecule of interest can be mixed with a known oligoamine to identify the better precipitator based on the stronger reduction in $^1$H NMR signal intensity.

# Results

## Polyamines and cationic peptides

The cell wall of diatoms is a composite material with a high content of organic molecules from various compound classes such as oligopropylenamines [6], polycationic peptides [7], proteins [8], and polysaccharides [9]. Even higher contents of organic material are found in sponges in which the biosilica is associated with collagen-type proteins [10]. The common feature of all these organic molecules is their modular assembly. We and others analyzed to what extent the mineralisation process and the morphology of the precipitate depends on the number of propyleneimino repeating units [11], the type of KXXK-boxes in silaffin proteins (K = Lys, X = other amino acid) [12], or the number of POG tripeptide repeating units in collagens [13]. The availability of relatively large amounts of pure material in reproducible quality is a benefit that links organic synthesis to material science. Different from silica-associated molecules of biological origin, which are characterized

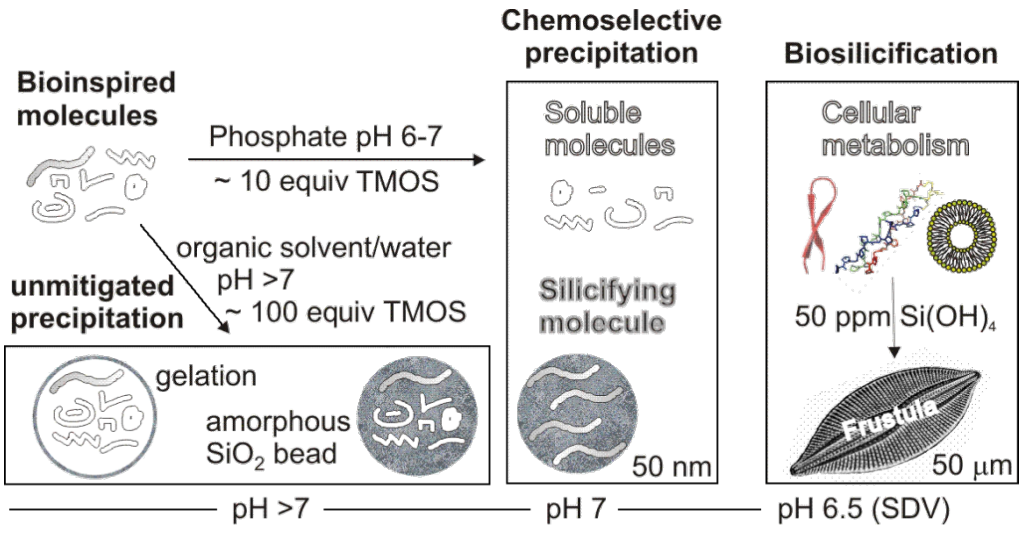


**Figure 1:** Chemoselective silica precipitation. Different symbols indicate a mixture of organic molecules from which only selected compounds form a precipitate with silicic acid. The remaining solution is analyzed by $^1$H NMR.

by structural and compositional microheterogeneity, the chemical synthesis of such molecules yields defined structures and allows for the comparison of individual chain lengths. The distribution of natural oligomers around an average value is replaced with a sequence of individual chain lengths for independent experiments. The aim is to unravel the interplay between different organic compound classes and inorganic components as well as the synergy on different levels of hierarchy from the charge interaction on the atomistic level to the micrometer scale of the frustula structure. Here, we focus on five compounds, which are all either known to or at least expected to precipitate silica (Figure 2). Three amines with increasing number of nitrogen atoms, a basic peptide, and a toxin [14] that is not involved in biomineralization but stands exemplary for other amines capable of silica precipitation.

## Synthetic methods

Figure 3 shows the synthetic strategies used to access the molecules **2**–**5**. CTC resin [chloro-(2'-chlorotrityl)polystyrene resin] served as a solid support and was functionalized directly with different amines [14]. The nucleophilicity of one nitrogen of 1,3-propylenediamine was annihilated by tritylation with CTC resin (Figure 3 upper row) while the other peripheral amine remains reactive for peptide coupling. The HBTU/HOBt-mediated condensation of a Fmoc-acylated amino acid and cleavage of the temporary protecting group Fmoc with piperidine was repeated in 15 cycles to obtain CTC-bound precursor of peptide **5** which was finally Boc-deprotected by TFA and simultaneously cleaved from the resin. This peptide bears an additional cationic charge instead of the unproductive C-terminal carboxylate, which would be obtained from traditional solid-phase peptide synthesis. CTC-resin has a double function here because it acts as a protecting group and as a solid support. This strategy can be expanded to other amines such as bis(3-aminopropyl)amine (sometimes called norspermidine) shown in the center of Figure 3. Again only one of the two primary amines reacts with the resin because the secondary amine is sterically too demanding to be tritylated. Avoiding large excess of acylating reagent, toxin **5** was obtained directly in high regioselectivity for acylation without necessity of a N-protecting group on the triamine. Protecting groups on both primary amines lead to a complementary reactivity of bis(3-aminopropyl)amine, now enabling the secondary amine as the only remaining nucleophile to react with the CTC-resin. This is shown in the bottom-

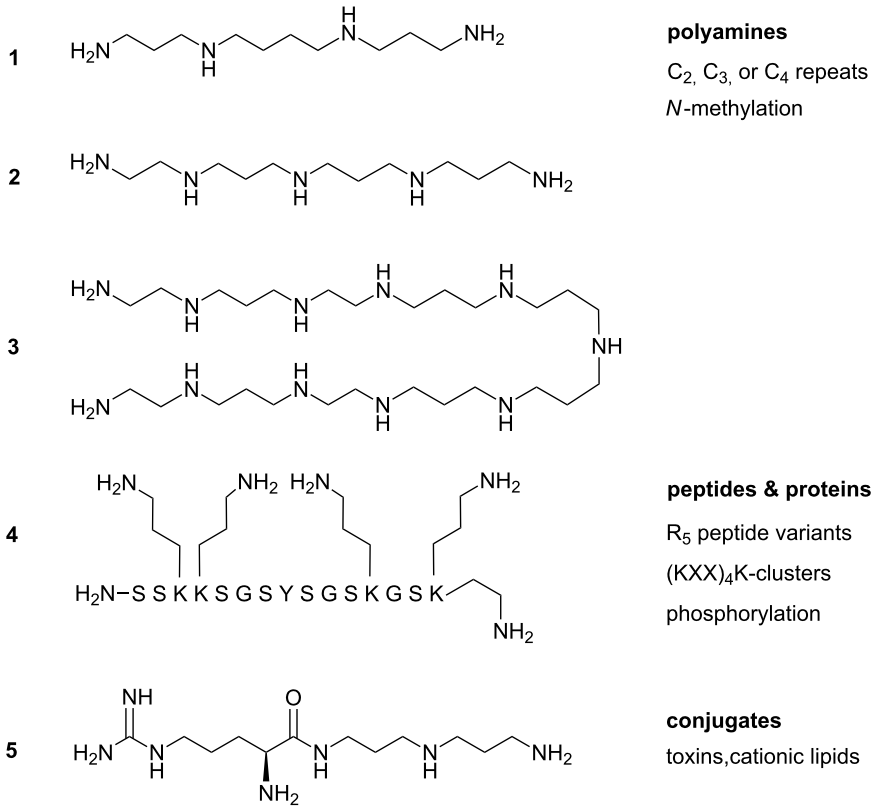


**Figure 2:** The polyamines **1**, **2**, and **3** have increasing numbers of 4, 5 and 11 basic nitrogens. Peptide **4** is a simplified sequence derived from the silaffins and bears 6 primary amines. Amino acids are characterized by the one-letter code (S Serin, K Lysin, G Glycin, Y Tyrosine). Toxine **5** is the condensation product of Arginine and bis(3-aminopropyl)amine.

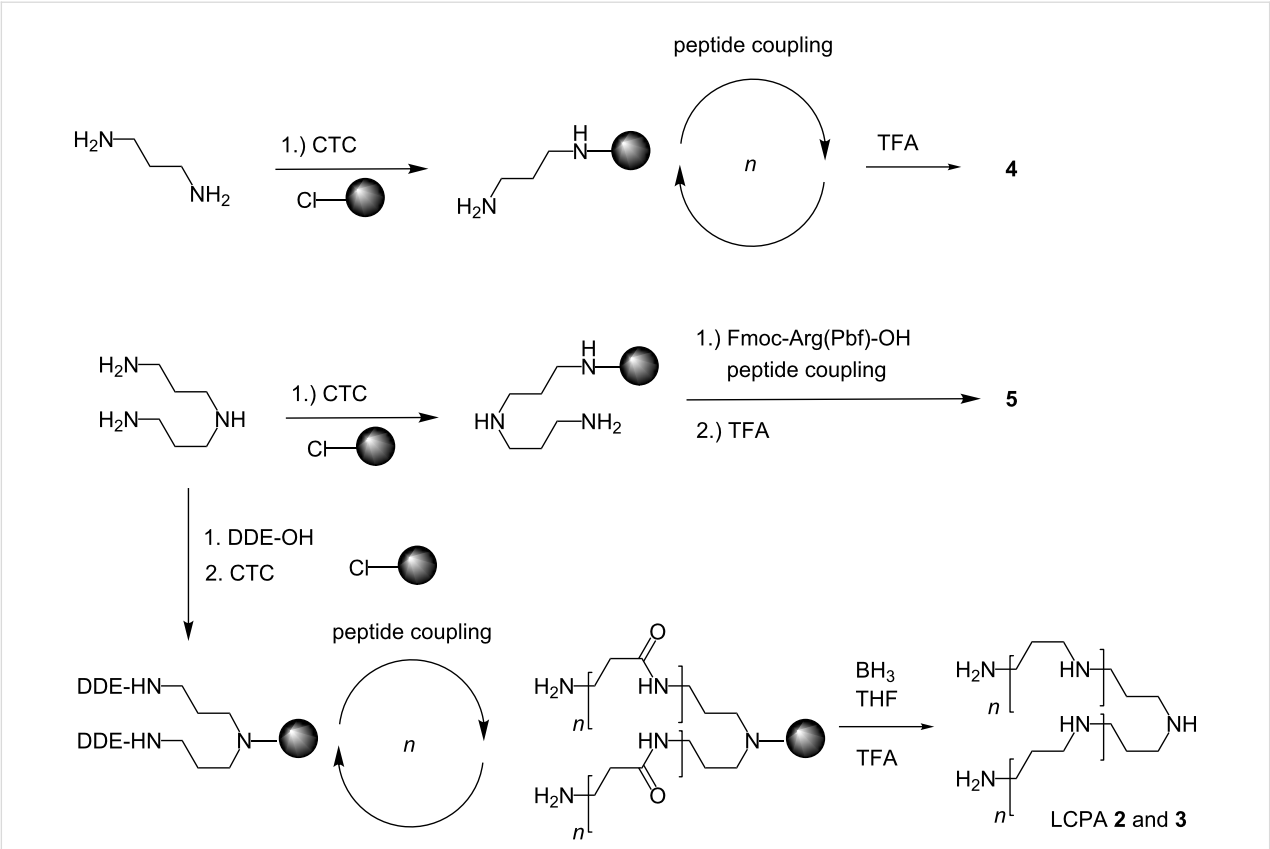


**Figure 3:** Three synthetic strategies for oligoamines and cationic peptides. The CTC-resin is shown as a grey ball and the arrows represent the coupling and Fmoc deprotection step. The letter *n* stands for the number of coupling and deprotection cycles. DDE = 1-(4,4-dimethyl-2,6-dioxocyclohex-1-ylidene). Top and center: Propylenediamine or bis(3-aminopropyl)amine acts as a spacer for the solid-phase peptide synthesis on CTC-resin. Bottom: Chain extension at both ends of a diamine.

most synthesis of Figure 3. For the synthesis of **3**, we introduce this handy method, which halves the number of synthetic transformations. Hydrazinolysis cleaved the DDE groups allowing the simultaneous chain extension at both primary amines. Fmoc-β-Ala-OH and Fmoc-Gly-OH were coupled to a suspension of this resin with HBTU. Key step in the synthesis of LCPAs is the borane reduction of oligoamides developed by the groups of Hall [15] and Houghten [16], which we adapted for the synthesis of LCPAs on trityl resin [11]. The amide reduction with excess of the THF-complex of borane removed the amide oxygen to obtain C2 and C3 extensions of the oligoamine. Borane–nitrogen complexes were destroyed in several washing cycles with piperidine before final TFA cleavage of the LCPA from the resin. LCPAs **2** and **3** were obtained with this strategy.

## NMR studies

A constant low concentration of orthosilicic acid is expected to be advantageous for chemoselective silicification studies instead of a single addition of a large excess of tetramethyl orthosilicate (TMOS), sometimes exceeding more than 100 equivalents. With the aim of obtaining a constant release of orthosilicic acid from TMOS we initially intended to slow down TMOS hydrolysis by organic solvents. Even the intermediates of TMOS hydrolysis are easily identified by $^1$H NMR in DMSO (Figure S1, Supporting Information File 1) but precipitation studies were not successful because the silica precipitation is slowed down, too. As consequence the unwanted background gelation dominates and the amount of residual water strongly influences the outcome of the experiments. The TMOS hydrolysis is much faster in aqueous environment and all TMOS was available as orthosilicic acid at the beginning of the NMR experiments (Figure S2, Supporting Information File 1). All measurements were conducted in buffered solution of deuterated water to simplify the experimental setting of the NMR measurement. Instead of a single addition of TMOS, we added small amounts (less than ten equivalents) stepwise until all organic molecules were precipitated and the integral in the $^1$H NMR approached zero. In the precipitation studies of isolated molecular species it made no difference whether TMOS was added in a single step or in several portions. Orthosilicic acid was consumed for silica precipitation as long as a mole-

cule that is capable of silica precipitation remains in solution. Whether TMOS was added in a single step or in portions had no influence on the overall result. For the precipitation studies of more than one dissolved component it was possible to measure the ratio of the dissolved molecules after each stepwise addition of TMOS as described in the competition experiments below. The dynamic range of modern NMR spectrometers (16 bit digitizer) is big enough to resolve the signal intensity of the organic molecule in the presence of a large methanol signal from the TMOS hydrolysis. Their relative intensities quantify the excess of orthosilicic acid present in the silicification experiment. Three typical outcomes of the silicification experiments are shown in Figure 4 in which gelation is directly visible from the clouding and solidification of the solvent (experiments A and B). Only precipitation of type "C" yields amorphous silica from the complete precipitation of orthosilicic acid without gelation of any remaining dissolved silica.

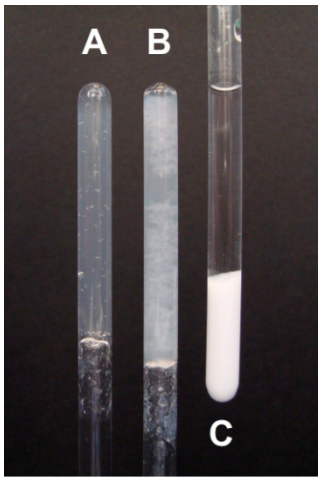


**Figure 4:** Precipitation of orthosilicic acid with amine **1** in NMR tubes at pH 6.5 (A), 7 (B), and 10 (C). Inefficient silicification in A and B is accompanied by gelation and high viscosity of the reaction mixture. Complete precipitation under the conditions of C shows a sharp separation between the clear solution and the precipitate which is separated by centrifugation to obtain a high-resolution $^1$H NMR spectrum again.

The increase in macroscopic viscosity, which is directly visible in the upside-down turned tubes in Figure 4, corresponds to the microscopic viscosity, which is visible as line broadening of all signals but quantified as the half width of the trimethylsilyl propanoic acid (TSP) singlet that serves as an internal standard. Gelation is accompanied by a significant increase of line broadening. While the initial viscosities of the buffered solutions are characterized by values which do not surpass 1.5 Hz, a factor of 10 is typical for the gelated NMR tubes. A second internal standard is histidine which has a p$K_a$ value of around 6.5 [17]. The signal separation of the imidazole singlets of histidine show significant changes around this pH value although it does not interfere with the precipitation process. In spite of its three nitrogen atoms, histidine does not get incorporated into the silica, which shows the special properties of the other investigated oligoamines. Precipitation studies were performed with all compounds shown in Figure 1. Typical NMR spectra under different pH conditions are shown in Figure 5 for compound **1**. Two well separated methylene groups of **1** at 2 ppm, which are not influenced by the released methanol from the added TMOS, are highlighted with a blue box. The increase of the line broadening at pH 6.5 (Figure 5a and Figure 5b) affects all signals but the signal integrals do not change except for **1,** which loses half of its intensity. Short-chained amines are not qualified to precipitate silica at this pH and therefore gets incorporated only by 50% while the remaining orthosilicic acid forms a gel. A

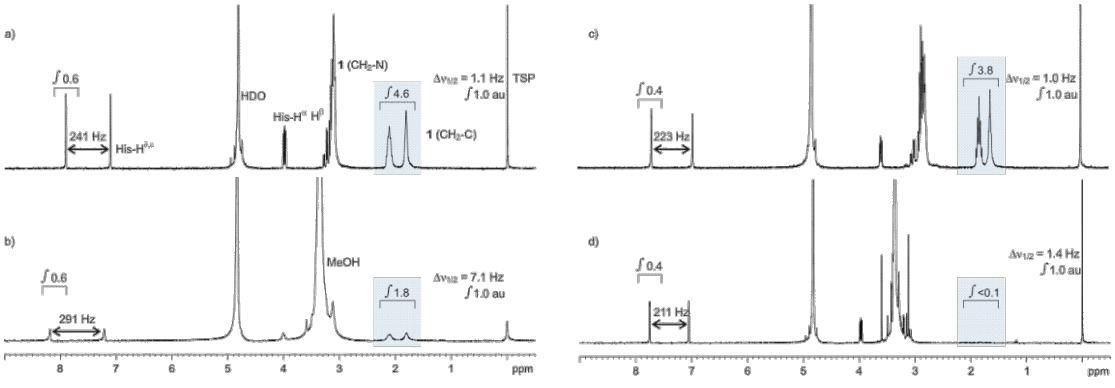


**Figure 5:** $^1$H NMR spectra (300 MHz, 300 K) of **1** a) without and b) in the presence of orthosilicic acid at pH 6 and the same experimental setting at pH 11 c) and d). TSP serves as an internal standard and the signal intensity (integral) was set to 1 a.u. (arbitrary units). Histidine is present as a second internal standard because the splitting of the imidazole CH groups (His-H$^\delta$ and His-H$^\varepsilon$) depends on the pH value in the region around the p$K_a$ value of the imidazole side chain. Signals of **1** which are not influenced by the resonance of the released methanol from the TMOS hydrolysis are highlighted by a blue box. Further details are given in the text.

further decrease in pH is detected by the increase of the signal splitting of the imidazole from 241 Hz (a) to 291 Hz (b). At significantly higher pH (Figure 5c,d) under typical Stöber conditions all amines are qualified to precipitate silica while the buffer keeps the high pH value. Therefore the signal of **1** is completely absent in d) and the signal splitting of imidazole does not change significantly. Furthermore, a change in solvent viscosity is not detectable. **1** becomes completely incorporated into the silica under strongly basic conditions and a low Si/N ratio of 4 is calculated under the assumption that the orthosilicic acid is consumed completely.

These NMR experiments were conducted for all compounds **1**–**5** (Table 1). With compound **1** silica cannot be precipitated at pH values below 7 without gelation [18]. All other experiments in Table 1 were conducted under high resolution conditions without gelation and polyamine **3** is quantitatively precipitated even at the lowest investigated value of pH 5.5. An amount of 50 equivalents of TMOS is precipitated by both longer LCPAs **2** and **3**, respectively, in phosphate buffer at slightly acidic pH values. Si/N is the ratio between orthosilicic acid and the number of basic nitrogens in the investigated compound minus the remaining peptide. Peptide **4** precipitates orthosilicic acid effectively but gets much less incorporated with a Si/N ratio above 100. Three additions of 40 equivalents of TMOS are necessary to precipitate it completely from solution. Toxin **5**, although completely unrelated to biosilicification, is able to precipitate silica, too. The dissolved molecules influence the buffer capacity and small changes in pH can influence the precipitation behavior of two different molecules. The reproducibility of each experimental setting was excellent but we consider it difficult to compare precipitation experiments of different molecules. Therefore, we designed experiments in which one amine serves as an internal standard for precipitation and the precipitation capacity of the second component can be easily judged by measuring a $^1$H NMR spectrum of the remaining solution after precipitation. The better precipitator is incorporated in the solid silica and removed from solution while the other component remains and yields signal intensity in the NMR spectrum. The technique can be expanded to more than two soluble components as long as at least one signal intensity is separated on the chemical shift scale. In this study, LCPA **3** is the compound that precipitates silica most efficiently and it is probably the most promising one to precipitate in the presence of other dissolved organic molecules. For **1** we observe significant chemoselectivity at neutral pH or slightly below. Commercially available spermine (**1**) was chosen as a reference to make the experimental setting independent from molecules which are only available in our group.

Figure 6 shows competition experiments with two amines competing for the silicic acid. From an equimolar mixture of **1** and **4**, two thirds of the amine precipitate without affecting the peptide concentration. Addition of another 40 equivalents of TMOS precipitates both molecules. Even from the 2:1 ratio of **1** and **4** with 28 equivalents of TMOS, approximately one third of the amine precipitates first. The second addition of the same amount of TMOS eliminates the signals of the amine completely and reduces the amount of peptide to 77% of the starting concentration. The chemoselectivity is less pronounced

**Table 1:** Silica precipitation experiments. The final column is the initial splitting of the imidazole signals which correlates with the observed pH value in brackets. The lower three rows list the numerical values for the bar diagrams in Figure 6.

| entry | compound | Si/N | random error[a] | equivalents TMOS, % peptide | $\Delta\nu_{1/2}$ [Hz] | $\Delta\delta$ $H^{\delta}$–$H^{\varepsilon}$, (pH) |
|---|---|---|---|---|---|---|
| 1 | **1** | 33:1 | ±0.3 | 16, 39% (gelation) | 1.1, 7 | 241, (6) |
| 2 | **1** | 4:1 | ±0.45 | 16, 0% | 1.0, 1.4 | 223, (11) |
| 3 | **2** | 50:1 | ±0.25 | 50, 0% | 1.1, 1.1 | 234, (6.8) |
| 4 | **3** | 50:1 | ±0.25 | 50, 0% | 1.1, 2.2 | 249, (5.5) |
| 5 | **4** | 142:1 | ±0.34 | 40, 81%; 40, 34%; 40, 0% | 0.9, 1.3 | 235, (6.8) |
| 6 | **5** | 98:1 | ±0.55 | 40, 32%; 40, 0% | 0.9, 1.2 | 230, (7) |
| 7 | **1 + 4** (1:1)[b] | 80:1 | ±0.55 | 40, 30% (**1**), 96% (**4**); 40, 0% | 0.9 1.6 | 231, (7) |
| 8 | **1 + 4** (2:1) | 72:1 | ±0.35 | 28, 72% (**1**), >98% (**4**); 28, 0% (**1**), 77% (**4**) | 1.0 1.1 | 248, (6) |
| 9 | **1 + 5** (1:1) | 24:1 | ±0.85 | 7, 39% (**1**), 74% (**5**); 7, 28% (**1**), 66% (**5**); 14, 15% (**1**), 35% (**5**); 30, 0% (**1**), 0% (**5**) | 1.0 1.0 | 224, (7) |

[a]The random error depends on the signal-to-noise ratio and uncertainties of signal integration in each $^1$H NMR spectrum. The experimental error increases parallel with the addition of TMOS because of the decreasing signal-to-noise ratio for the molecules of interest in the spectra. No error is given when the remaining amine is below the detection limit. Random errors are given only for the first addition of TMOS. [b]Ratio in brackets.

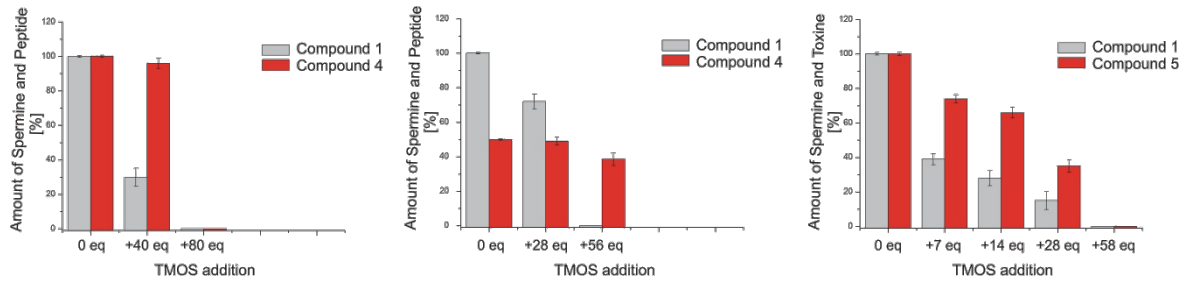


**Figure 6:** Silica precipitation competition experiments. Experimental details are according to the single component precipitations in Table 1. The addition of TMOS is shown on the *x*-coordinate and the starting conditions are set to 100% for better comparison. The left diagram shows spermine (**1**) vs $R_5$ peptide **4** in a 1:1 ratio (10 μmol/mL each) and the middle diagram shows them in a 2:1 ratio (15 μmol/mL both). In both precipitation experiments, **1** is consumed before a relevant amount of **4** precipitates. Right: **1** vs **5** in a 1:1 ratio (5 μmol/mL each). Again, **1** is the better precipitator although both organic molecules are consumed during the mineralization process.

for the mixture of **1** and **5**, which was titrated with the smallest first addition of only 7 equivalents of TMOS. From these competition experiments can be deduced that **5** is a better precipitator than **4**. An interesting observation is that **1** is a better precipitator in the presence of peptide **4** at pH 6 (Figure 6 right) than without (Table 1, entry 1).

Exemplary for the experiments of Table 1, the $^1$H NMR spectra of the equimolar competition experiment between amine **1** and peptide **4** (Table 1, entry 7) are shown in Figure 7. The amine and the cationic peptide are not expected to interact under the experimental conditions and the $^1$H NMR of the mixture represents the sum of the two single spectra. The chemoselective silica precipitation is documented in spectrum d) after the first addition of TMOS. The blue methylene group is incorporated in the silica precipitate while the yellow methylene group is still there. Spectrum e) proves that both molecules are competent to precipitate silica under the experimental conditions while the internal standards histidine and TSP remain in solution in all spectra.

## Discussion

LCPA phosphate microdrops are competent to precipitate silica [19] and the silaffin-matrix model attempts to explain silica precipitation inside of the silica deposition vesicle (SDV) at pH values as low as 5.5. Under these conditions, the nanostructure forms a template for the localized silicon dioxide precipitation in LCPA-rich but silaffin-poor areas [20]. From the numerous physical and experimental parameters, which differ from the literature experiments, only the chemical parameter of micro-

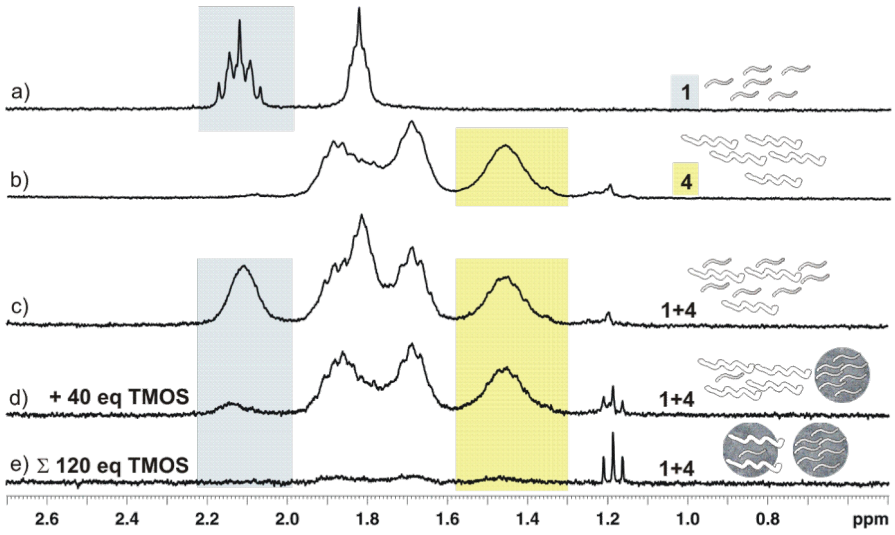


**Figure 7:** Expansions from the $^1$H NMR spectra (300 MHz, 300 K) of **1** a) and **4** b) and the spectrum of an equimolar mixture of both c) before the addition of orthosilicic acid at pH 7 together with the spectra of the stepwise addition of TMOS in d) and e). A methylene group that is only present in **1** and another that is only present in **4** are highlighted and document the stepwise precipitation of the two molecules. (Triplet at 1.19 ppm EtOH from residual tetraethyl orthoslicate (TEOS) in TMOS.) The complete $^1$H NMR spectra are shown in the Figure S3, Supporting Information File 1).

heterogeneity is resolved in our experiments, which consist of two-component mixtures of defined concentration of each individual molecular species. Polyamines and peptides compete for silicic acid in the NMR tube. Further parameters such as the excess of silicic acid, the pH value, and phosphate concentration are selected by us based on former precipitation experiments. In competition experiments of peptide **4** (Table 1, entry 7) and amine **5** (Table 1, entry 9), amine **1** serves as an internal standard that identifies **5** as the better precipitator than **4**, without the necessity of conducting the competitive precipitation of **4** and **5**.

## Conclusion

In conclusion, it is not our intension to advertise for NMR as a substitute for classical silica precipitation experiments but as a fast, rich in information, and fail-proof additional method for the identification of in vitro conditions for the development of synthetic silica nanocomposites. The better organic template is entrapped in the inorganic precipitate while the others remain in solution. This straightforward method identifies cooperativity of bioorganic templates in solution and can be easily transferred to other mineralization experiments.

## Experimental

The NMR spectra were recorded at 300 MHz and the pH values are not corrected to pD. Synthesis details are given in Supporting Information File 1.

## Supporting Information

### Supporting Information File 1

Synthesis details.
[http://www.beilstein-journals.org/bjnano/content/supplementary/2190-4286-6-10-S1.pdf]

## Acknowledgements

We thank Christian Haas for the synthesis of compounds **3** and **5**.

## References

1. Stöber, W.; Fink, A.; Bohn, E. *J. Colloid Interface Sci.* **1968,** *26,* 62–69. doi:10.1016/0021-9797(68)90272-5
2. Guisan, J. M. *Immobilization of Enzymes and Cells;* Springer, 2006. doi:10.1007/978-1-59745-053-9
3. Patwardhan, S. V. *Chem. Commun.* **2011,** *47,* 7567–7582. doi:10.1039/c0cc05648k
4. Kröger, N.; Deutzmann, R.; Bergsdorf, C.; Sumper, M. *Proc. Natl. Acad. Sci. U. S. A.* **2000,** *97,* 14133–14138. doi:10.1073/pnas.260496497
5. Poulsen, N.; Sumper, M.; Kröger, N. *Proc. Natl. Acad. Sci. U. S. A.* **2003,** *100,* 12075–12080. doi:10.1073/pnas.2035131100
6. Sumper, M.; Lehmann, G. *ChemBioChem* **2006,** *7,* 1419–1427. doi:10.1002/cbic.200600184
7. Kröger, N.; Deutzmann, R.; Sumper, M. *Science* **1999,** *286,* 1129–1132. doi:10.1126/science.286.5442.1129
8. Richthammer, P.; Börmel, M.; Brunner, E.; van Pée, K.-H. *ChemBioChem* **2011,** *12,* 1362–1366. doi:10.1002/cbic.201000775
9. Ogasawara, W.; Shenton, W.; Davis, S. A.; Mann, S. *Chem. Mater.* **2000,** *12,* 2835–2837. doi:10.1021/cm0004376
10. Ehrlich, H.; Deutzmann, R.; Brunner, E.; Cappellini, E.; Koon, H.; Solazzo, C.; Yang, Y.; Ashford, D.; Thomas-Oates, J.; Lubeck, M.; Baessmann, C.; Langrock, T.; Hoffmann, R.; Wörheide, G.; Reitner, J.; Simon, P.; Tsurkan, M.; Ereskovsky, A. V.; Kurek, D.; Bazhenov, V. V.; Hunoldt, S.; Mertig, M.; Vyalikh, D. V.; Molodtsov, S. L.; Kummer, K.; Worch, H.; Smetacek, V.; Collins, M. J. *Nat. Chem.* **2010,** *2,* 1084–1088. doi:10.1038/nchem.899
11. Bernecker, A.; Wieneke, R.; Riedel, R.; Seibt, M.; Geyer, A.; Steinem, C. *J. Am. Chem. Soc.* **2010,** *132,* 1023–1031. doi:10.1021/ja9061163
12. Wieneke, R.; Bernecker, A.; Riedel, R.; Sumper, M.; Steinem, C.; Geyer, A. *Org. Biomol. Chem.* **2011,** *9,* 5482–5486. doi:10.1039/c1ob05406f
13. Weiher, F.; Schatz, M.; Steinem, C.; Geyer, A. *Biomacromolecules* **2013,** *14,* 683–687. doi:10.1021/bm301737m
14. Nash, I. A.; Bycroft, B. W.; Chan, W. C. *Tetrahedron Lett.* **1996,** *37,* 2625–2628. doi:10.1016/0040-4039(96)00344-9
15. Hall, D. G.; Laplante, C.; Manku, S.; Nagendran, J. *J. Org. Chem.* **1999,** *64,* 698–699. doi:10.1021/jo982290w
16. Nefzi, A.; Ostresh, J. M.; Houghten, R. A. *Tetrahedron* **1999,** *55,* 335–344. doi:10.1016/S0040-4020(98)01043-6
17. Silverstein, T. P. *J. Chem. Educ.* **2012,** *89,* 1474–1475. doi:10.1021/ed3000028
18. Belton, D. J.; Patwardhan, S. V.; Annenkov, V. V.; Danilovtseva, E. N.; Perry, C. C. *Proc. Natl. Acad. Sci. U. S. A.* **2008,** *105,* 5963–5968. doi:10.1073/pnas.0710809105
19. Sumper, M.; Brunner, E. *Adv. Funct. Mater.* **2006,** *16,* 17–26. doi:10.1002/adfm.200500616
20. Sumper, M.; Kröger, N. *J. Mater. Chem.* **2004,** *14,* 2059–2065. doi:10.1039/b401028k

## License and Terms

BEILSTEIN JOURNAL OF NANOTECHNOLOGY

# Multifunctional layered magnetic composites

Maria Siglreitmeier[1], Baohu Wu[1,2], Tina Kollmann[3], Martin Neubauer[4], Gergely Nagy[5], Dietmar Schwahn[6], Vitaliy Pipich[2], Damien Faivre[7], Dirk Zahn[3], Andreas Fery[4] and Helmut Cölfen[*1]

Full Research Paper

Open Access

Address:
[1]Department of Chemistry, Physical Chemistry, University of Konstanz, Universitätsstraße 10, 78457 Konstanz, Germany, [2]Jülich Centre for Neutron Science JCNS-MLZ, Outstation at MLZ, Forschungszentrum Jülich, Lichtenbergstraße 1, 85748 Garching, Germany, [3]Theoretical Chemistry, University of Erlangen-Nürnberg, Nägelsbachstraße 25, 91052 Erlangen, Germany, [4]Physical Chemistry II, University of Bayreuth, Universitätsstraße 30, 95447 Bayreuth, Germany, [5]Laboratory for Neutron Scattering, Paul Scherrer Institute, 5232 Villigen PSI, Switzerland, [6]Technische Universität München, Forschungs-Neutronenquelle Heinz Maier-Leibnitz (FRM II), 85748 Garching, Germany and [7]Department of Biomaterials, Max Planck Institute of Colloids & Interfaces Science Park Golm, 14424 Potsdam, Germany

Email:
Helmut Cölfen[*] - helmut.coelfen@uni-konstanz.de

* Corresponding author

Keywords:
bio-inspired mineralization; biomineralization; chitin; ferrogel; hybrid materials; magnetite; nacre

*Beilstein J. Nanotechnol.* **2015,** *6,* 134–148.
doi:10.3762/bjnano.6.13

Received: 02 June 2014
Accepted: 09 December 2014
Published: 12 January 2015

This article is part of the Thematic Series "Towards multifunctional inorganic materials: biopolymeric templates".

Guest Editors: C. Steinem and J. Bill



## Abstract

A fabrication method of a multifunctional hybrid material is achieved by using the insoluble organic nacre matrix of the *Haliotis laevigata* shell infiltrated with gelatin as a confined reaction environment. Inside this organic scaffold magnetite nanoparticles (MNPs) are synthesized. The amount of MNPs can be controlled through the synthesis protocol therefore mineral loadings starting from 15 wt % up to 65 wt % can be realized. The demineralized organic nacre matrix is characterized by small-angle and very-small-angle neutron scattering (SANS and VSANS) showing an unchanged organic matrix structure after demineralization compared to the original mineralized nacre reference. Light microscopy and confocal laser scanning microscopy studies of stained samples show the presence of insoluble proteins at the chitin surface but not between the chitin layers. Successful and homogeneous gelatin infiltration in between the chitin layers can be shown. The hybrid material is characterized by TEM and shows a layered structure filled with MNPs with a size of around 10 nm. Magnetic analysis of the material demonstrates superparamagnetic behavior as characteristic for the particle size. Simulation studies show the potential of collagen and chitin to act as nucleators, where there is a slight preference of chitin over collagen as a nucleator for magnetite. Colloidal-probe AFM measurements demonstrate that introduction of a ferrogel into the chitin matrix leads to a certain increase in the stiffness of the composite material.

## Introduction

Biominerals, which are organic–inorganic hybrids and highly sophisticated materials with optimal assimilated properties, have evolved in nature. The mechanisms of biomineral formation are still far from being understood and there is currently large research activity from groups of different expertise. Most biominerals are hierarchically structured, which consequently adds favorable physical properties such as hardness and fracture resistance to the material. An intriguing and much investigated material is nacre which is the inner protecting layer of some marine sea shells. It is well-known for its beautiful iridescence but also for the outstanding mechanical properties. Nacre has a layered structure of aragonite platelets and an organic matrix mainly consisting of β-chitin covered with proteins [1]. This hybrid structure makes nacre 3000 times more fracture resistant as compared to aragonite which makes up ca. 95 wt % of this structure [2]. The reason for this is that crack propagation is hindered by the soft chitin layers that get disrupted before the crack can propagate further. In addition, the platelets are glued to the organic matrix by elastic proteins that also have sacrificial physical bonds [3]. Another amazing biomineral are chiton teeth, which are actually the hardest known biomineral [4]. Chitons scratch algae from rocks, which requires wear-resistant teeth. The animal maintains this ability by synthesizing rows of teeth and each time, a tooth is worn out, the next tooth in the row will be used. A reason for the mechanical wear resistance of the teeth is the presence of different iron oxide mineral phases incorporated into a protein–polysaccharide matrix. Especially, magnetite nanoparticles that are present in large amounts (ca. 70 wt %) at the tooth cap, covering the cutting surface, are responsible for the outstanding mechanical performance [5].

There are many approaches to produce an organic–inorganic hybrid material inspired by the structure of nacre [6-16]. But the fundamental knowledge of the underlying mechanisms as well as theoretical explanations were, so far, only provided for rare examples. One of the reasons is that many of the biomineralization mechanisms are still not fully understood due to their complexity. Recent work underlines the importance of amorphous precursor phases [17] and also nonclassical crystallization mechanisms in biomineralization [18,19].

In this manuscript we report a synthesis method to combine the favorable properties of two biominerals in one and the same material and, thus, to create a multifunctional hybrid material. We claim that this bioinspired material could find potential application in various fields. In general, it could be very interesting for the field of abrasive and fracture resistant materials that are found in hard coatings or in the field of construction. We used the organic nacre matrix of the shell *Haliotis laevigata*, which is insoluble in acetic acid, as a confined reaction environment. Within this organic matrix we infiltrated gelatin to mimic the silk gel precursor inside the chitin nacre scaffold [3]. Inside this organic gelatin matrix we synthesize magnetite nanoparticles to form a highly mineralized organic–inorganic hybrid body. The resulting material should mimic the fracture resistance of nacre and the hardness and abrasion resistance of the chiton teeth.

## Results and Discussion

### Synthetic concept

It is the aim to synthesize a material of larger dimensions by developing a multifunctional biomimetic composite structure, which combines properties of two biominerals in one and the same material, namely nacre and chiton teeth. To reach this goal we follow the key synthesis principles presented in Figure 1. The starting material is an original demineralized nacre matrix that is infiltrated by a thermo reversible gelatin solution mimic-

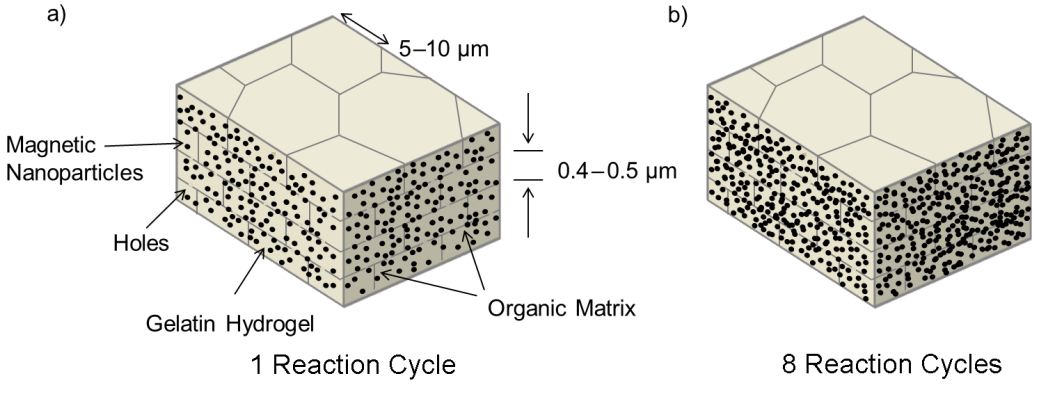


**Figure 1:** Magnetite formation inside a gelatin gel matrix (grey) that is placed inside the chitin scaffold of demineralized nacre (dark grey lines). Panel a) symbolizes the stage of mineralization after one reaction cycle, panel b) represents repeated mineralization cycles as demonstrated by the progress of mineralization shown by the increase of the magnetite nanoparticle number. At zero time, only the gel matrix is present.

king a gel precursor inside the chitin nacre scaffold. Within this gelatin matrix we synthesize magnetite nanoparticles to form a highly mineralized organic–inorganic hybrid body. This hybrid structure resembles the nacre aragonite platelets in size and shape. We repeated this reaction cycle up to eight times in order to enhance and thereby control the content of magnetite NPs inside the hybrid material. Systematic studies showed that after eight reaction cycles the upper limit of mineral load is reached and further repetition does not lead to an increase in the mineral content.

## Nacre organic matrix – SANS

Nacre, an inorganic and organic composite natural material, is typically found as the inner shells of mollusks, and is referred to as mother-of-pearl. Its structure is a layered arrangement of pseudo-hexagonally shaped aragonite mesocrystals with a diameter of around 10–15 μm and a thickness of about 500 nm [3] (every platelet consists of polygonal $CaCO_3$ nanograins with a size of 10–45 nm [20]). The aragonite mesocrystals are interspaced by an organic matrix which was identified as a β-chitin [21-23] core surrounded by protein layers that play an important role in the formation process of nacre [24-26]. The inorganic mesocrystals are connected by mineral bridges with a width ranging from 36–54 nm in between the neighboring lamellae. The mineral bridges represent the continuation of mineral growth along the vertical direction of the lamellar mesocrystals from a preceding layer of platelets [27,28]. The fraction of the organic matrix in nacre is only about 5 wt %, it plays an important role in the spatial control of mineralization, hierarchical structure and toughness enhancement [23,29]. Different techniques have been used to resolve the chemical and structural composition of the organic matrix. Small angle neutron scattering (SANS) is a non-destructive method to study the nacreous organic matrix without potential changes to the matrix, which might derive from the usage of staining media or dehydration. For comparison studies, the structure of the original nacre matrix (*Haliotis laevigata*) was analyzed as well. Figure 2 represents very-small (VSANS) and small (SANS) angle neutron scattering profiles of nacre (top) and its organic matrix (bottom) measured at two diffractometers for very small (VSANS) and conventional small angular scattering (SANS) in, respectively, $Q$-ranges from $10^{-3}$ to $2\cdot10^{-2}$ $nm^{-1}$ and from $10^{-2}$ to 3.5 $nm^{-1}$. The absolute value of the scattering vector $Q$ is related to the scattering angle θ and neutron wavelength λ according to $Q = (4\pi/\lambda)\cdot\sin(\theta/2)$. The neutron beam is parallel to the *c*-axis of the nacre or the organic matrix of the nacre (i.e., perpendicular to the sample surface, see Supporting Information File 1). Thus, nearly no information about the thickness of the lamellar platelets is found in the scattering curves. These measurements enable the determination of the hierarchical structures along the vertical direction of the lamellar platelets of the nacre and its organic matrix over a wide range of length scales from about 1 nm to 1 μm. The data in Figure 2 show several distinct $Q$-regimes that are described well by the solid line representing the best fit of the data using Beaucage's expression [30] and a correlation model [31] (see Supporting Information File 1). For nacre, scattering from the aragonite mesocrystals is dominant in the $Q$-regime less than 0.02 $nm^{-1}$ and is represented by a $Q^{-2}$ power law with an amplitude of $P_2 = 1.8$ $cm^{-1}\cdot nm^{-2}$. This exponent implies a platelet-like structural characteristic with a plate diameter larger than 2 μm as evaluated from the radius of gyration, $R_g$, assuming the form factor of a thin plate-like shape [32]. Above $Q^* \cong 0.063$ $nm^{-1}$ the power law transforms into $Q^{-3}$ and above 0.4 $nm^{-1}$ to a $Q^{-4}$ Porod behavior that yields an average size of the nanograins of about 10 nm as estimated from $D \equiv 2\pi/Q^*$. The diameter of the nanograins is around 11 nm as evaluated from $R_g$, assuming the form factor of a spherical shape, which is consistent with data reported in literature [29]. The scattering, which follows the $Q^{-2}$ power law between $3\cdot10^{-2}$ and 0.2 $nm^{-1}$ shows the presence of a shoulder which might correspond to the mineral bridges with an average diameter that is estimated to be $D \approx 80$ nm from $R_g \approx 28.9$ nm.

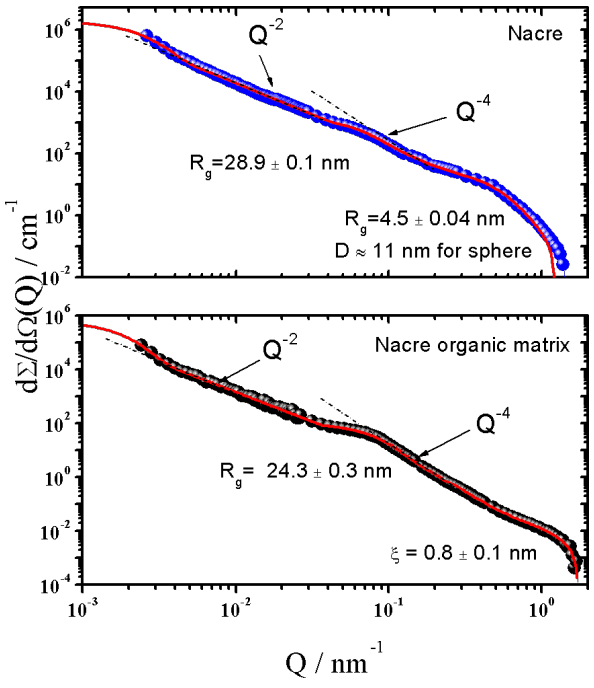


**Figure 2:** SANS macroscopic cross-section dΣ/dΩ versus scattering vector $Q$ for a 1 mm thick piece of nacre in air and a demineralized nacre matrix in $D_2O$ ($T$ = 20 °C). The neutron beam is parallel to the nacre/nacre organic matrix *c*-axis (perpendicular to the sample surface). At low $Q$ (<0.02 $nm^{-1}$) VSANS data are also presented after rescaling. The solid line represents a fit of the Beaucage equation [30] and correlation length model ($Q$ > 0.03 $nm^{-1}$) [31] (see Supporting Information File 1).

The scattering profile of the nacre organic matrix (Figure 2, bottom) indicates the same platelet-like structure as for nacre as it shows the same power laws, however with an amplitude of $P_2 = 0.13\ cm^{-1}{\cdot}nm^{-2}$, which is one order of magnitude smaller. This means that the demineralization has no significant influence on the original structure of the organic matrix. Above $Q = 0.03\ nm^{-1}$ a radius of gyration $R_g$ of about 24.3 nm is determined, which might correspond to the mineral bridges. The diameters of the cross section of the bridges were estimated to be roughly D ≈ 68 nm from $R_g$ ≈ 24.3 nm. This result is consistent with our TEM results. The size of the mineral bridge is much larger than the typical size of the gelatin molecule as determined from the correlation length ξ ≈ 15.9 ± 0.5 nm with SAXS (see Supporting Information File 1). This indicates that the molecular diffusion of gelatin into the organic chitin matrix through holes in the chitin layers, which originates from the former mineral bridges, is possible. Above $Q = 0.5\ nm^{-1}$ scattering from around 0.8 nm large particles appear, representing the scattering of the chitin chain. In summary, we can conclude that nacre is completely demineralized by our experimental procedure, which was also confirmed by TGA measurements, and that the structure of the demineralized nacre organic matrix has not significantly changed compared with the original nacre.

## Nacre organic matrix – Light microscopy and fluorescence microscopy

Original nacre (*Haliotis laevigata*) used for materials synthesis was analyzed by light microscopy and confocal fluorescence laser scanning microscopy (FCLSM) as can be seen in Figure 3. A freshly broken cross section of original nacre was analyzed by SEM (see below in Figure 4c) and clearly reveals the layered structure of aragonite tablets. The insoluble organic matrix can be seen in Figure 3 and in the transmission electron microscopy (TEM) image given below in Figure 5d. The embedded cross section of the demineralized chitin matrix shows that the matrix remains stable after demineralization and does not stick together. These results are in agreement with our findings from SANS and VSANS experiments, therefore we conclude that the demineralized nacre matrix can be used as a template for the synthesis of the composite material, which is in agreement with earlier work on nacre retrosynthesis [13]. The distance between the layers is around 250–500 nm (see below in Figure 5d), which is in part lower than that of the natural archetype (500 nm) due to a partial collapse of the demineralized matrix during preparation and handling. Figure 5d also illustrates vertical connections between the layers, these thin walls are the so-called "intertabular matrix" which has a stabilizing function [33]. The interruptions in the layers correspond to pores of around 50–70 nm thickness and act as mineral transport bridges during the formation of natural nacre, as also confirmed by SANS and VSANS experiments. In order to determine the arrangement of gelatin in between the insoluble organic nacre matrix layers a Coomassie stain is used. The light microscopy image in Figure 3a shows an embedded and thin cut section of demineralized nacre stained with Coomassie blue. The investigations clearly display a blue stain of the layered insoluble nacre structure as a result of a positive interaction of the insoluble proteins with Coomassie blue, whereas the space in between the layers does not show any significant stain. The same observation can be made by fluorescence confocal laser scanning microscopy (Figure 3b) for which the thin cuts have been stained with rhodamine B ITC. Also in these studies no staining of proteins in between the layers could be observed. Therefore we conclude that the insoluble matrix proteins are dominantly located directly at the β-chitin matrix and are not present in between the layers. Figure 3c and Figure 3d show an embedded sample of insoluble nacre matrix infiltrated with gelatin by a vacuum infiltration process. Staining of this sample illustrates not only blue stained chitin layers and insoluble matrix proteins but also colored areas in between the layers, indicating a filling of the matrix with gelatin. The interaction and positive stain of gelatin and Coomassie blue have been tested successfully in reference experiments (see Figure S3, Supporting Information File 1). For a better visualization of the stained areas in between the layers the light blue stained gelatin (see Supporting Information File 1) has been processed digitally. This means the green RGB channel of the images was exchanged by the red one to be able to better distinguish between the different matrix parts. As a result the stained gelatin parts appear purple in the image which makes it easier to differentiate between the blue chitin layers and the filling in between the layers. The purple area next to the matrix in Figure 3d represents excess of gelatin on the sample surface. These studies reveal that the chitin–gelatin composite can be used as a template for the mineralization of magnetite and therefore act as a building block for the formation of a multifunctional composite material. One key step for the formation of such a multifunctional hybrid material is the homogeneous infiltration of gelatin as the organic scaffold for mineralization inside the insoluble nacre matrix.

## General synthesis protocol and TEM/SEM studies

The synthesis of the multifunctional inorganic hybrid material is based on an already established three step protocol [34]. In the first step, the gelatin hydrogel is infiltrated into the demineralized nacre matrix through a vacuum infiltration process [35], in the second step this chitin–gelatin composite is introduced into a solution of ferrous ($FeCl_2$ 0.1 M) and ferric ions ($FeCl_3$ 0.2 M) in a molar ratio of 1:2. After complete diffusion of the ions inside the hydrogel template magnetite is precipitated in the third step by introducing the template in a base

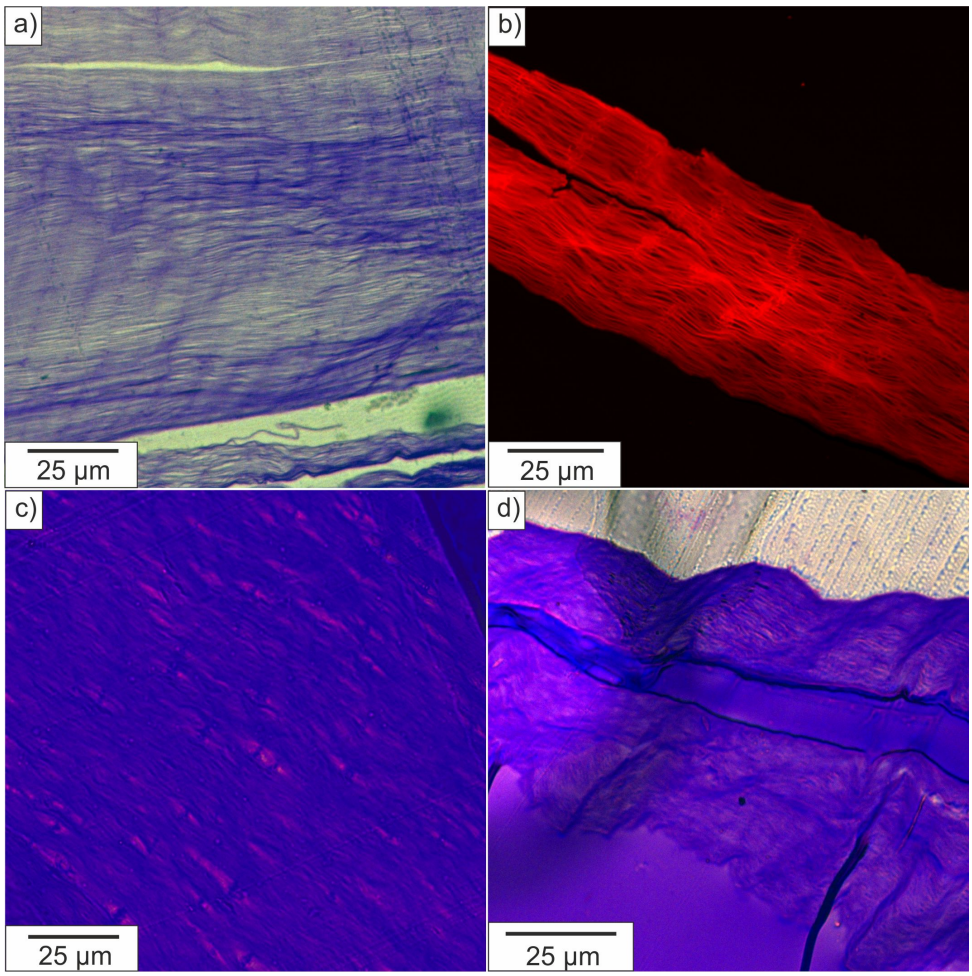


**Figure 3:** Light microscopy image of thin cuts of embedded and Coomassie stained samples. a) Demineralized nacre matrix, b) confocal laser scanning microscopy of embedded demineralized nacre matrix stained with rhodamine B ITC, c) and d) demineralized nacre matrix (blue) with infiltrated gelatin (purple).

(NaOH 0.1 M). The magnetite nanoparticles are synthesized through a so-called co-precipitation method following the reaction:

$$Fe^{2+} + 2Fe^{3+} + 8OH^- \rightarrow Fe_3O_4\left(\downarrow\right) + 4H_2O\,. \qquad (1)$$

This procedure can be repeated several times in order to obtain the desired degree of mineralization. We already reported a similar synthesis protocol for gelatin-based magnetic hydrogels [34] and now transfer these synthesis principles into the insoluble organic nacre matrix.

The amount of magnetite nanoparticles formed inside the synthesized hybrid material was determined by thermogravimetric measurements. The initial and final degradation temperatures have been determined from the thermogram curves. The loading of the composite material with iron oxide nanoparticles varies from 15–65 wt % depending on the number of reaction cycles (see Figure S3, Supporting Information File 1). Scanning electron microscopy (SEM) examinations of the dried hybrid materials indicate a dense layered hierarchical structure (see Figure 4a), which is similar to natural nacre. The distribution of magnetite nanoparticles inside the hybrid material was determined with electron dispersive X-ray spectroscopy (EDX) (Figure 4d). The mapping of the elements shows that Fe and C are homogeneously distributed throughout the material surface whereas there is less C detected at the freshly broken cross section of the material. It can be clearly seen that the spaces in between the layers mainly give signals for Fe. With the performed studies we could not observe a mineral gradient throughout the matrix arising from the synthesis of the magnetic nanoparticles produced by a diffusion approach. Therefore we claim that after full completion of the synthesis the particles are equally present over the whole matrix.

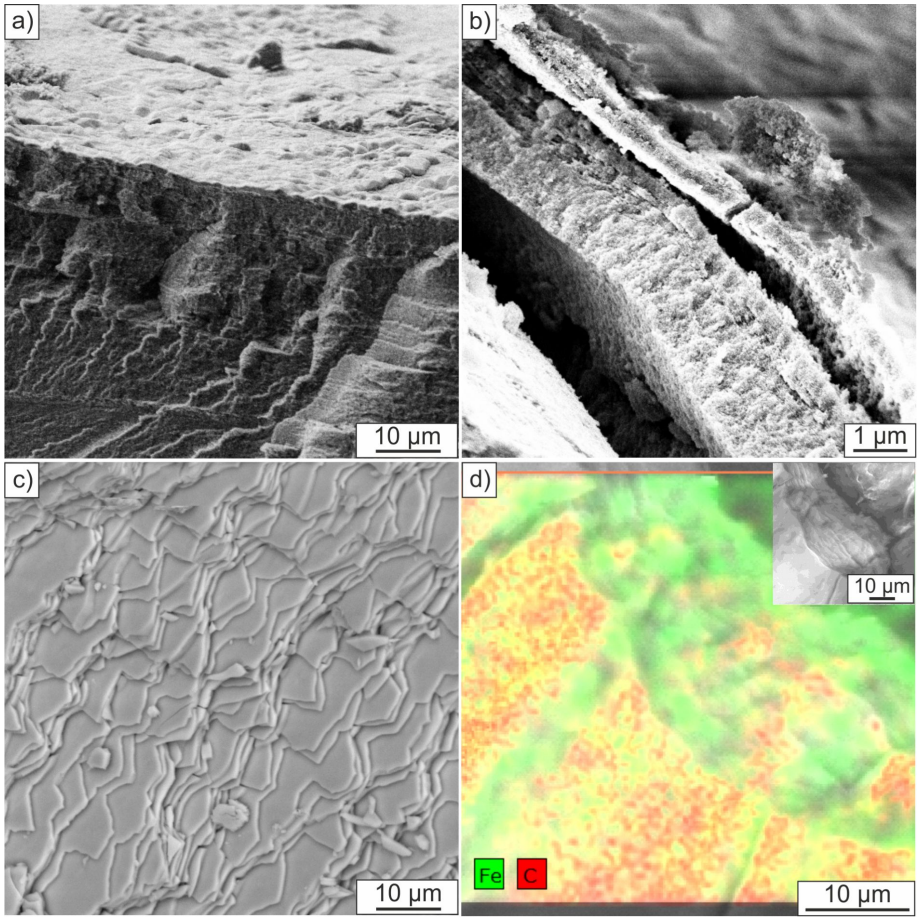


**Figure 4:** SEM micrographs of a) and b) fracture surfaces of artificial nacre and c) fracture surface of original nacre *Haliotis laevigata*. d) EDX mapping analysis of artificial nacre fracture surface.

In order to confirm this observation and to obtain information about the mineral nature in between the chitin sheets, TEM studies of embedded and microtome cut samples have been conducted (Figure 5). We note the presence of iron oxide nanoparticles homogeneously distributed in between the layers after one (Figure 5a) and four reaction cycles (Figure 5b). Moreover, it can also be seen that the number of particles after one reaction cycle is significantly lower than after four reaction cycles, which is in agreement with TGA studies of the hybrid materials. The studies show that the particles are in the size range of 10 ± 5 nm and do exist at the chitin surface as well as in between the chitin layers due to the presence of the carrying media gelatin. It is also worth to mention that besides the 10 nm sized particles also smaller particles in the size range of around 3 nm can be detected. Electron diffraction studies of these small particles show their amorphous nature, which leads to the conclusion that under the chosen synthesis conditions amorphous material or poorly crystallized ferrihydrite could be present. In this study we could not recognize a direct formation of magnetite through an amorphous or ferrihydrite precursor stage. However, the transformation of amorphous iron oxide species into magnetite was observed before and is also likely to happen in this synthesis set-up [36]. Reference experiments of the composite material without gelatin infiltration (Figure 5c) and repetition of four reaction cycles only show the presence of nanoparticles adsorbed on the chitin surface but not in between the layers. This material seems closer to the demineralized nacre matrix (Figure 5d) than to a multilayered composite material. Furthermore, the distance in between the layers for samples containing gelatin seems less collapsed than for samples without gelatin which results in a material closer in structure to that one of original nacre. Electron diffraction data taken from different areas in between the layers show the presence of polycrystalline nanoparticles with no preferred orientation (see Figure S5, Supporting Information File 1). The iron oxides magnetite and maghemite show very similar diffraction patterns and *d*-spacings, therefore it is not possible to differentiate these mineral phases with the used techniques. In summary

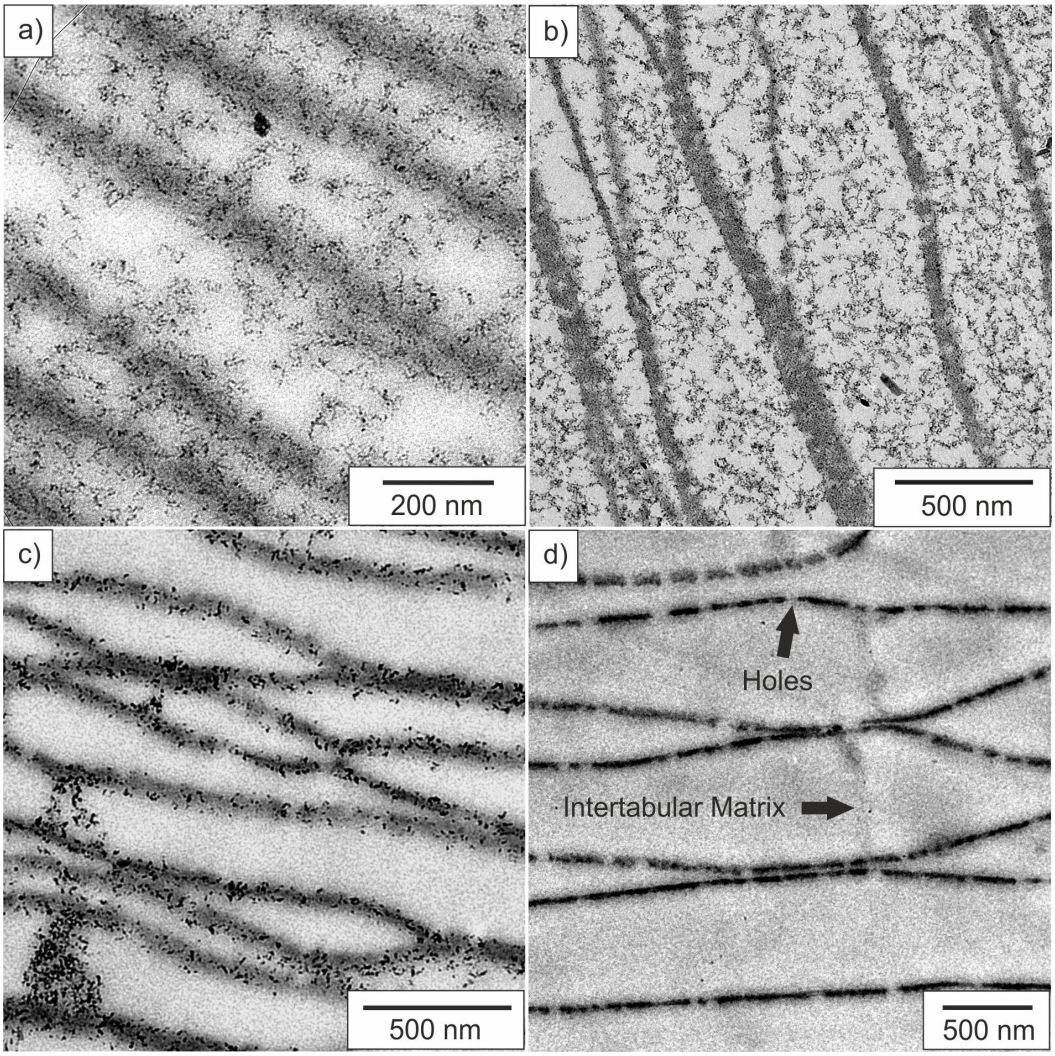


**Figure 5:** TEM micrographs of a) artificial nacre after one reaction cycle and b) after four reaction cycles, c) reference chitin–magnetite composite sample without gelatin, and d) completely demineralized matrix.

these observations demonstrate that it is possible to successfully infiltrate a demineralized nacre matrix with gelatin and to form magnetite nanoparticles inside the gel matrix.

## SANS on magnetite formation in the gelatin–chitin composite

The magnetite–gelatin–chitin structure was characterized by SANS contrast variation experiments, which is a beneficial method to obtain information about the inorganic components as well as the organic part. By using the matching point of gelatin (28 vol % $D_2O$) only the inorganic particles are visible whereas the organic structure can be visualized working in pure $D_2O$. This technique is a standard tool in various fields such as biomineralization [37,38]. Figure 6 demonstrates two SANS–VSANS scattering profiles of magnetite in a chitin–gelatin composite (top) and as a reference in a gel matrix (bottom). The structure of the ferrogel (the hybrid material without chitin) was investigated for comparison. The magnetite–gelatin–chitin sample shows a power law of $Q^{-1}$ in the low-$Q$ regime (<0.01 $nm^{-1}$), which is approximately valid for linear structures and thereby indicates rod-like particles or chains of particles of about $R_g$ = 0.58 µm. At larger $Q$ (>0.1 $nm^{-1}$) scattering is determined from individual magnetite nanoparticles of $R_g \cong 7.9$ nm showing a $Q^{-3}$ power law indicating a mass fractal structure (a structure containing branching and crosslinking to form a 3D network). The diameter $D$ of the magnetite particles can be estimated to be $D \approx 20$ nm ($R_g = D/2.58$) assuming a spherical shape. The scattering of magnetite in the gelatin matrix (ferrogel) qualitatively looks the same. Particles (or an assembly of particles) of about

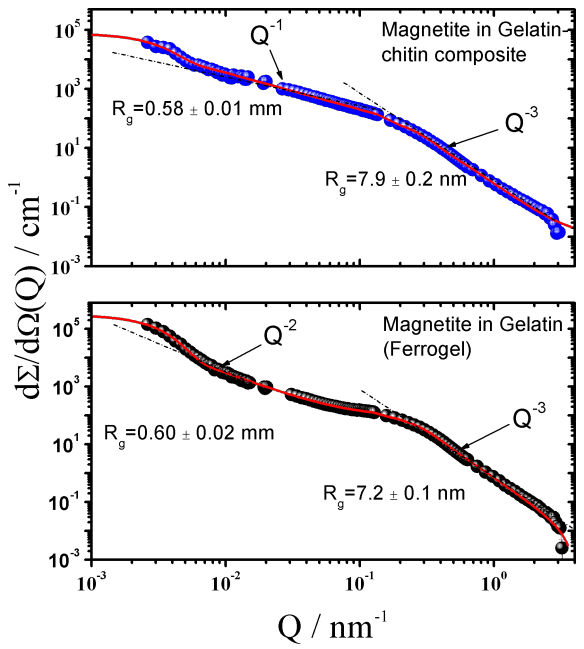


**Figure 6:** SANS and VSANS scattering patterns of magnetite in gelatin–chitin composite and of ferrogel in a mixed $D_2O/H_2O$ solvent of 28 vol % $D_2O$ and 72 vol % $H_2O$. The solid lines represent the fitting of the Beaucage expression [30].

$R_g$ = 0.6 µm with $Q^{-2}$ power law, which is characteristic for chain-like clusters, are found at small $Q$. Individual magnetite particles become visible at larger $Q$ showing a slightly smaller diameter of about $D \approx 18.5$ nm ($R_g$ = 7.2 nm). Thus, in the presence of nacre organic matrix, the fiber-like chitin structure helps with the formation of linearly aligned magnetite nanoparticles (pearl-necklace-like, power law of $Q^{-1}$), while in the gelatin gel matrix without chitin, the nanoparticles exhibit a branch-like arrangement (power law of $Q^{-2}$).

## Magnetization measurements

Magnetic properties of the nanocomposite were measured by using a superconducting quantum interference device (SQUID) magnetometer. Figure 7 illustrates the magnetization loops (magnetization $M$ versus applied field $H$) of a representative dried hybrid material with a mineral content of 65 wt % after eight mineralization cycles at 293 K and 2 K. At $T$ = 293 K the hysteresis curve shows zero coercivity and zero remanence as it is characteristic for superparamagnetic material [39] with a particle size less than 20 nm. Due to magnetic anisotropy the hysteresis curve at $T$ = 2 K shows ferrimagnetic hysteresis. The saturation magnetization for all analyzed samples is around 26 emu/g at 298 K and 36 emu/g at 2 K which are similar values already reported before for the synthesis of gelatin-based magnetic hydrogels [34]. Similar results can be obtained for the analysis of magnetite nanoparticles prepared by a co-precipitation method in water [40-42]. In order to determine the effect of varying mineral content onto the magnetic properties, samples with a particle load of 15 wt % to 65 wt % have been analyzed. For all analyzed samples similar results for the magnetic hysteresis as well as for the saturation magnetization have been obtained. Therefore, we conclude that the mineral content as well as the transfer of the synthesis protocol to the

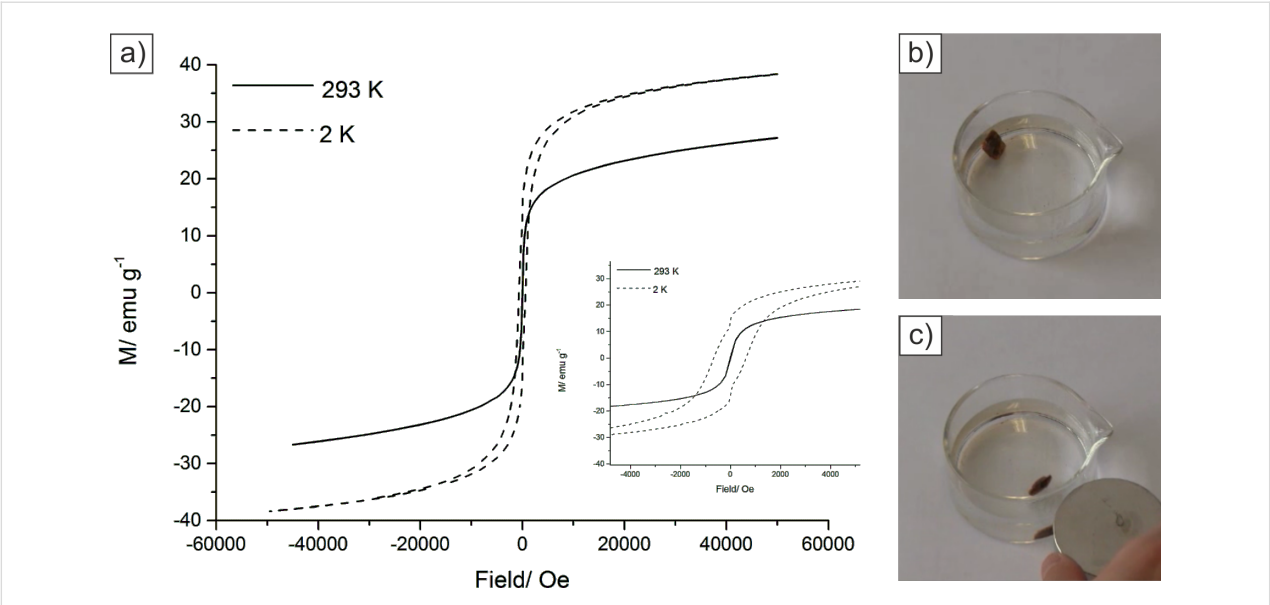


**Figure 7:** Magnetic properties of the synthesized hybrid materials. a) Magnetization curves of a representative dried sample at 2 K and 293 K. Inset: Enlargement of the low-field region showing the different coercive fields for the NPs at 2 and 293 K. Attraction of modified nacre with b) no magnetic field and c) external magnetic field (ca. 1 Tesla).

layered organic matrix does not affect the magnetic nature of the material.

## Swelling studies

In order to probe structural changes of the nanocomposite during gelatin infiltration as well as during magnetite synthesis, swelling studies were performed. The swelling capacity of the insoluble nacre matrix, the gelatin infiltrated chitin matrix and the magnetic nanocomposite are shown in Figure 8. The swelling degree, *Sd*, is defined as:

$$Sd = \frac{Ws - Wd}{Wd} \cdot 100 ,$$

where *Ws* stands for the weight of the swollen sample after swelling equilibrium was reached and *Wd* stands for the dry weight before water uptake.

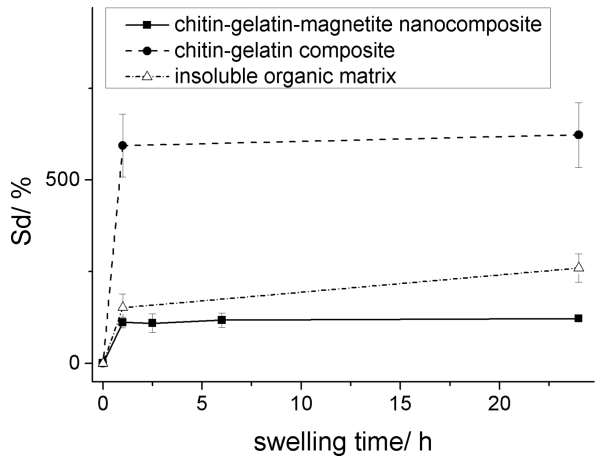


**Figure 8:** Degree of sample swelling plotted as a function of the swelling time at 23 °C for different samples with a gelatin concentration of 10 wt %. The equilibrium swelling degrees *Sd* (%) for the plotted samples are 622.97 ± 88.31 (chitin–gelatin), 259.70 ± 38.46 (chitin demineralized) and 121.94 ± 5.13 (chitin–gelatin–magnetite RC 6).

In the case of nacre matrix infiltrated with gelatin a distinct increase in swelling can be observed as compared to the insoluble matrix alone. This effect is not surprising as gelatin alone shows a higher swelling capacity as the insoluble organic matrix. The gravimetric water uptake of the gelatin–chitin composite is similar to already reported swelling capacities of gelatin. This observation is an additional proof for the successful infiltration of gelatin inside the chitin layers. In the case of the magnetic composite material, the swelling degree is significantly decreased due to the presence of magnetite nanoparticles, which act as additional crosslinkers in the gelatin hydrogel. This effect was discovered before for the studies of magnetic hydrogels [34] and shows similar values for the swelling degree. We can conclude that the gelatin hydrogel as well as the magnetic hydrogel do not change their swelling capacity inside the insoluble chitin matrix and therefore we conclude that the structural changes are similar than the one for already reported magnetic hydrogels.

## Simulation studies

To investigate the molecular scale interactions that account for the formation of the magnetite–protein composite, we performed molecular simulation studies of $Fe^{II}(OH)_2$ and $Fe^{III}(OH)_3$ motif association to two sets of biomolecular matrices. To allow direct comparison to our previous study on collagen-based composites [34,43], the association of an iron hydroxide ion cluster to collagen (mimicked by a triple helix of $(Gly–Pro–Hyp)_n$ peptides) is contrasted to ion association to chitin. The latter model was chosen as three poly-(1,4)-D-glucose chains of about 40 Å length (which corresponds to nine monomers) stacked in three layers, which are connected by hydrogen bonds.

As a starting point, the association of $Fe^{II}(OH)_2$ and $Fe^{III}(OH)_3$ ion clusters was investigated in vacuum. From a series of docking runs we found practically equivalent protein–ion complexes for either collagen or chitin. However, the nature of these complexes was found to differ significantly upon relaxation in aqueous solution. Figure 9 illustrates the association of the two ion cluster types to collagen and typical configurations as obtained from relaxation in aqueous solution based on 100 ps molecular dynamics simulation runs. While the $Fe^{III}(OH)_3$ ion clusters bind as stable moieties to the biomolecule, the association of $Fe^{II}(OH)_2$ to collagen was found to be less favored. Indeed, for 30% of the relaxation runs in aqueous solution the latter cluster was observed to partially dissociate, which led to (stable) $Fe^{II}(OH)^-$–collagen complexes. In contrast to this, the association of $Fe^{II}(OH)_2$ and $Fe^{III}(OH)_3$ ion clusters to chitin was found to be stable in both vacuum (Figure 10) and in aqueous solution (Figure 11). As the $Fe^{II}(OH)_2$ cluster reflects an important motif of the magnetite structure we conclude that our simulations show, at least from a qualitative point of view, a slight preference of chitin over collagen as a nucleator for magnetite [43].

## Mechanical characterization

To examine the mechanical properties of the composite materials we conducted some preliminary experiments. Force spectroscopy measurements with the colloidal probe technique [46,47] were performed on bare and nanoparticle-loaded gelatin as well as on bare and ferrogel loaded chitin scaffolds. From the obtained force versus deformation curves we can already see significant qualitative differences. Figure 12 shows a comparison of pure and nanoparticle-filled gelatin. With the addition of

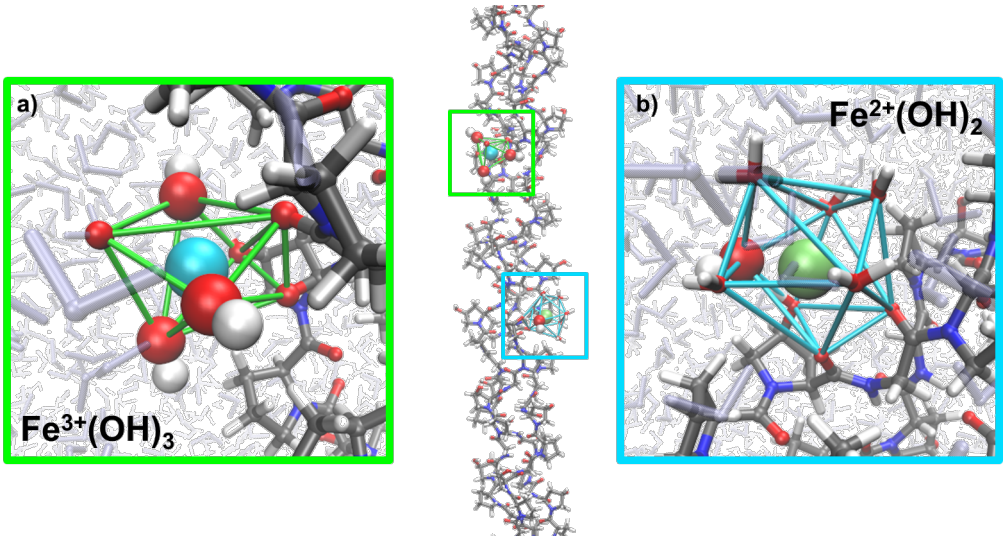


**Figure 9:** Representative structure of a triple helical $(Gly–Hyp–Pro)_n$ peptide [44] of 100 Å length with two associated iron clusters. a) The ferric ion (light blue) is coordinated by seven oxygen atoms of which the three hydroxides show the strongest interaction and an Fe–O distance of 2.7 Å. The Fe–O distances to the solvent and to carbonyl/hydroxy groups of collagen were found to be about 3 Å. b) The ferrous ion (green) is also coordinated by seven oxygen atoms, but does not show a bipyramidal structure. More importantly, one of the hydroxide ions dissociated into the solvent. The Fe–O distances for iron–collagen and iron–water contacts were found to be about 3 Å, whilst the remaining hydroxide ion exhibits an Fe–O distance of 3.2 Å. Colors: $Fe^{2+}$ (green), $Fe^{3+}$ (light blue), O (red), H (white), N (dark blue), C (grey).

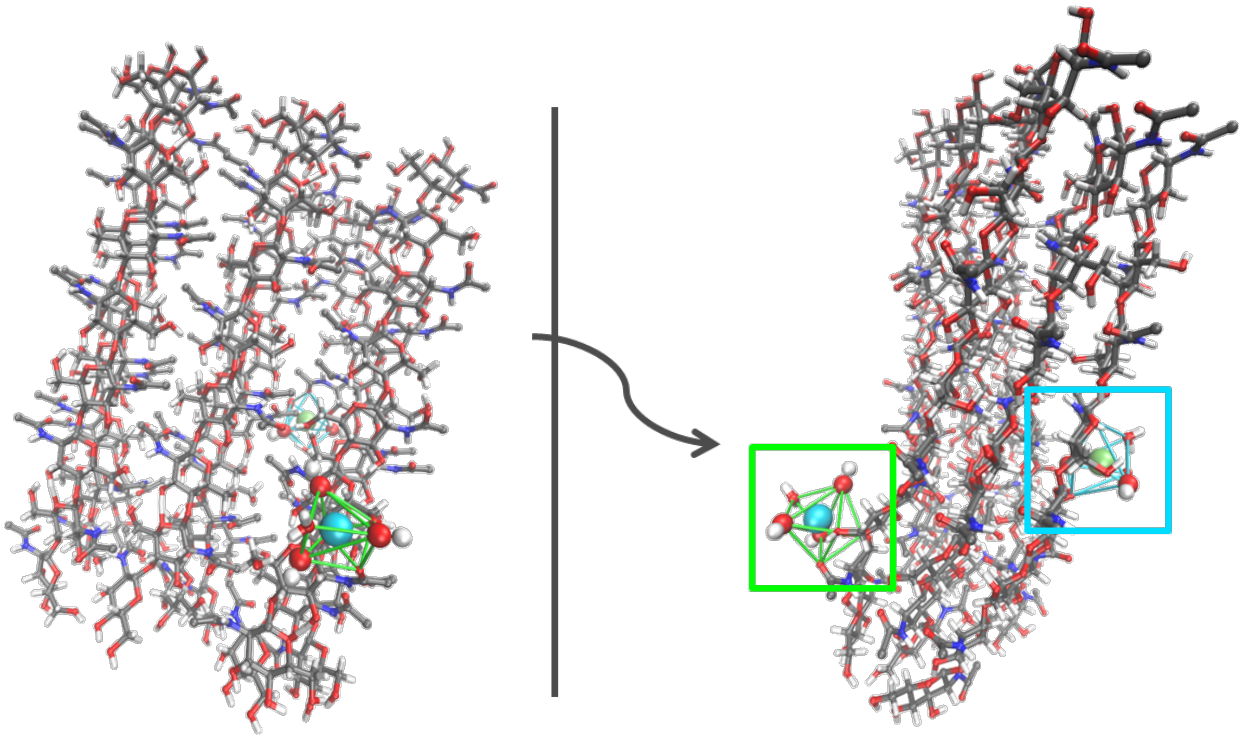

**Figure 10:** Illustration of a β-chitin model [45] consisting of three poly-(1,4)-D-glucose chains of nine monomers stacked in three layers.

the superparamagnetic particles the slope of the force curves increases, i.e., the stiffness or mechanical resistance of the gels is enhanced. This increase can be explained by the strengthening of the gelatin network by the rigid nanoparticles. These have been shown to interact with the amide bonds along the gelatin backbone [48] and might give rise to additional

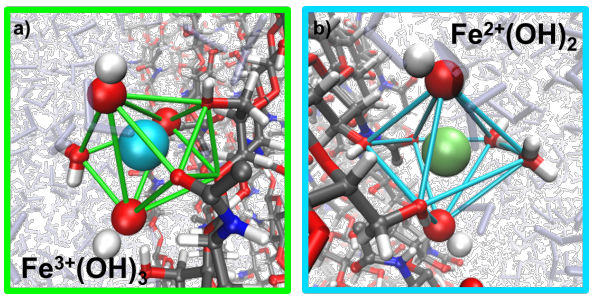


**Figure 11:** a) Representative structure for the coordination of $Fe^{III}(OH)_3$ by chitin. The ferric ion (light blue) is coordinated by four different types of oxygen atoms (red) forming seven coordinative interactions. b) Coordination of $Fe^{II}(OH)_2$ by chitin exhibiting a stable coordination by both hydroxide ions of the ion cluster. In summary, seven oxygen atoms coordinate the ferrous ion (green) building a pentagonal bipyramid, with the cluster hydroxide oxygens building the tops with a distance of 2.86 Å. The pentagonal plane consists of two oxygen atoms from solvent molecules forming weaker bonds of 3.1 Å and three protein contacts, whereby one carbonyl oxygen atom binds over 2.9 Å and two hydroxy oxygens over 3.1 Å.

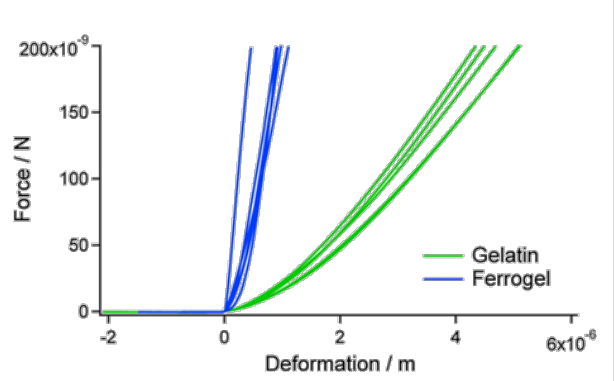


**Figure 12:** Force vs deformation characteristic of pure gelatin and gelatin with ferromagnetic particles. Introduction of nanoparticles leads to a significant increase of the stiffness of the material.

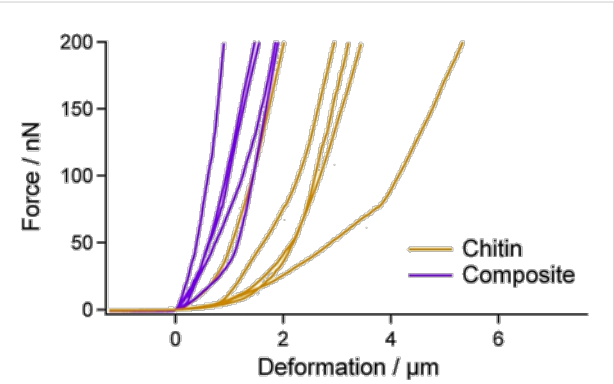


**Figure 13:** Force vs deformation characteristics of the chitin scaffold and the final composite. Introduction of ferrogel leads to a detectable increase of the stiffness of the material.

crosslinking. As a consequence, the flexibility of the gelatin chains is reduced resulting in the observed stiffness increase and the decreased swelling. Regarding the chitin scaffolds we notice a stiffening effect as well (Figure 13). Introducing the ferrogel reinforces the framework and gives the composite superior mechanical performance. Nanoindentation testing with AFM colloidal probe is a powerful technique as it combines high lateral and force resolution with well-defined contact geometry. It has successfully been applied to a range of systems including capsules [49-52], full particles [53-55] and films [56-59]. However, due to the morphological and structural inhomogeneity of our samples it is currently difficult to make a quantitative evaluation of the data. Continuum mechanics models typically require homogeneous and isotropic materials. For pure gelatin we can successfully fit the obtained curves assuming the Hertz model for a sphere in contact with a plane surface [60] (see Supporting Information File 1). Thus, an elastic modulus of 2.6 ± 0.3 kPa is calculated which is in good agreement with data from literature reporting modulus values in the low-kPa range [58,61]. In contrast, the data from experiments on ferrogel or composite show large scattering and the curves do not show a shape that can be described by one of the established mechanical theories. These deviations can be ascribed to the aforementioned non-ideal boundary conditions. It will be the aim of future research to investigate the mechanical properties more thoroughly.

## Conclusion

In summary, we have developed a synthetic method to fabricate a multifunctional hybrid material. We can successfully infiltrate gelatin into the insoluble nacre matrix and synthesize magnetite nanoparticles inside our template. We can control the mineral content of our hybrid material by repetition of reaction cycles, the mineral content varies form 15 wt % (one reaction cycle) to 65 wt % (eight reaction cycles). SQUID measurements showed that our composite material shows superparamagnetic behavior, which is typical for magnetite nanoparticles in this size range. Swelling studies indicate a structural change of the gelatin inside the hybrid material upon introduction of the magnetite nanoparticles. By incorporation of more and more inorganic material we can control the degree of swelling and therefore the mechanical properties of the composite material. This result is supported by preliminary AFM colloidal probe measurements. Simulation studies show the binding of iron and hydroxide ions to both collagen and β-chitin. Direct comparison, however, indicates that chitin should be the more favored nucleator macromolecule species for magnetite thus boosting composite growth along the chitin fibers.

In summary, we have managed to synthesize a bio-inspired organic–inorganic hybrid material, which combines the struc-

tural features of nacre and chiton teeth. Swelling studies and preliminary mechanical measurements indicate a change in the mechanical properties as compared to pure gelatin. This is controllable through the adjustable mineral content. In combination with the superparamagnetic behavior, we have therefore generated a material with improved mechanical performance coupled with magnetic properties. More quantitative future mechanical measurements will show in how far the fracture resistance of nacre could be combined with the wear resistance of chiton teeth.

# Experimental

## Chemicals

The following commercially available chemicals were purchased and applied in the syntheses without further purification: $FeCl_2 \cdot 4H_2O$ (Sigma-Aldrich), $FeCl_3 \cdot 6H_2O$ (Sigma-Aldich), 0.1 M NaOH solution (Merck), gelatin type B (~225 Bloom, Sigma-Aldrich), 4-chloro-*m*-cresol (Fluka), methanol (VWR). For the preparation of the reactant solutions double-distilled and deionized (Milli-Q) water was used. All solutions were degassed with argon before usage.

## Preparation of insoluble organic nacre matrix

Shells of *Haleotis laevigata* were sand-blasted to remove the calcite layer. After thorough washing with deionized water, the shells were dried overnight at room temperature and cut into pieces with an area of around 1 cm × 1 cm. The nacre pieces were demineralized with 10 vol % acetic acid and solvent exchange every day for at least 5 d. The remaining organic matrix was washed with Milli-Q water until neutral pH was reached.

## Gelatin preparation

The gelatin hydrogels were prepared as described elsewhere [34]. Here briefly, different amounts of gelatin powder were mixed with water and the gelatin granules were allowed to swell for 24 h at 6 °C. In order to obtain a homogeneous gel, the swollen mixture is heated for at least 2 h at 50 °C. 20 mL of the gelatin sol are filled into crystallization dishes and left at room temperature for gelation. In order to avoid bacterial growth, a 5 wt % solution of 4-chloro-*m*-cresol in methanol was added (0.15 mL per 1 g of gelatin granules).

## Infiltration of gelatin inside the insoluble nacre matrix

The cut demineralized insoluble organic nacre pieces are put into crystallization dishes filled with 20 mL liquid gelatin at 55 °C. To maintain uniform contact of the matrix pieces with the hot gelatin solution a filter paper covered the liquid surface to prevent floating. The complete set-up was then placed into a vacuum desiccator and the desiccator was attached to a vacuum pump. Vacuum was then applied until bubbling of the solution was observed. The vacuum was then removed to force the liquid gelatin to be drawn into the tissue. The whole process was repeated for three times. After gelatin infiltration the nacre matrix pieces were left inside the gelatin-filled crystallization dishes and allowed to stand for gelation first 5 h at room temperature and finally kept at 6 °C for 24 h before further usage. For further processing the gelatin-filled insoluble organic nacre parts were cut out of the gelatin hydrogel with a scalpel.

## Coomassie staining

Microtome cuts of embedded samples were incubated with 0.2 wt % Coomassie blue G-250 (Sigma-Aldrich) at room temperature for 2 h. After washing with acetic acid the cuts were carefully washed three times with destaining solution (30% ethanol/60% water/10% acetic acid).

## Rhodamine B ITC staining

Microtome cuts of embedded demineralized nacre matrix were incubated at 60 °C with 0.1 wt % rhodamine B ITC (Sigma-Aldrich) in water for 3 h. After washing with water the cuts were accurately washed with acidified ethanol for three times.

## In situ synthesis of magnetite nanoparticles

In situ mineralization of magnetite nanoparticles inside the gelatin hydrogel chitin composite material was carried out through co-precipitation of $FeCl_2$ and $FeCl_3$ after an already established synthesis protocol [34]. Briefly, the gelatin chitin composite sample was introduced into a solution, containing $FeCl_2$ (0.1 M) and $FeCl_3$ (0.2 M), where it was left for 96 h at 6 °C. The iron(II)- and iron(III)-loaded matrix was washed with water and placed in 0.1 M NaOH solution for 150 min.

## Sample characterizations

Samples of Coomassie-stained thin cuts were observed under bright field transmission mode by using a Zeiss optical microscope equipped with a video camera (AxioCam MRc5). Fluorescent labeled samples were analyzed with a confocal fluorescence laser scanning microscope (Zeiss LSM 510 Meta) at an excitation wavelength of 543 nm.

For TEM examination the formed composite material was dehydrated with a graded ethanol series and embedded in LR White Resin (Medium Grade). The sample was cut perpendicular with a diamond knife in a Leica ultracut UCT and transferred onto a Formvar-coated copper grid. TEM and electron diffraction were performed on a Zeiss Libra 120 operating at 120 kV. For SEM measurements the samples were air-dried at room temperature and cut perpendicular to the chitin layers with a scalpel. The

sample was placed on a sticky carbon tape and coated with a thin layer of gold in order to avoid charging effects. The SEM measurements were performed on Zeiss Neon 40 EsB operating in high vacuum. An InLens and SE detector was used for signal collection and an acceleration voltage of 5 kV was chosen for recording the images.

Small-angle neutron scattering (SANS and VSANS): SANS and VSANS experiments were carried out at the KWS1 and KWS 3 diffractometers operated by Jülich Center for Neutron Research (JCNS) at the Forschungs-Neutronenquelle Heinz Maier-Leibnitz (FRM II) in Garching, Germany [62]. Some of the SANS data at large Q range is based on experiments performed at the SANS II, Swiss spallation neutron source SINQ, Paul Scherrer Institute, Villigen, Switzerland.

The mineral content of the multifunctional hybrid material was determined by means of TGA (Netzsch, Selb, Germany). Measurements were carried out at a heating rate of 5 K/min under a constant oxygen flow. Samples were scanned from 293 K to 1273 K.

Magnetization measurements were carried out by using a quantum design superconducting quantum interference device (SQUID) 5 T magnetic properties measurement system (MPMS). For measurements, dried samples were introduced into gelatin capsules and magnetization loop measurements at 2 K and 293 K were performed.

## Simulation studies

Molecular Simulation: as described in [34] a series of $Fe^{III}(OH)_x(OH_2)_{4-x}$ and $Fe^{II}(OH)_y(OH_2)_{6-y}$ clusters were premodeled from ab-initio calculations in vacuum. For all clusters high-spin constellation was identified as preferred by several electron volts. Imposing overall charge neutrality (i.e., $x + y = 3 + 2$) we found the neutral $Fe^{III}(OH)_3{\cdot}(H_2O)$ and the $Fe^{II}(OH)_2{\cdot}4(H_2O)$ as energetically preferred. Docking to collagen and chitin was modeled in aqueous solution by using empirical force fields [44,45,63,64]. Investigation of biologically designed metal-specific chelators for potential metal recovery and waste remediation applications [65], and the Kawska–Zahn docking procedure were described previously [43].

Along this line, ion clusters initially docked to collagen/chitin in absence of water. Such putative association complexes are then immersed in aqueous solution (periodic simulation cell comprising more than 15000 water molecules) and subjected to relaxation from 100 ps molecular dynamics runs at room temperature and ambient pressure. To account for the manifold of possible arrangements intrinsic to the systems complexity a series of 200 independent docking runs were performed for each ionic species.

## Mechanical characterization

Force spectroscopy experiments were conducted at the atomic force microscope (AFM) Nanowizard® I (JPK Instruments, Berlin, Germany) in a custom-built liquid cell (diameter 2 cm, height 0.5 cm). Thin slices (1–2 mm) of swollen hydrogels were cut from the bulky samples with a scalpel and immobilized at the bottom of the cell by using two component epoxy glue (UHU Endfest 300, UHU GmbH & Co. KG, Bühl, Germany). All measurements were performed in Milli-Q-water at room temperature. As a probe a tipless silicon nitride cantilever (NSC 12, no Al coating, MikroMasch, Tallinn, Estonia) was used with a glass sphere (35 μm in diameter, Polysciences Europe GmbH, Eppelheim, Germany) attached to its front (colloidal probe). Before the actual measurements, the cantilevers were calibrated against the non-deformable glass substrate to determine their optical lever sensitivity resulting as the slope of the recorded force–displacement curve. The deformation of the sample was obtained by subtraction of the bending of the cantilever from the raw displacement data. The spring constant of the cantilever (0.56 N/m) was deduced from its thermal noise spectrum prior to the attachment of the colloidal probe [66].

# Supporting Information

### Supporting Information File 1

Additional experimental data.
[http://www.beilstein-journals.org/bjnano/content/supplementary/2190-4286-6-13-S1.pdf]

# Acknowledgements

Many thanks go to A. Laptev (University of Konstanz) for performing the SQUID measurements, Dr. Joachim Hentschel and Lauretta Nejedli for microtomy services (Electron Microscopy Center at the University of Konstanz). Fluorescence microscopy images were acquired at the Bioimaging Center at the University of Konstanz (BIC). This work was supported by the Deutsche Forschungsgemeinschaft within the priority program SPP 1569 "Generation of Multifunctional Inorganic Materials by Molecular Bionics".

# References

1. Lowenstam, H. A.; Weiner, S. *On Biomineralization;* Oxford University Press: New York, 1989.
2. Currey, J. D. *Proc. R. Soc. London, Ser. B* **1977,** *196,* 443. doi:10.1098/rspb.1977.0050
3. Addadi, L.; Joester, D.; Nudelman, F.; Weiner, S. *Chem. – Eur. J.* **2006,** *12,* 981–987. doi:10.1002/chem.200500980

4. Weaver, J. C.; Wang, Q.; Miserez, A.; Tantuccio, A.; Stromberg, R.; Bozhilov, K. N.; Maxwell, P.; Nay, R.; Heier, S. T.; DiMasi, E.; Kisailus, D. *Mater. Today* **2010,** *13,* 42–52. doi:10.1016/S1369-7021(10)70016-X
5. Wang, Q.; Nemoto, M.; Li, D.; Weaver, J. C.; Weden, B.; Stegemeier, J.; Bozhilov, K. N.; Wood, L. R.; Milliron, G. W.; Kim, C. S.; DiMasi, E.; Kisailus, D. *Adv. Funct. Mater.* **2013,** *23,* 2908–2917. doi:10.1002/adfm.201202894
6. Das, P.; Schipmann, S.; Malho, J.-M.; Zhu, B.; Klemradt, U.; Walther, A. *ACS Appl. Mater. Interfaces* **2013,** *5,* 3738–3747. doi:10.1021/am400350q
7. Munch, E.; Launey, M. E.; Alsem, D. H.; Saiz, E.; Tomsia, A. P.; Ritchie, R. O. *Science* **2008,** *322,* 1516–1520. doi:10.1126/science.1164865
8. Podsiadlo, P.; Liu, Z.; Paterson, D.; Messersmith, P. B.; Kotov, N. A. *Adv. Mater.* **2007,** *19,* 949–955. doi:10.1002/adma.200602706
9. Yao, H.-B.; Ge, J.; Mao, L.-B.; Yan, Y.-X.; Yu, S.-H. *Adv. Mater.* **2014,** *26,* 163–188. doi:10.1002/adma.201303470
10. Tang, Z.; Kotov, N. A.; Magonov, S.; Ozturk, B. *Nat. Mater.* **2003,** *2,* 413–418. doi:10.1038/nmat906
11. Tseng, Y.-H.; Lin, H.-Y.; Liu, M.-H.; Chen, Y.-F.; Mou, C.-Y. *J. Phys. Chem. C* **2009,** *113,* 18053–18061. doi:10.1021/jp905145y
12. Wang, J.; Cheng, Q.; Tang, Z. *Chem. Soc. Rev.* **2012,** *41,* 1111–1129. doi:10.1039/c1cs15106a
13. Gehrke, N.; Nassif, N.; Pinna, N.; Antonietti, M.; Gupta, H. S.; Cölfen, H. *Chem. Mater.* **2005,** *17,* 6514–6516. doi:10.1021/cm052150k
14. Walther, A.; Bjurhager, I.; Malho, J.-M.; Ruokolainen, J.; Berglund, L.; Ikkala, O. *Angew. Chem., Int. Ed.* **2010,** *49,* 6448–6453. doi:10.1002/anie.201001577
15. Tritschler, U.; Zlotnikov, I.; Zaslansky, P.; Aichmayer, B.; Fratzl, P.; Schlaad, H.; Cölfen, H. *Langmuir* **2013,** *29,* 11093–11101. doi:10.1021/la4007845
16. Tritschler, U.; Zlotnikov, I.; Zaslansky, P.; Fratzl, P.; Schlaad, H.; Cölfen, H. *ACS Nano* **2014,** *8,* 5089–5104. doi:10.1021/nn501153u
17. Weiner, S.; Sagi, I.; Addadi, L. *Science* **2005,** *309,* 1027–1028. doi:10.1126/science.1114920
18. Oaki, Y.; Kotachi, A.; Miura, T.; Imai, H. *Adv. Funct. Mater.* **2006,** *16,* 1633–1639. doi:10.1002/adfm.200600262
19. Cölfen, H.; Antonietti, M. Summary and Outlook. *Mesocrystals and Nonclassical Crystallization;* John Wiley & Sons, 2008; pp 265–270. doi:10.1002/9780470994603.ch13
20. Rousseau, M.; Bourrat, X.; Stempflé, P.; Brendlé, M.; Lopez, E. *Key Eng. Mater.* **2005,** *284–286,* 705–708. doi:10.4028/www.scientific.net/KEM.284-286.705
21. Weiner, S.; Traub, W.; Parker, S. B. *Philos. Trans. R. Soc. London, Ser. B* **1984,** *304,* 425–434. doi:10.1098/rstb.1984.0036
22. Bevelander, G.; Nakahara, H. *Calcif. Tissue Res.* **1969,** *3,* 84–92. doi:10.1007/BF02058648
23. Levi-Kalisman, Y.; Falini, G.; Addadi, L.; Weiner, S. *J. Struct. Biol.* **2001,** *135,* 8–17. doi:10.1006/jsbi.2001.4372
24. Sudo, S.; Fujikawa, T.; Nagakura, T.; Ohkubo, T.; Sakaguchi, K.; Tanaka, M.; Nakashima, K.; Takahashi, T. *Nature* **1997,** *387,* 563–564. doi:10.1038/42391
25. Marin, F.; Luquet, G.; Marie, B.; Medakovic, D. Molluscan Shell Proteins: Primary Structure, Origin, and Evolution. In *Current Topics in Developmental Biology;* Gerald, P. S., Ed.; Academic Press, 2007; Vol. 80, pp 209–276.
26. Evans, J. S. *Chem. Rev.* **2008,** *108,* 4455–4462. doi:10.1021/cr078251e
27. Song, F.; Soh, A. K.; Bai, Y. L. *Biomaterials* **2003,** *24,* 3623–3631. doi:10.1016/S0142-9612(03)00215-1
28. Schäffer, T. E.; Ionescu-Zanetti, C.; Proksch, R.; Fritz, M.; Walters, D. A.; Almqvist, N.; Zaremba, C. M.; Belcher, A. M.; Smith, B. L.; Stucky, G. D.; Morse, D. E.; Hansma, P. K. *Chem. Mater.* **1997,** *9,* 1731–1740. doi:10.1021/cm960429i
29. Sun, J. Y.; Bhushan, B. *RSC Adv.* **2012,** *2,* 7617–7632. doi:10.1039/c2ra20218b
30. Beaucage, G. *J. Appl. Crystallogr.* **1995,** *28,* 717–728. doi:10.1107/S0021889895005292
31. Hammouda, B.; Ho, D. L.; Kline, S. *Macromolecules* **2004,** *37,* 6932–6937. doi:10.1021/ma049623d
32. Roe, R. J. *Methods of X-ray and Neutron Scattering in Polymer Science;* Oxford University Press: New York, 2000.
33. Heinemann, F.; Launspach, M.; Gries, K.; Fritz, M. *Biophys. Chem.* **2011,** *153,* 126–153. doi:10.1016/j.bpc.2010.11.003
34. Helminger, M.; Wu, B.; Kollmann, T.; Benke, D.; Schwahn, D.; Pipich, V.; Faivre, D.; Zahn, D.; Cölfen, H. *Adv. Funct. Mater.* **2014,** *24,* 3187–3196. doi:10.1002/adfm.201303547
35. Hori, K.; Watanabe, Y. In Vivo Analysis of Plant Nonsense-Mediated mRNA Decay. In *Methods in Enzymology;* Lynne, E. M.; Megerditch, K., Eds.; Academic Press, 2008; Vol. 449, pp 165–176.
36. Baumgartner, J.; Dey, A.; Bomans, P. H. H.; Le Coadou, C.; Fratzl, P.; Sommerdijk, N. A. J. M.; Faivre, D. *Nat. Mater.* **2013,** *12,* 310–314. doi:10.1038/nmat3558
37. Heiss, A.; Jahnen-Dechent, W.; Endo, H.; Schwahn, D. *Biointerphases* **2007,** *2,* 16–20. doi:10.1116/1.2714924
38. Pipich, V.; Balz, M.; Wolf, S. E.; Tremel, W.; Schwahn, D. *J. Am. Chem. Soc.* **2008,** *130,* 6879–6892. doi:10.1021/ja801798h
39. Panda, R. N.; Gajbhiye, N. S.; Balaji, G. *J. Alloys Compd.* **2001,** *326,* 50–53. doi:10.1016/S0925-8388(01)01225-7
40. Cheng, F.-Y.; Su, C.-H.; Yang, Y.-S.; Yeh, C.-S.; Tsai, C.-Y.; Wu, C.-L.; Wu, M.-T.; Shieh, D.-B. *Biomaterials* **2005,** *26,* 729–738. doi:10.1016/j.biomaterials.2004.03.016
41. Sun, J.; Zhou, S.; Hou, P.; Yang, Y.; Weng, J.; Li, X.; Li, M. *J. Biomed. Mater. Res., Part A* **2007,** *80A,* 333–341. doi:10.1002/jbm.a.30909
42. Kang, Y. S.; Risbud, S.; Rabolt, J. F.; Stroeve, P. *Chem. Mater.* **1996,** *8,* 2209–2211. doi:10.1021/cm960157j
43. Tlatlik, H.; Simon, P.; Kawska, A.; Zahn, D.; Kniep, R. *Angew. Chem., Int. Ed.* **2006,** *45,* 1905–1910. doi:10.1002/anie.200503610
44. Zhao, L.; Liu, L.; Sun, H. *J. Phys. Chem. C* **2007,** *111,* 10610–10617. doi:10.1021/jp071775y
45. Blackwell, J. *Biopolymers* **1969,** *7,* 281–298. doi:10.1002/bip.1969.360070302
46. Butt, H.-J. *Biophys. J.* **1991,** *60,* 1438–1444. doi:10.1016/S0006-3495(91)82180-4
47. Ducker, W. A.; Senden, T. J.; Pashley, R. M. *Nature* **1991,** *353,* 239–241. doi:10.1038/353239a0
48. Gaihre, B.; Aryal, S.; Khil, M. S.; Kim, H. K. *J. Microencapsulation* **2008,** *25,* 21–30. doi:10.1080/02652040701737697
49. Fery, A.; Dubreuil, F.; Möhwald, H. *New J. Phys.* **2004,** *6,* 18. doi:10.1088/1367-2630/6/1/018
50. Lebedeva, O. V.; Kim, B.-S.; Vinogradova, O. I. *Langmuir* **2004,** *20,* 10685–10690. doi:10.1021/la048665s
51. Fery, A.; Weinkamer, R. *Polymer* **2007,** *48,* 7221–7235. doi:10.1016/j.polymer.2007.07.050

52. Poehlmann, M.; Grishenkov, D.; Kothapalli, S. V. V. N.; Härmark, J.; Hebert, H.; Philipp, A.; Hoeller, R.; Seuss, M.; Kuttner, C.; Margheritelli, S.; Paradossi, G.; Fery, A. *Soft Matter* **2014,** *10,* 214–226. doi:10.1039/c3sm51560e
53. Neubauer, M. P.; Blüm, C.; Agostini, E.; Engert, J.; Scheibel, T.; Fery, A. *Biomater. Sci.* **2013,** *1,* 1160–1165. doi:10.1039/c3bm60108k
54. Ma, S.; Natoli, M.; Liu, X.; Neubauer, M. P.; Watt, F. M.; Fery, A.; Huck, W. T. S. *J. Mater. Chem. B* **2013,** *1,* 5128–5136. doi:10.1039/c3tb20851f
55. Cappella, B.; Wassenberg, J. R.; Heim, L.-O.; Klostermann, M.; Venzmer, J.; Bonaccurso, E. *Polymer* **2014,** *55,* 1209–1216. doi:10.1016/j.polymer.2014.01.021
56. Gensel, J.; Dewald, I.; Erath, J.; Betthausen, E.; Müller, A. H. E.; Fery, A. *Chem. Sci.* **2013,** *4,* 325–334. doi:10.1039/c2sc20836a
57. Trenkenschuh, K.; Erath, J.; Kuznetsov, V.; Gensel, J.; Boulmedais, F.; Schaaf, P.; Papastavrou, G.; Fery, A. *Macromolecules* **2011,** *44,* 8954–8961. doi:10.1021/ma201974g
58. Domke, J.; Radmacher, M. *Langmuir* **1998,** *14,* 3320–3325. doi:10.1021/la9713006
59. Dimitriadis, E. K.; Horkay, F.; Maresca, J.; Kachar, B.; Chadwick, R. S. *Biophys. J.* **2002,** *82,* 2798–2810. doi:10.1016/S0006-3495(02)75620-8
60. Hertz, H. *J. Reine Angew. Math.* **1881,** *92,* 156171.
61. Benmouna, F.; Johannsmann, D. *Langmuir* **2003,** *20,* 188–193. doi:10.1021/la0355794
62. Home - MLZ - Heinz Maier-Leibnitz Zentrum. http://www.mlz-garching.de/englisch (accessed Dec 9, 2013).
63. Kirschner, K. N.; Yongye, A. B.; Tschampel, S. M.; González-Outeiriño, J.; Daniels, C. R.; Foley, B. L.; Woods, R. J. *J. Comput. Chem.* **2008,** *29,* 622–655. doi:10.1002/jcc.20820
64. Bayly, C. I.; Cieplak, P.; Cornell, W.; Kollman, P. A. *J. Phys. Chem.* **1993,** *97,* 10269–10280. doi:10.1021/j100142a004
65. Hornak, V.; Abel, R.; Okur, A.; Strockbine, B.; Roitberg, A.; Simmerling, C. *Proteins: Struct., Funct., Bioinf.* **2006,** *65,* 712–725. doi:10.1002/prot.21123
66. Hutter, J. L.; Bechhoefer, J. *Rev. Sci. Instrum.* **1993,** *64,* 1868. doi:10.1063/1.1143970

## License and Terms

BEILSTEIN JOURNAL OF NANOTECHNOLOGY

# Microwave assisted synthesis and characterisation of a zinc oxide/tobacco mosaic virus hybrid material. An active hybrid semiconductor in a field-effect transistor device

Shawn Sanctis[1], Rudolf C. Hoffmann[1], Sabine Eiben[2] and Jörg J. Schneider[*1,§]

Full Research Paper

Open Access

Address:
[1]Fachbereich Chemie, Eduard-Zintl-Institut, Fachgebiet Anorganische Chemie, Technische Universität Darmstadt, Alarich-Weiss Straße 12, 64287 Darmstadt, Germany and [2]Institute of Biomaterials and Biomolecular Systems, Dept. of Molecular Biology and Plant Virology, University of Stuttgart, 70550 Stuttgart, Germany

Email:
Jörg J. Schneider[*] - joerg.schneider@ac.chemie.tu-darmstadt.de

* Corresponding author
§ Fax: +49 6151 163470; Tel: +49 6151 163225

Keywords:
field-effect transistor; microwave synthesis; molecular precursor; thin film transistor; tobacco mosaic virus; zinc oxide

*Beilstein J. Nanotechnol.* **2015,** *6,* 785–791.
doi:10.3762/bjnano.6.81

Received: 12 September 2014
Accepted: 16 February 2015
Published: 20 March 2015

This article is part of the Thematic Series "Towards multifunctional inorganic materials: biopolymeric templates" and is dedicated to Prof. Dr. mult. Günther Wilke on the occasion of his 90th birthday.

Guest Editors: C. Steinem and J. Bill



## Abstract

Tobacco mosaic virus (TMV) has been employed as a robust functional template for the fabrication of a TMV/zinc oxide field effect transistor (FET). A microwave based approach, under mild conditions was employed to synthesize stable zinc oxide (ZnO) nanoparticles, employing a molecular precursor. Insightful studies of the decomposition of the precursor were done using NMR spectroscopy and material characterization of the hybrid material derived from the decomposition was achieved using dynamic light scattering (DLS), transmission electron microscopy (TEM), grazing incidence X-ray diffractometry (GI-XRD) and atomic force microscopy (AFM). TEM and DLS data confirm the formation of crystalline ZnO nanoparticles tethered on top of the virus template. GI-XRD investigations exhibit an orientated nature of the deposited ZnO film along the c-axis. FET devices fabricated using the zinc oxide mineralized virus template material demonstrates an operational transistor performance which was achieved without any high-temperature post-processing steps. Moreover, a further improvement in FET performance was observed by adjusting an optimal layer thickness of the deposited ZnO on top of the TMV. Such a bio-inorganic nanocomposite semiconductor material accessible using a mild and straightforward microwave processing technique could open up new future avenues within the field of bio-electronics.

## Introduction

In recent years, the synthesis and fabrication of bio-inorganic nanostructures have gained tremendous importance for the fabrication of nanoscale devices with defined functional properties [1-3]. Significant interest has been dedicated to the generation of multifunctional devices by employing a unique combination of functional biological molecules and inorganic ma-

terials. The use of biological building blocks at the nanoscale include DNA, peptides, bacteriophages and viruses which exhibit diverse properties for the controlled formation of devices with possible application in areas such as sensors, photonics, energy storage as well as electronic transistors [4-8]. Fabrication of necessary functional hybrid materials often require well-defined 1D and 2D biological molecules as structure-directing agents, enabling a "bottom-up" approach for building these complex nanoarchitectures. Among the several biological templates, the tobacco mosaic virus (TMV) has shown great potential to function as a robust biological template for the deposition of a variety of inorganic materials under mild fabrication conditions. With its well-defined tube-like structure, the tobacco mosaic virus is one the most widely studied plant virus consisting of ≈2130 identical protein units, a length of 300 nm and an outer and inner diameter of 18 nm and 4 nm, respectively. It is also displays a remarkable stability for temperatures of up to about 60 °C in a pH range between 2 and 10. Such a rigid nanostructured template offers an interesting opportunity for the directed assembly of inorganic, metallic and semiconducting materials [9,10].

With the aim to generate defined semiconducting nanostructures in the nanometer range, deposition of ZnO nanoparticles onto the wild type TMV (wt TMV) presents itself to be an ideal choice of material combination.

Zinc oxide (ZnO) is one the most widely studied, non-toxic, n-type semiconducting inorganic oxide with a direct band-gap of ≈3.37 eV. This enables the fabrication of functional zinc oxide based transistors [11,12]. The ability to fabricate zinc oxide based transistors from various precursor solutions, under mild basic conditions, makes it a suitable candidate to be deposited upon the TMV template [13]. We have previously reported on the synthesis of air-stable, Schiff base type, molecular zinc complex diaqua-bis[2-(methoxyimino)propanato]zinc(II) which represents an ideal molecular single source precursors for the fabrication of functional zinc oxide transistors at low-temperatures [14]. Employment of such a class of molecular precursor complexes, with a low decomposition temperature and volatile and well defined byproducts ensures the formation of a resultant zinc oxide material with high purity. Additionally, microwave assisted decomposition of this class of precursors in solution has shown to yield stable colloidal nanoparticle dispersions [15,16]. In order to assist the in situ deposition of nanoparticulate zinc oxide onto the wt TMV template, mild microwave synthesis conditions for the zinc oximate precursor were used by us for the first time.

Herein, we report on the fabrication of a functional hybrid semiconducting material based on a microwave assisted ZnO mineralization of the TMV [17]. The resultant TMV/ZnO nanoscale hybrid material exhibits functional transistor behaviour with a reasonable performance without any post-processing at higher temperature.

## Experimental section

All reagents were purchased from Sigma-Aldrich or Carl Roth and used as received unless otherwise stated. The molecular precursor, diaqua-bis[2-(methoxyimino)propanato]zinc(II), referred to as the zinc oximato complex in this work, was synthesized as previously reported [14]. The deposition solution was prepared by mixing solutions of the zinc oximato complex and polyvinylpyrrolidone (PVP) (mol. wt ≈ 10k) in methanol and drop wise addition of a solution of tetraethylammonium hydroxide (TEAOH) in methanol, so that the final concentrations were $[Zn^{2+}]$ = 10 mM, [PVP] = 10 mM, and [TEAOH] = 12.5 mM. The microwave reactions were performed in a Discover (CEM Corporation) microwave oven using commercially available glassware supplied by the manufacturer. A few drops of 0.5 mM aqueous zinc acetate solution were deposited on the FET substrate for 5 min and excess was removed and blow-dried under a stream of argon flow. Thereafter, a drop TMV (0.5 µL, 0.5 mg/mL) was placed onto the FET substrate surface and incubated for 10 min. The excess virus suspension was removed by blow drying the substrate under a mild argon flow. The positively charged zinc cations facilitate the efficient immobilization of the negatively charged TMV particles on to the substrate. The FET substrate with the immobilized TMV was immersed in the microwave reaction vessel containing 10 mL of the reaction solution. Reactions were carried out by heating for 30 min, with a maximum applied power of 50 W (dynamic power mode), with an average power of ≈15 W, throughout the experiment. The prefabricated FET substrates (Fraunhofer IWS, Dresden) were sequentially cleaned in an ultra-sonic bath with acetone, DI-water and isopropanol, respectively for ten minutes each, prior to its immersion in the microwave vessel containing the reaction solution. Substrates for the FET devices (15 × 15 $mm^2$) consisted of n-doped silicon with a 90 nm layer of $SiO_2$, on which gold electrodes were attached with an intermediate adhesion layer of indium tin oxide. The electrodes possessed an inter-digital structure with a channel width W of 10 mm and a channel length of 20 µm.

$^{13}C$ nuclear magnetic resonance spectroscopy (NMR) was undertaken using a DRX500 (Bruker) spectrometer. Experiments to study the decomposition of the precursor in the microwave were performed by preparing the reaction solution (with and without the TEAOH) in tetra-deuteromethanol (methanol-$d_4$). The reactions were performed in the absence of the virus to avoid any influence from the TMV. For the NMR studies the

decomposed precursor solution after microwave processing was filtered through a 0.22 μm PTFE syringe filter and was directly analyzed using NMR. Transmission electron microscopy (TEM) was performed using Tecnai F20 G20 (FEI) electron microscope working at 200 kV, using lacey carbon coated copper grids. Dynamic light scattering (DLS) measurements for the ZnO suspensions were carried out using a Zetasizer Nano (Malvern). Atomic force microscopy was performed with CP-II (Bruker-Veeco) microscope using ultra sharp silicon cantilevers. Optical profilometry measurements were performed using the optical Profilometer-NewView 6200 (Zygo). Grazing incidence XRD (GI-XRD) investigations were performed with a Seifert PTS 3003 diffractometer using a Cu anode and a graphite monochromator with an applied current and voltage of 40 mA and 40 kV, respectively. FET characterizations were measured in the dark, using an HP 4155A semiconductor parameter analyzer (Agilent) in a glove box under constant $O_2$ and $H_2O$ (<0.5 ppm). Charge carrier mobility in the saturation regime $\mu_{SAT}$ and the threshold voltage $V_{th}$ were derived from a linear fitting of the square root of the drain-source current ($I_{DS}$) as a function of the gate–source voltage ($V_{GS}$).

Tobacco mosaic virus strain U1 was propagated in Nicotiana tabacum 'Samsun' nn plants for 25 days and purified according to the modified protocol of Gooding and Hebert [18].

## Results and Discussions

### Synthesis and characterization of the wt TMV/ZnO hybrid material

In order to facilitate the controlled mineralization of zinc oxide onto the TMV template, the microwave conditions for synthesis of the zinc oxide in due consideration of the stability of the TMV template had to be optimized. Use of the molecular precursor diaqua-bis[2-(methoxyimino)propanato]zinc(II) [14,19] (referred to as – the zinc oximato complex – in the following) as a source of zinc oxide was employed, herein. Solutions for the controlled formation and deposition of the ZnO nanoparticles were obtained by using a methanolic solution of zinc complex as a zinc source and polyvinylpyrrolidone (PVP) as a growth inhibiting and stabilizing agent for the zinc oxide nanoparticles. PVP has been reported to have a higher efficiency in suppressing the growth of zinc oxide during its formation, in comparison to other polymeric additives [20]. Additionally, a defined amount of tetraethylammonium hydroxide (TEAOH) was added to the precursor solution to create a mild basic environment which assists the controlled formation of the ZnO nanoparticles.

The addition of the optimal amount of the base TEAOH provides mild but sufficient basic conditions to ensure an efficient decomposition of the zinc complex at a low temperature as 60 °C (±3 °C) enabling the successful formation of crystalline zinc oxide. An increased reaction rate, although, with a rapid formation of zinc oxide resulting in unstable aggregates ranging up to several hundred nanometres in size, was observed in the presence of higher amounts of the base. In order to gain insight into the microwave decomposition process of the molecular precursor, the microwave decomposition process was studied in the absence and presence of the base TEAOH using $^{13}C$ NMR spectroscopy. Without the addition of the base, the precursor complex did not undergo any decomposition after the completion of the microwave reaction under typical reaction conditions. However, in the presence of the base, the precursor does undergo decomposition with appearance of a characteristic $^{13}C$ chemical shift corresponding to the formation of acetonitrile ($\delta$ = 117.30 ppm) under post decomposition conditions of the precursor complex. Additional chemical shifts from still coordinated as well as from residual free ligands were also present as expected due to the base-catalyzed decomposition of the precursor complex (see Supporting Information File 1, Figure S2). The products observed in the microwave initiated decomposition of the oximato complex is in full accordance with a second-order type Beckmann rearrangement reaction as observed for its solution based thermal decomposition pathway [13]. Besides the characteristic signals of the decomposition products, chemical shifts from the undecomposed precursor are still observed after the completion of the microwave reaction. Attempts to completely decompose the precursor were not pursued since long reaction time lead to the formation of undesirable precipitates of zinc oxide aggregates, in a very similar way as addition of excess base TEAOH does. Thus it can be concluded that the microwave decomposition reaction has to be fine tuned in order to obtain pure precipitates of the desired nanoscale ZnO product. A comprehensive reaction and decomposition pathway of the precursor can thus be proposed on the basis of the observed decomposition products from the described NMR experiments (Figure 1).

Systematic experiments have shown that a maximum microwave power of 50 W, temperature of 60 °C (±2 °C) and a synthesis time of 30 min display the optimum conditions leading to the formation of nanocrystalline ZnO. Dynamic light scattering measurements indicate the formation of stable ≈5 nm particles, after a synthesis period of 30 min (see Supporting Information File 1, Figure S1). The indicated particle size is in good agreement with HRTEM investigations of the as-synthesized particles formed from the precursor solution, which yield stable zinc oxide nanoparticles (Figure 2a). TEM also indicates the successful formation of ZnO nanocrystals in solution after the completion of the microwave irradiation process. Grazing incidence X-ray diffractometry (GI-XRD) analysis was employed to gain a deeper insight into the crystallinity of the as deposited

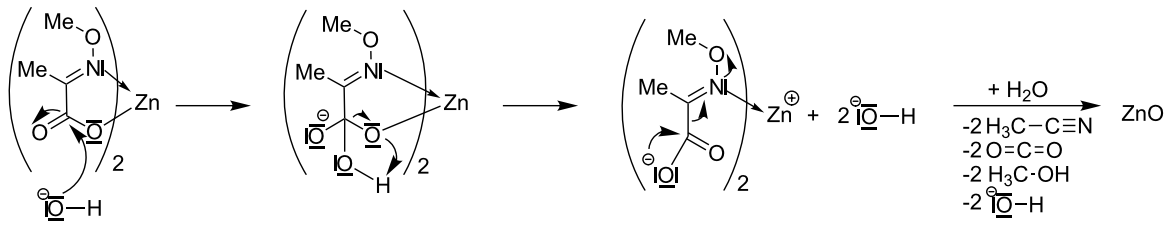


**Figure 1:** Schematic representation of the microwave decomposition pathway of the zinc oximato precursor in the presence of TEAOH as a base based on NMR spectroscopy. Note that the water ligands are omitted in the starting compound.

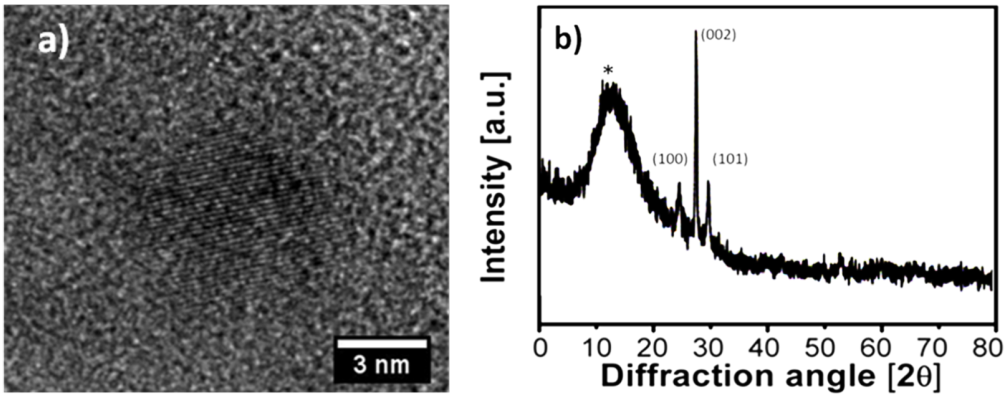


**Figure 2:** a) HRTEM image of the ZnO nanoparticle obtained from solution and b) GI-XRD spectra of the ZnO thin film after 6 deposition cycles (* = peak intensity arising from the $Si/SiO_2$ substrate).

ZnO thin film. The ZnO films display a polycrystalline nature of the ZnO being essential for the formation of an active semiconducting layer. Reflection peaks corresponding to the (100), (002) and (101) planes are characteristic of the zincite structure (Figure 2b). A greater intensity in the direction of the c-axis (i.e., perpendicular to the (002) plane) was observed. ZnO nanoparticles undergo an oriented attachment during thin film formation in the presence of PVP which hints at texturing of the ZnO nanoparticles within the deposited ZnO film [21,22].

In order to perform an in situ microwave-based mineralization of the TMV, it is essential to ensure that the virus particle adheres to the substrate during the microwave irradiation. Intense microwave irradiations are known to have a strong tendency to denature proteins and cause potentials damage to its structural integrity [23]. Additionally, prolonged high-power microwave irradiation could lead to unexpected heating of the substrate onto which the TMV are immobilized. The substrates with the docked virus were thus immersed in a control methanolic solution containing the predetermined amounts of the TEAOH and PVP in the absence of the zinc precursor. These substrates were then subjected to the desired microwave irradiation time of 30 min. This ensures that the virus particles do not detach from the substrate. AFM investigations for a control experiment reveal an intact TMV template on the $Si/SiO_2$ substrate, even after 30 min of mild microwave irradiation showing no visible deformation of its rod-like structure and its original dimensions and morphology (Figure 3a). Irradiation of the reference solution containing the virus-coated substrate with higher microwave power led to uncontrolled, rapid increase of the solution temperature and boiling of the solvent methanol (bp ≈ 65 °C). This led to a detachment of the viruses as no visible virus structures afterwards could be detected on the substrate surface by AFM analysis after this procedure. Once the reliable microwave conditions of the virus attachment and the retention of its structural integrity were confirmed, the virus-coated substrates were immersed in the reaction solution which then leads to the mineralization of the zinc oxide nanoparticles onto the virus template. Such successful mineralization of the zinc oxide onto the TMV template is obtained under low power microwave assisted decomposition of the precursor solution (Figure 3b). Hence, reliable docking of the TMV onto the silicon/silicondioxide ($Si/SiO_2$) and simultaneous formation of zinc oxide nanoparticles could be achieved. AFM analysis for the bare TMV layer as well as the ZnO mineralized TMV layer after one deposition cycle reveal an average layer thick-

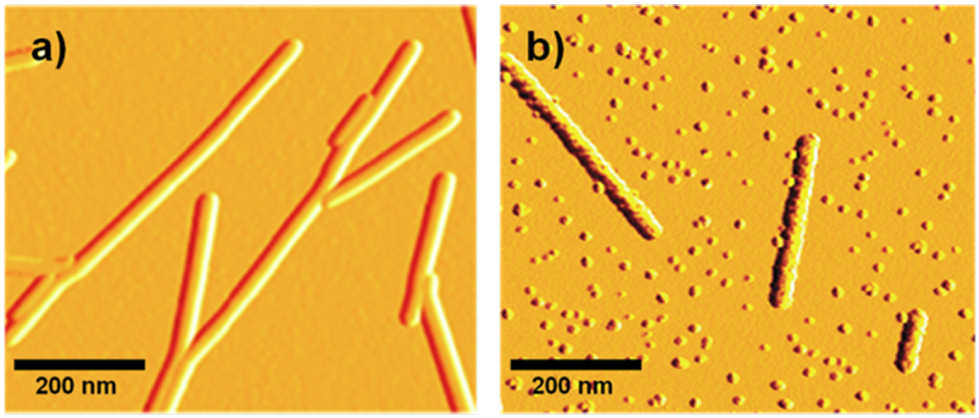


**Figure 3:** AFM micrographs of (a) the bare wt TMV template immobilized on a $Si/SiO_2$ substrate as well as (b) the wt TMV template after 1 cycle of ZnO mineralization.

ness of 15.5 nm and 25.8 nm respectively (see Supporting Information File 1, Figure S3).

In order to ensure an optimum thickness and to promote a good transistor performance ZnO layers with increasing number of deposition cycles were analyzed. The increasing thickness of the ZnO films after various cycles was measured using optical profilometry (Figure 4).

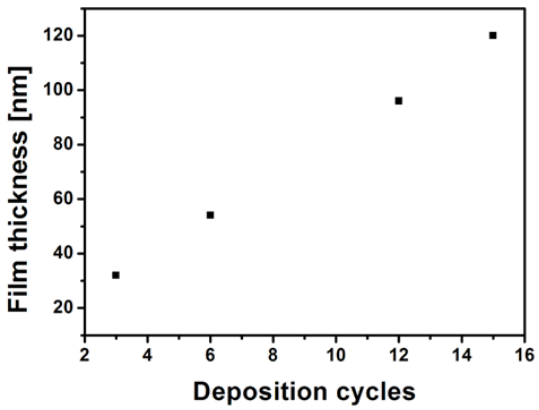


**Figure 4:** Overall thickness of the wt TMV/ZnO hybrid material as a function of the number of deposition cycles as determined by optical profilometry. ZnO was deposited onto the wt TMV template with an increasing number of deposition cycles from the precursor solution.

The thickness and uniformity of the deposited semiconductor layer bear a crucial importance for FET device performance [12]. Variation in the layer thickness severely affects the transistor performance. For example, a thicker layer increases the resistance across the active material, while thinner layers could possibly lead to non-uniform layer deposition [24]. Therefore the layer thickness should be optimized according to these parameters.

## Field effect transistor (FET) properties

In order to assess its FET properties, the wt TMV/ZnO hybrid material template was realised in a bottom gate, bottom contact FET geometry, by employing pre-fabricated FET substrates with external gold electrodes. All fabricated devices exhibit functional transistor properties without any post-processing treatment. As a reference we had measured the electrical characteristics of microwave processed bare nanoscale ZnO without TMV, obtained again from the molecular zinc oximato precursor complex under similar conditions. These results showed only noisy and almost indiscernible signals (measurements not shown). This fact substantiates the point that the FET properties are indeed intrinsic for the microwave processed wt TMV/ZnO hybrid material. Similar results have been reported for thermally processed bare nanoscale ZnO material using the zinc oximato complex as precursor [13].

The transistor behaviour of the wt TMV/ZnO hybrid material was then optimized based on the crucial characteristic FET values, current on/off ratio ($I_{on/off}$), threshold voltage ($V_{th}$) and charge carrier mobility (μ) which are considered to be essential parameters for the FET performance. Based on these performance parameters, the electrical characteristics of the devices display a stark contrast due to the difference in the number of ZnO deposition cycles which led to the formation of thicker layers. FET characteristics of the ZnO films with increased layer thickness are displayed below (Figure 5 and Table 1).

Fewer deposition cycles (3 cycles) for the ZnO exhibited very weak transfer characteristics with significantly low On and well as Off currents, high $V_{th}$ and poor mobility values. On the other hand, increased number of deposition cycles (12 cycles) of the ZnO led to a slight increase in the mobility values. Also, a positive increase in the On currents accompanied by a drastic

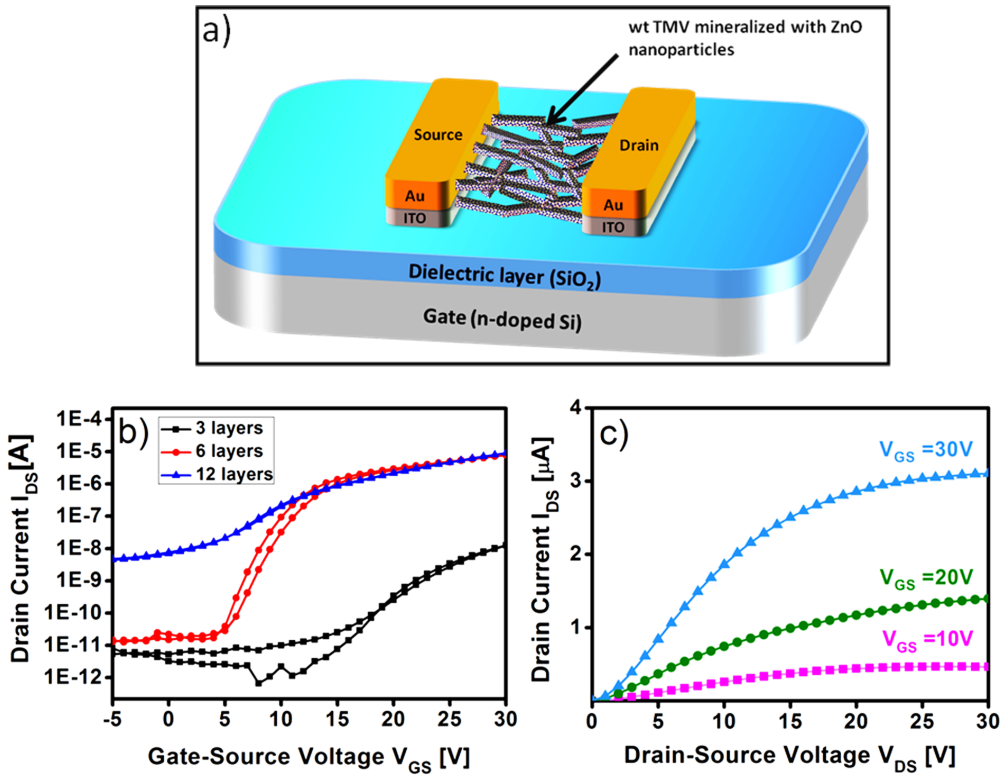


**Figure 5:** Schematic representation of the wt TMV/ZnO based FET device (a). Performance of the FET device fabricated by increasing the number of ZnO deposition cycles on the wt TMV template; (b) Transfer characteristics for constant drain–source voltage at 30 V; (c) output characteristics of TMV/ZnO hybrid after 6 deposition cycles, obtained at drain–source voltage of 30 V, for gate–source voltage varied from 0–30 V in 10 V steps.

**Table 1:** Characteristic values for field-effect mobility μ, threshold voltage ($V_{th}$), and on/off current ratio ($I_{on/off}$) of wt TMV/ZnO hybrid material based transistor devices.

| ZnO deposition cycles | μ (mobility in $cm^2/Vs$) | $V_{th}$ (V) | $I_{on/off}$ |
|---|---|---|---|
| 3 | $8.0 \times 10^{-6}$ | 17.79 | $10.2 \times 10^2$ |
| 6 | $6.7 \times 10^{-4}$ | 4.76 | $9.0 \times 10^5$ |
| 12 | $8.4 \times 10^{-4}$ | 6.80 | $2.1 \times 10^3$ |
| 15 | $1.6 \times 10^{-3}$ | 12.02 | $1.0 \times 10^2$ |

increase in the Off currents led to a deteriorated $I_{on/off}$ ratio. Moreover, an undesirable higher $V_{th}$ value was observed. Further increase in the number of deposition cycles (15 cycles) deteriorated the overall transistor performance giving no significant semiconducting properties. For an optimum number (6 cycles) of ZnO deposition, the best overall FET performance values were obtained with a field-effect mobility (μ) of $6.7 \times 10^{-4}$ $cm^2/Vs$, $V_{th}$ of +4.7 V and an $I_{on/off}$ of $9.0 \times 10^5$. A higher $I_{on/off}$ in comparison to previously reported values could possibly be attributed to a greater degree of ZnO nanoparticle orientation on the wt TMV template resulting from the use of the molecular precursor complex employed [25].

## Conclusion

The ability of the virus template to maintain its structural integrity under mild microwave radiations, while facilitating the deposition of zinc oxide nanoparticles has been implemented for virus-based templating of inorganic nanomaterials, towards functional devices with diverse applications. We have successfully employed a molecular precursor to synthesize zinc oxide nanoparticles, for an in situ deposition on to a virus template. A facile, microwave-assisted approach for generating a TMV/ZnO hybrid bio-inorganic material has been implemented. We confirmed the clean in situ decomposition of the molecular precursor under mild conditions as well as the desired zinc oxide phase formation by resonance, diffractometry and microscopic methods. Moreover, the as-synthesized hybrid material has been successfully employed in a FET device. The best FET performance has been achieved by systematically controlling the thickness of the deposited zinc oxide films. The fabricated FET shows a reasonable performance for the as-prepared device, without any post processing of the bio-inorganic hybrid nanomaterial. Such an approach towards generation of a bio-inorganic material encourages the use of nanoscale virus templates to obtain hybrid materials with functional properties that can be implemented into future device applications.

## Supporting Information

### Supporting Information File 1

Additional figures.
[http://www.beilstein-journals.org/bjnano/content/supplementary/2190-4286-6-81-S1.pdf]

## Acknowledgements

This work has been supported within the DFG SPP 1596, and the Cooperative Research Lab Alliance between Merck KGaA, Darmstadt, and Technische Universität Darmstadt (Merck Lab). We thank Dr. J. Engstler (TEM) and Dr. J. Brötz (GI-XRD) at Technische Universität Darmstadt for material characterizations. TEM studies at ERC, Jülich, Germany, are supported through the ERC-TUD1 contract collaboration. SS would like to acknowledge discussions with Dr. M. Nowotny concerning the NMR studies.

## References

1. Sanchez, C.; Julián, B.; Belleville, P.; Popall, M. *J. Mater. Chem.* **2005,** *15,* 3559–3592. doi:10.1039/B509097K
2. Wen, J.; Wilkes, G. L. *Chem. Mater.* **1996,** *8,* 1667–1681. doi:10.1021/cm9601143
3. Niemeyer, C. M. *Angew. Chem.* **2001,** *113,* 4254–4287. doi:10.1002/1521-3757(20011119)113:22<4254::AID-ANGE4254>3.0.CO;2-D
4. Mirkin, C. A.; Letsinger, R. L.; Mucic, R. C.; Storhoff, J. J. *Nature* **1996,** *382,* 607–609. doi:10.1038/382607a0
5. Hoffmann, R. C.; Atanasova, P.; Dilfer, S.; Bill, J.; Schneider, J. J. *Phys. Status Solidi A* **2011,** *208,* 1983–1988. doi:10.1002/pssa.201127064
6. Chen, C.-L.; Rosi, N. L. *Angew. Chem., Int. Ed.* **2010,** *49,* 1924–1942. doi:10.1002/anie.200903572
7. Gazit, E. *Chem. Soc. Rev.* **2007,** *36,* 1263–1269. doi:10.1039/B605536M
8. Scolaro, L. M.; Castriciano, M. A.; Romeo, A.; Micali, N.; Angelini, N.; Lo Passo, C.; Felici, F. *J. Am. Chem. Soc.* **2006,** *128,* 7446–7447. doi:10.1021/ja061726j
9. Shenton, W.; Douglas, T.; Young, M.; Stubbs, G.; Mann, S. *Adv. Mater.* **1999,** *11,* 253–256. doi:10.1002/(Sici)1521-4095(199903)11:3<253::Aid-Adma253>3.0.Co;2-7
10. Balci, S.; Hahn, K.; Kopold, P.; Kadri, A.; Wege, C.; Kern, K.; Bittner, A. M. *Nanotechnology* **2012,** *23,* 045603. doi:10.1088/0957-4484/23/4/045603
11. Sun, B.; Sirringhaus, H. *Nano Lett.* **2005,** *5,* 2408–2413. doi:10.1021/nl051586w
12. Hoffman, R. L.; Norris, B. J.; Wager, J. F. *Appl. Phys. Lett.* **2003,** *82,* 733–735. doi:10.1063/1.1542677
13. Atanasova, P.; Rothenstein, D.; Schneider, J. J.; Hoffmann, R. C.; Dilfer, S.; Eiben, S.; Wege, C.; Jeske, H.; Bill, J. *Adv. Mater.* **2011,** *23,* 4918–4922. doi:10.1002/adma.201102900
14. Schneider, J. J.; Hoffmann, R. C.; Engstler, J.; Dilfer, S.; Klyszcz, A.; Erdem, E.; Jakes, P.; Eichel, R. A. *J. Mater. Chem.* **2009,** *19,* 1449–1457. doi:10.1039/B816376F
15. Schneider, J. J.; Hoffmann, R. C.; Engstler, J.; Klyszcz, A.; Erdem, E.; Jakes, P.; Eichel, R.-A.; Pitta-Bauermann, L.; Bill, J. *Chem. Mater.* **2010,** *22,* 2203–2212. doi:10.1021/cm902300q
16. Sanctis, S.; Hoffmann, R. C.; Schneider, J. J. *RSC Adv.* **2013,** *3,* 20071–20076. doi:10.1039/C3RA44222E
17. Lipowsky, P.; Hoffmann, R. C.; Welzel, U.; Bill, J.; Aldinger, F. *Adv. Funct. Mater.* **2007,** *17,* 2151–2159. doi:10.1002/adfm.200600399
18. Gooding, G. V.; Hebert, T. T. *Phytopathology* **1967,** 1285.
19. Schneider, J. J.; Hoffmann, R. C.; Engstler, J.; Soffke, O.; Jaegermann, W.; Issanin, A.; Klyszcz, A. *Adv. Mater.* **2008,** *20,* 3383–3387. doi:10.1002/adma.200800819
20. Guo, L.; Yang, S.; Yang, C.; Yu, P.; Wang, J.; Ge, W.; Wong, G. K. L. *Chem. Mater.* **2000,** *12,* 2268–2274. doi:10.1021/cm9907817
21. Niwa, D.; Fujie, T.; Lang, T.; Goda, N.; Takeoka, S. *J. Biomater. Appl.* **2012,** *27,* 131–141. doi:10.1177/0885328210394470
22. Lipowsky, P.; Jia, S.; Hoffmann, R. C.; Jin-Phillipp, N. Y.; Bill, J.; Rühle, M. *Z. Metallkd.* **2006,** *97,* 607–613. doi:10.3139/146.101278
23. Bohr, H.; Bohr, J. *Phys. Rev. E* **2000,** *61,* 4310–4314. doi:10.1103/PhysRevE.61.4310
24. Zhang, L.; Zhang, H.; Bai, Y.; Ma, J. W.; Cao, J.; Jiang, X.; Zhang, Z. L. *Solid State Commun.* **2008,** *146,* 387–390. doi:10.1016/j.ssc.2008.03.036
25. Meulenkamp, E. A. *J. Phys. Chem. B* **1999,** *103,* 7831–7838. doi:10.1021/jp9914673

## License and Terms

BEILSTEIN JOURNAL OF NANOTECHNOLOGY

# Morphology control of zinc oxide films via polysaccharide-mediated, low temperature, chemical bath deposition

Florian Waltz[‡1], Hans-Christoph Schwarz[‡1], Andreas M. Schneider[1], Stefanie Eiden[2] and Peter Behrens[*1]

Full Research Paper

Open Access

Address:
[1]Institut für Anorganische Chemie, Leibniz Universität Hannover, Callinstraße 9, 30167 Hannover, Germany and [2]Bayer Technology Services GmbH, 51368 Leverkusen, Germany

Email:
Peter Behrens[*] - peter.behrens@acb.uni-hannover.de
*Corresponding author

* Corresponding author ‡ Equal contributors

Keywords:
chemical bath deposition; hyaluronic acid; polysaccharide; transparent conductive oxide; zinc oxide

*Beilstein J. Nanotechnol.* **2015,** *6,* 799–808.
doi:10.3762/bjnano.6.83

Received: 28 May 2014
Accepted: 20 February 2015
Published: 24 March 2015

This article is part of the Thematic Series "Towards multifunctional inorganic materials: biopolymeric templates".

Guest Editors: C. Steinem and J. Bill



## Abstract

In this study we present a three-step process for the low-temperature chemical bath deposition of crystalline ZnO films on glass substrates. The process consists of a seeding step followed by two chemical bath deposition steps. In the second step (the first of the two bath deposition steps), a natural polysaccharide, namely hyaluronic acid, is used to manipulate the morphology of the films. Previous experiments revealed a strong influence of this polysaccharide on the formation of zinc oxide crystallites. The present work aims to transfer this gained knowledge to the formation of zinc oxide films. The influence of hyaluronic acid and the time of its addition on the morphology of the resulting ZnO film were investigated. By meticulous adjustment of the parameters in this step, the film morphology can be tailored to provide an optimal growth platform for the third step (a subsequent chemical bath deposition step). In this step, the film is covered by a dense layer of ZnO. This optimized procedure leads to ZnO films with a very high electrical conductivity, opening up interesting possibilities for applications of such films. The films were characterized by means of electron microscopy, X-ray diffraction and measurements of the electrical conductivity.

## Introduction

Zinc oxide is a unique material with a number of interesting properties such as piezo- and pyro-electricity [1,2], high optical transparency [3], catalytic activity [4,5], and chemical sensing [6-8]. It is also one of the most promising candidates for the replacement of indium tin oxide (ITO) in transparent conductive oxide (TCO) applications [9,10]. Hence, ZnO films are a key research area in industry as well as in academia with more than 2100 publications in 2013 (Thomson Reuters, Web of Knowledge). Several methods have been used to deposit ZnO on different substrates, for example, pulsed laser deposition (PLD) [11], chemical vapor deposition (CVD) [12,13], as well as wet chemical approaches such as sol–gel synthesis [14] and

chemical bath deposition (CBD) [15-18]. Among these, CBD methods have gained increasing interest since they allow the deposition of ZnO films in large-scale applications at low temperature, on a number of different substrates and with minimal effort.

ZnO is a semiconducting, ceramic material with a direct band gap of 3.37 eV and an exciton binding energy of 60 meV [19]. Although ZnO is reported to be an n-type semiconductor (most likely due to the hydrogen impurities which act as shallow donors), it is a challenging task to control its conductivity [20]. In general, in applications where highly conductive materials are required (e.g., solar cells and light emitting diodes (LEDs)), ZnO must be doped.

Several groups have reported the successful doping of ZnO films with dopants such as magnesium [21], iodine [22], boron [23,24], titanium [25], manganese [26], and aluminium [27-29]. These films were grown via CBD or related techniques (e.g., double dipping or hot water dipping). In CBD processes, hexamethylenetetramine (HMTA) is usually dissolved in a solution containing Zn(II) ions. At a certain temperature, HMTA decomposes and consequently delivers hydroxide ions, forcing the formation of crystalline ZnO [30]. Doping is carried out by the simple addition of the corresponding dopant salt to the deposition solution. In addition to doping, the microstructure of the resulting film, which involves the crystallite size as well as the morphology of the crystallites and the degree of their intergrowth, has a decisive influence on many applications, for example, in sensors and catalysts [8,31].

As the wurtzite structure of ZnO is polar, crystals of the substance feature two differently charged surfaces: the oxygen terminated (00−1) and the zinc terminated (001) faces, on both of which charged molecules can be chemisorbed by electrostatic interactions. In addition, the uncharged {100} faces of ZnO can support the physisorption of molecules. Such adsorption phenomena can influence the growth rates of the corresponding faces, leading to different crystal habits.

Solvent-based chemical deposition processes are particularly suited for the addition of molecules that may affect the morphology of ZnO crystals and their aggregates as well as of ZnO films. Molecules such as citrate [31,32], histidine [33], 1-butan-2-ylpyrrolidin-2-one (PVP) [34,35], 2-hydroxybutanedioate (malate) [36], ascorbate [37], diaminopropane [38], hexadecyl(trimethyl)azanium bromide (CTAB) [39], and block copolymers [40] have been used for this purpose, in addition to naturally occurring amino acids and peptides [41], which have already been successfully applied in this respect. We recently investigated the influence of two polysaccharides, hyaluronic acid (HYA) and chondroitin-6 sulfate (C6S), on the morphology of primary ZnO crystallites and on their aggregates, as they are formed in precipitation experiments [42]. Whereas C6S leads to a pronounced platelet-like morphoplogy of the primary crystallites, HYA leads to the growth of small wedge-like particles and the aggregation of these particles into bundles. We surmised that this influence of HYA might be beneficial to the quality of deposited, thin, ZnO films by increasing the number of primary crystallites. This should lead to finer structured films with more strongly intergrown crystals, thus enhancing the electrical conductivity and optical transparency. Therefore, we have undertaken the study presented here, where ZnO films were prepared in a three-step process: a seeding step, followed by two CBD steps (Figure 1). In the first of the two CBD steps, HYA was added at different time intervals in order to optimize the quality of the resulting films. The properties of the films were studied by means of field emitting scanning electron microscopy (FE-SEM), X-ray diffraction (XRD), UV–vis spectroscopy and electrical conductivity measurements.

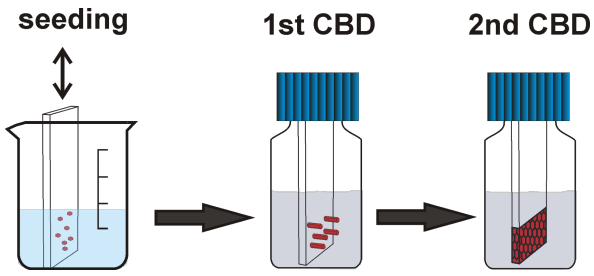


**Figure 1:** Scheme of the three-step, ZnO film deposition process. Seeds were deposited on glass slides by immersion in a Zn(II) solution, followed by annealing. In the first CBD step, different ZnO morphologies can be grown depending on the time of the HYA addition. In the second CBD step, a dense film can be formed.

## Results and Discussion

ZnO films were prepared according to the three-step process described in the Experimental section and depicted in Figure 1.

### Step 1: Seeding

The solution-based growth of zincite in general requires prior application of crystalline seeds on the support. In our work, the solution deposition procedure according to Greene et al. reproducibly led to high film quality in the final product [43]. The seeding did not result in clouding of the glass slides, which would have been observable with the naked eye. The XRD patterns of glass slides seeded in this way displayed only a broad signal originating from the amorphous glass (data not shown). FE-SEM also failed to visualize the seeds on the glass slides, probably due to their small size and the strong electric charging of the substrate.

However, indirect evidence of a successful seeding was possible. Contact angle measurements showed that the slides are slightly more hydrophobic after the seeding process. The contact angle of a seeded glass slide was about 58° in comparison to 46° for a clean glass slide. Furthermore, the UV–vis spectra of seeded glass slides showed an absorption band in the UV range at approximately the energy of the ZnO band gap (3.37 eV) (data not shown). However, the final evidence is presented by the efficient growth of ZnO on the seeded slides; in contrast, unseeded slides did not properly support the growth of ZnO.

## Step 2: First CBD

In the absence of hyaluronic acid (HYA), highly vertically aligned ZnO nanorods grow on priorly seeded glass slides, when the procedure described in the Experimental section is applied. The growth of aligned ZnO nanorods arrays on different substrates has been previously reported [15,17,43,44]. The scanning electron micrographs in Figure 2 show a nanorod array that was grown for 1 h. In X-ray diffraction experiments, arrays of this kind display only the (002) reflection of zincite due to the strong texture of the crystals with their *c* axis perpendicular to the support (Figure 3).

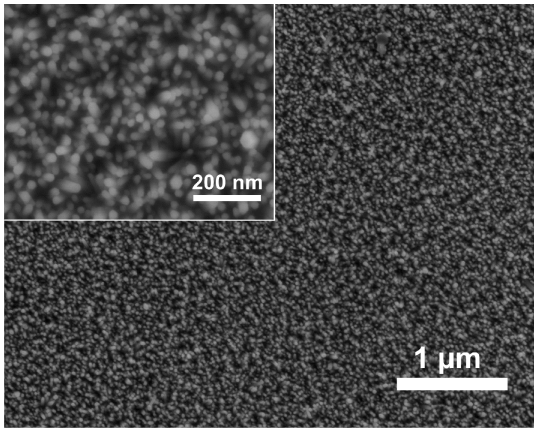


**Figure 2:** SEM micrographs of a ZnO nanorod array grown on a seeded glass slide for 1 h without the addition of HYA; the inset shows a higher magnification image.

As previously demonstrated, the addition of natural polysaccharides affects the morphology of the ZnO crystallites precipitated from solution [42,46,47]. This occurs largely due to the blocking of specific crystal faces during growth. In precipitation experiments, performed under conditions that are very similar in concentration and temperature to typical ZnO CBD processes, the addition of HYA led to the formation of well-defined and highly symmetric ZnO mesocrystals. Using this procedure, the size of the individual ZnO particles was dramatically decreased from the micrometer down to the nanometer scale [42].

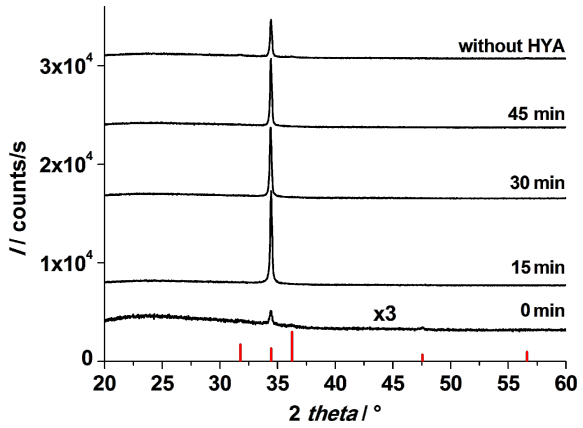


**Figure 3:** X-ray diffraction patterns of ZnO films after the first CBD. Growth was performed for 1 h in total with and without the addition of HYA. HYA was added after different time intervals as indicated in the figure. The red bars mark the XRD reflection peaks from a zincite reference [45].

In order to investigate the influence of HYA on the morphology of the resulting zinc oxide, HYA was dissolved in water during the first CBD at different time intervals (0, 15, 30 and 45 min). The growth of the ZnO nanorods (Figure 2) is assumed to proceed continuously on the seeded glass slides until HYA is added to the reaction mixture, which at this point may affect the further deposition and growth of ZnO.

The XRD patterns of films obtained after the first CBD (Figure 3) display only the (002) reflection of zincite, irrespective of whether HYA was supplied or not. This finding evidences the perpendicular alignment of the *c* axis of the ZnO crystallites with respect to the glass surface, which is unaffected by the addition of HYA. However, the intensity of the (002) reflection is very weak for the film grown when HYA was immediately added, indicating a strong decrease in the deposited amount of ZnO for this case. When HYA was added to the solution at a later point in time (15, 30 or 45 min), the (002) signal was more intense, indicating that more ZnO was grown on the substrate. These findings agree with the assumption that the presence of HYA decreases the ZnO deposition rate, for example by blocking the growth of certain crystal faces. Curiously, the sample prepared without the addition of HYA displays a weaker signal than samples with HYA added after 15, 30 and 45 min. This finding will be further discussed with regard to SEM investigations.

Whereas the crystallographic orientation of the ZnO crystallites on the support is not affected by the addition of HYA, the ZnO

film morphology changes dramatically when the CBD is performed in the presence of HYA. This is exhibited in SEM micrographs, which provide views of the plane of the deposited films (Figure 4). In general, the diameter of the individual ZnO nanorods decreased strongly when the HYA was added within the first 30 min of reaction, specifically, much finer structures were obtained. However, the individual nanocrystallites aligned themselves to larger aggregates, and the deposits can better be described as bundles of needles rather than as individual nanorods. This is comparable to precipitation experiments in which HYA adsorbs onto ZnO crystallites during their growth and thereby influences their size and aspect ratio. Furthermore, those ZnO subunits aggregate under the influence of HYA into highly ordered mesocrystals, which was evidenced by SEM investigations and selected area electron diffraction [42]. In the film deposition experiments described here, these aggregates even display a common hexagonal morphology, which can for example be seen in Figure 4 on the product prepared with HYA addition after 30 min. When HYA is added only after 45 min of reaction time, it has no significant influence on the morphology of the film. In fact, the SEM image of this sample is similar to that of the sample prepared without HYA addition. We assume that the zinc ions have already been almost completely consumed after this reaction time and that growth had completed before HYA addition.

With regard to the increasing intensity of the (002) reflections in the XRD patterns of the films after 15, 30 and 45 minutes of reaction, the SEM micrographs indicate that this increase is due to an increased lateral growth of the ZnO crystallites, which confirms that more ZnO was deposited when HYA was added at a later point in time. On the contrary, the sample in which HYA was immediately added shows also a very dense lateral growth, whereas the XRD reflection intensity is very weak. Therefore, we assume that the axial growth perpendicular to the support is inhibited by the immediate addition of HYA, leading to a lower mass of ZnO and consequently to a less intense signal in the XRD pattern. This assumption will be further discussed by support of cross-section SEM investigations presented in the next section.

During the first CBD, the morphology of ZnO grown on the seeded glass slides can be tailored by the addition of HYA: When no HYA is added or when it is added only after 45 min, arrays of individual nanorods are formed. When HYA is immediately added or up to a reaction time of 30 min, finely structured bundles of needle-shaped ZnO crystals are observed. Since the crystalline domains of these small crystallites do not overlap very well after the first CBD growth step, the electrical conductivity is only moderate. The sheet resistance of the films after the first CBD is typically in the range of MΩ/sq. Therefore, an additional step is necessary to grow a dense, ZnO film in order to yield low electrical resistance for the final sample.

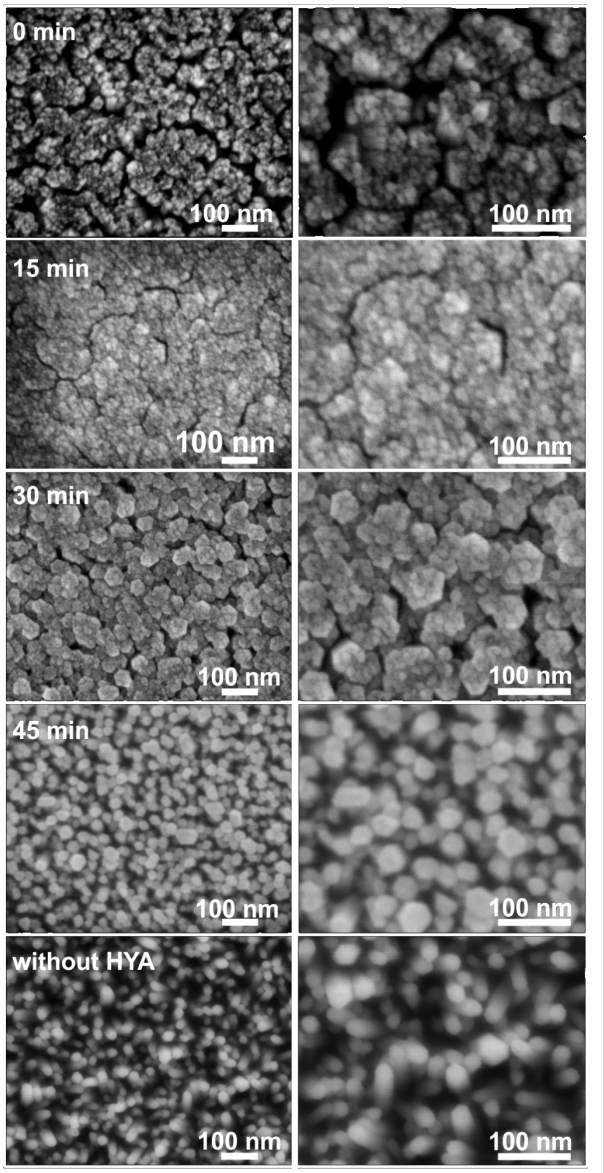


**Figure 4:** SEM micrographs of ZnO films after the first CBD. Growth was performed for 1 h in total with and without the addition of HYA. HYA was supplied after specific time intervals during the growth process as indicated.

## Step 3: Second CBD

The reaction conditions for the final growth step were adopted from Baxter and Schmuttenmaer, who obtained intergrown ZnO films after a reaction time of 3 h [48]. In our experiments, the reaction time could be reduced to 1 h due to the excellent growth conditions provided by the substrate during the first CBD step. The XRD patterns recorded after this third step show only (002) reflections (Figure 5), irrespective of the details of

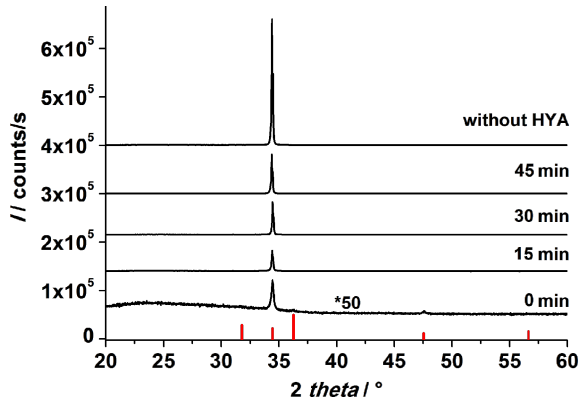


**Figure 5:** X-ray diffraction patterns of ZnO films after the second CBD. The films differ in the addition time of the HYA in the first CBD step (from 0 min up to 45 min). The red lines represent the XRD reflection peaks from a zincite reference [45].

the first CBD step, proving that the growth of ZnO continues to proceed with the *c* axis perpendicular to the support.

In general, the intensity of the (002) signal strongly increased after the third step as compared with the signals obtained on samples after the first CBD. This further indicates the successful deposition of ZnO. However, the intensity of this peak differs between the samples after the third step:

- The film which was grown in the first CBD step with immediate HYA addition shows the weakest signal, suggesting that this film supports further ZnO growth the least.
- The samples prepared in the first CBD step with HYA addition over the time intervals between 15 to 45 min showed a slight increase in the intensity of the (002) signal after the third step. The increase was stronger when HYA was added later.
- The film which was prepared with no HYA addition showed a 3× higher signal than films grown with HYA in the first CBD, indicating that a higher amount of ZnO was deposited.

Obviously, not only the growth of the films in the first CBD step is affected by the HYA addition, but also the growth rate in the second CBD step is strongly influenced. The film morphology after the second CBD step determines the final properties of the films. Figure 6 displays SEM micrographs of these films taken in plan view and as cross sections. All films show hexagonal poles oriented perpendicular to the support with lateral sizes in the range of 200 nm. However, they differ strongly in the degree of intergrowth, depending upon the addition time of HYA during the first CBD. Whereas the films prepared with HYA exhibit highly intergrown crystallites

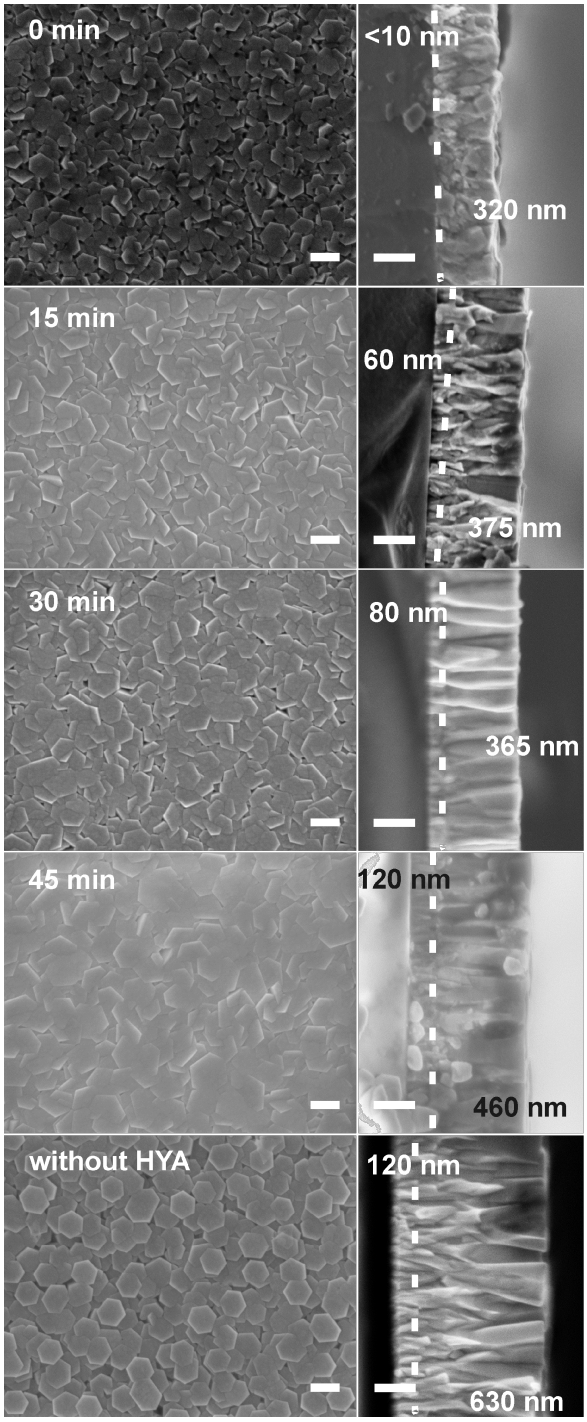


**Figure 6:** SEM micrographs in plan view (left) and corresponding cross sections (right) of ZnO films after the second CBD step. The films were prepared both without HYA and with different addition times of HYA during the first CBD step (scale bars: 200 nm). The dotted lines indicate the interface between the ZnO grown in the first and the second CBD steps. The values in nm correspond to the film thicknesses of the ZnO grown within the first (to the left of the dotted line) and the second CBD (to the right of the dotted line) steps, respectively.

(among these, the effect is weakest for the film prepared with an addition time of 30 min), the crystallites on the film prepared without HYA display a much weaker crystallite intergrowth.

The corresponding cross section SEM micrographs of the ZnO films confirm the results of the XRD analysis. The addition of HYA during the first CBD step affects the amount of ZnO deposited during the second CBD step. The maximum overall film thickness was achieved without addition of HYA, where the film grew to a thickness of approximately 750 nm. The earlier the HYA was added during the first CBD, the more the perpendicular growth was inhibited in the second CBD step. Thus, the thinnest films (approximately 320 nm) are obtained by immediate addition of HYA. The film thickness consecutively increased in a nonlinear manner from 435 nm, 460 nm to 590 nm for addition times of 15, 30 and 45 min, respectively.

The closer inspection of the cross section SEM images of the films (micrographs on the right of Figure 6) reveals further details of their morphology. A rod-like morphology can be assigned to zincite crystallites deposited during the first CBD step, whereas a more branched growth has obviously occurred during the second CBD (these two regions are separated by dotted lines in the micrographs in Figure 6). The individual film thicknesses taken from the cross section SEM micrographs are compiled in Table 1.

**Table 1:** Individual film thicknesses of ZnO films. The films were grown with different addition times of HYA during the first CBD or without HYA. The individual film thicknesses of the films grown in the first and in the subsequent CBD steps were deduced from cross section SEM micrographs.

| | Film thickness in nm (±10 nm) | |
|---|---|---|
| Time of HYA addition (first CBD) | After first CBD | After second CBD |
| 0 min | <10 | 320 |
| 15 min | 60 | 375 |
| 30 min | 80 | 365 |
| 45 min | 120 | 460 |
| no addition | 120 | 630 |

Obviously, the thickness of the films grown during the first CBD step varies strongly with the addition time of HYA: The later the HYA is added, the thicker the film grows during this step. The thickness increased from <10 nm for films prepared with immediate HYA addition to 120 nm when HYA was added after 45 min. Notably, the film grown without HYA also displays a thickness of 120 nm, corroborating the finding that the growth of the ZnO film has already ceased at this point in time. We conclude that the addition of HYA during the first growth step strongly suppresses the growth of ZnO perpendicular to the support.

The thickness of the films grown during the second CBD step on the layers formed in the first CBD also follow a particular trend, that is, the films deposited during the first CBD step influence the thickness of the films grown during the second CBD step. The earlier the HYA is added during the first CBD step, the thinner the films obtained after the second CBD grow. The ZnO film thicknesses increased from 320 nm (for films which were prepared with immediate addition of HYA during the first CBD) to 460 nm (when the addition took place only after 45 min). The film grown on the substrate prepared during the first CBD without HYA displays the largest thickness of about 630 nm. This also demonstrates that the films obtained in the first CBD strongly influence the further ZnO deposition.

The transmittance of the films is not influenced by the addition of HYA. For films prepared with and without HYA addition, average transmittances of approximately 80% were observed in the visible range.

Combining the results from XRD and FE-SEM investigations to form a cohesive theory, we propose the following mechanism for the film formation, as illustrated in Figure 7. First, the seeds deposited during the first step support the growth of ZnO. On such seeds, an array of highly vertically aligned ZnO nanorods grows under CBD conditions as previously reported [15,17,43,44]. Notably, these nanorods do not overlap. Thus, although the thickness of such a nanorod array is quite large (120 nm), the actual mass deposited (as inferred from the intensity of the XRD signal) is rather small. During the subsequent CBD process following the protocol of Baxter and Schmutten-

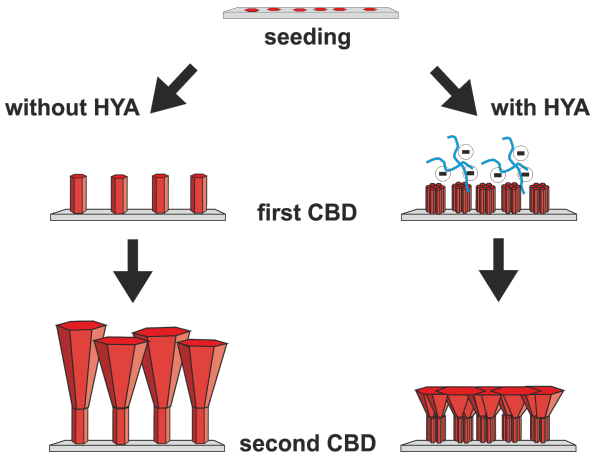


**Figure 7:** Scheme of the proposed mechanism for the three-step ZnO film deposition process described in this work.

maer [48], the $Zn^{2+}$ ion concentration is drastically increased. In addition to ongoing axial growth, lateral growth of the ZnO nanorods is also supported. Thus, they grow together and form a dense layer on top of the deposited film. Compared to the films reported by Baxter and Schmuttenmaer, our films prepared in the presence of HYA appear more dense and regular at the surface. When HYA is added during the first CBD step, vertical growth is hindered. This effect is more noticeable when HYA is immediately added and such a film has a thickness of less than 10 nm. When HYA was added at 15 or 30 min after the start of the CBD step, the film thickness increased to 60 or 80 nm, respectively. However, according to the XRD intensity, much more ZnO is deposited in these cases. This can be explained by an enhanced lateral growth of the nanorod bundles onto the support during the first CBD step, as revealed by the SEM images in Figure 4. The earlier the HYA is added during this step, the more the individual nanorods overlap. These differences in the films then lead to different growth characteristics in the subsequent CBD process. In general, the films become thinner and are more strongly intergrown after the final CBD when HYA was present in the first CBD. We surmise that due to the enhanced lateral deposition of ZnO in the first CBD step, more supporting surface area for further ZnO growth during the final CDB is available. This surface area is finely structured as it is based on bundles of thin zincite crystallites; each of the latter could possibly serve as nucleation centers for crystal deposition during the subsequent CBD steps. Thus, the bundled ZnO rods, which have preferably grown laterally during the first CBD step, allow the formation of a more dense ZnO layer during the final CBD. Consequently, as the total material supply is limited, axial growth is diminished, that is, the films become thinner.

## Electrical properties of the films

ZnO is a semiconductor with a direct bandgap of 3.37 eV [19]. At room temperature and without light illumination, ZnO provides only very few charge carriers in the conduction band leading to a moderate electrical conductivity [49]. The conductivity of ZnO dramatically increases when it is exposed to a light source.

Improved conductivity can also be achieved via doping of ZnO [50-52], which is not a topic covered in this work. Here, we use electrical conductivity data as an additional means to judge the quality of the films. In order to obtain reproducible and meaningful results, and to be able to compare the quality of our films, the electrical properties were determined under UV irradiation corresponding to the bandgap energy (370 nm). The values of the sheet resistance as well as the specific resistance of completely processed ZnO films after the second CBD are listed in Table 2. The sheet resistance of our films was above 1 kΩ/sq and the sheet resistance of the samples which were only seeded was larger than 100 MΩ/sq.

**Table 2:** Electrical properties of ZnO films: comparison of the specific resistance and sheet resistance of ZnO films after the second CBD step. The films were grown with different addition times of HYA during the first CBD step and without HYA. The films were exposed to UV irradiation during the measurement.

| Time of HYA addition [min] | Specific resistance [Ω·cm] | Sheet resistance [kΩ/sq] |
|---|---|---|
| 0 | 0.09 | 3.1 ± 0.7 |
| 15 | 0.08 | 1.9 ± 0.5 |
| 30 | 0.29 | 6.4 ± 0.7 |
| 45 | 0.17 | 2.7 ± 0.4 |
| no addition | 0.86 | 11.5 ± 0.7 |

The film prepared without addition of HYA yielded a sheet resistance of 11.5 kΩ/sq, or normalized to its thickness of ≈750 nm, a specific resistance of 0.86 Ω·cm results. All films prepared with HYA showed lower sheet resistances than the unmodified film, regardless of the time when HYA was added. The lowest sheet resistances with values of 1.9 and 2.7 kΩ/sq were obtained for fully processed films when HYA was added after 15 or 45 min during the first CBD step. The films prepared with an early addition of HYA are much thinner, as was previously explained in detail. Consequently, the films grown with immediate HYA addition or with HYA addition after 15 min displayed small specific resistances of 0.09 and 0.08 Ω·cm. For comparable films (e.g, undoped ZnO films prepared via CBD methods), specific resistances of 0.25 Ω·cm [48] and 0.648 Ω·cm [53] have been reported for as-grown and annealed films, respectively. We therefore claim that the use of the biological additive hyaluronic acid can improve the electrical conductivity and the general quality of zinc oxide films grown with CBD processes.

# Conclusion

This study describes a three-step deposition process of ZnO films from solution at low temperature. The process consists of a seeding step and two subsequent CBD steps. During the first CBD step, hyaluronic acid (a natural polysaccharide) is added. The time of the addition strongly influences the morphology of the deposited ZnO. The ZnO structure can be tailored from individual rods to finer structures consisting of bundles of rods [42]. The HYA suppresses the ZnO growth perpendicular to the support but enhances the lateral deposition of ZnO. In general, the earlier the HYA is added during the first CBD step, the finer the crystallites appear and the denser and thinner the films grow. The films grown under the influence of HYA during the first CBD step were used as supports for the third step – an ad-

ditional CBD process where the films were "sealed". The film thickness and the degree of intergrowth after this CBD step strongly depend on the morphology of the support obtained after the first CBD step. In general, films which are denser and more finely structured after the first CBD lead to thinner and more strongly intergrown layers in the final CBD. Both findings can be linked to the availability of more nucleation sites on the finer-structured and denser support.

The fully processed ZnO films deposited under the influence of HYA show significantly lower film sheet resistance and specific resistance as compared with ZnO films prepared without additives. These lower specific resistances are most probably a result of enhanced crystal domain intergrowth caused by mediation of the deposition by hyaluronic acid. The introduction of this naturally occurring polysaccharide thus enhances the quality of chemical bath-deposited zinc oxide films. This opens up further possibilities for the use of natural polymers such as polysaccharides for the preparation of technologically relevant materials and devices. In bio-inspired synthetic approaches, such polymers can act in a similar way as in biomineralization processes, influencing the growth and controlling the morphology and arrangement of the resulting crystallites.

# Experimental

## Synthesis

All experiments were performed with micropore-filtered water (Clear UV, SG Wasseraufbereitung und Regenerierungsstation GmbH, Hamburg; maximum conductivity of 0.055 µS/cm). The films were prepared on glass slides in three steps according to Figure 1.

First step: seeding. The crystal precursors were deposited on glass slides using a protocol according to Greene and co-workers [43]. For this purpose, the glass slides were immersed in a 5 mM zinc diacetate dihydrate (reagent grade, Aldrich) ethanolic solution for 10 sec, then cleaned with ethanol. This procedure was repeated five times. Afterwards the films were annealed at 350 °C for 20 min. The whole procedure was repeated once [43].

Second step: first CBD. The deposition of ZnO on the seeded glass slides was performed in 100 mL screw cap bottles containing 0.75 g zinc dinitrate hexahydrate (purum, Aldrich) and 0.35 g hexamethylentetramine (HMTA, puriss, Aldrich) dissolved in 75 mL water. The mixture was vigorously stirred until a nearly clear solution was obtained. The seeded glass slides were immersed into this solution and fixed in a vertical position by using a holding device machined from Teflon. This corresponds to the start of the time measurement. The reaction was initiated by rapid heating to 90 °C while gently stirring. 83 mg of hyaluronic acid (HYA, sodium salt from *Streptococcus equi*, MW ≈1600 kDa, Aldrich) was dissolved in 25 mL of water under vigorous stirring and added to the solution described above after a certain time (0, 15, 30 or 45 min). The amount of HYA added corresponds to a molar ratio of (1/12):1 with regard to the repeating unit of HYA ($M$ = 0.4013 kg/mol) and the Zn(II) ion concentration. The combined solutions were kept at 90 °C for one hour in total. Afterwards, the glass slides were taken out of the screw cap bottle, rinsed with water, carefully washed with ethanol in an ultrasonic bath, and dried at 60 °C.

Third step: second CBD. The second CBD step was performed according to the reaction conditions reported by Baxter and Schmuttenmaer [48]. 2.97 g of zinc dinitrate hexahydrate (purum, Aldrich) and 1.405 g hexamethylentetramine (HMTA, puriss, Aldrich) were dissolved in 100 mL of water under vigorous stirring in a screw cap bottle until an almost clear solution was obtained. The glass slides treated according to step 1 and 2 were dipped into this solution and vertically arranged by a Teflon holder. The reaction was initiated by heating the screw cap bottle rapidly to 85 °C under gentle stirring. After one hour, the glass slides were removed from the screw cap bottle, rinsed with water, carefully washed with ethanol in an ultrasonic bath, and dried at 60 °C.

## Characterization

X-ray diffraction patterns were recorded on a STOE (Darmstadt, Germany) Theta-Theta diffractometer in reflection geometry using monochromatic, Cu Kα radiation. SEM micrographs were taken on a JEOL (Tokyo, Japan) 6700F FE-SEM operating at an acceleration voltage of 2 kV and a working distance of 3 mm. For electron microscopy analysis, the glass slides with ZnO were properly cut and fixed with silver paste (Plano GmbH, Wetzlar, Germany) onto a copper block. The average film thicknesses were determined with ImageJ 1.43 software based on cross section FE-SEM micrographs by measurement of at least four different locations. UV–vis transmission measurements were performed on a Cary 5E spectrometer (Varian Inc., Palo Alto, USA) in order to determine the optical transparency of the ZnO films. To ensure that only the transmittance of the ZnO films was measured, the spectrum of a cleaned glass slide was used for a background correction. The contact angle measurement of the ZnO films was carried out using a Surftens apparatus (OEG GmbH, Frankfurt, Germany). The electrical conductivity measurements were performed with a 2100 Multimeter (Keithley Instruments Inc., Cleveland, USA). For the conductivity measurement, the films were contacted by 2 parallel lines of silver paste (Plano GmbH, Wetzlar, Germany) of 1 cm in length and with 1 cm distance between them. The sheet resistance of the fully processed films was

recorded under UV irradiation (370 nm, 8 W power). The specific resistance values were calculated as a product of the sheet resistance with the thickness of the corresponding film.

## Acknowledgements

We gratefully acknowledge the financial support from the BMBF, which funds the Carbofilm project within the Inno.CNT initiative. We also thank our partners for the excellent collaboration within this project. Help in the laboratory from Robert Zahn, Jan Hartwig, David Käter, Kim Dana Kreisköther and Niklas Burblies is gratefully acknowledged, as is the support from Werner Hoheisel for the UV–vis analysis.

## References

1. Wang, X.; Song, J.; Liu, J.; Wang, Z. L. *Science* **2007,** *316,* 102–105. doi:10.1126/science.1139366
2. Gao, P. X.; Song, J.; Liu, J.; Wang, Z. L. *Adv. Mater.* **2007,** *19,* 67–72. doi:10.1002/adma.200601162
3. Gordon, R. G. *Mater. Res. Bull.* **2000,** *25,* 52–57. doi:10.1557/mrs2000.151
4. Lu, F.; Cai, W.; Zhang, Y. *Adv. Funct. Mater.* **2008,** *18,* 1047–1056. doi:10.1002/adfm.200700973
5. Wan, Q.; Wang, T. H.; Zhao, J. C. *Appl. Phys. Lett.* **2005,** *87,* 083105. doi:10.1063/1.2034092
6. Kim, J.; Yong, K. *J. Phys. Chem. C* **2011,** *115,* 7218–7224. doi:10.1021/jp110129f
7. Huang, J.; Wu, Y.; Gu, C.; Zhai, M.; Sun, Y.; Liu, J. *Sens. Actuators, B* **2011,** *115,* 126–133. doi:10.1016/j.snb.2010.11.036
8. Qiu, Y.; Yang, S. *Adv. Funct. Mater.* **2007,** *17,* 1345–1352. doi:10.1002/adfm.200601128
9. Minami, T. *Thin Solid Films* **2008,** *516,* 5822–5828. doi:10.1016/j.tsf.2007.10.063
10. Minima, T. *Thin Solid Films* **2008,** *516,* 1314–1321. doi:10.1016/j.tsf.2007.03.082
11. Sun, X. W.; Kwok, H. S. *J. Appl. Phys.* **1999,** *86,* 408–411. doi:10.1063/1.370744
12. Deng, H.; Russell, J. J.; Lamb, R. N.; Jiang, B.; Li, Y.; Zhou, X. Y. *Thin Solid Films* **2004,** *458,* 43–46. doi:10.1016/j.tsf.2003.11.288
13. Barnes, T. M.; Leaf, J.; Fry, C.; Wolden, C. A. *J. Cryst. Growth* **2005,** *274,* 412–417. doi:10.1016/j.jcrysgro.2004.10.015
14. Lee, J.-H.; Park, B.-O. *Thin Solid Films* **2003,** *426,* 94–99. doi:10.1016/S0040-6090(03)00014-2
15. Lee, G. J.; Min, S.-K.; Oh, C.-H.; Lee, Y.; Lim, H.; Cheong, H.; Nam, H. J.; Hwangbi, C. K.; Min, S.-K.; Han, S.-H. *J. Nanosci. Nanotechnol.* **2011,** *11,* 511–517. doi:10.1166/jnn.2011.3260
16. Govender, K.; Boyle, D. S.; Kenway, P. B.; O'Brien, P. *J. Mater. Chem.* **2004,** *14,* 2575–2591. doi:10.1039/b404784b
17. Yi, S.-H.; Choi, S.-K.; Jang, J.-M.; Kim, J.-A.; Jung, W.-G. *J. Colloid Interface Sci.* **2007,** *313,* 705–710. doi:10.1016/j.jcis.2007.05.006
18. O'Brien, P.; Saeed, T.; Knowles, J. *J. Mater. Chem.* **1996,** *6,* 1135–1139. doi:10.1039/jm9960601135
19. Huang, M. H.; Mao, S.; Feick, H.; Yan, H.; Wu, Y.; Kind, H.; Weber, E.; Russo, R.; Yang, P. *Science* **2001,** *292,* 1897–1899. doi:10.1126/science.1060367
20. Janotti, A.; van de Walle, C. G. *Rep. Prog. Phys.* **2009,** *72,* 126501. doi:10.1088/0034-4885/72/12/126501
21. Chandramohan, R.; Thirumalai, J.; Vijayan, T. A.; Valanarasu, S.; Vizhian, S. E.; Srikanth, M.; Swaminathan, V. *Adv. Sci. Lett.* **2010,** *3,* 319–322. doi:10.1166/asl.2010.1129
22. Barka-Bouaifel, F.; Sieber, B.; Bezzi, N.; Benner, J.; Roussel, P.; Boussekey, L.; Szunerits, S.; Boukherroub, R. *J. Mater. Chem.* **2011,** *21,* 10982–10989. doi:10.1039/c1jm11351h
23. Rakhshani, A. E. *J. Phys. D: Appl. Phys.* **2008,** *41,* 015305. doi:10.1088/0022-3727/41/1/015305
24. Izaki, M.; Katayama, J. *J. Electrochem. Soc.* **2000,** *147,* 210–213. doi:10.1149/1.1393176
25. Hsu, C. H.; Chen, W. S.; Lai, C. H.; Yan, S. F. *Adv. Mater. Res. (Durnten-Zurich, Switz.)* **2011,** *194–196,* 2254–2258. doi:10.4028/www.scientific.net/AMR.194-196.2254
26. Lang, J.; Han, Q.; Li, C.; Yang, J.; Li, X.; Yang, L.; Wang, D.; Zhai, H.; Gao, M.; Zhang, Y.; Liu, X.; Wei, M. *Appl. Surf. Sci.* **2010,** *256,* 3365–3368. doi:10.1016/j.apsusc.2009.12.035
27. Hsu, C.-H.; Chen, D.-H. *Nanotechnology* **2010,** *21,* 285603. doi:10.1088/0957-4484/21/28/285603
28. Shishiyanu, A. T.; Lupan, O. I.; Monaico, E. V.; Ursaki, V. V.; Shishiyanu, T. S.; Tiginyanu, I. M. *Thin Solid Films* **2005,** *488,* 15–19. doi:10.1016/j.tsf.2005.04.004
29. Chen, J. T.; Wang, J.; Zhuo, R. F.; Yan, D.; Feng, J. J.; Zhang, F.; Yan, P. X. *Appl. Surf. Sci.* **2009,** *255,* 3959–3964. doi:10.1016/j.apsusc.2008.10.086
30. McPeak, K. M.; Le, T. P.; Britton, N. G.; Nickolov, Z. S.; Elabd, Y. A.; Baxter, J. B. *Langmuir* **2011,** *27,* 3672–3677. doi:10.1021/la105147u
31. Tian, Z. R.; Voigt, J. A.; Liu, J.; McKenzie, B.; McDermott, M. J.; Rodriguez, M. A.; Konishi, H.; Xu, H. *Nat. Mater.* **2003,** *2,* 821–826. doi:10.1038/nmat1014
32. Wagata, H.; Ohashi, N.; Taniguchi, T.; Katsumata, K.-i.; Okada, K.; Matsushita, N. *Cryst. Growth Des.* **2010,** *10,* 4968–4975. doi:10.1021/cg1010693
33. Wu, Q.; Chen, X.; Zhang, P.; Han, Y.; Chen, X.; Yan, Y.; Li, S. *Cryst. Growth Des.* **2008,** *8,* 3010–3018. doi:10.1021/cg800126r
34. Wei, S. F.; Lian, J. S.; Jiang, Q. *Appl. Surf. Sci.* **2009,** *255,* 6978–6984. doi:10.1016/j.apsusc.2009.03.023
35. Hoffmann, R. C.; Jia, S.; Jeurgens, L. P. H.; Bill, J.; Aldinger, F. *Mat. Sci. Eng. C* **2006,** *26,* 41–45. doi:10.1016/j.msec.2005.05.001
36. Liang, J.; Bai, S.; Zhang, Y.; Li, M.; Yu, W.; Qian, Y. *J. Phys. Chem. C* **2007,** *111,* 1113–1118. doi:10.1021/jp0662808
37. Raula, M.; Rashid, M. H.; Paira, T. K.; Dinda, E.; Mandal, T. K. *Langmuir* **2010,** *26,* 8769–8782. doi:10.1021/la904507q
38. Zhang, T.; Dong, W.; Keeter-Brewer, M.; Konar, S.; Njabon, R. N.; Tian, Z. R. *J. Am. Chem. Soc.* **2006,** *128,* 10960–10968. doi:10.1021/ja0631596
39. Cong, H.-P.; Yu, S.-H. *Adv. Funct. Mater.* **2007,** *17,* 1814–1820. doi:10.1002/adfm.200601082
40. Taubert, A.; Palms, D.; Weiss, Ö.; Piccini, M.-T.; Batchelder, D. N. *Chem. Mater.* **2002,** *14,* 2594–2601. doi:10.1021/cm011670m
41. Gerstel, P.; Hoffmann, R. C.; Lipowsky, P.; Jeurgens, L. P. H.; Bill, J.; Aldinger, F. *Chem. Mater.* **2006,** *18,* 179–186. doi:10.1021/cm051542o
42. Waltz, F.; Wißmann, G.; Lippke, J.; Schneider, A. M.; Schwarz, H.-C.; Feldhoff, A.; Eiden, S.; Behrens, P. *Cryst. Growth Des.* **2012,** *12,* 3066–3075. doi:10.1021/cg3002674
43. Greene, L. E.; Law, M.; Tan, D. H.; Montano, M.; Goldberger, J.; Somorjai, G.; Yang, P. *Nano Lett.* **2005,** *5,* 1231–1236. doi:10.1021/nl050788p

44. Chu, D.; Hamada, T.; Kato, K.; Masuda, Y. *Phys. Status Solidi A* **2009,** *206,* 718–723. doi:10.1002/pssa.200824495
45. JCPDS (Joined Committee on Powder Diffraction Standards)-ICPP (International Center for Diffraction Data) **1997,** Card No. 36-1451.
46. Wang, A.-J.; Liao, Q.-C.; Feng, J.-J.; Zhang, P.-P.; Li, A.-Q.; Wang, J.-J. *CrystEngComm* **2012,** *14,* 256–263. doi:10.1039/c1ce05830d
47. Mumalo-Djokic, D.; Stern, W. B.; Taubert, A. *Cryst. Growth Des.* **2008,** *8,* 330–335. doi:10.1021/cg0701372
48. Baxter, J. B.; Schmuttenmaer, C. A. *J. Phys. Chem. B* **2006,** *110,* 25229–25239. doi:10.1021/jp064399a
49. Wang, Y.; Liao, Z.; She, G.; Mu, L.; Chen, D.; Shi, W. *Appl. Phys. Lett.* **2011,** *98,* 203108. doi:10.1063/1.3590926
50. Minami, T.; Yamamoto, T.; Miyata, T. *Thin Solid Films* **2000,** *366,* 63–68. doi:10.1016/S0040-6090(00)00731-8
51. Agura, H.; Suzuki, A.; Matsushita, T.; Aoki, T.; Okuda, M. *Thin Solid Films* **2003,** *445,* 263–267. doi:10.1016/S0040-6090(03)01158-1
52. Cao, H. T.; Pei, Z. L.; Gong, J.; Sun, C.; Huang, R. F.; Wen, L. S. *Surf. Coat. Technol.* **2004,** *184,* 84–92. doi:10.1016/j.surfcoat.2003.09.046
53. Khallaf, H.; Chai, G.; Lupan, O.; Heinrich, H.; Park, S.; Schulte, A.; Chow, L. *J. Phys. D: Appl. Phys.* **2009,** *42,* 135304. doi:10.1088/0022-3727/42/13/135304

## License and Terms

BEILSTEIN JOURNAL OF NANOTECHNOLOGY

# Peptide-equipped tobacco mosaic virus templates for selective and controllable biomineral deposition

Klara Altintoprak[1], Axel Seidenstücker[2], Alexander Welle[3,4], Sabine Eiben[1], Petia Atanasova[5], Nina Stitz[5], Alfred Plettl[2], Joachim Bill[5], Hartmut Gliemann[4], Holger Jeske[1], Dirk Rothenstein[5], Fania Geiger[1] and Christina Wege*[1]

Full Research Paper

Open Access

Address:
[1]Department of Molecular Biology and Plant Virology, Institute of Biomaterials and Biomolecular Systems, University of Stuttgart, Pfaffenwaldring 57, 70569 Stuttgart, Germany, [2]Institute of Solid State Physics, University of Ulm, Albert-Einstein-Allee 11, 89081 Ulm, Germany, [3]Karlsruhe Nano Micro Facility (KNMF), Karlsruhe Institute of Technology, Hermann-von-Helmholtz-Platz 1, 76344 Eggenstein-Leopoldshafen, Germany, [4]Institute of Functional Interfaces (IFG), Karlsruhe Institute of Technology, Hermann-von-Helmholtz-Platz 1, 76344 Eggenstein-Leopoldshafen, Germany and [5]Institute for Materials Science, University of Stuttgart, Heisenbergstraße 3, 70569 Stuttgart, Germany

Email:
Christina Wege* - christina.wege@bio.uni-stuttgart.de

* Corresponding author

Keywords:
biomineralization; charge-relay system; peptide; silica; tobacco mosaic virus (TMV)

*Beilstein J. Nanotechnol.* **2015,** *6,* 1399–1412.
doi:10.3762/bjnano.6.145

Received: 24 March 2015
Accepted: 29 May 2015
Published: 25 June 2015

This article is part of the Thematic Series "Towards multifunctional inorganic materials: biopolymeric templates".

Associate Editor: K. Koch



## Abstract

The coating of regular-shaped, readily available nanorod biotemplates with inorganic compounds has attracted increasing interest during recent years. The goal is an effective, bioinspired fabrication of fiber-reinforced composites and robust, miniaturized technical devices. Major challenges in the synthesis of applicable mineralized nanorods lie in selectivity and adjustability of the inorganic material deposited on the biological, rod-shaped backbones, with respect to thickness and surface profile of the resulting coating, as well as the avoidance of aggregation into extended superstructures. Nanotubular tobacco mosaic virus (TMV) templates have proved particularly suitable towards this goal: Their multivalent protein coating can be modified by high-surface-density conjugation of peptides, inducing and governing silica deposition from precursor solutions in vitro. In this study, TMV has been equipped with mineralization-directing peptides designed to yield silica coatings in a reliable and predictable manner via precipitation from tetraethoxysilane (TEOS) precursors. Three peptide groups were compared regarding their influence on silica polymerization: (i) two peptide variants with alternating basic and acidic residues, i.e. lysine–aspartic acid $(KD)_x$ motifs expected to act as charge-relay systems promoting TEOS hydrolysis and silica polymerization; (ii) a tetrahistidine-exposing polypeptide ($CA_4H_4$) known to induce silicification due to the positive charge of its clustered imidazole side chains; and (iii) two peptides with high ZnO binding affinity. Differential effects on the mineralization of the TMV surface were demonstrated, where a $(KD)_x$ charge-relay

peptide (designed in this study) led to the most reproducible and selective silica deposition. A homogenous coating of the biotemplate and tight control of shell thickness were achieved.

## Introduction

Amorphous silica ($SiO_2$) precipitated from silicate precursor sols comprises a wide range of versatile materials applied in various technological approaches, for example, as a structural modifier or filler in rubber [1], food [2,3] or healthcare products [4], bioceramics for medical purposes [5], mesoporous nanoparticulate or tubular drug delivery systems as reviewed in [6], sensor surfaces [7], or biocatalytic formulations as reviewed in [8]. An important focus of research and industry lies on the development of nanoscale materials, enabling the further miniaturization of devices and effector units, in addition to a reduced consumption of resources. In the field of functional mineral synthesis, significant progress has been made in using nanodimensional biological templates, allowing specific coating with inorganic materials to yield hybrid particles of predetermined structure and composition [9-11]. The surfaces of optimal templates nucleate and direct the formation of inorganic materials from suitable precursors, resembling a natural matrix-mediated mineral deposition in living organisms known also as "biologically controlled mineralization" [12,13]. Such bio-inspired mineralization approaches can accomplish precise coating processes and offer several benefits such as environmentally friendly fabrication routes and reaction parameters compatible with biological structures, namely low synthesis temperature and aqueous deposition media. In this context, tube- or rod-like templates of high aspect ratio are of particular interest, since they enable the fabrication of elongated nanostructures, which are otherwise difficult to obtain. This is because chemical synthesis or technical approaches applied at mild conditions commonly generate spherical structures [14]. Mineral nanofibers of predetermined size are of major importance for the preparation of functional films and extended 3D materials. Hence, anisotropic scaffolds such as high molecular weight polymers [15], carbon nanotubes [16], peptide nanotubes [17], certain plant viruses [18-21], filamentous bacteriophages [22,23], and bacterial flagellae [24] have been evaluated for their applicability on a technical scale. To achieve control over mineral precipitation, the modification of the template by chemical conjugation of peptides [16], poly(ethylene glycol) (PEG) [22], aniline [25,26], or succinamate [27] has been reported.

Virus-based templates have gained especially important roles in the synthesis of organic–inorganic hybrid nanostructures. They combine several advantages, namely high availability, robustness and an exact replication of the particle shape and dimension, which are genetically determined and result in a narrow size distribution. Different species such as the fibrous bacteriophage M13, icosahedral cowpea mosaic virus (CPMV), or tubular tobacco mosaic virus (TMV) were used as templates for coating with inorganic materials including Pt, Au [28], Ag [29,30], Pd [31,32], $TiO_2$ [33], $SiO_2$ [34], NiO [35], CdS [21], CoPt, FePt, ZnS [27,36] and ZnO [37-39]. Among the virus-based templates, plant viruses are especially suitable nanostructured scaffolds because of their biological safety for humans, animals, and their commensal bacteria. TMV is a widespread plant-infecting pathogen, which can be isolated in large amounts from susceptible plants [40]. TMV particles are highly ordered, supramolecular complexes, consisting of a single-stranded helical RNA and ≈2130 identical coat protein (CP) subunits arranged around the RNA molecule, which is completely buried inside the protein shell [41-46]. The viral particle has an average length of 300 nm and an outer and inner (channel) diameter of 18 nm and 4 nm, respectively. TMV has become a powerful building block in bionanotechnology due to its tube-like structure, high stability under a wide range of different conditions (e.g., pH, temperature, solvent), low production costs and multivalent CP surface [18,47,48].

The CP subunits of TMV can be genetically or chemically modified for the presentation of effector molecules [35,49-52]. Modified TMV templates maintain their 3D structure along with preserved particle stability, which is a prerequisite for the subsequent mineralization of inorganic materials. Furthermore, the length and also the overall shape of TMV-derived particles can be altered by means of engineered, non-natural RNA molecules, supporting the assembly of artificial, non-infectious, TMV-like nucleoprotein tube systems. This technology was even refined to allow the production of kinked boomerang, branched tetrapod and multiarmed nanostar structures [53,54], or into particles fashioned evenly with mixtures of two or more functional groups at predefined ratios [51].

To vary and control the deposition of inorganic minerals on TMV templates, extensive modifications of the surface amino acids are desirable. They enable defined alterations of the outer TMV–CP surface charge and the introduction of specific amino acid motifs, guiding the nucleation and growth of mineral coatings around the TMV core. This is in analogy to natural biomineralization-directing protein domains identified for various organisms [55-59]. Direct genetic modification of the TMV–CP sequence is, however, limited in view of the extent of alteration tolerated by virus particles upon their multiplication in plants,

regarding number and composition of exchanged or inserted amino acids. In addition, high-throughput screening of different surface-expressed peptides is restricted upon TMV "farming" due to the required 10–14 days for TMV mutant accumulation. Bacterially expressed CP can be engineered to a much higher extent and integrated into TMV-like particles reconstituted in vitro in substantial amounts [51]. However, purification of such protein types from the bacteria cultures is much less efficient compared to CP isolation from intact TMV particles from leaf tissues.

Therefore, we have followed a third strategy and made use of plant-enriched, moderately engineered TMV templates, exposing selectively addressable reactive surface groups. These were subjected to chemical conjugation of synthetic peptides meant to regulate subsequent coating with silica (workflow indicated in Figure 1). This procedure is insensitive to both size and sequence of the peptide of choice, and the generation of various types of decorated TMV rods is fast. The amino acid sequences employed had been previously delimited by phage display to affect mineralization in our work [60] or by other researchers [17], or were predicted to influence silica deposition based on the literature [61]. Control experiments were carried out in parallel with bare TMV equally treated, in order to assess its capacity for silica nucleation in the absence of additional peptide domains.

Generally, it still remains a challenge to predictably, selectively and uniformly coat individual nanotemplate particles with silica. For this purpose, sol–gel condensation from precursors in alcoholic solutions seems most viable according to the conditions established by Stöber et al. [62] for the fabrication of plain silica spheres. Reaction parameters such as time, temperature, pH, solvent composition and precursor, as well as catalyst concentration, affect the thickness of the mineral coating, in interdependence with the chemistry and charge distribution of the surface of the core [22,26,27,63,64]. During the mineralization process, great effort is needed to avoid non-templated byproducts, as well as aggregation, re-organization and precipitation of the templates into extended superstructures of amorphous silica-template composites.

Several earlier studies have demonstrated that native TMV capsids are effective biological nucleation cores for the deposition of mineral layers from silicate sols on their surfaces. This is typically carried out via hydrolysis and condensation of tetraethoxysilane (also known as tetraethylorthosilicate, TEOS) in alcohol-containing media (see Figure 1 for the mechanistic scheme). Obviously, the viral coating (which exhibits patches of both positively and negatively charged amino acids in nanometric vicinity to each other) is prone to silica deposition by itself. Concomitant with silicification reactions, however, TMV particles presented extensive rearrangement into head-to-tail

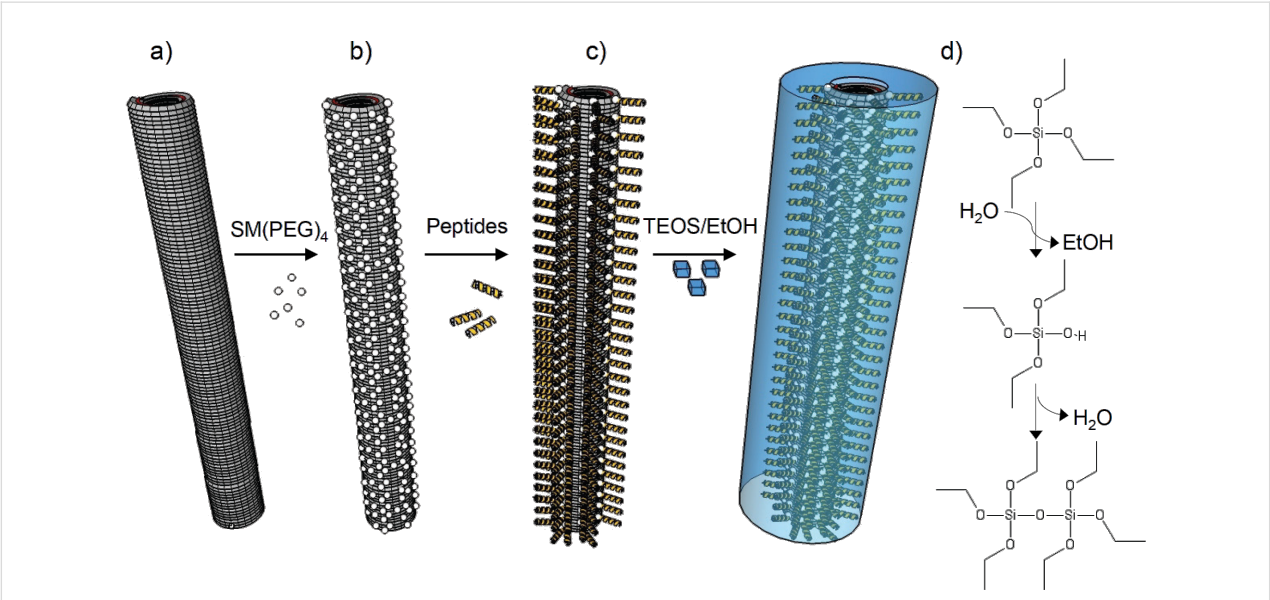


**Figure 1:** Schematic representation of the chemical modification and mineralization of tobacco mosaic virus (TMV) nucleoprotein nanotubes. (a) Genetically engineered virus particles with thousands of surface-exposed amino groups of lysine residues ($TMV_{Lys}$) served as biotemplates for chemical conjugation reactions. (b) Hetero-bifunctional linker molecules (succinimidyl-(*N*-maleimidopropionamido) ester, $SM(PEG)_4$) were coupled to $TMV_{Lys}$ via *N*-hydroxysuccinimide (NHS) ester-mediated crosslinking with lysine primary amines, yielding amide bonds. (c) Mineralization-affecting peptides were conjugated to the maleimide-activated $SM(PEG)_4$ linker portion via the sulfhydryl groups of their terminal cysteine residues, yielding stable thioether linkages. The resulting functionalized TMV templates fashioned with a dense peptide coating were (d) subjected to silica mineralization via hydrolysis and condensation of a tetraethoxysilane (TEOS) precursor in solution (mechanism indicated).

structures [34,65]. These were laterally aligned or even star-shaped [64] 3D arrays in many of the studies, reflecting and expanding the well-known capacities of these bio-nanorods to form various aggregates up to liquid–crystalline phases. In contrast, protocols resulting in nanoparticulate TMV–silica composites devoid of inorganic background granules and, moreover, with closed shells of well-adjustable thickness, are a matter of intense investigation. Such methods would enable the manufacture of novel TMV derivatives, further expanding their application potential to miniaturized arrays and devices [66-68] and "smart" functional materials [31,69] for numerous purposes. TMV–inorganic hybrids will likely yield rigid and durable [70] technical components, which are also compatible with biological molecules and activities [71].

To fabricate thick, continuous silica coatings (e.g., on immobilized TMV rods), polyaniline interlayers were employed to shield both charges and hydrophobic patches of the viral protein coating before subjecting it to TEOS-mediated mineralization [26]. A more refined and tighter control of the silica mineralization can be achieved by ordered, repetitive arrangements of differently charged protein domains and specific functional groups therein. This was demonstrated in vitro by help of various mineralization-inducing peptides [55,56,61,72]. Positively charged amino acid residues (Lys, Arg) in such peptides electrostatically interact with siloxane groups, while Ser, His and Asp may undergo hydrogen bonding or polar interactions with solute or nanosized colloidal mineral precursors [7,60,63,72-74]. Additionally, negatively charged amino acids that are present are supposed to have an enhancing effect on TEOS hydrolysis. This is especially true if they are closely adjacent to positive charges, where such combinations may act as charge-relay systems [61,75]. Effective peptides may resemble motifs found in natural silica biomineralization-directing proteins (in both their amino acid composition and sequence [58]), but may also comprise randomly assembled sequences resulting from mere in vitro library screening.

Since a growing body of experience with relatively diverse silicification-guiding peptides is available, we decided to install a number of distinct amino acid sequence types on structure-directing TMV nanorods. This allows for the systematic investigation of their influence on silica coating reactions via ethanol-containing TEOS on this viral backbone for the first time.

Genetically modified TMV particles ($TMV_{Lys}$) with an accessible amino group on every CP subunit [76] were chemically equipped with a dense peptide coating via succinimidyl ester-activated, bifunctional, PEG-based linkers, and their subsequent maleimide-mediated conjugation to thiol groups of terminal cysteine residues present in every peptide. Five different peptide sequences were selected (see Table 1): (i) $(KD)_5C$ and $(KD)_{10}C$ with alternating amino and carboxyl functionalities (sequences KDKDKDKDKDC and KDKDKD-KDKDKDKDKDKDKDC, respectively) on the basis of Kuno et al. [61]; (ii) $CA_4H_4$ (sequence CAAAAHHHH) according to Yuwono and Hartgerink [17], with two stretches of different amino acid residues arranged blockwise to expose a cluster of imidazole side chains; and (iii) 44C (HSSHHQPKGTNPC) and 31C (HHGHSPTSPQVRC), two ZnO-binding peptides isolated by phage display [60]. The distinct peptide-fashioned $TMV_{Lys}$ templates were incubated in TEOS precursor solution in parallel with linker-coated and plain $TMV_{Lys}$ controls (and in some tests wildtype $TMV_{wt}$) under equal conditions. The products were analyzed and compared to determine favorable TMV template–peptide combinations for specific silica mineralization.

## Results and Discussion

### Surface functionalization of $TMV_{Lys}$ templates by conjugation of mineralization-promoting peptides

To nucleate and govern the deposition of silica shells, functionalized plant viral nanorod templates were generated by linker-assisted chemical conjugation of mineralization-active peptides

**Table 1:** Mineralization-affecting peptides installed on TMV templates to compare their influence on silica deposition from TEOS. Amino acid sequence and total number (aa) are indicated for each peptide. Molecular weight ($M_w$), isoelectric point (pI), and net charge at pH 8.0 and 5.5 were calculated with Protein Calculator v3.4 [77].

| Name | Abbreviation | Sequence | aa | $M_w$ (g/mol) | pI | Net charge at pH | |
|---|---|---|---|---|---|---|---|
| | | | | | | 8.0 | 5.5 |
| $(KD)_5C$ | KD5 | KDKDKDKDKDC | 11 | 1337.5 | 6.25 | −0.8 | 0.4 |
| $(KD)_{10}C$ | KD10 | $(KDKDKDKDKD)_2C$ | 21 | 2553.8 | 6.62 | −0.8 | 0.7 |
| $CA_4H_4$ | AH | CAAAAHHHH | 9 | 945.0 | 7.52 | −0.6 | 3.6 |
| 44C | 44C | HSSHHQPKGTNPC | 13 | 1429.5 | 8.31 | 0.3 | 3.7 |
| 31C | 31C | HHGHSPTSPQVRC | 13 | 1442.6 | 8.31 | 0.4 | 3.7 |

to the outer surface of genetically modified $TMV_{Lys}$ particles from plants. Every $CP_{Lys}$ subunit provided a primary amine group of a lysine residue at the protein's C terminus. This resulted in ≈2130 sites selectively accessible to NHS ester-mediated coupling reactions per rod [76]. These were equipped with hetero-bifunctional crosslinker molecules (succinimidyl-(*N*-maleimidopropionamido)-tetraethylene glycol ester, $SM(PEG)_4$) serving as spacers and adapters for mineralization-affecting peptides. These were installed via maleimide-mediated conjugation of the cysteine sulfhydryl groups of the peptides. The resulting five distinct types of $TMV_{Lys}$–PEG–peptide particles with their different CP derivatives are listed in Table 2, as well as the linker-fashioned and plain $TMV_{Lys}$ templates used as references. The abbreviation scheme used was the following: abbreviations underscore the relevant functionalities or amino acids exposed; therefore, $TMV_{Lys}$ is named TMV–Lys from now on. Covalent conjugation of peptides was confirmed for both single CPs and intact TMV particles by denaturing and native gel electrophoresis, respectively. Peptide modification of CPs resulted in a band shift with respect to increasing molecular weight, as compared to nonmodified CP in denaturing sodium dodecyl sulphate polyacrylamide gel electrophoresis (SDS-PAGE) (Figure 2a). The efficiency of peptide conjugation was determined by the ratio of the band intensities of modified and nonmodified CPs after Coomassie Blue staining. The binding efficiencies to individual CP subunits were ≈60% for all investigated peptides, corresponding to about 1250 peptides exposed on every 300 nm rod. The molecular weights of the differently modified CPs were in good agreement with the values calculated for the distinct conjugates (Table 2).

The intact TMV particles were analyzed by native gel electrophoresis (0.9% agarose in TBE buffer, pH 8.0; Figure 2b).

**Table 2:** Composition of TMV derivatives used in this study. Calculated and measured molecular weight ($M_w$) of modified CP species were in good agreement.

| TMV derivative | Abbreviation (TMV–) | Composition of TMV derivative | | | Calculated $M_w$ of CP conjugate (kDa) | Measured $M_w$ of CP conjugate[a] (kDa) |
|---|---|---|---|---|---|---|
| | | $TMV_{Lys}$ | $SM(PEG)_4$ | Peptide | | |
| $TMV_{Lys}$–PEG–$(KD)_5C$ | KD5 | + | + | $(KD)_5C$ | 19.5 | 19.9 |
| $TMV_{Lys}$–PEG–$(KD)_{10}C$ | KD10 | + | + | $(KD)_{10}C$ | 20.7 | 21.9 |
| $TMV_{Lys}$–PEG–$CA_4H_4$ | AH | + | + | $CA_4H_4$ | 19.1 | 20.2 |
| $TMV_{Lys}$–PEG–44C | 44C | + | + | 44C | 19.6 | 20.4 |
| $TMV_{Lys}$–PEG–31C | 31C | + | + | 31C | 19.6 | 20.9 |
| $TMV_{Lys}$–PEG | PEG | + | + | – | 18.1 | 18.2 |
| $TMV_{Lys}$ | Lys | + | − | – | 17.6 | 17.4 |

[a]Measured $M_w$ values are derived from SDS-PAGE band analyses via retardation factor values determined by ImageJ software [78] and calibration curves obtained from $M_w$ standards separated on the same gel.

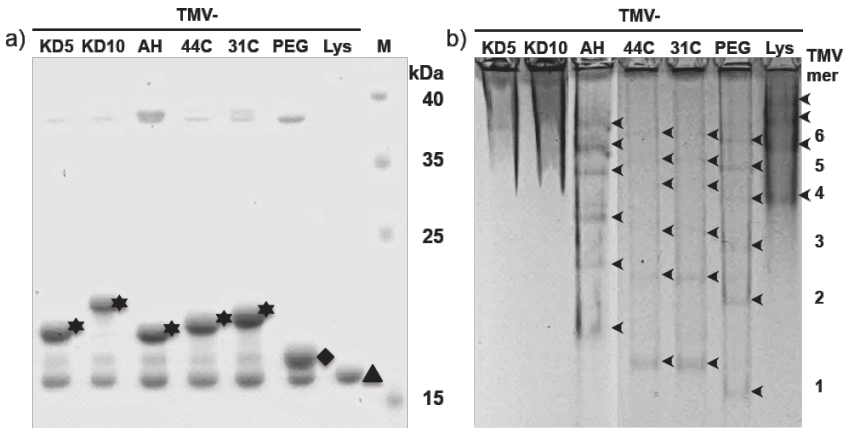


**Figure 2:** Gel electrophoretic analysis of chemically modified TMV–Lys particles. (a) SDS-PAGE shows retarded bands of CPs modified with the linker $SM(PEG)_4$ (diamond, PEG), or after coupling $SM(PEG)_4$ and different peptides (stars, peptides as indicated above), compared to unmodified $CP_{Lys}$ (triangle, Lys). (b) Peptide-equipped TMV–Lys particles exhibiting different separation patterns during native agarose gel electrophoresis, indicating various states of head-to-tail aggregation in combination with distinct negative overall charges. Moieties exposed on the TMV templates are indicated (abbreviations as in Table 2). Numbers on the right: approximate numbers of TMV particles in head-to-tail aggregates (in relation to lane "TMV–PEG").

The linker coating of the control derivative $TMV_{Lys}$–PEG (TMV–PEG) exhibited an increase in negative net charge in comparison to TMV–Lys, resulting in a higher electrophoretic mobility. This effect was reduced by the conjugation of mineralization-affecting peptides: $TMV_{Lys}$–PEG–$CA_4H_4$ (TMV–AH), $TMV_{Lys}$–PEG–44C (TMV–44C) and $TMV_{Lys}$–PEG–31C (TMV–31C) exhibited retarded bands, which indicated the linkage of the peptides to the TMV–PEG template. TMV derivatives $TMV_{Lys}$–PEG–$(KD)_5C$ (TMV–KD5) and $TMV_{Lys}$–PEG–$(KD)_{10}C$ (TMV–KD10) could not be separated under the conditions applied: both samples did not migrate into the gel phase to a sufficient extent.

## Zeta potential measurement

The zeta potentials (ZPs) of TMV–Lys nanorods and their derivatives were determined using a Malvern NanoSizer at a virus particle concentration of 0.5 mg/mL in ultrapure water ($ddH_2O$) and in 30 mM Tris-HCl buffer, pH 8.0, respectively (Figure 3). The ZPs measured in $ddH_2O$ were in general more negative (−28 mV to −78 mV) compared to those determined in buffer (−10 mV to −25 mV), owing to the lower pH of ≈5.5 of ultrapure water with $CO_2$ dissolved in equilibrium with that in the air [79]. In addition, the increased electrolyte concentrations in the buffer lead to an enrichment of counter ions in the proximity of the TMV nanorods and thus a steeper decrease of the potential within a shorter distance from their surface (decrease of the Debye length). Therefore, ZP values measured in $ddH_2O$ are closer to the electric surface (Stern) potential of the particles [80].

The ZPs of the TMV derivatives (Figure 3) were correlated with the calculated isoelectric point (pI) of the conjugated peptides (see Table 1), and in most cases with the effective particle charges affecting their relative mobility in native agarose gel electrophoresis (see Figure 2b). Peptides 44C and 31C both are predicted to exhibit moderate positive charges (of about 0.3 or 0.4, respectively) at pH 8.0, while peptides AH (−0.6), KD5 and KD10 (both −0.8) are supposed to be negative. As coating of the TMV particles with maleimide-reactive $SM(PEG)_4$ linker molecules devoid of peptides (TMV–PEG) introduced the most negative net charge (Figure 2b), all peptide-fashioned TMV derivatives had less negative ZPs compared to the linker-modified control (with about −80 mV in water and about −25 mV in buffer). While the ZP values of four products were largely in line with the calculated charges of the peptides (with TMV–44C and TMV–31C shifted to significantly less negative ZP values compared to those of TMV–KD5 and –KD10), the absolute ZP determined for TMV–AH was shifted most extensively to more positive values, due to the contribution of the uncharged alanines (Figure 3). This reflects the sheath of tetrahistidine clusters exposed by the C-termini of peptide AH. Bare TMV–Lys templates with their plain protein coating exhibited ZP values close to those of TMV–KD5.

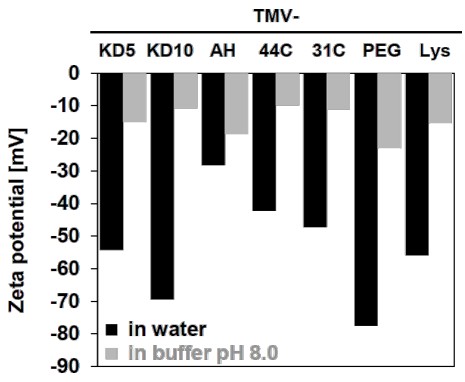


**Figure 3:** Zeta potential of bare and chemically modified TMV–Lys particles in $ddH_2O$ or 30 mM Tris-HCl pH 8.0, respectively (modifications of TMV rods indicated above).

At high concentrations, TMV–AH aggregated into bundle-like structures in water but not in buffer. Such agglomerates could be separated by ultrasound; however, re-aggregation occurred after short time. 44C- or 31C-functionalized TMV formed raft-like aggregates in both water and buffer (as detected also after their mineralization, see SEM analysis below).

For inorganic particles, the physical stability of dispersions increases with the magnitude of the ZP. That is, highly negative or highly positive ZPs typically both result in stable suspensions [81,82] due to Coulomb repulsion. The organic TMV template structures thus behaved analogously, with the agglomerating species TMV–AH, –44C, and –31C exhibiting the lowest ZP magnitudes in water. TMV–Lys with an absolute ZP value above 55 did not show aggregation at all.

## Mineralization of functionalized TMV templates

The different TMV templates were subjected to silica deposition by dispersion in a buffer-free deposition solution of ≈11% (v/v) TEOS precursor solution in ≈45% (v/v) ethanol in ultrapure water (resulting in a pH of ≈5.5) under agitation (500 rpm) at 25 °C for up to twelve days in parallel experiments (see Experimental section). These conditions were adapted with respect to the ethanol concentration from an earlier comparative study on the mineralization capacities of distinct kinds of peptides [61]. The method was established in initial tests to achieve improved control over mineralization kinetics and product characteristics with peptide-equipped TMV templates. This is in comparison to protocols used for the TEOS-mediated silicification of bare [21,34,64,65,83] or aniline-coated [26] TMV. Those protocols all employed reac-

tion mixes of either alkaline or significantly lower pH (in most cases in buffer-free solutions) in variable ethanol concentrations and in one study supplemented by (3-aminopropyl)triethoxysilane (APTES) [64].

All TMV templates with absolute ZP magnitudes above 50 mV showed a good dispersion in the mineralization solution, while TMV–AH, –44C and –31C did not form stable suspensions. At different reaction times, products were collected by centrifugation. After seven days of incubation, inorganic material sedimented from all reaction mixes, regardless of the presence or absence of TMV templates (Figure 4a). The precipitates were transparent in the presence of TMV–KD5, –PEG, and –Lys, as well as for the reference sample without template, whereas the sediments of TMV–KD10, –AH, –44C and –31C appeared milky white. In the absence of TMV, the reaction solution completely solidified, while all suspensions containing TMV templates remained liquid during the course of silica condensation (Figure 4a).

The morphology of TMV hybrid products subjected to mineralization for ten days was analyzed by transmission electron microscopy (TEM; see below, data not shown), and high resolution scanning electron microscopy (HRSEM; Figure 4b). A clear difference in the mineralization of functionalized and non-functionalized TMV templates was observed: Only nanorods presenting the silica-binding peptides KD5 or KD10 showed continuous inorganic surface coatings on every single particle, with no significant agglomeration of the virus hybrids. Furthermore, deposition on these templates was highly specific; only a low amount of non-bound silica particles had formed (Figure 4b). The templates TMV–AH, –31C, and –44C induced silica deposition as well, but in contrast to TMV–KD5 and –KD10, the resulting composites did not contain separate rods anymore, but rather formed extended aggregates and bundles up to the μm size regime, especially pronounced for –31C and –44C. TMV templates lacking specific effector peptides (i.e., TMV–PEG, TMV–Lys, $TMV_{wt}$) did not show any substantial inorganic coating at all, instead, some unspecific silica precipitation was observed (Figure 4b). It is known for in vitro systems that an alternating arrangement of lysine and aspartic acid residues (as in peptides KD5 and KD10) enhances dehydration of the TEOS precursor in the mineralization solution, in direct comparison to blockwise arrangements of the same amino acids. This results from an increased number of active sites for charge-relay effects [61]. The results of our comparative tests showing superior capacities of KD5 and KD10 to induce local silicification are in line with these earlier observations. This illustrates the beneficial effect of amino acid-based charge relay on a spatially directed TEOS conversion. Silica precipitation by sol–gel reaction from precursor solutions is likely to involve a gradual growth of individual silica nucleation cores rather than single or few specific phase transformations [74]. Hence, high surface densities of cooperating starter sites (such as repetitive KD pairs) may provide the best chance for an even growth of mineral shells, which are induced simultaneously at numerous closely adjacent sites.

The other peptides explored in this study, AH, 31C and 44C, all contain histidine residues as potential mineralization effectors. Their imidazole rings can catalyze hydrolysis of the TEOS precursor, resulting in deprotonated, negatively charged silicic acid, which then accumulates in the vicinity of the positively charged amino acids to facilitate silica mineralization [17]. The good efficiency of AH in promoting silica sheath formation from TEOS in the context of amphiphilic peptide fibers has been demonstrated [17]. 31C and 44C had not been tested with TEOS before, as they were originally identified due to their ZnO binding properties (data not shown) [60]. The agglomeration and bundle formation we found for all three respective mineralized TMV templates might be due to their aggregation before the mineralization process, as it is known for histidine-presenting TMV particles [51,84,85]. This is also indicated by their absolute ZP values of <50 mV measured in this study.

Most of the silicification-active peptides that convey the dehydration of precursor molecules such as TEOS [55,56,73,86,87] contain disproportionate amounts of positively charged amino acid residues (lysine, arginine or histidine). This reflects the design of silaffin, a natural silica-mineralizing protein rich in lysine and arginine residues [58,88]. Therefore, we speculated that bare TMV–Lys templates could also support the formation of silica shells in TEOS solution. The effect could be greater since the viral CPs are known to be N-terminally acetylated [89] and thereby might act as repetitive charge-relay systems on the viral surface. However, we could not detect any silica coating on TMV–Lys templates under the conditions applied. This may be due to the surrounding amino acids in the CP environment, which might slow down or even inhibit putative mineralization-supporting activity of the lysine moiety of the CP.

$TMV_{wt}$ was also not mineralized in this experimental setup to an electron-optically detectable extent. This is in contrast to the strong and much faster mineralization of $TMV_{wt}$ particles from TEOS solution in alkaline or more acidic pH regimes, as performed in other labs and described above.

TEM analyses of the mineralized products confirmed the findings for the distinct TMV templates (not shown), with TMV–KD10–silica composites showing the strongest and most homogeneous contrast of otherwise non-stained samples. This template was therefore selected for a twelve day time course

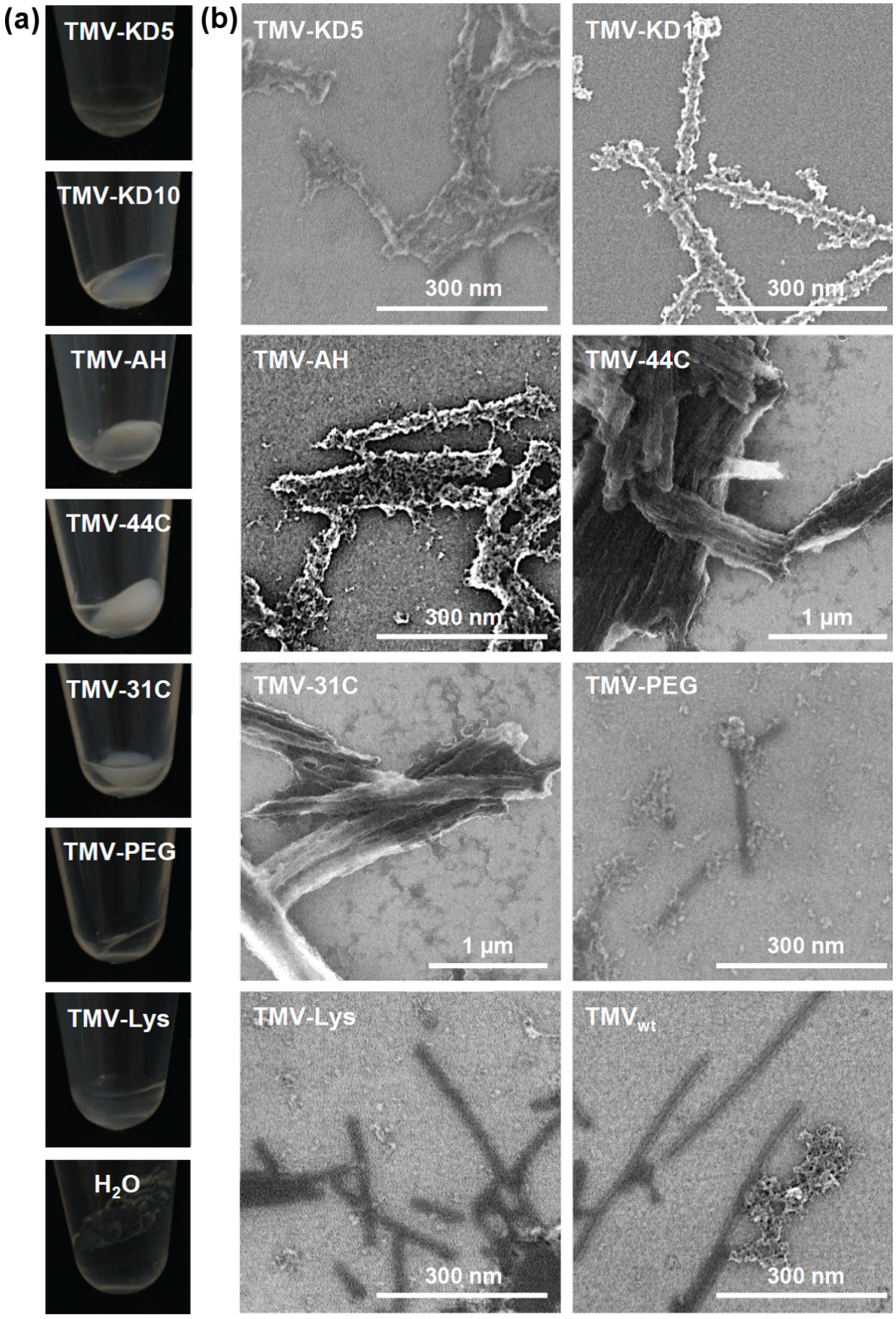


**Figure 4:** $SiO_2$ deposition reactions using functionalized and non-modified TMV templates, as indicated. (a) Images of sedimented products, and (b) corresponding SEM analysis. TMV–Lys-template (or water control) solutions were mixed with absolute EtOH (99.9%) and TEOS in a 4:4:1 volume ratio. Reaction products were sedimented by centrifugation (after 7 days of incubation in (a) or 10 days in (b)), resuspended in $ddH_2O$ and prepared for SEM (for details, refer to text).

experiment to investigate the growth kinetics of its mineral shells, and if the thickness of the silica coating might be controlled via the TEOS incubation time. Total widths of randomly selected, low-contrast TMV–KD10 cores surrounded by electron-dense sheaths were measured in digital TEM images by help of image processing software from the fifth day onwards. This revealed an increase of layer thickness with progressing time (Figure 5). After ten days of reaction time, the TMV–silica hybrids exhibited average diameters of about 29 ± 2 nm, which did not further increase upon extended incubation. At the same time, granular $SiO_2$ deposits began to differentiate on the nanotube surfaces, rendering them less smooth than during earlier stages. The overall diameter, that is, the height of TMV–KD10-templated hybrid rods, after ten days of mineralization was additionally measured by AFM (data not shown). For this purpose, mineralized viruses were deposited on a silicon substrate. The average of the resulting mean values of the virus height was in good agreement with the TEM data and revealed a typical particle diameter of 30 nm, corresponding to a ≈6 nm linker–peptide–silica coating of the 18 nm TMV core. Different from non-modified viral rods immobilized on a silicon substrate, where reduction of the virus height due to attraction to the substrate surface is observed [32], the adhesion of mineralized viruses from suspensions to the wafer substrates did not reduce the objects' height. This indicated the formation of a rigid composite not radially compressed upon its surface adsorption.

## ToF-SIMS analysis of the deposited material

An analysis of the deposited materials with time-of-flight secondary ion mass spectrometry (ToF-SIMS) [90] was performed on air-dried, drop cast suspensions of $TMV_{wt}$ or TMV–KD10 particles (both with and without 10 days of exposure to TEOS). Positive and negative secondary ion spectra were recorded from random positions of the TMV deposits. The peak assignment is based on high mass resolution data and isotope patterns for Si. As shown in Figure 6, the intensity of the $Si^+$ signal decreases substantially from TMV–KD10 particles incubated with TEOS (blue) to the $TMV_{wt}$ control with TEOS (red) to both negative controls not incubated in TEOS solutions (green and purple). Analyzing $SiOH^+$ and several fragments characteristic of silica in negative polarity spectra ($SiO_2^-$, $SiO_3^-$, $SiO_3H^-$) indicated

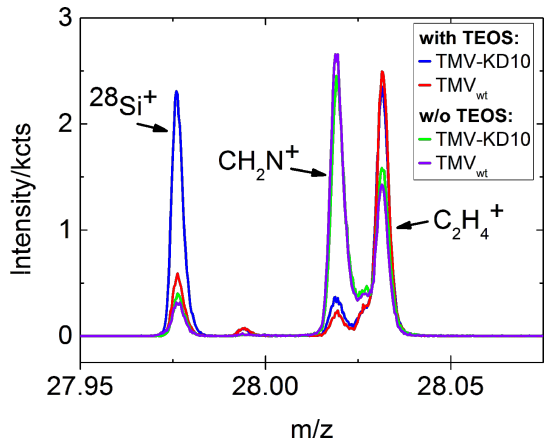


**Figure 6:** ToF-SIMS analysis for determination of silica deposition. TMV–KD10 with TEOS (blue) and without TEOS (green), $TMV_{wt}$ with TEOS (red) and without TEOS (purple) after ten days of incubation. The peak at *m/z* 27.97 indicates Si, the peak at m/z 28.02 $CH_2N^+$, and the peak at m/z 28.03 $C_2H_4^+$. For TMV–KD10 with TEOS and $TMV_{wt}$ with TEOS, the decrease of the $CH_2N^+$ peak, indicating peptide/protein components, is an indirect effect of the mineralization, shielding the soft-matter surface of biotemplate particles.

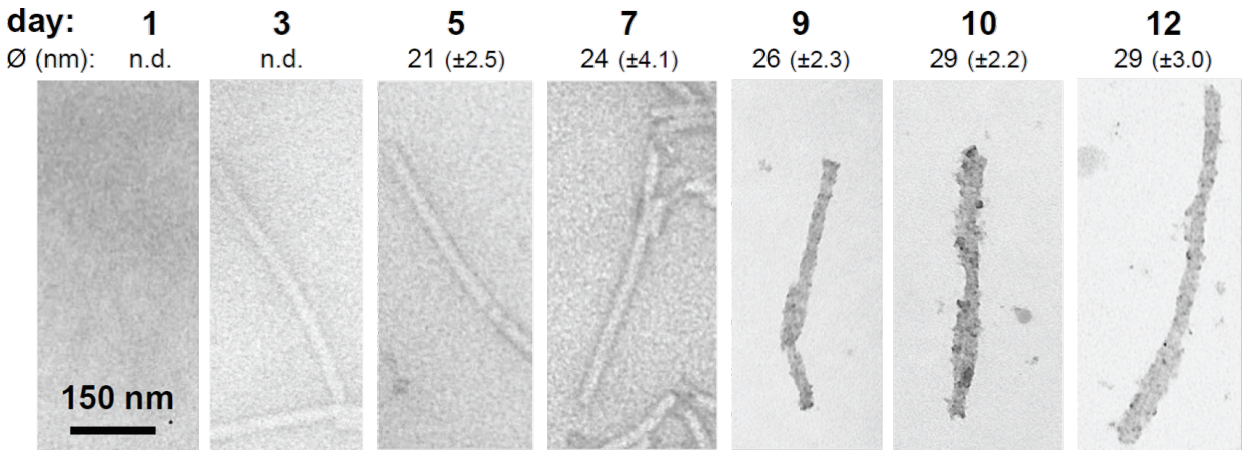


**Figure 5:** Time-resolved monitoring of silica shell growth on TMV–KD10 templates: TEM analysis of non-stained specimens, after the reaction times indicated above. Total average diameters (Ø ± standard deviations) of mineralized TMV–KD10-hybrids were determined from 11–15 randomly selected nanorod products collected between one and twelve days of incubation.

the same trend. Since the sample preparation method did not yield fully TMV-covered samples, the recorded mass spectra averaged over a field of view of 500 × 500 μm$^2$ show individual levels of $Au^-$ stemming from the underlying substrate. In order to correct for this dispersion or area effect, the raw intensities of $Si^+$ and $SiOH^+$ were normalized according to the gold signals of each analyzed spot. Semi-quantitative silicification levels obtained thereof are presented in Table 3.

**Table 3:** Relative silicification levels determined from normalized $Si^+$ and $SiOH^+$ intensities in SIMS. TEOS exposure 10 days, when applicable.

| Construct | Normalized $Si^+$ | Normalized $SiOH^+$ |
|---|---|---|
| TMV–KD10 with TEOS | 100% | 100% |
| $TMV_{wt}$ with TEOS | 18% | 17% |
| TMV–KD10 without TEOS | 1% | 1% |
| $TMV_{wt}$ without TEOS | <1% | <1% |

As shown in Table 3, the normalized intensities of two silica-derived fragments obtained with SIMS allow for a rough but reasonable quantification of the conversion of TEOS to silica induced by bare and KD10-functionalized TMV particles. While all negative controls not exposed to TEOS show negligible levels of $Si^+$ and $SiOH^+$, both TMV–KD10 and $TMV_{wt}$ exposed to TEOS did form insoluble silica to considerably different extents. This resulted in about five times higher amounts of mineral on the peptide-modified virus. This finding is in agreement with our microscopic observations, which were not sufficient to resolve the deposition of silica on the wild type viral template. The ToF-SIMS analysis therefore revealed either a spontaneous hydrolysis of TEOS (also occurring in the absence of effector peptides) or a low but specific mineralization-promoting activity of the bare viral CP surface (not detectable by electron-optical imaging). The low SIMS $Si^+$ and $SiOH^+$ signal intensities, and the necessary high mass resolution for unambiguous fragment assignments, precluded SIMS imaging with high lateral resolution. Hence, the obtained SIMS data cannot visualize mineralized individual TMV particles or distinguish between silica bound to virus particles and silica deposited by self-hydrolysis.

## Conclusion

A systematic comparison of TMV-based nanobiotemplates chemically functionalized with different types of mineralization-affecting peptides revealed superior capacities of repetitive, alternating KD sequences in guiding the deposition of silica sheaths from TEOS precursor solutions around the viral soft-matter cores. The peptide KD10 designed in this study on the basis of earlier tests [61] allowed for the most selective and controllable silicification by sol–gel condensation. This was likely due to its charge-relay activity, in comparison to different histidine-containing effector peptides and the bare or linker-coated viral scaffold surface. To our knowledge, this is the first evaluation of peptide-equipped TMV templates with regard to the generation of silica nanostructures of adjustable diameter. The previous studies of other researchers, all of which employed natural or aniline-modified TMV to nucleate silica deposition (as specified above), yielded either nanometric coatings of individual particles, or differently organized bio-inorganic mesostructures, but did not focus on fine-tuning the growth of the silica shells on the one-to-ten nm range. This was intended here and best achieved by the KD10-exposing TMV variant, for which a convincing correlation between silicification time and mineral layer thickness could be demonstrated.

The KD10-fashioned plant viruses thus enable the one-pot manufacture of freely suspended silica nanorods with a soft-matter core, devoid of significant amounts of byproducts. It would be interesting to characterize the mechanical properties of these composites in comparison to synthetically synthesized silica nanorods. This could potentially lead to fundamentally novel types of fiber-reinforced biohybrid materials. Furthermore, the method may also give rise to an efficient fabrication of rigid, ultrasmall components of unusual shapes, on the basis of different nonlinear kinked and branched TMV-based architectures generated recently in our lab [54].

Finally, peptides spatially immobilized in a selective manner on certain target sites of biotemplates might also be a clue to the use of silica deposition as a “bionic glue”. On appropriate TMV variants, specific coupling groups of amino acids are confined to outer, inner or end surfaces of the nucleoprotein tubes, respectively. Serial in vitro assembly of different genetically engineered CP types on RNA scaffolds can even generate nanorod subdomains, offering unique coupling functionality [76]. Addressing such sites for a selective conjugation of mineralization-guiding peptides such as KD10 might pave future routes towards a firm and controlled integration of TMV-based nanostructures into miniaturized devices. Here they might act, for example, as adaptor templates, enabling an ultradense presentation of functional molecules on the non-mineralized regions of their multivalent protein surfaces.

Taken together, extended composite bio-hybrid materials and complex miniaturized systems both might profit from the precise shapes, high availabilities and immense in vitro tuning potential of plant viral templates, and their peptide-controlled transformation into mineralized nanostructured composites adapted to specific future applications.

# Experimental

## Materials

The peptides, $(KD)_5C$, $(KD)_{10}C$, and $CA_4H_4$, of 90% purity were provided by GeneCust (Dudelange, Luxembourg). Peptides 31C and 44C were purchased from EMC Microcollections (Tübingen, Germany).

## TMV functionalization with bifunctional linker molecules and peptides

Wild type $TMV_{wt}$ and genetically modified $TMV_{Lys}$ [76] (also named TMV–Lys here to underscore the functional amino groups exposed by its lysine side chains) were purified according to Gooding and Hebert [91]. Peptide conjugation onto the virus surface followed a protocol established on the basis of literature data [92,93] and instruction kindly provided by Sourabh Shukla and Nicole Steinmetz, Case Western Reserve University, Cleveland, Ohio, U.S.A. For this procedure, 1200 µL of TMV–Lys particles (5 mg/mL) in 10 mM sodium potassium phosphate (SPP) pH 7.2 were mixed with 9 µL of 1 M hetero-bifunctional crosslinker, succinimidyl-(*N*-maleimidopropionamido)-tetraethylene glycol ester ($SM(PEG)_4$, Thermo Scientific, Karlsruhe, Germany) dissolved in dimethyl sulfoxide and incubated at 37 °C for 2 h under agitation (horizontal shaking at 500 rpm). The TMV particles were sedimented for 1.5 h at 90,500 *g* and 4 °C in an Optima L-90K ultracentrifuge (Beckman Coulter, Krefeld, Germany). The resulting pellet of linker-equipped TMV (named TMV–PEG) was resuspended in 600 µL of 10 mM SPP pH 7.2. A volume of 100 µL of TMV–PEG solution was mixed with 800 µL of 10 mM SPP pH 7.2 and 40 µL of peptides (3.3 mg/mL) dissolved in dimethylformamide and incubated at 30 °C for 2 h and subsequently at 4 °C overnight under agitation as above. The TMV particles with conjugated peptides were sedimented by ultracentrifugation as above. The pellets were washed with 1 mL of ultrapure water ($ddH_2O$, 18.3 MΩ cm, purified by a membraPure system, Aquintus, Bodenheim, Germany) and resuspended in 100 µL of $ddH_2O$. The $TMV_{wt}$ and TMV–Lys concentrations were determined by UV spectroscopy with a NanoDrop ND-1000 spectrophotometer (PeqLab, Erlangen, Germany) at a wavelength of 260 nm, using the extinction coefficient of TMV particles (3 mL $mg^{-1}$ $cm^{-1}$ [94]) . For estimating concentrations of the different biotemplate rods, the band intensities of modified CPs and unmodified $CP_{Lys}$ after SDS-PAGE separation and Comassie Blue staining were compared (see below).

## Electrophoretic analysis

The modified CPs were analyzed by denaturing SDS-PAGE [95]. Samples containing 0.2 µg of protein were heated for 5 min at 95 °C in sample buffer (50 mM Tris-HCl (tris-(hydroxymethyl)aminomethan hydrochloride) pH 6.8, 2% (w/v) SDS, 0.1% (w/v) bromophenol blue, 10% glycerol, 100 mM dithiothreitol) and separated on 15% PA gels. Fixed gels were stained with Coomassie Brilliant Blue R250 (Serva Electrophoresis, Heidelberg, Germany) according to standard procedures [96].

Modified and unmodified TMV–Lys templates were separated as intact particles in native 0.9% agarose gels in 98 mM Tris pH 8.0, 89 mM boric acid, 2 mM EDTA. 12 µg of total protein in sample buffer (10 mM SPP pH 7.2, 0.1% (w/v) bromophenol blue, 10% glycerol) were applied per lane. TMV bands were stained with Coomassie Brilliant Blue R250.

## Zeta potential determination and charge calculation

The zeta potential was measured with a Malvern Zetasizer Nano ZS (Malvern Instruments, Worcestershire, UK) using disposable folded cuvettes. The Smoluchowski approximation was used according to instrument settings to convert the electrophoretic mobility to a zeta potential. The experiments consisted of 30 runs per measurement. All experiments were conducted in triplicate. The zeta potential was measured for each sample with a concentration of 0.5 mg/mL TMV particles solution in $ddH_2O$ (pH 5.5) as well as in 30 mM Tris-HCl at pH 8.0.

## TMV particle mineralization

Peptide-functionalized TMV templates resuspended in water (see above) were kept for one to two days at 4 °C to allow their complete dispersion after ultracentrifugation. For the mineralization of particles with and without linkers and conjugated peptides, a 40 µL TMV template solution (10 mg/mL) was mixed with 50 µL 20% (v/v) TEOS (Sigma-Aldrich, München, Germany) in ethanol (99.8% p.a.), resulting in final concentrations in the mineralization reaction mixture of 4.4 mg/mL TMV, 11.1% (v/v) TEOS, and 44.4% (v/v) ethanol in an aqueous solution of pH 5.5–5.6. It was crucial to mix TEOS and ethanol before combining it with TMV particles in order to preserve their structural integrity. Mineralization reactions were incubated for 1, 2, 5, 7, 10 or 12 days under agitation (horizontal shaking at 500 rpm) at 25 °C. The reaction mixture was precipitated in a table centrifuge for 15 min at 20,000*g* and 18 °C. The supernatant was discarded and the pellet washed twice with 200 µL of 50% (v/v) ethanol to remove residual unconverted TEOS. The pellet was resuspended in 50 µL of $ddH_2O$ and centrifuged for 30 min at 10,000*g*. The resulting pellet was dissolved in 50 µL of ultrapure water.

## Characterization of mineralized TMV particles

The surface of mineralized TMV particles was characterized by SEM analysis. 20 µL of 1:250 diluted, mineralized TMV solutions in ultrapure water (for the mineralized TMV particle solu-

tion preparation see the previous section) were pipetted on n-Si wafer substrates and air dried. The samples were analyzed in an ultrahigh resolution field emission SEM (FE-SEM; S-5200, Hitachi Ltd., Tokyo, Japan) at 30 kV.

The TEM analysis was carried out to determine the silica shell thickness of TMV–KD10 particles after different reaction times. 3 µL of mineralized TMV particles in solution were incubated on a 400-mesh formvar, carbon-covered copper grid for 5 min. The droplet was removed with five droplets of ultrapure water and air dried. The samples were analyzed under a Zeiss EM-10A TEM (Carl Zeiss, Oberkochen, Germany) at 60 kV.

For ToF-SIMS analysis, Si chips (5 × 10 mm) were cut from n-Si wafers (CrysTec, Berlin, Germany) and used as supporting substrates. These were coated with a 4 nm thick chromium layer for adhesion and a 30 nm thick gold layer by physical vapor deposition (PVD; Varian NRC 836, Palo Alto, California, U.S.A.). All samples used for mineralization analysis were found to be free of Si and silicon oil contamination, which could potentially interfere with the analysis.

10 µL of a 1:250 diluted solution of mineralized TMV or control preparations in ultrapure water (see TMV particle mineralization) were pipetted on a gold-covered n-Si wafer and air dried. ToF-SIMS was performed on a TOF.SIMS5 instrument (ION-TOF GmbH, Münster, Germany). The spectrometer was equipped with a Bi cluster primary ion source and a reflection-type time-of-flight analyzer. The UHV base pressure was $<5 \times 10^{-9}$ mbar. For high mass resolution, the Bi source was operated in the "high current bunched" mode, providing short $Bi_1^+$ primary ion pulses at 25 keV energy and a lateral resolution of approximately 4 µm. The short pulse length of 0.6 to 1.0 ns allowed for high mass resolution. The primary ion beam was rastered across a 500 × 500 $\mu m^2$ field of view on the sample, and 128 × 128 data points were recorded. Primary ion doses were kept below $10^{11}$ ions/$cm^2$ (static SIMS limit). The spectra were calibrated against $C^-$, $CH^-$, $CH_2^-$, and $Au^-$, or on the $C^+$, $CH^+$, $CH_2^+$, and $CH_3^+$ peaks, respectively. Based on these datasets, the chemical assignments for characteristic fragments were determined.

## Acknowledgements

The authors are grateful to Diether Gotthardt and Sigi Kober for gardening and technical assistance at the University of Stuttgart, and to Sourabh Shukla and Nicole Steinmetz, Case Western Reserve University, Cleveland, Ohio, U.S.A., for sharing laboratory instructions with us. Many thanks go to the DFG (SPP1569 and PAK415) for funding, and the Carl-Zeiss-Stiftung for additional financial support via the Projekthaus NanoBioMater at the University of Stuttgart.

## References

1. Leblanc, J. L. *Prog. Polym. Sci.* **2002,** *27,* 627–687. doi:10.1016/S0079-6700(01)00040-5
2. Bouwmeester, H.; Brandhoff, P.; Marvin, H. J. P.; Weigel, S.; Peters, R. J. B. *Trends Food Sci. Technol.* **2014,** *40,* 200–210. doi:10.1016/j.tifs.2014.08.009
3. Stark, W. J.; Stoessel, P. R.; Wohlleben, W.; Hafner, A. *Chem. Soc. Rev.* **2015,** in press. doi:10.1039/c4cs00362d
4. Henstock, J. R.; Canham, L. T.; Anderson, S. I. *Acta Biomater.* **2015,** *11,* 17–26. doi:10.1016/j.actbio.2014.09.025
5. Vallet-Regí, M.; Ruiz-Hernández, E. *Adv. Mater.* **2011,** *23,* 5177–5218. doi:10.1002/adma.201101586
6. Tang, F.; Li, L.; Chen, D. *Adv. Mater.* **2012,** *24,* 1504–1534. doi:10.1002/adma.201104763
7. Yildirim, A.; Acar, H.; Erkal, T. S.; Bayindir, M.; Guler, M. O. *ACS Appl. Mater. Interfaces* **2011,** *3,* 4159–4164. doi:10.1021/am201024w
8. Yang, X.; Tang, H.; Cao, K.; Song, H.; Sheng, W.; Wu, Q. *J. Mater. Chem.* **2011,** *21,* 6122–6135. doi:10.1039/c0jm04516k
9. Mann, S. *Nat. Mater.* **2009,** *8,* 781–792. doi:10.1038/nmat2496
10. Paris, O.; Burgert, I.; Fratzl, P. *MRS Bull.* **2010,** *35,* 219–225. doi:10.1557/mrs2010.655
11. Zollfrank, C.; Scheibel, T.; Seitz, H.; Travitzky, N. Bioinspired Materials Engineering. *Ullmann's Encyclopedia of Industrial Chemistry;* Wiley-VCH Verlag GmbH & Co. KGaA: Weinheim, Germany, 2014; pp 1–22. doi:10.1002/14356007.s04_s01
12. Mann, S. Mineralization in biological systems. *Inorganic Elements in Biochemistry;* Structure and Bonding, Vol. 54; Springer: Berlin, Germany, 1983; pp 125–174. doi:10.1007/BFb0111320
13. Weiner, S.; Dove, P. M. *Rev. Mineral. Geochem.* **2003,** *54,* 1–29. doi:10.2113/0540001
14. Wu, Z. J.; Xiang, H.; Kim, T.; Chun, M.-S.; Lee, K. *J. Colloid Interface Sci.* **2006,** *304,* 119–124. doi:10.1016/j.jcis.2006.08.055
15. Cademartiri, R.; Brook, M. A.; Pelton, R.; Brennan, J. D. *J. Mater. Chem.* **2009,** *19,* 1583–1592. doi:10.1039/b815447c
16. Aljabali, A. A. A.; Shah, S. N.; Evans-Gowing, R.; Lomonossoff, G. P.; Evans, D. J. *Integr. Biol.* **2011,** *3,* 119–125. doi:10.1039/C0IB00056F
17. Yuwono, V. M.; Hartgerink, J. D. *Langmuir* **2007,** *23,* 5033–5038. doi:10.1021/la0629835
18. Bittner, A. M.; Alonso, J. M.; Górzny, M. Ł.; Wege, C. Nanoscale Science and Technology with Plant Viruses and Bacteriophages. In *Structure and physics of viruses: An integrated textbook;* Mateu, M. G., Ed.; Subcellular Biochemistry, Vol. 68; Springer Netherlands: Dordrecht, Netherlands, 2013; pp 667–702. doi:10.1007/978-94-007-6552-8_22
19. Mao, C.; Liu, A.; Cao, B. *Angew. Chem., Int. Ed.* **2009,** *48,* 6790–6810. doi:10.1002/anie.200900231
20. Lomonossoff, G. P.; Evans, D. J. Applications of Plant Viruses in Bionanotechnology. In *Plant Viral Vectors;* Palmer, K.; Gleba, Y., Eds.; Current Topics in Microbiology and Immunology, Vol. 375; Springer: Berlin, Germany, 2014; pp 61–87. doi:10.1007/82_2011_184
21. Shenton, W.; Douglas, T.; Young, M.; Stubbs, G.; Mann, S. *Adv. Mater.* **1999,** *11,* 253–256. doi:10.1002/(SICI)1521-4095(199903)11:3<253::AID-ADMA253>3.0.CO;2-7
22. Pouget, E.; Grelet, E. *Langmuir* **2013,** *29,* 8010–8016. doi:10.1021/la401170m
23. Yang, S. H.; Chung, W.-J.; McFarland, S.; Lee, S.-W. *Chem. Rec.* **2013,** *13,* 43–59. doi:10.1002/tcr.201200012

24. Li, D.; Qu, X.; Newton, S. M. C.; Klebba, P. E.; Mao, C. *J. Mater. Chem.* **2012,** *22,* 15702–15709. doi:10.1039/c2jm31034a
25. Niu, Z.; Liu, J.; Lee, L. A.; Bruckman, M. A.; Zhao, D.; Koley, G.; Wang, Q. *Nano Lett.* **2007,** *7,* 3729–3733. doi:10.1021/nl072134h
26. Royston, E. S.; Brown, A. D.; Harris, M. T.; Culver, J. N. *J. Colloid Interface Sci.* **2009,** *332,* 402–407. doi:10.1016/j.jcis.2008.12.064
27. Aljabali, A. A. A.; Barclay, J. E.; Cespedes, O.; Rashid, A.; Staniland, S. S.; Lomonossoff, G. P.; Evans, D. J. *Adv. Funct. Mater.* **2011,** *21,* 4137–4142. doi:10.1002/adfm.201101048
28. Rothenstein, D.; Facey, S. J.; Ploss, M.; Hans, P.; Melcher, M.; Srot, V.; Van Aken, P. A.; Hauer, B.; Bill, J. *Bioinspired, Biomimetic Nanobiomater.* **2013,** *2,* 173–185. doi:10.1680/bbn.13.00004
29. Evans, D. J. *Biochem. Soc. Trans.* **2009,** *37,* 665–670. doi:10.1042/BST0370665
30. Dujardin, E.; Peet, C.; Stubbs, G.; Culver, J. N.; Mann, S. *Nano Lett.* **2003,** *3,* 413–417. doi:10.1021/nl034004o
31. Yang, C.; Choi, C.-H.; Lee, C.-S.; Yi, H. *ACS Nano* **2013,** *7,* 5032–5044. doi:10.1021/nn4005582
32. Knez, M.; Sumser, M. P.; Bittner, A. M.; Wege, C.; Jeske, H.; Hoffmann, D. M. P.; Kuhnke, K.; Kern, K. *Langmuir* **2004,** *20,* 411–447. doi:10.1021/la035425o
33. Fujikawa, S.; Kunitake, T. *Langmuir* **2003,** *19,* 6545–6552. doi:10.1021/la026979e
34. Royston, E.; Lee, S.-Y.; Culver, J. N.; Harris, M. T. *J. Colloid Interface Sci.* **2006,** *298,* 706–712. doi:10.1016/j.jcis.2005.12.068
35. Chiang, C.-Y.; Epstein, J.; Brown, A.; Munday, J. N.; Culver, J. N.; Ehrman, S. *Nano Lett.* **2012,** *12,* 6005–6011. doi:10.1021/nl303579z
36. Mao, C.; Solis, D. J.; Reiss, B. D.; Kottmann, S. T.; Sweeney, R. Y.; Hayhurst, A.; Georgiou, G.; Iverson, B.; Belcher, A. M. *Science* **2004,** *303,* 213–217. doi:10.1126/science.1092740
37. Atanasova, P.; Rothenstein, D.; Schneider, J. J.; Hoffmann, R. C.; Dilfer, S.; Eiben, S.; Wege, C.; Jeske, H.; Bill, J. *Adv. Mater.* **2011,** *23,* 4918–4922. doi:10.1002/adma.201102900
38. Balci, S.; Bittner, A. M.; Schirra, M.; Thonke, K.; Sauer, R.; Hahn, K.; Kadri, A.; Wege, C.; Jeske, H.; Kern, K. *Electrochim. Acta* **2009,** *54,* 5149–5154. doi:10.1016/j.electacta.2009.03.036
39. Atanasova, P.; Stitz, N.; Sanctis, S.; Maurer, J. H. M.; Hoffmann, R. C.; Eiben, S.; Jeske, H.; Schneider, J. J.; Bill, J. *Langmuir* **2015,** *31,* 3897–3903. doi:10.1021/acs.langmuir.5b00700
40. Adams, M. J.; Heinze, C.; Jackson, A. O.; Kreuze, J. F.; MacFarlane, S. A.; Torrance, L. Family Virgaviridae. In *Virus taxonomy: Ninth report of the International Committee on Taxonomy of Viruses;* King, A. M. Q.; Adams, M. J.; Carstens, E. B.; Lefkowitz, E. J., Eds.; Elsevier: San Diego, CA, U.S.A., 2012; pp 1139–1162.
41. Culver, J. N. *Annu. Rev. Phytopathol.* **2002,** *40,* 287–308. doi:10.1146/annurev.phyto.40.120301.102400
42. Butler, P. J. G. *Philos. Trans. R. Soc., B* **1999,** *354,* 537–550. doi:10.1098/rstb.1999.0405
43. Namba, K.; Pattanayek, R.; Stubbs, G. *J. Mol. Biol.* **1989,** *208,* 307–325. doi:10.1016/0022-2836(89)90391-4
44. Ge, P.; Zhou, Z. H. *Proc. Natl. Acad. Sci. U. S. A.* **2011,** *108,* 9637–9642. doi:10.1073/pnas.1018104108
45. Clare, D. K.; Orlova, E. V. *J. Struct. Biol.* **2010,** *171,* 303–308. doi:10.1016/j.jsb.2010.06.011
46. Sachse, C.; Chen, J. Z.; Coureux, P. D.; Stroupe, M. E.; Fändrich, M.; Grigorieff, N. *J. Mol. Biol.* **2007,** *371,* 812–835. doi:10.1016/j.jmb.2007.05.088
47. Alonso, J. M.; Górzny, M. Ł.; Bittner, A. M. *Trends Biotechnol.* **2013,** *31,* 530–538. doi:10.1016/j.tibtech.2013.05.013
48. Culver, J. N.; Brown, A. D.; Zang, F.; Gnerlich, M.; Gerasopoulos, K.; Ghodssi, R. *Virology* **2015,** *479–480,* 200–212. doi:10.1016/j.virol.2015.03.008
49. Schlick, T. L.; Ding, Z.; Kovacs, E. W.; Francis, M. B. *J. Am. Chem. Soc.* **2005,** *127,* 3718–3723. doi:10.1021/ja046239n
50. Smith, M. L.; Lindbo, J. A.; Dillard-Telm, S.; Brosio, P. M.; Lasnik, A. B.; McCormick, A. A.; Nguyen, L. V.; Palmer, K. E. *Virology* **2006,** *348,* 475–488. doi:10.1016/j.virol.2005.12.039
51. Eiben, S.; Stitz, N.; Eber, F.; Wagner, J.; Atanasova, P.; Bill, J.; Wege, C.; Jeske, H. *Virus Res.* **2014,** *180,* 92–96. doi:10.1016/j.virusres.2013.11.019
52. Shukla, S.; Eber, F.; Nagarajan, A. S.; DiFranco, N. A.; Schmidt, N.; Wen, A. M.; Eiben, S.; Twyman, R. M.; Wege, C.; Steinmetz, N. F. *Adv. Healthcare Mater.* **2015,** *4,* 874–882. doi:10.1002/adhm.201400641
53. Eber, F. J.; Eiben, S.; Jeske, H.; Wege, C. *Angew. Chem., Int. Ed.* **2013,** *52,* 7203–7207. doi:10.1002/anie.201300834
54. Eber, F. J.; Eiben, S.; Jeske, H.; Wege, C. *Nanoscale* **2015,** *7,* 344–355. doi:10.1039/C4NR05434B
55. Baio, J. E.; Zane, A.; Jaeger, V.; Roehrich, A. M.; Lutz, H.; Pfaendtner, J.; Drobny, G. P.; Weidner, T. *J. Am. Chem. Soc.* **2014,** *136,* 15134–15137. doi:10.1021/ja5078238
56. Zane, A. C.; Michelet, C.; Roehrich, A.; Emani, P. S.; Drobny, G. P. *Langmuir* **2014,** *30,* 7152–7161. doi:10.1021/la501444t
57. Cha, J. N.; Shimizu, K.; Zhou, Y.; Christiansen, S. C.; Chmelka, B. F.; Stucky, G. D.; Morse, D. E. *Proc. Natl. Acad. Sci. U. S. A.* **1999,** *96,* 361–365. doi:10.1073/pnas.96.2.361
58. Kröger, N.; Deutzmann, R.; Sumper, M. *Science* **1999,** *286,* 1129–1132. doi:10.1126/science.286.5442.1129
59. Poulsen, N.; Kröger, N. *J. Biol. Chem.* **2004,** *279,* 42993–42999. doi:10.1074/jbc.M407734200
60. Rothenstein, D.; Claasen, B.; Omiecienski, B.; Lammel, P.; Bill, J. *J. Am. Chem. Soc.* **2012,** *134,* 12547–12556. doi:10.1021/ja302211w
61. Kuno, T.; Nonoyama, T.; Hirao, K.; Kato, K. *Langmuir* **2011,** *27,* 13154–13158. doi:10.1021/la202576v
62. Stöber, W.; Fink, A.; Bohn, E. *J. Colloid Interface Sci.* **1968,** *26,* 62–69. doi:10.1016/0021-9797(68)90272-5
63. Kim, Y. J.; Hwang, K. H.; Park, S.-J.; Jeon, D.-Y.; Nam, C.-H.; Kim, G.-T. *J. Nanosci. Nanotechnol.* **2013,** *13,* 6203–6207. doi:10.1166/jnn.2013.7683
64. Fowler, C. E.; Shenton, W.; Stubbs, G.; Mann, S. *Adv. Mater.* **2001,** *13,* 1266–1269. doi:10.1002/1521-4095(200108)13:16<1266::AID-ADMA1266>3.0.CO;2-9
65. Rong, J.; Oberbeck, F.; Wang, X.; Li, X.; Oxsher, J.; Niu, Z.; Wang, Q. *J. Mater. Chem.* **2009,** *19,* 2841–2845. doi:10.1039/b901130g
66. Mueller, A.; Eber, F. J.; Azucena, C.; Petershans, A.; Bittner, A. M.; Gliemann, H.; Jeske, H.; Wege, C. *ACS Nano* **2011,** *5,* 4512–4520. doi:10.1021/nn103557s
67. Chen, X.; Gerasopoulos, K.; Guo, J.; Brown, A.; Ghodssi, R.; Culver, J. N.; Wang, C. *Electrochim. Acta* **2011,** *56,* 5210–5213. doi:10.1016/j.electacta.2011.03.037
68. Li, F.; Wang, Q. *Small* **2014,** *10,* 230–245. doi:10.1002/smll.201301393
69. Luckanagul, J.; Andrew Lee, L.; Nguyen, Q. L.; Sitasuwan, P.; Yang, X.; Shazly, T.; Wang, Q. *Biomacromolecules* **2012,** *13,* 3949–3958. doi:10.1021/bm301180c

70. Wu, Z.; Mueller, A.; Degenhard, S.; Ruff, S. E.; Geiger, F.; Bittner, A.; Wege, C.; Krill, C. E., III. *ACS Nano* **2010,** *4,* 4531–4538. doi:10.1021/nn100645e
71. Luckanagul, J. A.; Lee, L. A.; You, S.; Yang, X.; Wang, Q. *J. Biomed. Mater. Res., Part A* **2015,** *103,* 887–895. doi:10.1002/jbm.a.35227
72. Patwardhan, S. V.; Emami, F. S.; Berry, R. J.; Jones, S. E.; Naik, R. R.; Deschaume, O.; Heinz, H.; Perry, C. C. *J. Am. Chem. Soc.* **2012,** *134,* 6244–6256. doi:10.1021/ja211307u
73. Steinmetz, N. F.; Shah, S. N.; Barclay, J. E.; Rallapalli, G.; Lomonossoff, G. P.; Evans, D. J. *Small* **2009,** *5,* 813–816. doi:10.1002/smll.200801348
74. Gebauer, D.; Kellermeier, M.; Gale, J. D.; Bergström, L.; Cölfen, H. *Chem. Soc. Rev.* **2014,** *43,* 2348–2371. doi:10.1039/c3cs60451a
75. Almora-Barrios, N.; Austen, K. F.; de Leeuw, N. H. *Langmuir* **2009,** *25,* 5018–5025. doi:10.1021/la803842g
76. Geiger, F. C.; Eber, F. J.; Eiben, S.; Mueller, A.; Jeske, H.; Spatz, J. P.; Wege, C. *Nanoscale* **2013,** *5,* 3808–3816. doi:10.1039/c3nr33724c
77. Protein Calculator V3.4. http://protcalc.sourceforge.net (accessed May 27, 2015).
78. *ImageJ software;* 2011, http://imagej.nih.gov/ij/.
79. Hong, J. H.; Duncan, S. E.; Dietrich, A. M. *Food Qual. Prefer.* **2010,** *21,* 132–139. doi:10.1016/j.foodqual.2009.08.010
80. Hunter, R. J. *Zeta potential in colloid science: principles and applications;* Academic Press: London, United Kingdom, 1981.
81. Müller, R. H.; Hildebrand, G. E., Eds. *Zetapotential und Partikelladung in der Laborpraxis: Einführung in die Theorie praktische Messdurchführung Dateninterpretation,* Colloidal Drug Carriers - cdc - 1st Expert Meeting, Berlin, Germany, June 15–17, 1995; Wissenschaftliche Verlagsgesellschaft: Stuttgart, Germany, 1995.
82. Reed, J. S. *Principles of ceramics processing,* 2nd ed.; John Wiley & Sons, Inc.: New York, NY, U.S.A., 1995.
83. Niu, Z.; Kabisatpathy, S.; He, J.; Lee, L. A.; Rong, J.; Yang, L.; Sikha, G.; Popov, B.; Emrick, T.; Russell, T.; Wang, Q. *Nano Res.* **2009,** *2,* 474–483. doi:10.1007/s12274-009-9043-6
84. Bruckman, M. A.; Soto, C. M.; McDowell, H.; Liu, J. L.; Ratna, B. R.; Korpany, K. V.; Zahr, O. K.; Blum, A. S. *ACS Nano* **2011,** *5,* 1606–1616. doi:10.1021/nn1025719
85. Kadri, A.; Maiß, E.; Amsharov, N.; Bittner, A. M.; Balci, S.; Kern, K.; Jeske, H.; Wege, C. *Virus Res.* **2011,** *157,* 35–46. doi:10.1016/j.virusres.2011.01.014
86. Altunbas, A.; Sharma, N.; Lamm, M. S.; Yan, C. Q.; Nagarkar, R. P.; Schneider, J. P.; Pochan, D. J. *ACS Nano* **2010,** *4,* 181–188. doi:10.1021/nn901226h
87. Acar, H.; Garifullin, R.; Guler, M. O. *Langmuir* **2011,** *27,* 1079–1084. doi:10.1021/la104518g
88. Sumper, M.; Kröger, N. *J. Mater. Chem.* **2004,** *14,* 2059–2065. doi:10.1039/b401028k
89. Filner, B.; Marcus, A. *Virology* **1974,** *61,* 537–546. doi:10.1016/0042-6822(74)90288-8
90. Belu, A. M.; Graham, D. J.; Castner, D. G. *Biomaterials* **2003,** *24,* 3635–3653. doi:10.1016/S0142-9612(03)00159-5
91. Gooding, G. V.; Hebert, T. T. *Phytopathology* **1967,** *57,* 1285.
92. Bruckmann, M. A.; Steinmetz, N. F. Chemical Modification of the Inner and Outer Surfaces of Tobacco Mosaic Virus (TMV). In *Virus hybrids as nanomaterials: methods and protocols;* Lin, B.; Ratna, B., Eds.; Methods in Molecular Biology, Vol. 1108; Humana Press: New York, NY, U.S.A., 2014; pp 173–185. doi:10.1007/978-1-62703-751-8_13
93. Bruckman, M. A.; Jiang, K.; Simpson, E. J.; Randolph, L. N.; Luyt, L. G.; Yu, X.; Steinmetz, N. F. *Nano Lett.* **2014,** *14,* 1551–1558. doi:10.1021/nl404816m
94. Description of Plant Viruses. http://www.dpvweb.net/dpv/showdpv.php?dpvno=370 (accessed May 27, 2015).
95. Laemmli, U. K. *Nature* **1970,** *227,* 680–685. doi:10.1038/227680a0
96. Green, M. R.; Sambrook, J. *Molecular cloning: a laboratory manual,* 4th ed.; Cold Spring Harbor Laboratory Press: New York, NY, U.S.A., 2012.

## License and Terms

BEILSTEIN JOURNAL OF NANOTECHNOLOGY

# Template-controlled mineralization: Determining film granularity and structure by surface functionality patterns

Nina J. Blumenstein[*1], Jonathan Berson[2,3], Stefan Walheim[*2,3], Petia Atanasova[1], Johannes Baier[1], Joachim Bill[1] and Thomas Schimmel[2,3]

Full Research Paper

Open Access

Address:
[1]Institute for Materials Science, University of Stuttgart, Heisenbergstraße 3, D-70569 Stuttgart, Germany, [2]Institute of Nanotechnology, Karlsruhe Institute of Technology (KIT), Hermann-von-Helmholtz-Platz 1, Eggenstein-Leopoldshafen, D-76344, Germany and [3]Institute of Applied Physics and Center for Functional Nanostructures, Karlsruhe Institute of Technology (KIT), Wolfgang-Gaede-Strasse 1, D-76131 Karlsruhe, Germany

Email:
Nina J. Blumenstein[*] - nina.blumenstein@imw.uni-stuttgart.de;
Stefan Walheim[*] - stefan.walheim@kit.edu

* Corresponding author

Keywords:
bioinspired synthesis; polymer-blend lithography; surface functionality; template-controlled self-assembly; zinc oxide thin film

*Beilstein J. Nanotechnol.* **2015,** *6,* 1763–1768.
doi:10.3762/bjnano.6.180

Received: 24 April 2015
Accepted: 31 July 2015
Published: 20 August 2015

This article is part of the Thematic Series "Towards multifunctional inorganic materials: biopolymeric templates".

Guest Editor: C. Steinem



## Abstract

We present a promising first example towards controlling the properties of a self-assembling mineral film by means of the functionality and polarity of a substrate template. In the presented case, a zinc oxide film is deposited by chemical bath deposition on a nearly topography-free template structure composed of a pattern of two self-assembled monolayers with different chemical functionality. We demonstrate the template-modulated morphological properties of the growing film, as the surface functionality dictates the granularity of the growing film. This, in turn, is a key property influencing other film properties such as conductivity, piezoelectric activity and the mechanical properties. A very pronounced contrast is observed between areas with an underlying fluorinated, low energy template surface, showing a much more (almost two orders of magnitude) coarse-grained film with a typical agglomerate size of around 75 nm. In contrast, amino-functionalized surface areas induce the growth of a very smooth, fine-grained surface with a roughness of around 1 nm. The observed influence of the template on the resulting clear contrast in morphology of the growing film could be explained by a contrast in surface adhesion energies and surface diffusion rates of the nanoparticles, which nucleate in solution and subsequently deposit on the functionalized substrate.

## Introduction

Self-organization plays an important role in nature – and more and more in technology [1,2]. Increasingly complex structures can evolve from using principles of self-organization in a bottom-up approach rather than from lithography-based top-down approaches. The key issue for intelligent self-assembly of complex structures is the design of local geometrically selec-

tive and site-selective interactions on the nanometer scale [3-6]. The more selective the interaction between the individual assembled components, the higher the complexity of the resulting structures that can be achieved.

One type of self-assembly is template-guided self-assembly, which plays an important role in biological processes relevant for biomineralization [7-12]. There are numerous approaches to harness and use this principle for artificial processes, which may be of great technological significance [13-15]. Recently, we reported the site-selective mineralization of a semiconductor material, zinc oxide (ZnO), on a chemically patterned surface [3]. ZnO thin films are of special interest since they can be used for different applications such as solar cells [16], biosensing devices [17] and others [18]. By using a nearly topographically flat (<1 nm roughness), but chemically patterned surface as a template, it was possible to guide the deposition – mainly by means of surface polarity. While deposition took place at sites with amino functionalization, no deposition was observed at locations with a fluorinated surface functionality. In this way, it was possible to guide the deposition using only chemical surface functionality with a topography-free, flat template.

In a next step towards template-controlled deposition, it would be desirable not only to predetermine the deposition sites by means of a chemical pattern template, but also the type of material deposited. In this way the properties of the deposited material are controlled depending on the surface functionality of the template. The properties that can be controlled by template functionality can be structural, topographical, electrical, mechanical, piezoelectrical, adhesive, tribological, catalytic activity [19] or properties connected with the granularity of the film [20-23]. Additionally, the reflectivity or light scattering properties may be controlled – the latter of which are highly relevant for the fields of optical data storage [24,25] and lithography (where increasingly smaller structures are sought, e.g., in the field of semiconductor nanolithography). Here, the copying of a given structure by self-templating may provide an alternative to conventional replication.

In this study, ZnO-containing films were prepared using chemical bath deposition. Two self-assembled monolayers (SAMs) with amino or fluorinated functionality were used to control the structure, and therefore, the roughness of the deposited film. A possible mechanism is presented that explains the influence of the template on the film formation.

## Results and Discussion

Structured templates with polar 3-(aminopropyltriethoxy)-silane (APTES) and nonpolar 1H,1H,2H,2H-perfluorodecyl trichlorosilane (FDTS) areas were used for the deposition of nanostructured ZnO-containing films. Figure 1 shows atomic force microscopy (AFM) and scanning electron microscopy (SEM) images of the original templates and the resulting films together with schematic representations of the deposition mechanism (Figure 1a,d,i,n). The height difference between the two SAMs is 0.6 nm (Figure 1c). Analysis of the topographic images shows no significant difference in roughness between the different templates, as both surfaces exhibit an rms-roughness value of 0.1 nm. After mineralization, the APTES islands are covered by a homogenous, smooth film with an rms-roughness of 1 nm. AFM images show a granular structure that is not clearly visible in the corresponding SEM image. This might be due to the lower sensitivity to topographic features of the SEM.

Temperature has a significant influence on the deposition behavior. For higher temperatures, there is bulk precipitation and an inhomogenous film is formed. At lower temperatures, the growth rate is drastically reduced so that film formation is very slow. The reaction temperature of 70 °C is optimum for controlled deposition of the NPs.

In contrast to the situation on the APTES islands, on the FDTS matrix, large agglomerates with a diameter of 75 nm were deposited. Finally, this leads to a continuous and unperforated film with a roughness of 2.5 nm.

These ZnO-containing structures consist of particles formed in the deposition solution. These NPs grow in solution under the presence of histidine. Gerstel et al. [26,27] found that histidine controls NP growth and is incorporated in the resulting films. XRD measurements show that the deposited ZnO is X-ray-amorphous (data not shown). The investigation of the suspensions from the reaction solution by zeta potential measurements revealed that the particles possess a potential of +22.0 mV at pH 6.7 [26]. Since the pH of the reaction solution is around 5.3, the formed NPs are positively charged (Figure 2).

The zeta potential of the amino-functionalized SAM is charged slightly positive during the reaction [28,29] due to protonation of the amino groups ($–NH_3^+$) at this pH. Additionally, a Stern layer is present, which is formed by negatively charged counter ions [29,30]. The particles in solution can interact with these anions and Coulomb forces lead to a strong binding to the surface (Figure 2). Furthermore, entropic forces, including counterion release forces, may contribute to an enhanced interaction. This leads to closer contact between the NPs and the template, providing a means to activate van der Waals short-range forces. Together these mechanisms lead to a homogenous film with a smooth surface in the APTES-functionalized holes (Figure 1).

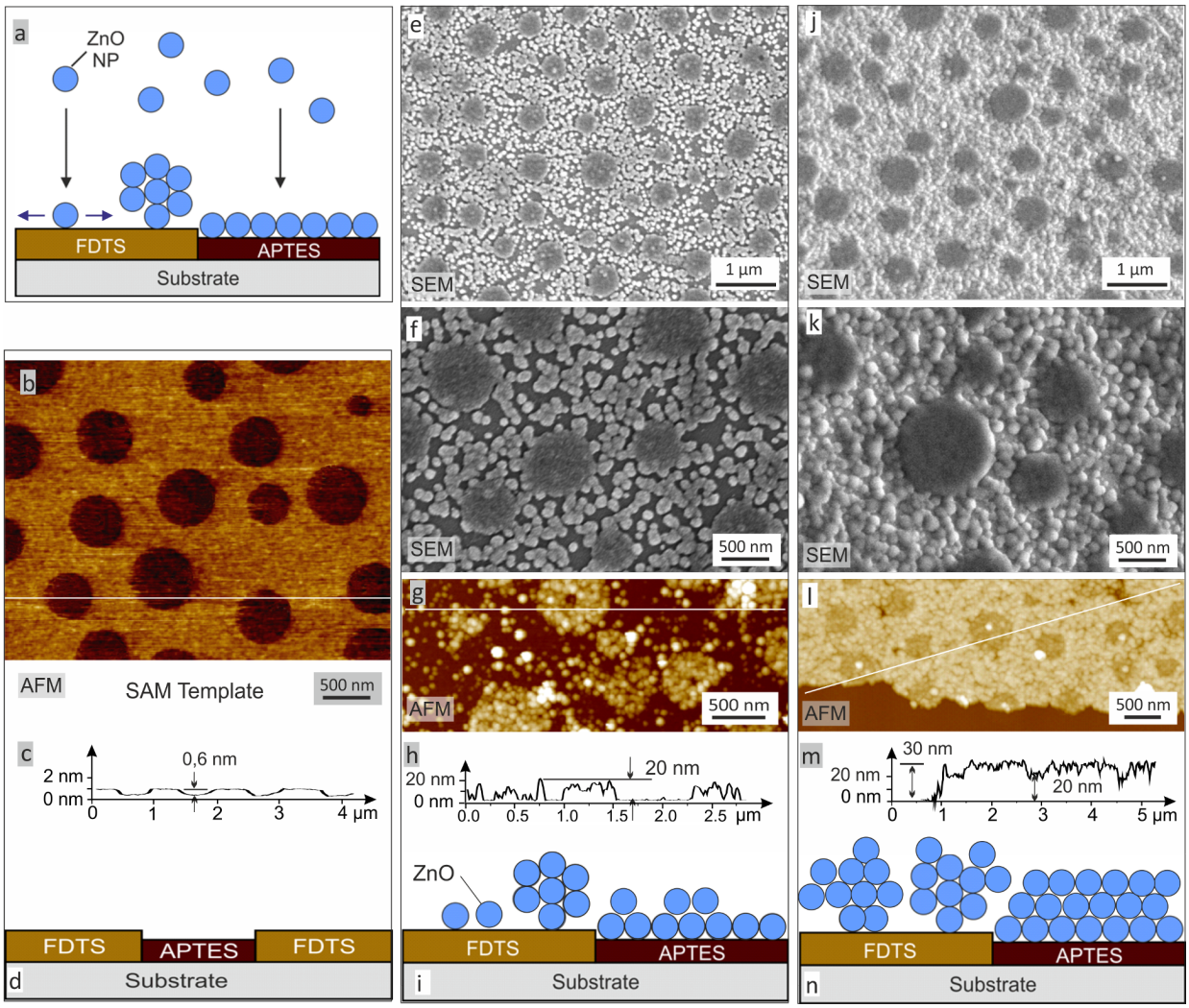


**Figure 1:** Self-assembly of ZnO-containing material on prepatterned substrates. (a) Schematic representation of the deposition mechanism. (b–d) The nonmineralized substrate shows the APTES islands (dark red) in the FDTS matrix (yellow). (e–i) SEM and AFM images show the deposited material on the templates. On the APTES, a smooth and compact film is formed, whereas on the FDTS agglomerates are deposited. With an increasing amount of deposited material, those agglomerates grow together (j–n) resulting in a rough surface for the final morphology.

The FDTS on the other hand is highly hydrophobic [31]. Electrostatic interactions with the particles are minimal compared to the deposition on APTES, where a homogenous and dense distribution of the surface charges leads to a high probability of interaction with particles. In the FDTS areas, small defects with low density can explain the presence of particles on the hydrophobic surface. During the template preparation process, APTES molecules may be deposited in these sites. The ZnO particles are attracted to these polar areas. Other particles are highly mobile due to the decreased interaction with the template. They can diffuse to the immobilized ones and decrease the interfacial energy by agglomeration. The result is a coarse granular structure that can be observed in SEM and AFM (Figure 1) on the FDTS regions of the substrate. When more and more material is deposited, those agglomerates can form a closed film, but with a significantly higher roughness compared to the films formed on the polar APTES-monolayer as shown in Figure 1j–n.

Forthcoming investigations will reveal if other properties such as piezoelectric activity, conductivity, optical or mechanical properties can also be controlled by the patterned surface chemistry of the substrate.

## Conclusion

Here we demonstrate the control of the structure and granularity of a growing film by means of a chemical functionality pattern of the substrate, where the chemical pattern acts as a

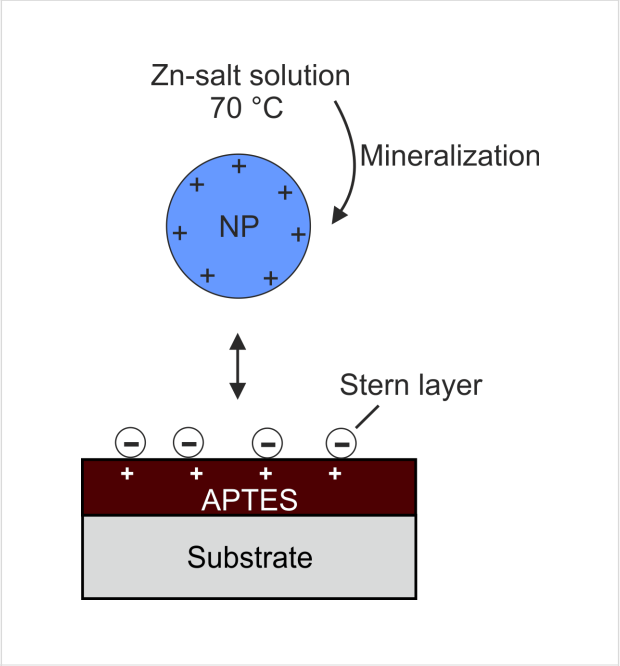


**Figure 2:** Deposition mechanism of mineralized ZnO nanoparticles on amino SAMs. The negative charges represent counterions attached to the positive surface charge (Stern layer) provided by protonated amino groups ($–NH_3^+$).

template. A site-dependent granularity in mineralized ZnO-containing films is observed by self-assembly of nanoparticles during chemical bath deposition on patterned self-assembled monolayers. The influence of template regions of different polarities and surface energies on the deposition of thin ZnO-containing films was investigated. The positively charged amino-functionalized surface areas lead to a homogenous film with low roughness. The use of an uncharged hydrophobic SAM molecule (FDTS) supports the formation of coarse agglomerates with a higher roughness and irregular surface structure.

These findings open intriguing perspectives to control further properties that depend on film granularity such as optical, mechanical, piezoelectrical or tribological properties, by means of the chemical functionality pattern of a templating substrate – properties which, in turn, are key properties for nanodevices.

# Experimental

## Template preparation by polymer-blend lithography

Polymer solution: Polystyrene (PS, $M_w$ = 96 kg/mol, PDI 1.04) and poly(methyl methacrylate) (PMMA, $M_w$ = 9.59 kg/mol, PDI 1.05) were purchased from Polymer Standards Service GmbH and dissolved directly in methyl ethyl ketone (MEK, Aldrich). The mass ratio between PS and PMMA was 3:7 and the total concentration of the two polymers was 15 mg/mL.

Thin polymer-blend films were spin-coated at 1500 revolutions per minute (rpm) onto silicon substrates that were previously cleaned by $CO_2$ snow-jet treatment (at least 20 s for a 2 × 2 cm substrate). The relative humidity, measured by a Testo 635 Hygrometer, was adjusted to 40–45% during the spin-coating process. For the adjustment of the humidity, a mixture of water-saturated and pure nitrogen were led into the spin-coating chamber (approximately 1 L volume) at a flow rate of approximately 40 standard cubic centimeters per minute (40 sccm).

## Fabrication of SAM templates

After spin coating, the polymer films were treated with acetic acid where PMMA was selectively dissolved. The silicon samples were rinsed with the acid for 30 s and gently dried in a nitrogen flow. This procedure was repeated two times with fresh solvent. The fluorinated SAM was deposited from the gas phase: The samples were positioned face down at the lid of a desiccator containing two droplets of 1H,1H,2H,2H-perfluorodecyl trichlorosilane (Sigma-Aldrich) and evacuated to a pressure of 50 mbar. After 10–12 h in the desiccator, the samples were treated by $CO_2$ snow-jet in order to remove the PS islands and to expose islands of bare $SiO_x$-surface within the FDTS background. These islands were then back-filled by exposure to the vapor of 3-(aminopropyltriethoxy)-silane (Sigma-Aldrich). Further details and important parameters of the polymer-blend lithography process are described in [32]. The resulting pattern, consisting of amino-functionalized islands in a Teflon-like matrix (Figure 1b–d), was used as a template for the mineralization.

## Mineralization experiment

All deposition solutions were freshly prepared prior to use to ensure clear starting solutions. Stock solutions of $Zn(NO_3)_2{\cdot}6H_2O$ (Sigma-Aldrich, ≥99.0%), hexamethylene tetramine (HMTA, Sigma-Aldrich, ≥99.5%) and L-histidine (Sigma-Aldrich, ≥99%) in Milli-Q water each at a concentration of 45 mM, and were prepared according to Gerstel et al. [26]. For the preparation of the mineralization solution, equal amounts of HMTA and histidine stock solutions were mixed. Afterwards, the zinc nitrate solution was added dropwise to obtain a ratio of $[Zn^{2+}]$/[HMTA]/[His] of 1:1:1. The prestructured wafer was placed in 2 mL of the mineralization solution in a closed vessel and heated to 70 °C for 4 h. Several deposition experiments were performed and most yielded similar results; however, for some samples, no deposition was observed even after 4 h.

## Characterization

Atomic force microscopy images were obtained with a commercial Dimension Icon system (Bruker) in tapping mode under ambient conditions. SAM templates were scanned under water

in order to exclude the effect of meniscus forces of possible surface adsorbed water films on the topographic measurements.

Scanning electron micrographs were taken using a DSM 982 Gemini (Zeiss) at 3 kV and a working distance of 1–3 mm. To ensure conductivity, 0.2 nm of Pt/Pd (80:20) was sputtered onto the samples.

## Acknowledgements

We thank Peter Gerstel for experimental support and helpful discussions.

This work was supported by the Deutsche Forschungsgemeinschaft (DFG) within the Center for Functional Nanostructures (CFN) and by the Baden-Wuerttemberg Stiftung within the Network of Excellence "Functional Nanostructures". The support within the scope of the DFG priority program 1569 "Generation of multifunctional inorganic materials by molecular bionics" is also gratefully acknowledged.

## References

1. Liu, B.; Cao, Y.; Huang, Z.; Duan, Y.; Che, S. *Adv. Mater.* **2015,** *27,* 479–497. doi:10.1002/adma.201401485
2. Ryu, J.; Kim, S.; Kim, H. I.; Jo, E.-H.; Kim, Y. K.; Kim, M.; Jang, H. D. *Chem. Eng. J.* **2015,** *262,* 409–416. doi:10.1016/j.cej.2014.10.001
3. Pitta Bauermann, L.; Gerstel, P.; Bill, J.; Walheim, S.; Huang, C.; Pfeifer, J.; Schimmel, T. *Langmuir* **2010,** *26,* 3774–3778. doi:10.1021/la903636k
4. Coltrin, M. E.; Hsu, J. W. P.; Scrymgeour, D. A.; Creighton, J. R.; Simmons, N. C.; Matzke, C. M. *J. Cryst. Growth* **2008,** *310,* 584–593. doi:10.1016/j.jcrysgro.2007.11.030
5. Hsu, J. W. P.; Clift, W. M.; Brewer, L. N. *Langmuir* **2008,** *24,* 5375–5381. doi:10.1021/la703919w
6. Collins, R. J.; Shin, H.; DeGuire, M. R.; Heuer, A. H.; Sukenik, C. N. *Appl. Phys. Lett.* **1996,** *69,* 860–862. doi:10.1063/1.117916
7. Schmahl, W. W.; Griesshaber, E.; Kelm, K.; Ball, A.; Goetz, A.; Xu, D.; Kreitmeier, L.; Jordan, G. *Z. Kristallogr.* **2012,** *227,* 604–611. doi:10.1524/zkri.2012.1479
8. Kellermeier, M.; Cölfen, H.; García-Ruiz, J. M. *Eur. J. Inorg. Chem.* **2012,** *32,* 5123–5144. doi:10.1002/ejic.201201029
9. Ma, J.; Wang, J.; Ai, X.; Zhang, S. *Biotechnol. Adv.* **2014,** *32,* 744–760. doi:10.1016/j.biotechadv.2013.10.014
10. Checa, A. G.; Rodríguez-Navarro, A. B. *Biomaterials* **2005,** *26,* 1071–1079. doi:10.1016/j.biomaterials.2004.04.007
11. Petrack, J.; Jost, S.; Boenigk, J.; Epple, M. *Beilstein J. Nanotechnol.* **2014,** *5,* 554–560. doi:10.3762/bjnano.5.65
12. Pohl, A.; Weiss, I. M. *Beilstein J. Nanotechnol.* **2014,** *5,* 1823–1835. doi:10.3762/bjnano.5.193
13. Eisele, R.; Blumenstein, N. J.; Baier, J.; Walheim, S.; Schimmel, T.; Bill, J. *CrystEngComm* **2014,** *16,* 1560–1567. doi:10.1039/C3CE41701H
14. Detsri, E.; Popanyasak, J. *Colloids Surf., A* **2015,** *467,* 57–65. doi:10.1016/j.colsurfa.2014.11.019
15. Kadiri, H.; Kostcheev, S.; Turover, D.; Salas-Montiel, R.; Nomenyo, K.; Gokarna, A.; Lerondel, G. *Beilstein J. Nanotechnol.* **2014,** *5,* 1203–1209. doi:10.3762/bjnano.5.132
16. Rensmo, H.; Keis, K.; Lindström, H.; Södergren, S.; Solbrand, A.; Hagfeldt, A.; Lindquist, S.-E.; Wang, L. N.; Muhammed, M. *J. Phys. Chem. B* **1997,** *101,* 2598–2601. doi:10.1021/jp962918b
17. Arya, S. K.; Saha, S.; Ramirez-Vick, J. E.; Gupta, V.; Bhansali, S.; Singh, S. P. *Anal. Chim. Acta* **2012,** *737,* 1–21. doi:10.1016/j.aca.2012.05.048
18. Ozgur, U.; Hofstetter, D.; Morkoc, H. *Proc. IEEE* **2010,** *98,* 1255–1268. doi:10.1109/JPROC.2010.2044550
19. Assaud, L.; Monyoncho, E.; Pitzschel, K.; Allagui, A.; Petit, M.; Hanbücken, M.; Baranova, E. A.; Santinacci, L. *Beilstein J. Nanotechnol.* **2014,** *5,* 162–172. doi:10.3762/bjnano.5.16
20. Ismail, B.; Abaab, M.; Rezig, B. *Thin Solid Films* **2001,** *383,* 92–94. doi:10.1016/S0040-6090(00)01787-9
21. Inamdar, A. I.; Mujawar, S. H.; Ganesan, V.; Patil, P. S. *Nanotechnology* **2008,** *19,* 325706. doi:10.1088/0957-4484/19/32/325706
22. Gardeniers, J. G. E.; Rittersma, Z. M.; Burger, G. J. *J. Appl. Phys.* **1998,** *83,* 7844–7854. doi:10.1063/1.367959
23. Wang, Z. L. *J. Phys.: Condens. Matter* **2004,** *16,* R829. doi:10.1088/0953-8984/16/25/R01
24. Yang, P.; Yan, H.; Mao, S.; Russo, R.; Johnson, J.; Saykally, R.; Morris, N.; Pham, J.; He, R.; Choi, H.-J. *Adv. Funct. Mater.* **2002,** *12,* 323–331. doi:10.1002/1616-3028(20020517)12:5<323::AID-ADFM323>3.0.CO;2-G
25. AlZayed, N. S.; Ebothé, J.; Michel, J.; Kityk, I. V.; Yanchuk, O. M.; Prots, D. I.; Marchuk, O. V. *Physica E* **2014,** *60,* 220–223. doi:10.1016/j.physe.2014.01.032
26. Gerstel, P.; Hoffmann, R. C.; Lipowsky, P.; Jeurgens, L. P. H.; Bill, J.; Aldinger, F. *Chem. Mater.* **2006,** *18,* 179–186. doi:10.1021/cm051542o
27. Gerstel, P.; Lipowsky, P.; Durupthy, O.; Hoffmann, R. C.; Bellina, P.; Bill, J.; Aldinger, F. *J. Ceram. Soc. Jpn.* **2006,** *114,* 911–917. doi:10.2109/jcersj.114.911
28. Lin, W.-C.; Lee, S.-H.; Karakachian, M.; Yu, B.-Y.; Chen, Y.-Y.; Lin, Y.-C.; Kuob, C.-H.; Shyue, J.-J. *Phys. Chem. Chem. Phys.* **2009,** *11,* 6199–6204. doi:10.1039/b902044f
29. Shyue, J.-J.; De Guire, M. R.; Nakanishi, T.; Masuda, Y.; Koumoto, K.; Sukenik, C. N. *Langmuir* **2004,** *20,* 8693–8698. doi:10.1021/la049247q
30. Cuvillier, N.; Rondelez, F. *Thin Solid Films* **1998,** *327–329,* 19–23. doi:10.1016/S0040-6090(98)00579-3
31. Janssen, D.; De Palma, R.; Verlaak, S.; Heremans, P.; Dehaen, W. *Thin Solid Films* **2006,** *515,* 1433–1438. doi:10.1016/j.tsf.2006.04.006
32. Huang, C.; Moosmann, M.; Jin, J. H.; Heiler, T.; Walheim, S.; Schimmel, T. *Beilstein J. Nanotechnol.* **2012,** *3,* 620–628. doi:10.3762/bjnano.3.71